

2018-07-11

# Multimodal Imaging of Cortical Networks Controlling Lower Limb Locomotion: Towards the Development of Brain-Computer Interfaces

Kline, Adrienne

---

Kline, A. (2018). Multimodal Imaging of Cortical Networks Controlling Lower Limb Locomotion: Towards the Development of Brain-Computer Interfaces (Doctoral thesis, University of Calgary, Calgary, Canada). Retrieved from <https://prism.ucalgary.ca>. doi:10.11575/PRISM/32360  
<http://hdl.handle.net/1880/107138>

*Downloaded from PRISM Repository, University of Calgary*

UNIVERSITY OF CALGARY

Multimodal Imaging of Cortical Networks Controlling  
Lower Limb Locomotion: Towards the Development of Brain-Computer Interfaces

by

Adrienne Kline

A THESIS

SUBMITTED TO THE FACULTY OF GRADUATE STUDIES  
IN PARTIAL FULFILLMENT OF THE REQUIREMENTS FOR THE  
DEGREE OF DOCTOR OF PHILOSOPHY

GRADUATE PROGRAM IN BIOMEDICAL ENGINEERING  
CALGARY, ALBERTA

JULY, 2018

© Adrienne Kline 2018

## **ABSTRACT**

In 2015 the National Spinal Cord Injury Association of Canada reported that 30,000 Canadians suffer from paralysis in two or more limbs. In many cases this takes away the fundamental ability to walk. Walking, an intricate sensorimotor task, involves the interactions of both dynamic and balancing neurological processes. Brain computer interfaces (BCIs) are attempting to bridge the gap that will allow persons with compromised mobility to interact with the world via control of prosthetic devices that can ‘act’ by using solely neural input (i.e. thoughts). The goal of this thesis was to aid in the development of a BCI for lower limb locomotion by identifying similarities and differences between cortical activity associated with executed and imagined left and right lower limb movements using electroencephalogram (EEG) and functional magnetic resonance imaging (fMRI). Data from 16 participants showed that it was possible to differentiate between right versus left executed and imagined thought processes for lower limb locomotion using solely information from an EEG, and that these patterns of brain activity were generalizable across time points and trials. It was also found, through the use of fMRI, that areas of brain activation in executed and imagined conditions were similar for some areas but showed unique activation areas as well. A novel paradigm to co-register EEG and fMRI data was developed that can easily be utilized in other contexts. Finally, using EEG and fMRI data allowed for an efficient model to use in a machine learning paradigm that successfully predicted left versus right lower limb movement. This research adds to the existing body of knowledge in understanding psychomotor brain activity associated with thought coordination processes involved in the task of walking in normal persons represented by algorithmic patterns.

## **ACKNOWLEDGEMENTS**

This project would not have been possible without the support of many individuals. I'd like to thank my supervisors, Dr. Janet Ronksy and Dr. Bradley Goodyear, and my supervisory committee members, Dr. Nils Forkert and Dr. Naweed Syed, for sharing your most precious commodity, your time and wisdom. Special thanks to Dan Pittman, without whose help this project would not have been possible. In addition, thanks go to the technicians of the Seaman Family MR Research Centre for MR data collection without fail, and to all my administrators (gate keepers) who pushed all my paperwork through and scheduled multiple events on my behalf over the past four years. Thanks go to the many lab members: Payam Zandiyyeh, Banafshe Felfeliyan, Tomasz Bugajski, Jess Küpper, Alonso Figuerawho were there for me to bounce ideas off of and who acted as a support group. And my summer student (minion) Calin Gaina Ghiroaga, without whose help I would still be collecting data. Finally, I'd like to thank my parents for supporting me emotionally and intellectually over these past 25 years, my grandfather for encouraging me into sciences from a young age, my sister Jocelyn for being my first friend and my loving family. In addition, this work was financially supported by the Natural Science and Engineering Research Council of Canada (NSERC), Alberta Innovates Technology Futures (AITF), Canadian Institutes of Health Research (CIHR), and the Biomedical Engineering Program at the University of Calgary.

## **DEDICATION**

To my giants,

Dr. Donald and Dr. Theresa Kline.

You have provided me with footsteps to follow in, and shoulders to stand on.

*“I would rather have questions that can’t be answered than answers that can’t be questioned.”*

~ Richard Feynman

*“When you have exhausted all possibilities, remember this; you haven’t.”*

~ Thomas Edison

*“Chaos: When the present predicts the future, but the approximate present does not approximately determine the future.”*

~Edward Lorenz

## TABLE OF CONTENTS

<b>ABSTRACT.....</b>	<b>II</b>
<b>ACKNOWLEDGEMENTS .....</b>	<b>III</b>
<b>DEDICATION .....</b>	<b>IV</b>
<b>TABLE OF CONTENTS .....</b>	<b>VI</b>
<b>LIST OF FIGURES.....</b>	<b>X</b>
<b>LIST OF TABLES.....</b>	<b>XIII</b>
<b>LIST OF SYMBOLS, ABBREVIATIONS AND NOMENCLATURE .....</b>	<b>XV</b>
<b>CHAPTER 1: THESIS INTRODUCTION .....</b>	<b>1</b>
1.1 OVERVIEW AND STATEMENT OF PROBLEM .....	1
1.2 GOALS OF THE THESIS AND THESIS STRUCTURE.....	4
1.3 MY ROLE AND THE CONTRIBUTIONS OF OTHERS .....	6
<b>CHAPTER 2: BACKGROUND AND HYPOTHESES .....</b>	<b>8</b>
2.1 RECIPROCAL INHIBITION AND WALKING .....	8
2.2 IMAGINED WALKING .....	12
2.3 ELECTROENCEPHALOGRAPHY (EEG).....	14
2.3.1 <i>BASIC PRINCIPLES</i> .....	14
2.3.2 <i>EEG IN LOWER LIMB STUDIES</i> .....	17
2.4 MAGNETIC RESONANCE IMAGING (MRI).....	20
2.4.1 <i>BASIC PRINCIPLES</i> .....	20
2.5 FUNCTIONAL MRI (fMRI).....	25
2.5.1 <i>BASIC PRINCIPLES</i> .....	25
2.5.2 <i>fMRI STUDIES OF LOWER LIMB MOVEMENTS</i> .....	27

2.6 COMBINING EEG AND FMRI DATA.....	29
2.7 MACHINE LEARNING .....	31
2.8 HYPOTHESES.....	35
<b>CHAPTER 3: THE COMPARABILITY OF LEG MOVEMENT KINEMATICS DURING TYPICAL WALKING AND DURING SIMULATED WALKING IN A SUPINE POSITION .....</b>	<b>37</b>
3.1 INTRODUCTION .....	37
3.2 METHODS.....	38
3.2.2 <i>DATA COLLECTION</i> .....	39
3.3 RESULTS .....	45
3.4 DISCUSSION .....	53
3.5 LIMITATIONS.....	54
3.6 CONCLUSION.....	54
<b>CHAPTER 4: AN MR-COMPATIBLE APPARATUS FOR SIMULATED STEPPING.....</b>	<b>56</b>
4.1 INTRODUCTION .....	56
4.2 METHODS.....	57
4.3 RESULTS .....	64
4.4 DISCUSSION .....	66
<b>CHAPTER 5: MAIN STUDY METHODOLOGY .....</b>	<b>68</b>
5.1 METHODS.....	68
<b>CHAPTER 6: DIFFERENTIATING THE CORTICAL CONTRIBUTIONS OF RIGHT AND LEFT STEPPING MOVEMENTS USING ELECTROENCEPHALOGRAPHY .....</b>	<b>74</b>
6.1 INTRODUCTION .....	74
6.2 METHODS.....	75
6.3 RESULTS .....	79
6.4 DISCUSSION .....	88

6.5 LIMITATIONS.....	90
6.6 FUTURE WORK .....	91
6.7 CONCLUSION.....	91
<b>CHAPTER 7: DIFFERENTIATING THE BRAIN'S INVOLVEMENT IN EXECUTED AND IMAGING STEPPING USING FMRI .....</b>	<b>92</b>
7.1 INTRODUCTION .....	92
7.2 METHODS.....	93
7.3 RESULTS .....	97
7.4 DISCUSSION .....	112
7.5 LIMITATIONS.....	117
7.6 FUTURE WORK .....	119
7.7 CONCLUSION.....	119
<b>CHAPTER 8: FMRI INFORMED EEG FOR THE COMPUTER-GENERATED IMAGE TASKS .....</b>	<b>120</b>
8.1 INTRODUCTION .....	120
8.2 METHODS.....	121
8.3 RESULTS .....	129
8.4 DISCUSSION .....	133
8.5 LIMITATIONS.....	135
8.6 FUTURE WORK .....	135
8.7 CONCLUSION.....	136
<b>CHAPTER 9: THE INTERPRETATION OF BRAIN ACTIVITY USING MACHINE LEARNING .....</b>	<b>137</b>
9.1 INTRODUCTION .....	137
9.2 METHODS.....	143

9.4 DISCUSSION .....	156
9.5 LIMITATIONS.....	158
9.6 FUTURE WORK .....	159
9.7 CONCLUSIONS.....	162
<b>CHAPTER 10: REVIEW OF FINDINGS, SIGNIFICANCE, LIMITATIONS, FUTURE WORK, AND CONCLUSION.....</b>	<b>163</b>
10.1. INTRODUCTION .....	163
10.2 PILOT WORK.....	163
10.3 SUPPORT FOR HYPOTHESES .....	164
10.4 LIMITATIONS.....	167
10.5 SIGNIFICANCE .....	168
10.6 FUTURE WORK – BASED ON COLLECTED DATA .....	169
10.7 FUTURE WORK – NEW DIRECTIONS .....	171
10.8 CONCLUSION.....	173
<b>REFERENCES .....</b>	<b>175</b>
<b>APPENDIX A: SAMPLE MRI SCREENING FORM.....</b>	<b>197</b>
<b>APPENDIX B: REGISTRATION OF MRI DATA .....</b>	<b>198</b>
<b>APPENDIX C: PREDICTING FMRI FROM EEG.....</b>	<b>199</b>

## LIST OF FIGURES

### Chapter 1

FIGURE 1.1 OVERVIEW OF A BRAIN-COMPUTER INTERFACE AND FOCAL AREA OF CURRENT RESEARCH.....	2
---	---

### Chapter 2

FIGURE 2.1 OVERVIEW OF THE CENTRAL NERVOUS SYSTEM CONTROLLING LOCOMOTION.....	12
FIGURE 2.2 PYRAMIDAL NEURON WITH THE VOLTAGE POTENTIAL LINES .....	15
FIGURE 2.3 THE 10-20 EEG ELECTRODE SET UP AND BRAIN MODEL FROM A TOP DOWN VIEW.....	16
FIGURE 2.4 A PARALLEL SPIN AND AN ANTI PARALLEL SPIN IN AN EXTERNAL MAGNETIC FIELD.....	21
FIGURE 2.5 APPLICATION OF A 90 DEGREE RF PULSE TO THE NET MAGNETIZATION IN EQUILIBRIUM .....	22
FIGURE 2.6 DIAGRAM OF TIME CONSTANTS T1 AND T2 IN THE LONGITUDINAL AND TRANSVERSE PLANES.....	23
FIGURE 2.7 HEMODYNAMIC RESPONSE FUNCTION. ....	26
FIGURE 2.8 OVERVIEW OF MACHINE LEARNING. ....	33

### Chapter 3

FIGURE 3.1 MARKER SETUP DISPLAYING THE ANATOMICAL LANDMARKS .....	39
FIGURE 3.2 EULER COORDINATE SYSTEM. ....	42
FIGURE 3.3 EXAMPLE OF ONE CYCLE OF KNEE FLEXION .....	46
FIGURE 3.4 WALKING AND SUPINE KNEE FLEXION (MEASURED IN DEGREES) FOR PARTICIPANT 1, FOR 5 TRIALS .....	47
FIGURE 3.5 WALKING AND SUPINE KNEE FLEXION (MEASURED IN DEGREES) FOR PARTICIPANT 2, FOR 5 TRIALS .....	48
FIGURE 3.6 WALKING AND SUPINE KNEE FLEXION (MEASURED IN DEGREES) FOR PARTICIPANT 3, FOR 5 TRIALS .....	48
FIGURE 3.7 AN AVERAGED KNEE FLEXION FOR UPRIGHT WALKING AND SUPINE LOCOMOTION .....	49
FIGURE 3.8 HEAD FLEXION DURING SUPINE LOCOMOTION OVER NORMALIZED TIME FOR 3 PARTICIPANTS .....	50
FIGURE 3.9 HEAD FLEXION (BLUE) DURING NORMALIZED TIME OF A SUPINE KNEE FLEXION (ORANGE) .....	51
FIGURE 3.10 HEAD TRANSLATION WITH RESPECT TO CHEST. ....	53

### Chapter 4

FIGURE 4.1 MR SCANNER BED DIMENSIONS .....	58
FIGURE 4.2 CAD DESIGN OF LAMRI.....	60
FIGURE 4.3 MR COMPATIBLE BOARD. THE TAPE MEASURE IN THE PICTURE DENOTES (2 FT) FOR SCALE.....	60
FIGURE 4.4 RIG PEDAL FROM THE END VIEW.....	61
FIGURE 4.5 RESPONSE BUTTON PAD INCORPORATED FOR TIME STAMPING DATA IN EEGS .....	62

FIGURE 4.6 MR COMPATIBLE RIG IN MR SCANNER WITH PARTICIPANT POSITIONED IN STEPPING MOVEMENT.....	63
FIGURE 4.7 HEAD TRANSLATIONS OF THE 3 PARTICIPANTSESTIMATED FROM FSL.....	65
FIGURE 4.8 KNEE FLEXION ANGLE OVER THE COURSE OF 5 TRIALS.....	66

## Chapter 5

FIGURE 5.1 PARTICIPANT LYING IN A SUPINE POSITION ON THE MR- COMPATIBLE RIG .....	69
FIGURE 5.2 CGI STIMULUS OF A HUMAN.....	71
FIGURE 5.3 GREEN (LEFT) AND BLUE (RIGHT) CIRCLE STIMULI.....	71
FIGURE 5.4 SAMPLE OF BLOCK DESIGN OF THE STEPPING TASK .....	72

## Chapter 6

FIGURE 6.1 VISUAL REPRESENTATION OF EPOCHING RIGHT (R) AND LEFT (L) STEPPING.....	76
FIGURE 6.2 EEG PROCESSING PIPELINE .....	77
FIGURE 6.3 TRACES DURING A RIGHT STEP FOR ELECTRODES C1 AND C2, .....	80
FIGURE 6.4 TRACES OF DURING A LEFT STEP FOR ELECTRODES C1 AND C2 .....	80
FIGURE 6.5 PLOTS OF EEG FREQUENCY BAND DATA FOR ELECTRODES C1 AND C2 .....	83
FIGURE 6.6 PLOTS OF EEG FREQUENCY BAND DATA FOR ELECTRODES C1 AND C2 .....	83
FIGURE 6.7 PLOTS OF EEG FREQUENCY BAND DATA FOR ELECTRODES C1 AND C2.....	83
FIGURE 6.8 PLOTS OF EEG FREQUENCY BAND DATA FOR ELECTRODES C1 AND C2 .....	84

## Chapter 7

FIGURE 7.1 A MODEL FOR ON/OFF VOXEL ACTIVATION OVER TIME FOR A SINGLE VOXEL. ....	95
FIGURE 7.2 HARVARD-OXFORD BRAIN ATLAS.....	96
FIGURE 7.3 EXAMPLE OF A PAIRED-T TEST SETUP WITHIN FSL.....	97
FIGURE 7.4 GROUP MAPS OF BRAIN REGION DURING CGI-EXECUTED LEG MOVEMENTS .....	98
FIGURE 7.5 GROUP MAPS OF BRAIN REGIONS DURING CGI-IMAGINED LEG MOVEMENTS .....	99
FIGURE 7.6 GROUP MAPS OF BRAIN R DURING BLUE/GREEN-EXECUTED LEG MOVEMENTS. ....	100
FIGURE 7.7 GROUP MAPS OF BRAIN REGIONS DURING BLUE/GREEN-IMAGINED LEG MOVEMENTS .....	101
FIGURE 7.8 GROUP MAPS OF BRAIN REGIONS DURING CGI-EXECUTED THAN CGI-IMAGINED LEG MOVEMENTS.....	103
FIGURE 7.9 GROUP MAPS OF BRAIN REGIONS DURING CGI-IMAGINED THAN CGI-EXECUTED LEG MOVEMENTS.....	105
FIGURE 7.10 GROUP MAPS OF BRAIN REGIONS DURING BLUE/GREEN-EXECUTED THAN BLUE/GREEN-IMAGINED .....	106
FIGURE 7.11 GROUP MAPS OF BRAIN REGIONS DURING BLUE/GREEN-IMAGINED THAN DBLUE/GREEN EXECUTED.....	107

FIGURE 7.12 GROUP MAPS OF BRAIN REGIONS DURING BLUE/GREEN-EXECUTED THAN CGI-EXECUTED .....	108
FIGURE 7.13 GROUP MAPS OF BRAIN REGIONS DURING CGI-EXECUTED THAN BLUE/GREEN-EXECUTED .....	109
FIGURE 7.14 GROUP MAPS OF BRAIN REGIONS DURING BLUE/GREEN THAN DURING CGI IMAGINED .....	110
FIGURE 7.15 GROUP MAPS OF BRAIN REGIONS DURING CGI THAN DURING BLUE/GREEN IMAGINED .....	111
FIGURE 7.16 REPRESENTATION OF DUAL-STREAM THEORY .....	117

## Chapter 8

FIGURE 8.1 FLOWCHART OVERVIEW OF THE PROCESS USED TO CO-REGISTER EEG AND fMRI.....	122
FIGURE 8.2 SEGMENTATION OF THE EEG ELECTRODES .....	123
FIGURE 8.3 EXAMPLE OF A MAGLINK 64 ELECTRODE EEG CAP .....	124
FIGURE 8.4 fMRI CLUSTERS FROM THE CGI IMAGINED CONDITION, LABELLED 1 THROUGH 7 .....	126
FIGURE 8.5 fMRI CLUSTERS FROM THE CGI EXECUTED CONDITION, LABELLED 1 THROUGH 3 .....	126
FIGURE 8.6 CLOSE-UP OF A MOCK UP SECTION OF FIGURES 8.4 AND 8.5.....	127

## Chapter 9

FIGURE 9.1 OVERVIEW OF A BRAIN-COMPUTER INTERFACE .....	137
FIGURE 9.2 CORTICAL HOMUNCULUS (CORONAL SLICE).....	139
FIGURE 9.3 A) BIOLOGICAL NEURON (BN) AND B) AN ARTIFICIAL NEURON (AN). .....	140
FIGURE 9.4 SIMPLE ANN.....	141
FIGURE 9.5 FLOW CHART FOR DETERMINING RIGHT OR LEFT LOWER LIMB MOVEMENT. .....	143
FIGURE 9.6 GRAPHICAL REPRESENTATION OF THE SIGMOID ACTIVATION FUNCTION.....	145
FIGURE 9.7 FINAL NETWORK ARCHITECTURE .....	150
FIGURE 9.8 AN EXAMPLE OF GROUP TRAINING (LEFT) AND INDIVIDUAL TRAINING (RIGHT) .....	151

## LIST OF TABLES

### Chapter 2

TABLE 2.1 EEG FREQUENCY BANDS AND THEIR ASSOCIATED FUNCTIONS [51] ..... 17

TABLE 2.2 AN EXAMPLE OF A 2-CLASS CONFUSION MATRIX FOR EVALUATING A CLASSIFICATION ..... 33

### Chapter 3

TABLE 3.1 AVERAGE HEAD DISPLACEMENT DURING SUPINE KNEE FLEXION MOVEMENTS..... 52

### Chapter 4

TABLE 4.1 HEAD TRANSLATION DURING SUPINE MOVEMENT..... 64

### Chapter 6

TABLE 6.1 EEG DIFFERENTIATION OF RIGHT AND LEFT STEPPING USING THE CGI STIMULUS ..... 81

TABLE 6.2 EEG DIFFERENTIATION OF RIGHT AND LEFT STEPPING ..... 82

TABLE 6.3 GENERALIZABILITY FINDINGS FOR THE CGI EXECUTED AND IMAGINED CONDITIONS ..... 85

TABLE 6.4 GENERALIZABILITY FINDINGS FOR THE CGI EXECUTED AND IMAGINED CONDITIONS ..... 86

TABLE 6.5 GENERALIZABILITY FINDINGS FOR THE BLUE-GREEN EXECUTED AND IMAGINED CONDITIONS ..... 87

TABLE 6.6 GENERALIZABILITY FINDINGS FOR THE BLUE-GREEN EXECUTED AND IMAGINED CONDITIONS ..... 88

### Chapter 7

TABLE 7.1 BRAIN REGIONS SIGNIFICANTLY ACTIVATED DURING ( $P < 0.05$ )..... 98

TABLE 7.2 BRAIN REGIONS SIGNIFICANTLY ACTIVATED DURING ( $P < 0.05$ )..... 99

TABLE 7.3 BRAIN REGIONS SIGNIFICANTLY ACTIVATED DURING ( $P < 0.05$ )..... 100

TABLE 7.4 BRAIN REGIONS SIGNIFICANTLY ACTIVATED DURING ( $P < 0.05$ )..... 101

TABLE 7.5 BRAIN REGIONS WHOSE ACTIVITY WAS SIGNIFICANTLY GREATER ( $P < 0.05$ ) ..... 102

TABLE 7.6 BRAIN REGIONS WHOSE ACTIVITY WAS SIGNIFICANTLY GREATER ( $P < 0.05$ ). ..... 104

TABLE 7.7 BRAIN REGIONS WHOSE ACTIVITY WAS SIGNIFICANTLY GREATER ( $P < 0.05$ ). ..... 105

TABLE 7.8 BRAIN REGIONS WHOSE ACTIVITY WAS SIGNIFICANTLY GREATER ( $P < 0.05$ ) ..... 107

TABLE 7.9 BRAIN REGIONS WHOSE ACTIVITY WAS SIGNIFICANTLY GREATER ( $P < 0.05$ ) ..... 108

TABLE 7.10 BRAIN REGIONS WHOSE ACTIVITY WAS SIGNIFICANTLY GREATER ( $P < 0.05$ ) ..... 109

TABLE 7.11 BRAIN REGIONS WHOSE ACTIVITY WAS SIGNIFICANTLY GREATER ( $P < 0.05$ ) ..... 110

TABLE 7.12 BRAIN REGIONS WHOSE ACTIVITY WAS SIGNIFICANTLY GREATER ( $P < 0.05$ ) ..... 111

## Chapter 8

TABLE 8.1 WEIGHTING OF EEG ELECTRODES ON AN FMRI CLUSTER-WISE BASIS FOR CGI IMAGINED CONDITION ... 130

TABLE 8.2 WEIGHTING OF EEG ELECTRODES ON AN FMRI CLUSTER-WISE BASIS FOR CGI EXECUTED CONDITION .. 132

## Chapter 9

TABLE 9.1 EFFECT OF LEARNING RATE ON TRAINING ACCURACY ..... 149

TABLE 9.2 EFFECT OF NUMBER OF HIDDEN LAYERS ON TRAINING ACCURACY ..... 149

TABLE 9.3 EFFECT OF NUMBER OF NEURONS IN EACH HIDDEN LAYER ON TRAINING ACCURACY ..... 149

TABLE 9.4 EFFECT OF NUMBER OF TRAINING EPOCHS ON TRAINING ACCURACY ..... 150

TABLE 9.5 CONFUSION MATRIX FOR GROUP CLASSIFICATION OF ACTIVE THOUGHT VERSUS REST THOUGHT. .... 153

TABLE 9.6 CONFUSION MATRIX FOR ACTIVE THOUGHT VERSUS REST THOUGHT ..... 153

TABLE 9.7 CONFUSION MATRIX FOR GROUP CLASSIFICATION FOR IMAGINED STEPPING ..... 153

TABLE 9.8 CONFUSION MATRIX FOR INDIVIDUAL CLASSIFICATION FOR IMAGINED STEPPING ..... 154

TABLE 9.9 CONFUSION MATRIX FOR FMRI INFORMED EEG SELECTED ELECTRODES (FC1, FCZ, FC3, F5)..... 154

TABLE 9.10 CONFUSION MATRIX FOR FMRI INFORMED EEG SELECTED ELECTRODES (FC1, FCZ, FC3, FC5) ..... 155

TABLE 9.11 TOP FOUR PREDICTORS SELECTED FOR BCI USE BY RELIEFF ALGORITHM FROM 192 PREDICTORS ..... 156

## LIST OF SYMBOLS, ABBREVIATIONS AND NOMENCLATURE

AgCl	Silver Chloride
AN	Artificial neuron
ANOVA	Analysis of variance
BCI	Brain-Computer Interface
BN	Biological Neuron
BOLD	Blood Oxygen Level Dependent
CAD	Computer-Aided Drafting
CGI	Computer-Generated Image
CPG	Central Pattern Generator
DFT	Discrete Fourier Transform
ECG	Electrocardiogram
EEG	Electroencephalography
fMRI	functional Magnetic Resonance Imaging
G	Gauss
GEE	Generalized Estimating Equations
GLM	General Linear Model
G-theory	Generalizability Theory
HRF	Hemodynamic Response Function
ICA	Independent Component Analysis
ICC	Intra-class correlation coefficient
MNI	Montreal Neurological Institute
MRI	Magnetic Resonance Imaging
NN	Neural Network
ReLU	Rectified Linear Unit
SVM	Support Vector Machine
T	Tesla
V	Volts

## **CHAPTER 1: THESIS INTRODUCTION**

### **1.1 Overview and Statement of Problem**

Walking is fundamental for a healthy quality of life. Spinal cord injury (SCI) and neurodegenerative diseases such as Parkinson's disease (PD), amyotrophic lateral sclerosis (ALS), and multiple sclerosis (MS), can render a person paraplegic. The healthcare and economic costs associated with paraplegia are staggering, from the initial injury through the weeks and months of rehabilitation, if it is even possible. While neurodegenerative diseases are typically associated with deterioration of central and peripheral neural pathways, in SCI these pathways remain essentially intact, although there is degradation of spinal neuronal activity over the long term if neuronal activity is not maintained [1], highlighting the need for training after injury. Thus, hope remains for those with compromised mobility to regain the ability to walk if these connections can be repaired or circumvented. Stem cell therapy offers one alternative for repairing the spinal cord in some cases. In other cases, brain-computer interfaces (BCIs) may provide a means to circumvent the injured site by providing thought control of muscle groups or exoskeletons [2],[3]. The current research focuses on BCI development.

Figure 1.1 shows an overview of how a BCI operates. The first stages in the development of an effective BCI are to acquire and process brain activity data, and these are the focal areas of the current research project. Maximizing the success of a lower limb BCI requires that accurate data are acquired and the most efficient way of processing those data is determined. To get to this point, however, a better understanding of the brain's involvement in human locomotion is needed.

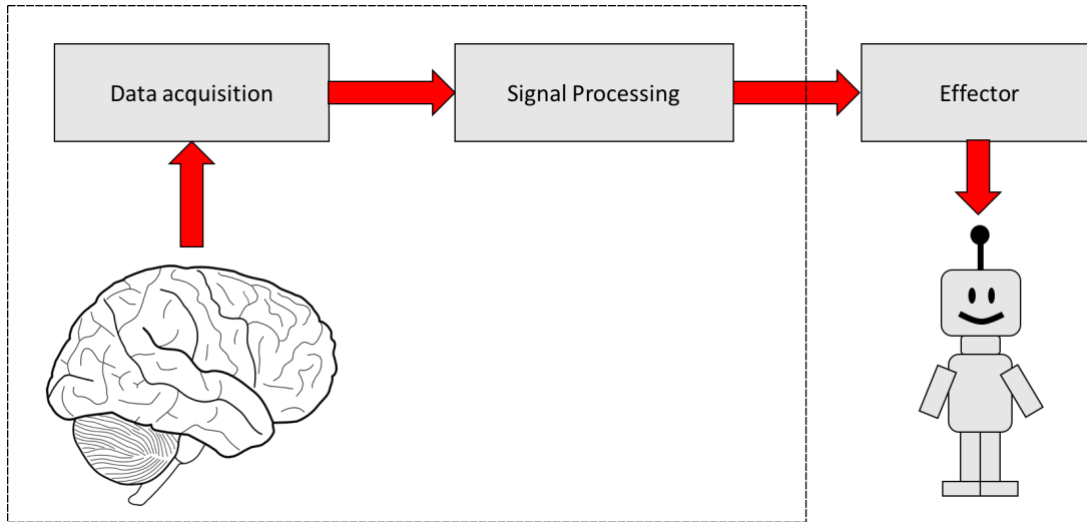


**Figure 1.1 Overview of a Brain-Computer Interface and Focal Area of Current Research**

Normal walking is an intricate task involving the integration of sensorimotor and cognitive neurological processes [4], [5]. Research on these processes is limited, due in part to difficulties associated with acquiring brain signals during locomotion [6]. To date, two modalities have been primarily used to study walking and other lower limb movements: electroencephalography (EEG) and functional magnetic resonance imaging (fMRI). EEG has been used to study and identify areas of cortical activity involved in lower limb movements [7],[8]. In addition, EEG has been used in the design of a BCI system to control robotic hands during a grasping task [9]. Indeed, several classification algorithms have successfully been developed in the design of EEG-based BCIs [10]. The addition of fMRI data to our collective understanding has led to more comprehensive models of the network architecture associated with hand grasping tasks [11],[12],[13]. However, BCIs for the lower limbs using data acquired from these methodologies have not been investigated fully. This represents a major research gap.

fMRI data collection during lower limb movement is non-trivial, as fMRI requires participants to lie in a supine position within a physically restrictive space that doesn't readily allow leg movements to mimic walking. Thus, research in this area has been more recent and

confined primarily to describing the brain activation patterns associated with simple lower limb movements such as ankle dorsiflexion [14],[15],[16]. Some studies have used devices located immediately outside the fMRI scanner that allow the participant to simulate walking, such as a robotic assisted stepper [17] or a rolling cylinder [18]; however, these technologies have seen limited usage and do not account for some of the intricate properties of walking, such as knee joint kinematics and the influence of gravity on the stepping motion.

As an alternative to executed walking, some fMRI studies have asked participants to imagine themselves walking (imagined walking) as a proxy for executed walking [19], [20], because it is believed that imagined and executed actions, including walking, share similar neural substrates [21]. Most fMRI studies using imagined tasks, however, have been confined to upper limb movements [22],[23]; this is also the case for the majority of the body of work done with EEG [24]. The development of an effective BCI for lower limb movements greatly depends on establishing that imagined lower limb movements have a similar cortical signature to that of executed movements. Of equal importance are the stimuli used to facilitate the imagination of lower limb movement. These have been varied and include task memorization [25], instruction to imagine [26], presentation of a fixation cross followed by a visual word instruction [22], and flashing lights [23], generally without rationale.

It is clear then that the development of BCIs for use in lower-limb movements remains in its infancy. For example, EEG-driven BCIs have been used to control an avatar in virtual environments (forward, left, right movements) [27], [28]. Others have used robot-assisted [29], [30] or non-robot assisted BCIs on a training treadmill [29]. Modelling the neural activity associated with the components of the walking sequence (e.g., alternating left and right movements of the hip, knee, and ankle) in more detail may improve the design of such devices.

This project contributes to the BCI development process insofar as it aims to increase the fidelity of the input process through accurate feature extraction and translation for lower limb movement and classification. All of these considerations provided the impetus for this current research project as well as the methodology used therein.

## **1.2 Goals of the Thesis and Thesis Structure**

The goal of this thesis was to aid in the development of a BCI for lower limb locomotion. Within the goal it was important to accurately determine the similarity and differences between cortical activity associated with executed and imagined left and right lower limb movements, while observing two different visual stimuli, using EEG and fMRI. Second, information from both technologies was used to better understand the spatial and temporal aspects of imagined and executed walking. And lastly these data were used to predict activity associated with left versus right lower limb movement. This information is anticipated to be useful in a machine learning context that will assist in the long-term development of a lower limb BCI. The background, specific hypotheses, and rationales for them, associated with this goal will be described in the next chapter.

The thesis is divided into 10 chapters. The current chapter, Chapter 1, provides an overview that: a) provides a brief, compelling rationale for the work, b) places the work in the context of extant research, c) outlines the goals of the thesis, and d) describes how the project will be presented.

Chapter 2 is an introduction to the current understanding of the neuromotor control mechanisms underlying walking, as well as a review of EEG and fMRI and their use to date in

studies of locomotion. An overview of machine learning, including the various types and what applications these might have will provide context as to the approach used in the current study.

Chapter 3 details a pilot study of three healthy participants to compare the kinematics of upright walking relative to lower limb locomotion executed in a supine position in the MR scanner. In addition, this chapter quantified the amount of head motion that occurs during supine locomotion that would need to be addressed in neuroimaging.

Chapter 4 describes the iterative design and development of an MRI-compatible device to allow participants to move the lower body extremities while inside the MR scanner, appropriately restricting head motion and accurately mimicking lower limb kinematics during stepping.

Chapter 5 describes the data collection methodology (participants and procedures) common to all of the experiments of the subsequent chapters.

Chapters 6-9 present the results of the studies conducted for this thesis. Each of the four chapters is devoted to the four specific hypotheses that are developed in Chapter 2.

Chapter 6 describes the main EEG findings, including the isolation of executed and imagined walking EEG brain activity patterns that permit differentiation between right and left leg movements and an assessment of the reliability of the EEG data.

Chapter 7 describes the main fMRI findings, including the differences between executed and imagined movements, with computer-generated versus neutral visual stimuli, and the visual pathways associated with this difference.

Chapter 8 outlines a novel way to integrate EEG with fMRI data that were collected during the computer-generated stimulus walking condition.

Chapter 9 describes predictive models developed using machine learning of EEG parameters, and how the model changes by introducing relevant fMRI parameters.

Chapter 10 summarizes the thesis work, identifies limitations, and suggests future avenues of research.

### **1.3 My Role and the Contributions of Others**

My contribution to this research project was as lead investigator responsible for project formation, experimental design and project planning. I conducted the EEG data collection and analysis, designed and collected the fMRI data, developed customized software required for stimuli and analysis, designed necessary hardware that did not previously exist, performed statistical analyses and was lead author on manuscripts.

Many individuals contributed to this body of work. Dr. Janet Ronsky and Dr. Bradley Goodyear and supervisory committee members, Dr. Naweed Syed and Dr. Nils Forkert, were responsible for guidance in planning and conducting the studies. Dan Pittman aided in fMRI data collection, as well as troubleshooting and fabrication of mechanical designs. A research assistant student (summer 2017), Calin Gaina Ghiroaga, participated in the data collection. Peter Byrne was also responsible for some of the fabrication of machined parts. Dr. Bradley Goodyear and Dr. Janet Ronsky assisted in manuscript editing and journal selection for this body of work.

## **1.4 Publication of Findings Generated from Thesis**

Two abstracts and one presentation have resulted from this research thus far. The abstracts were presented at the Organization for Human Brain Mapping (OHBM) conference proceedings in Singapore, June 2018. These were generated from the isolation of right and left stepping (Chapter 6) and the generalizability-theory analysis with respect to EEG (Chapter 6). A paper based on Chapter 3, on control of head movement during lower limb movement will be presented at the Biennial Meeting of the Canadian Society for Biomechanics in Halifax, August 2018.

Abstract 1:

A. Kline, D. Pittman, C. Ghiroaga, B. Goodyear, J. Ronsky, “*Isolating Right and Left Stepping in EEG*”, 24th Annual Meeting of the Organization for Human Brain Mapping, Singapore, June 2018.

Abstract 2:

A. Kline, D. Pittman, C. Ghiroaga, B. Goodyear, J. Ronsky, “*Generalizability Theory: Demonstrating the Process and its Utility with EEG Measurements*”, 24th Annual Meeting of the Organization for Human Brain Mapping, Singapore, June 2018.

Presentation:

A. Kline, P. Zandiyyeh, T. Bugajski, B. Goodyear, J. Ronsky, “*Controlling Head Movement During Lower Limb Locomotion to Understand Neuromotor Control*”, 20<sup>th</sup> Biennial Meeting of the Canadian Society for Biomechanics, Halifax, Canada, August 2018.

## CHAPTER 2: BACKGROUND AND HYPOTHESES

This chapter reviews the brain's involvement in walking, followed by a description of the methodologies used in this research: electroencephalography (EEG), magnetic resonance imaging (MRI), functional magnetic resonance imaging (fMRI) and machine learning. In addition, the literature associated with motor imagery and mirror neurons is presented. Finally, the extant literature in these areas relevant for this project are described, leading to the research hypotheses.

### 2.1 Reciprocal Inhibition and Walking

Walking is a sensorimotor task that involves the coordinated flexion and extension of muscles of the hips, legs and feet. At the simple motor level, this coordination is accomplished by reciprocal inhibition of neurons controlling the flexor muscles on one side of a joint, such as the muscles of the hamstrings for the knee, contract, causing flexion, while simultaneously the neurons controlling the extensor muscles on the other side of the joint are inhibited allowing for stretching (quadricep). Then the opposite occurs, in that those muscles that were flexed now relax and extend, while the extensors fire and flex. This alternating sequence is integral for smooth repetitive movements like walking [31].

Over a hundred years ago, Brown [32] stated that “acts of progression”, such as mammalian walking, are automatic, in that there is an integration of reflex movements that follow each other smoothly and successively. What was particularly interesting about this concept was that neither descending nor sensory input was needed to generate a stepping motion. While this idea was revolutionary at the time, by the latter part of the 20<sup>th</sup> century it was commonly accepted that rhythmic movements are generated by the central nervous system and do not require sensory feedback for their execution [33]. Brown's model, called “reciprocal inhibition” or “half-center”,

suggested there were opposing paired centers in the spinal cord – one that excited flexors and inhibited extensors, and another that excited extensors and inhibited flexors [31]. These centers would mutually inhibit each other so as to generate the flexor-extensor rhythm, where the rhythmic output was modulated by sensory and proprioceptive input.

Brown's work went largely unnoticed for several decades, while the prevailing theory of locomotion at that time was to attribute its rhythmic nature to reflexes and sensory input generated through motion itself [31]. Lundberg in the 1960s revived Brown's earlier hypotheses, and by the end of the century, building on Brown's early work, it became well established that the basic pattern of alternating flexion and extension in mammalian locomotion was produced by spinal central pattern generators (CPGs) [34].

There has been extensive study of CPGs in invertebrates and some animals, but very little in mammals; of particular importance is how the CPG integrates descending commands and incorporates sensory feedback [35]. For example, supraspinal control in walking is needed to change direction or avoid obstacles, and has been observed via enhanced EEG activity [36]. Mental imagery studies using fMRI suggest that supraspinal locomotor cortical commands originate in the supplementary motor cortices and are conveyed to the basal ganglia to brainstem locomotor centers located in the pontomesencephalic tegmentum [37], [38]. Further, with increasing age there is an increase in multisensory cortical activation control during imagined walking that is consistent with reduced reciprocal inhibitory sensory interaction; while subcortical areas are similarly activated in younger individuals [39]. This has been suggested as a compensatory strategy due to peripheral sensory decline with age.

The current neuro-motor paradigm regarding walking is that supraspinal inputs interact with CPGs to produce the final motoric output [5]. A review article of how humans walk provides

a summary of this paradigm [40], where it is a combination of CPGs, input from the cortex where feedback is received through muscles, joints, skin and the visual system. A remarkable degree of precision and coordination of muscles and joints is needed to lift the distal portion of the foot sufficiently above the ground to avoid stumbling, but no more than is necessary (energetically efficient). The interplay of these numerous muscles and joints to deliver a coordinated task is extremely complex, given that the possible number of combinations is almost infinite. This poses a computing problem for the brain to handle all of this information. It has been suggested that the brain reduces this computational load by controlling only the position of the joints, leaving the musculature some degree of flexibility in coordination. The primary feature of the muscular activity (flexors/extensors) is that it needs to be scaled to each other. Neuronal networks in the central nervous system have been proposed that generate, coordinate, and control these muscle movements [41].

Three systems in the central nervous system have been proposed to detail the controlled movement associated with walking [40]. One that has been described in detail already is that of the CPG. This network, located in the spinal cord, is capable of generating a basic locomotor rhythm even in the absence of supraspinal or sensory input. A second control system resides in the sensory feedback system with three unique roles: 1) driving the active motoneurons, 2) contributing to corrective reflexes when confronted with perturbations, and 3) providing error signals (differences between intended and actually executed movement, essential in skill development). Finally, motor cortex plays a role in control of walking. Various studies using brain imaging and electrophysiological evidence indicate that motor cortex contributes to the activation of muscles through direct monosynaptic projections to the spinal motoneurons. These monosynaptic projections in mammals are formed, in part, from the axons of descending systems

in the brain and are characterized by their high conduction velocity [42]. With higher levels of encephalization of the nervous system, the number of these direct connections between the brain and spinal motoneurons increases, with most of them shifting to motor cortex. As a result, unlike the cat, which can walk over flat ground after a lesion of motor cortex, primates cannot [40]. Figure 2.1 highlights how human bipedal walking integrates spinal neuronal activity with sensory feedback and motor commands originating in the brain. While the CPG system and sensory feedback systems are important in and of themselves, the present study is confined primarily to the role of brain signals associated with both executed and imagined conscious movement.

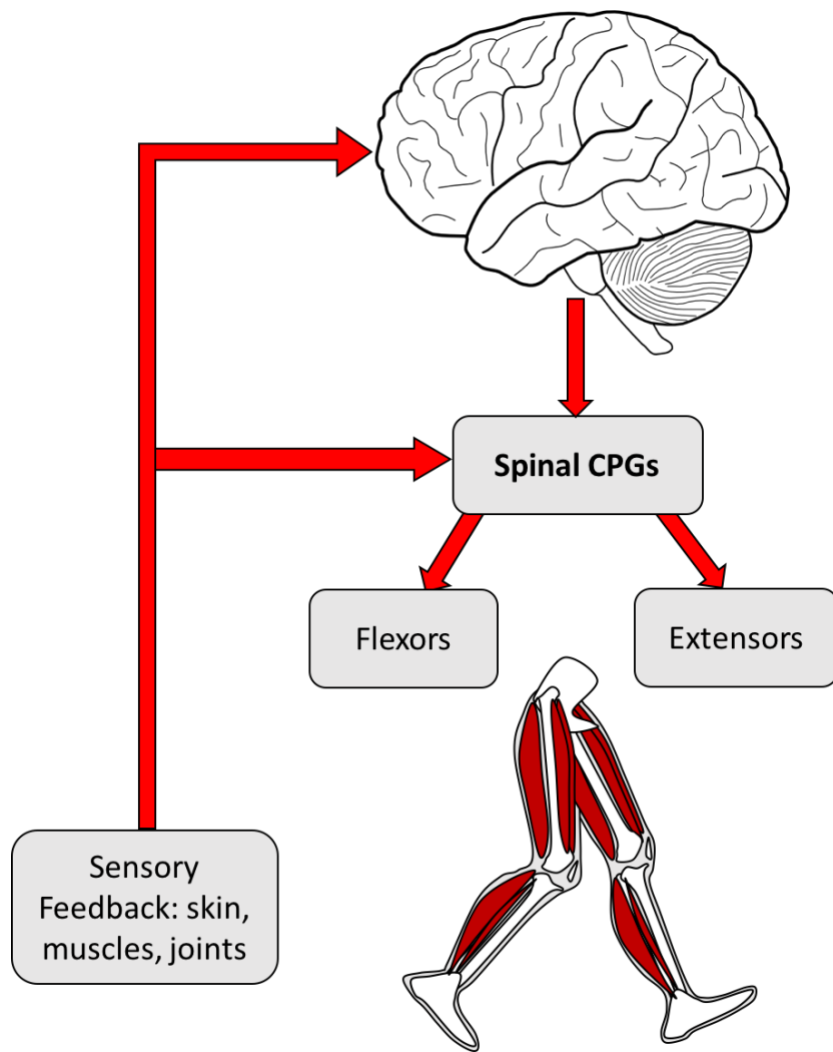


**Figure 2.1 Overview of the central nervous system controlling locomotion, a combination of CPG, alternating flexor and extensor neurons while feedback is provided via skin, muscles and joints back to the spinal cord as well as cortex.**

## 2.2 Imagined Walking

The results of this project are to be ultimately used to help guide the creation of BCIs for individuals with compromised mobility of the legs. That is, although patients cannot perform a lower limb movement, they can imagine the action.

The assumption with imagined movement studies is that neural activity associated with imagined movements is similar to that of the movement if it was executed. By the mid-1990s, there was converging evidence that motor imagery and actual motor control share neural mechanisms and processes [21], [43]. This seems to be a tenable assumption and it is based primarily on the notion of a mirroring motor system.

Mirror neurons (visiomotor neurons) discharge not only when an individual performs an action, but also when observing the same behaviour in another individual. This system is also fundamental in the imitation of action [44]. Although observing someone else perform an action and imagining the action are different, premotor and posterior parietal cortices have been shown to exhibit similar activation patterns [45]. The inferior parietal lobule, precentral gyrus and inferior frontal gyrus are also involved in imagined motion [44]. Recent electrocorticography evidence in humans also strongly supports the notion of a mirror neuron system; gamma band neural activity (from MEG) was observed during a grasping task within parietal areas, the inferior frontal gyrus, motor and somatosensory cortices [46].

Given the purpose of the current research and the foundation on which motor imagery is based, including an imagined motor task condition is a plausible methodological approach. The current research utilized observation of a visual stimulus that mimics actual human lower limb movement as well as a neutral stimulus. Consistent with the mirror neuron system theory, the data from the more realistic stimulus is likely to perform more robustly.

## **2.3 Electroencephalography (EEG)**

### *2.3.1 Basic Principles*

The electrochemical activity of neurons in the brain (e.g., action potentials, neurotransmitter release, intracellular/extracellular exchange of ions) generates small voltages fluctuations. Electroencephalography (EEG) is a noninvasive technology that uses scalp electrodes to non-invasively record these voltages [47]. That is, EEG electrodes can detect the transmission of electrical impulses between neurons in two ways: the direct connection between one neuron and the next via linker proteins (electrical synapse), and the diffusion of neurotransmitters across a synapse (chemical transmission synapse). In a chemical transmission synapse, neurotransmitters are released from the synaptic terminals of the pre-synaptic neuron. Acetylcholine is an excitatory neurotransmitter that binds to the dendrites of the post-synaptic neuron. Upon binding, sodium gates are opened, initiating the depolarization of the post-synaptic neuron, changing the voltage from -70 mV to approximately +30 mV [48],[49]. This results in an action potential that is then transmitted along the length of the neuron's axon. When the action potential reaches the synaptic terminals of the post-synaptic neuron, it stimulates the release of neurotransmitters, and the process repeats itself as the signal continues on to the next neuron. EEG, however, does not detect the voltage fluctuation of an individual neuron. Rather, EEG is sensitive to voltages generated by millions of pyramidal neurons, whose long finger-like projections are oriented perpendicular to the cortical surface (Figure 2.2). This specific geometry allows for the summing of voltages to generate a signal detectable by EEG [47].

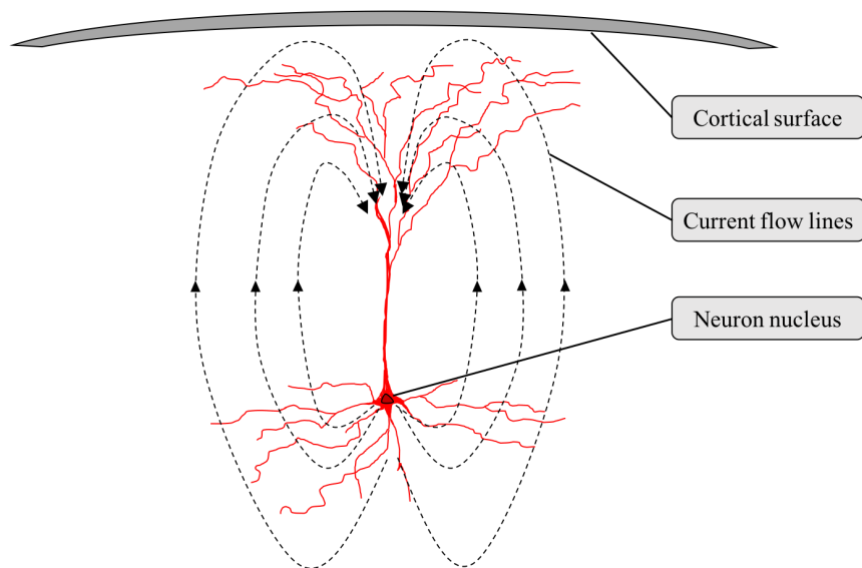


**Figure 2.2 Pyramidal neuron with the voltage potential lines shown in with the dashed black lines where they are oriented perpendicular to the cortical surface.**

The positioning of EEG electrodes on the scalp follow a standardized layout called the 10-20 International System (Figure 2.3), where each electrode is separated by 10% or 20% of the circumference of the skull. The letters ‘F’ (frontal), ‘T’ (temporal), ‘P’ (parietal) and ‘O’ (occipital) indicate the lobe of the brain from where the signal originates, and is recorded via an EEG sensor. Any sensor that falls along the midline of the body (sagittal plane) is denoted with a ‘z’, and locations with odd number subscripts are located on the left hemisphere while those with even numbers are on the right. Medical grade EEG caps contain between 64 and 128 electrodes.

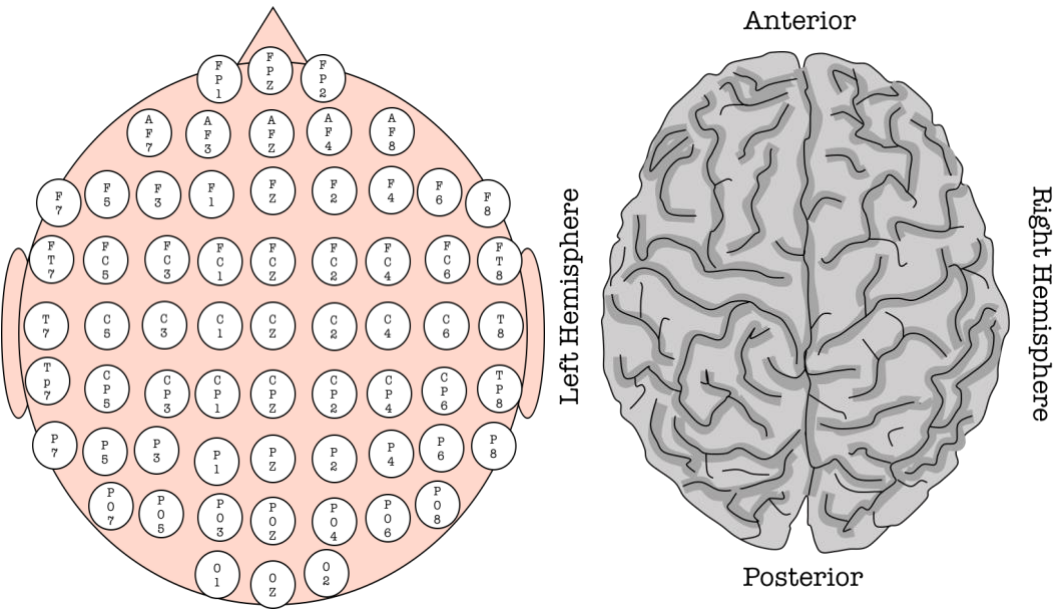


**Figure 2.3 The 10-20 EEG electrode set up and brain model from a top down view.**

At resting state levels of cortical activity, pyramidal cells are synchronized and the EEG shows wide slow wave complexes. During cortical stimulation, the pyramidal cells become desynchronized, resulting in waves of higher frequency and lower amplitude. These waves are biorhythmic and are influenced both by age and the environment. This can result in amplitude variation of signals ranging from 10-100  $\mu$ V [50]. This amplitude is approximately one one-hundredth of that seen in an electrocardiogram (ECG), which measures voltage fluctuations due to heart contractions. There are five main frequency bands used to classify EEG signals: delta, theta, alpha, beta and gamma (Table 2.1).

**Table 2.1 EEG frequency bands and their associated functions [51]**

<b>Band</b>	<b>Frequency range (Hz)</b>	<b>Associated Functions</b>
Delta	0.5 – 4.0	Adult slow wave sleep
Theta	4.0 – 8.0	Drowsiness or arousal
Alpha	8.0 – 13.0	Relaxed, thinking, reflection
Beta	14 – 30	Alert, active thinking, concentration
Gamma	30 – 45	Short term memory, multiple sensory processing

### *2.3.2 EEG in Lower Limb Studies*

EEG has demonstrated that many cortical areas are involved in the gait cycle when walking on a treadmill (e.g., anterior cingulate cortex, dorsal anterior cingulate cortex, posterior parietal lobe, sensorimotor cortex) [52], as evidenced by changes in alpha, beta and gamma frequencies of the EEG signal. A study of lower limb movement, where participants lay on a table and were assisted in flexing the ankle, knee and hip, demonstrated increased EEG activity in the alpha and beta frequencies within the primary motor, premotor, supplementary motor, cingulate, primary somatosensory and somatosensory association cortices [8]. EEG has also been used to accurately decode the kinematics of the hip, knee and ankle joints when walking [7].

Not just the motor areas of the brain are important when executing movement. Language processing centers of the brain also have been found to modulate motor processes [53]. Action words such as ‘write’ or ‘throw’ briefly presented visually on a screen, but too short to be consciously perceived, elicit readiness potentials (RPs) - a peak in EEG signals associated with motor preparation. This has implications for imagined and executed movement as to where in the

brain to expect activation both in EEG and fMRI, as well as the effects different stimuli have on motor movement (e.g., visual, auditory).

Although alpha and beta frequency bands are most commonly studied because they are linked to active thinking and fluctuate the most during external stimuli [50], one study using robots to assist in gait training (passive walking) during rehabilitation observed modulation of the gamma band along the central midline in relation to the phases of the gait cycle, while gamma and beta bands were suppressed when active (robot assisted) and passive walking were compared [54]. A similar pattern was observed comparing walking to standing [55].

EEG has also been used in motor imagery studies. EEG patterns associated with imagining left and right hand movements were found to be similar to those observed during planning the movements [24]. When subjects imagine different types of motor movements (hand, tongue, foot), systematic variations in EEG signals are observed from sensorimotor areas [56]. Another motor imagery study of hand, foot and tongue movements also showed activation of cortex similar to that of actual motion; however, this was most prominent for hand movements leading to the conclusion that “*...EEG phenomena may be utilized in a multi-class brain-computer interface (BCI) operated simply by motor imagery [57].*”

Given the predominance of hand movements in EEG imagery studies, it is not surprising that much of BCI development has focused on the upper limbs. These have included BCIs for finger movement [58] and classifying left and right hand using motor imagery [59]. More complex BCIs based on EEG signals have been designed that: 1) focus on discriminating rest, imagined grasp, and imagined elbow movement [60]; 2) control of both hands in a grasping movement [9]; and 3) integration of motoric feedback to assist in lifting and drinking a glass of water [3].

EEG-based BCI for lower limbs is more complex, but some progress has been made. For example, one study developed a classifier for left hand, right hand or right foot [61]. One of these included the classification of walking versus non-walking (forward and backward) and for imagined walking versus non-imagined walking (forward and backward) [62]. The use of a BCI in driving the right leg of an avatar on a treadmill using information from the left leg movement showed significant movement correspondence at the hip, knee, and ankle joints [28]. Participants have been able to idle/walk an avatar, and to make stops at predetermined places using kinematic imagery within a virtual environment significantly better than chance [27].

The use of robot-assistance in perturbed-balance training [63] is another lower limb BCI example. Specifically, a stroke patient walked on a treadmill with a robot that interfaced at the person's pelvis. Perturbing pushes to the pelvis by the robotic device assisted in training the individual to counteract the perturbations. A BCI system that significantly classified robot-assisted active and passive walking from non-walking was successful in healthy and stroke patients [29]. A BCI system that assists in over ground walking has also been developed [30] and used successfully by one participant, but is very cumbersome and so its adoption is unlikely. Research that will allow streamlining such a system will be important to continue this line of inquiry.

There are several limitations to the use of EEG in studying lower limb neural activity. Specifically, the EEG data do not possess the spatial resolution necessary to accurately localize or resolve activity to single gyrus or sulcus, on the order of cm<sup>3</sup>. In addition, because EEG cannot accurately probe the activity of subcortical brain regions, data are based primarily from activity located near the surface of the skull, first centimeter of brain tissue [8]. This is of unique concern for accurate assessment of lower limb motor activity because the leg area of

motor cortex is deeply and medially located (1-4cm deep), as well as vertical in its orientation [64]. Because of this it is also difficult to distinguish left and right leg movements due to the minor spatial distance between the left and right hemispheres [8]. The fundamental advantage of EEG methodology is that it captures neural responses rapidly, so it has excellent temporal resolution (in milliseconds) in monitoring neural activation. On the other hand, fMRI provides excellent spatial resolution of all areas of the brain (on the order of millimeters).

## **2.4 Magnetic Resonance Imaging (MRI)**

### *2.4.1 Basic Principles*

Magnetic resonance imaging (MRI) is a non-invasive imaging modality that makes use of the fact that some nuclei are charged particles that possess an inherent spin (the origin of this spin can be described quantum mechanically but is beyond the scope of this thesis). For purposes of this discussion, the description will be limited to the hydrogen nucleus, as it is the most abundant in the human body and is thus used in the vast majority of MR imaging applications, including those used in this thesis. As a result of spin, a small magnetic moment is generated along its axis. When no external magnetic field is present, the magnetic moments of hydrogen nuclei are randomly oriented, and thus sum to zero. However, when placed in an external magnetic field, some of these moments (or spins, as is often used in the literature) will orient themselves either parallel or antiparallel to the external field. In actuality, the alignment is off-axis from the external field (the existence of these two discrete states can also be described using quantum mechanics that is beyond the scope of the thesis). As a result, the external field applies a torque on the magnetic moments, causing the spins to rotate (“precess”) about the axis of the external field (Figure 2.4,

left) [65]. The frequency ( $\omega$ ) at which a spin precesses about the magnetic field is referred to as the precessional frequency (or Larmor frequency) (Eq. 2.1):

$$\omega = \gamma B_o \quad (2.1)$$

where ( $\gamma$ ) is the nucleus-specific gyromagnetic ratio and  $B_o$  is the external magnetic field strength (in Tesla).

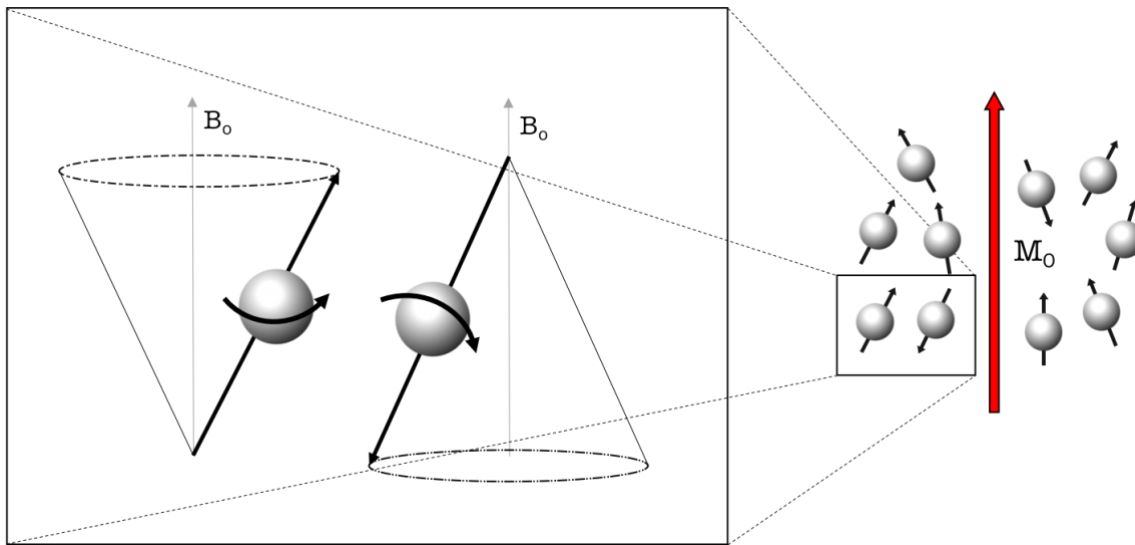


**Figure 2.4 A parallel spin and an antiparallel spin in an external magnetic field,  $B_o$  (left). The parallel state is the lower energy of the two, and thus there is a slight excess of spins in this state relative to the antiparallel state, giving rise to a net magnetization,  $M_o$  (right).**

At equilibrium, there is a slight excess of spins in the parallel state relative to the antiparallel state. Thus, the net magnetization,  $M_o$ , is non-zero and aligned along the direction of the external magnetic field. For the purposes of imaging, a secondary magnetic field, a radiofrequency (RF) pulse,  $B_1$ , is often applied in a direction perpendicular to  $B_o$ , pulling  $M_o$  away from the direction of  $B_o$  (as a result of forcing spins into the higher-energy antiparallel state). After this secondary magnetic field is released, the spins gradually return to equilibrium (Figure 2.5).

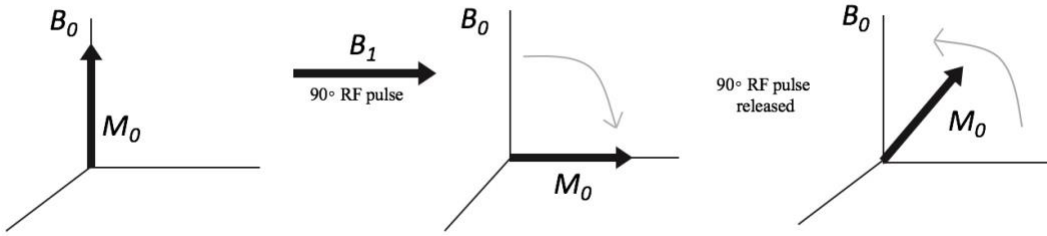


**Figure 2.5 Application of a 90 degree RF pulse to the net magnetization in equilibrium (oriented with the external magnetic field) and the recovery of the net magnetization after the RF pulse is released.**

The rate of this return to equilibrium differs for spins in different tissues [65] and thus acts as a source of contrast between tissue types in MRI (called T<sub>1</sub> contrast, where T<sub>1</sub> is a time constant that characterizes the rate of return to equilibrium along the longitudinal axis – parallel to direction of external field). Another source of contrast in MRI is based on the fact that hydrogen nuclei in different tissue types and chemical environments experience slightly different Larmor frequencies because of the proximity of neighboring spins that either add to or subtract from the main magnetic field. The result of these differing Larmor frequencies is a rapid decay of signal due to dephasing. This decay occurs at different rates in different tissues and is thus a form of contrast (called T<sub>2</sub> contrast, where T<sub>2</sub> is the time constant that characterizes the rate of signal decay in the transverse plane) [65] (Figure 2.6).

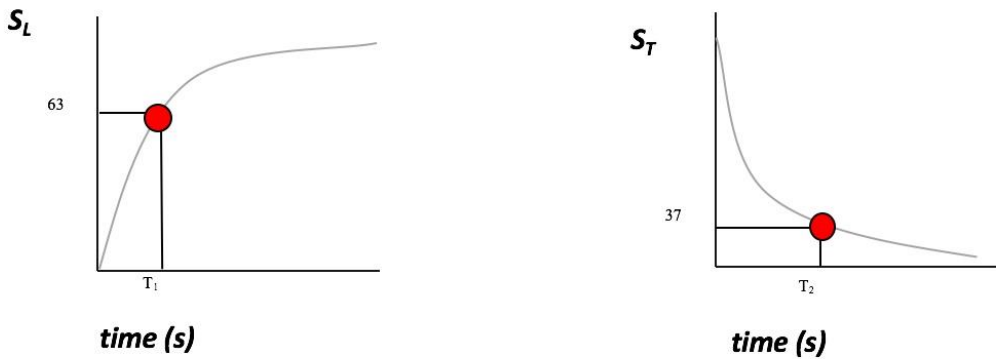


**Figure 2.6 Diagram of time constants  $T_1$  and  $T_2$  in the longitudinal and transverse planes, where  $T_1$  is characterized by 63% of the longitudinal magnetization having returned to equilibrium, and  $T_2$  is characterized by 37% of the remaining magnetization in the transverse plane while it returns to equilibrium.**

MRI thus involves the disturbance of net magnetization equilibrium using an RF pulse, and then a recording of the generated signal (i.e., amount of magnetization in the plane perpendicular to the main magnetic field) as it simultaneously decays due to dephasing and returns to equilibrium. What is actually recorded is a voltage induced in a coil loop as the magnetic flux generated by the rotating magnetization passes through the loop (i.e., Faraday induction).

It takes a number of RF pulses and subsequent signal recordings to generate the data necessary to obtain an MR image. The repetition time (TR) is how frequently the RF pulses are applied (in milliseconds) and the echo time (TE) is the time at which the peak of the signal is recorded relative to the application of the RF pulse (in milliseconds). Thus, the magnitude of MR signal present is determined by the density of spins present and is represented by  $S$  in Equation 2.2, where equilibrium is represented by ( $S_o$ ).

$$S = S_0(1 - e^{-TR/T_1})e^{-TE/T_2} \quad (2.2)$$

TR determines the amount of T<sub>1</sub> contrast because it is related to how many spins are allowed to relax (return to equilibrium) between RF pulses. TE determines the amount of T<sub>2</sub> contrast because it is related to how much the MR signal is allowed to dephase before it is collected.

There are additional sources of dephasing caused by spatial inhomogeneities of the magnetic field, leading to a more rapid decay of the signal, characterized by a time constant T<sub>2\*</sub>. Certain types of MR imaging can refocus this dephasing to regain a signal amplitude that is governed by T<sub>2</sub>. Other types keep this extra dephasing, as it contains information on important sources of magnetic field distortion like iron, which can indicate inflammation or can also quantify neural activity. This process is further described when introducing functional MRI [65].

For each RF pulse, a different combination of magnetic field gradients (i.e., linear alterations in B<sub>0</sub> in specific directions) is used to alter the phase and frequency of the recorded signals so that it can be spatially localized. The signal that is collected is digitized and stored until all the necessary data are collected. An inverse two-dimensional Fourier transform is then applied to reconstruct the MR image [65], converting the information from k-space (Fourier space, where frequency is encoded along ‘x’ and phase is encoded along ‘y’) to image space. This process is applied iteratively on a stack of MR images.

To generate 3D information slice selection occurs to elect where in the 3D volume data will be acquired from, giving rise to voxels (volume pixels), and therefore a 3D matrix of data, where each element is represented by the MR signal present.

## 2.5 Functional MRI (fMRI)

### 2.5.1 Basic Principles

Functional magnetic resonance imaging (fMRI) is a non-invasive imaging technique that detects the fluctuations in the blood oxygenation level dependent (BOLD) response and is an indirect measure of neural activity, as oxygenated blood is delivered to neural cells via the hemoglobin macromolecule of red blood cells. Although oxygen is extracted during increased neural activity, there is actually an over-compensatory increase in oxygenated blood to the area (via increased blood flow and blood volume) [66].

Oxygenated hemoglobin is diamagnetic (has zero magnetic moment and disperses the magnetic field), whereas deoxygenated hemoglobin changes the susceptibility in the magnetic field because it is paramagnetic (i.e., concentrates magnetic field). The presence of paramagnetic deoxygenated hemoglobin thus distorts the local magnetic field experienced by the hydrogen nuclei of water molecules. fMRI utilizes the  $T_2^*$  contrast described earlier, as it is sensitive to field inhomogeneities caused by deoxygenated hemoglobin. Because of the increase in blood flow and volume, the result of increased neural activity is a decrease in the local concentration of deoxygenated hemoglobin and thus an MR signal increase. The timing of these mechanisms is characterized by the hemodynamic response function (HRF) (Figure 2.7).

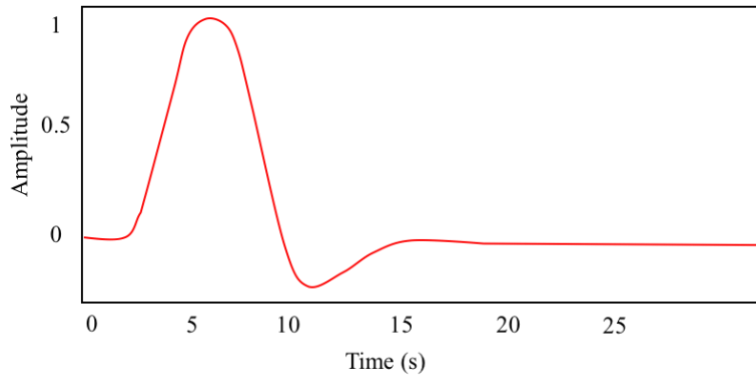


**Figure 2.7 Hemodynamic response function.** This models the expected BOLD response (ratio of deoxyhemoglobin to oxyhemoglobin) for a voxel and represents an indirect measure of neuronal activity via metabolic activity.

Typically, the spatial resolution of an fMRI image is about 3 mm on each side (x, y and z) of a voxel (3D pixel) [67]. This permits the localization of brain activity on the order of millimeters. The anatomical location of brain activity is typically evaluated through the use of standard brain atlases, such as the Brodmann's areas (BA) or Harvard-Oxford Atlas. For the purposes of this dissertation, the Harvard-Oxford Atlas will be used to ascribe structural locations to functional MRI results. The Harvard-Oxford atlas consists of subdivisions of the brain, based first on left versus right hemisphere and then divided into 48 cortical regions and 21 subcortical structural areas. These are registered to the MNI152 standard brain, which can be combined across subjects to provide a population probability map for each label [68].

fMRI signals, however, can fluctuate for reasons other than neuronal activity [67], and fMRI is also very sensitive to head movement artifacts. Any head movement greater than the dimension of a voxel (~3 mm) causes the signal to become distorted. This has proven to be an issue when using experimental tasks that require participant movement, such as leg bending or straightening. Thus, studies to understand motor movement have been largely restricted to using

finger and hand tasks, as they have little to no effect on head movement [69], (with the exception of patient investigations such as motor stroke or tremor).

### *2.5.2 fMRI Studies of Lower Limb Movements*

fMRI studies of lower limb movement have been somewhat limited due to the difficulty in obtaining data from participants in a restricted space as well as effectively dealing with the problem of head movement. In one study of assisted movement and visually-stimulated movement [14], areas of the brain that were activated included primary somatosensory and motor areas, and cingulate cortex. Robotic assisted and active multi-joint movements also showed activation in sensorimotor cortex, anterior vermis of the cerebellum and the right supramarginal gyrus [17]. Passively generated knee movements in infants showed activation in the sensorimotor areas [70]. One study assessed the activation of different brain regions when participants engaged in variations of robotic controlled locomotion, all of which showed a similar response in the primary sensorimotor network, frontal cortex, insula and cingulate cortex, and some cerebellar areas [15]. Another study measured the torque of ankle dorsiflexion, ankle plantarflexion, and knee extension using a specially designed testing apparatus [16]. All three tasks showed activation in primary motor cortex, premotor cortex, supplementary motor area, secondary somatosensory cortex, putamen, thalamus and cerebellum. In another knee extension study, the effects of patellar taping on proprioception were assessed [71]. In the non-patellar tap condition (control), there was activation in the medial supplementary motor area, cingulate motor area, basal ganglion, thalamus, and medial primary sensorimotor cortex.

Like EEG, fMRI has also utilized imagery tasks. Most of these have been in the upper limbs, but a few have examined lower limb imagined tasks. An early study using imagined and executed hand motor tasks found that both similarly activated primary motor cortex, primary

somatosensory cortex, and premotor areas [23]. Similar neural substrates for executed and imagined hand movements have also been demonstrated in another study [72], including premotor cortex, primary motor cortex, and supplementary motor area. In a more recent study, participants observed a series of video clips of an individual executing a hand movement, standing and walking. They were then asked to mentally imitate the movements. Activation patterns for the tasks of hand movement, standing and walking were significantly different from each other [5]; cortical areas involved in imaginary walking included sensorimotor areas, bilateral precentral gyrus, left dorsal premotor and cingulate motor area. Another study examined visual imagery versus kinesthetic imagery using a finger movement task [25]. The primary motor-related areas were similarly activated for both conditions. However, visual imagery activated primarily the occipital and superior parietal lobes, while kinematic imagery showed more activation in pre-motor structures, inferior parietal lobe, dorsolateral prefrontal area, cingulate nucleus, putamen and the cerebellum (lobule IV, Crus I, and Lobe VIIb).

A study that assessed skilled versus novice motor imaging using a high-jumping task found that novices used more occipital and parietal areas when imagining the task, while the skilled high jumpers activated more of the pre-motor cortex and cerebellum [73]. It was concluded that imagery of a skilled task takes time; that is, in order to use an internal perspective (i.e., motoric), one must have well established motor representations of the skill, otherwise an external (i.e., visual) perspective is used. One study used a rolling cylinder at the base of the feet outside the MR scanner to mimic walking [18]. The purposes were to assess if the observation/execution matching system would be activated for walking, and if these activations would be moderated by the spatial context of the walking task (i.e., an open versus a narrow space). The results showed activations in the dorsal premotor area, supplementary motor area, and

posterior parietal lobe for both executed and observed walking. Occipital-temporal areas and middle temporal gyrus were activated in the narrow space condition. The authors suggested the need for the latter activation when walking in a more narrowed space.

Together the findings thus far suggest that executed and imagined lower limb movements are likely to engage similar neural activation patterns, although some differences may be expected.

## **2.6 Combining EEG and fMRI Data**

It has been pointed out that the EEG has excellent temporal resolution and fMRI provides excellent spatial resolution. The effective use of both has been a source of interest by the research community. MR-compatible EEG technology is now available to permit the simultaneous collection of EEG and fMRI data. This requires non-ferromagnetic electrodes and wires for EEG. To date, much of the reported research in this area has focused on epilepsy [74], imagined tasks [75], or simple tasks such as eye-open/eye-closed [76] or hand-grip [13]. While the combination of EEG and fMRI has been used to study brain activity in response to hand movements [11], it has not been used for the study of lower limb movements.

A particularly useful review article summarizes the integration of EEG and fMRI data, discussing four primary approaches for doing so [77]. The first two are asymmetrical in that one modality is used to guide the analysis of the other (fMRI-informed EEG and EEG-informed fMRI) and thus the data do not have to be collected simultaneously, while the other two do not put either EEG or fMRI in a preeminent role (neurogenerative modeling, multimodal data fusion) and the data are collected simultaneously.

In fMRI-informed EEG, the paths of currents to the scalp are identified and an algorithm can be applied to find the optimal constellation of neural generators that best explain the scalp

potential field. In essence the fMRI data identify the locations and the EEG-derived information provides the time course of the neural event. This has been used in studies of visual stimulation [78],[79], auditory stimulation [80] as well as sleep, epilepsy, and cognition [81].

In EEG informed fMRI, it is assumed that EEG fluctuations are correlated over time with fluctuations observed in the fMRI signal. The analysis of voxel activation in fMRI does not only include the primary predictor of the timing of stimulus onset and offset, it also includes as another predictor(s), extracted EEG features (e.g., alpha signal), assuming this will allow for a better model fit to the data. This approach appears to be most useful in revealing functional networks that are identified at the single trial level. Studies using this approach have focused on epilepsy [82], decision-making [83], and hand grip [13].

Neurogenerative modeling specifies the physiological processes that give rise to EEG fMRI data. Based on computations of a given model, brain states can be reconstructed from simultaneous EEG-fMRI recordings that best explain the observed data. A key component in this process is the ability to properly model the biophysical processes that underlie both the EEG and fMRI signals. Given the computational intensity of this approach, it has been used mostly to model activity in small areas of the brain and is useful in testing hypotheses regarding physiological mechanisms and biophysical properties underlying EEG and fMRI signals. One study using this approach was based on auditory stimulation [84].

Multimodal data fusion uses the data generated from both EEG and fMRI to pinpoint temporal and spatial aspects of a task. For example, fMRI statistical maps and EEG data are merged into a single matrix and subjected to joint independent component analysis (ICA). The application of this approach is somewhat new, and there are currently a variety of mathematical approaches suggested to accomplish the merging [85],[86]. There is as of yet no clear

determination of which algorithms are to be used under what circumstances. Studies using this approach have focused on working memory [87] semantic processing [88], and auditory stimuli [89].

One article concluded that: “*When one is primarily interested in the neural generators of scalp EEG phenomena, fMRI-informed EEG is the method of choice. This approach is founded on well-established methods for EEG source reconstruction, and so constitutes the most direct technique for assessing related research questions*” [77]. Due to the relatively new process of using fMRI to assess lower limb movement in general, and the non-existence of literature on combining EEG with fMRI for lower limb movement, as well as the research question of interest for this study, the fMRI informed EEG approach was the analytical method of choice in the current project.

## **2.7 Machine Learning**

Machine learning is a discipline that combines mathematics, statistics and computer science within a particular facet or domain of knowledge, as a means of improving performance on a task without being explicitly programmed to do so. Typically, this requires a large initial dataset that is “mined” in order to discover relationships within the data that will enhance the ability to accurately predict an outcome given new data [90].

Approaches to machine learning fall into two broad categories: unsupervised and supervised. Unsupervised, as the name would suggest, is used when the nature of the data mining is exploratory and the outputs remain unspecified (are unknown). This allows the creation of algorithms that will determine what data are important and how many ‘bins’ into which to classify the data; some unsupervised algorithms, however, allow the user to select the number of bins. For example, using a large number of facial images, an unsupervised machine learning algorithm

demonstrated it is possible to train a face detector without having to label images as containing a face or not [91]. This study simulated neurons that classified unlabeled data, such as that of a baby learning to group types of faces together simply by seeing many of them.

Supervised machine learning is used when the outcomes are known, the data can be labelled, and the classifiers can be trained with the associated classification. For example, data of past temperatures and co-occurring weather conditions provide a storehouse of information. Using the information about current weather conditions could predict a future temperature. Supervised machine learning can be broken down further, depending on whether the nature of the outcome is continuous or discrete. The weather example is a continuous outcome. A discrete outcome would be whether an event occurred or not (e.g., a tornado) [90].

Depending on the nature of the machine learning task, clustering (unsupervised) or regression/classification (supervised) techniques are used. Some of these are support vector machines (SVMs), linear discriminate analysis (LDA), k-means, forests, k-medoids, linear or polynomial regression, and neural networks [90]. This hierarchical schematic is summarized in Figure 2.8, and showcases some of the methods available.

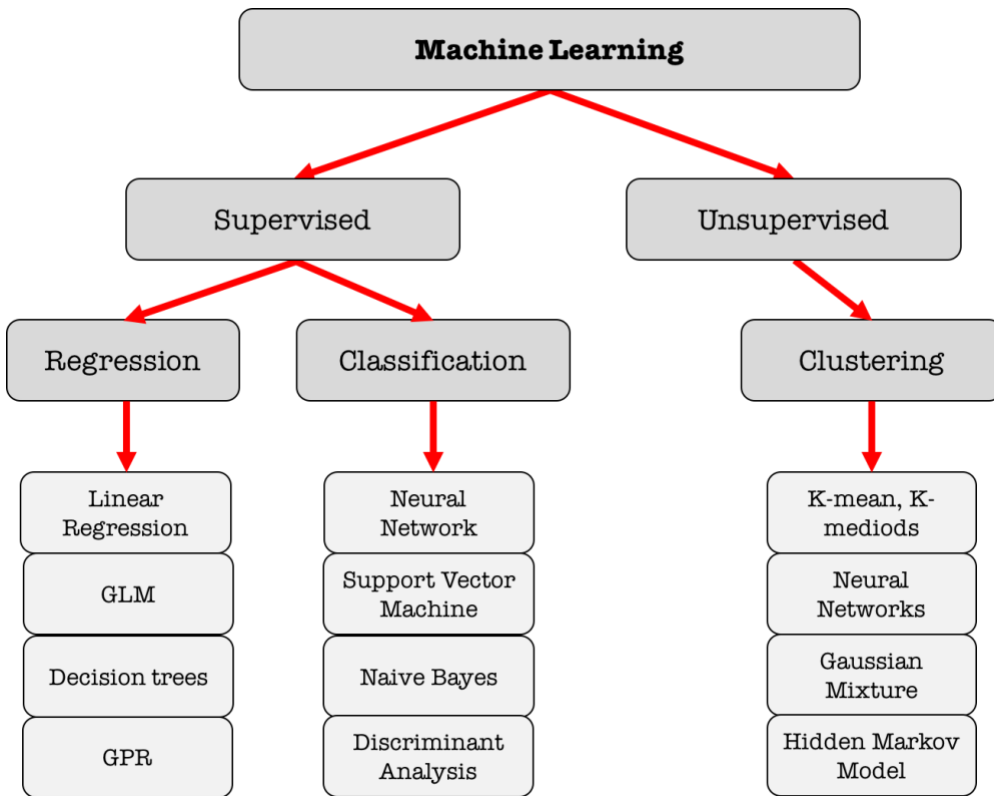


**Figure 2.8 Overview of how machine learning is broken down first into supervised and unsupervised, and subsequently into regression, classification and clustering. From there, a few examples that fall within each of these classes are provided.**

Machine learning protocols can be evaluated as to their efficacy on a number of dimensions. These include, but are not limited to: memory usage, speed of classification, accuracy of classification, and transparency of the algorithm. Table 2.2 provides a summary of how these can be evaluated for a two-class classification problem [92]. For regression, evaluation alternatives often include mean square error (MSE) or root mean square error (RMSE) [92].

**Table 2.2 An example of a 2-class confusion matrix for evaluating a classification modality of machine learning**

Confusion Matrix	Predicted Negative	Predicted Positive
Actual Negative	True negative (TN)	False Positive (FP)
Actual Positive	False negative (FN)	True positive (TP)

The complexity of the data, which includes the number of predictors, and complexity of the interactions of the predictors, will also determine the type of machine learning technique used. Best practice is to begin with simple classifiers, as they are computationally efficient, while maintaining their interpretability [90]. Assuming classification is high with these simpler techniques, they should be employed. However, if these techniques provide poor results, more complicated systems such as artificial neural networks may be used.

Artificial neural networks (often referred to simply as neural networks) are comprised of artificial neurons (AN) that are based on the anatomy and physiology of biological neurons (BN). As described earlier in this chapter, biological neurons can be divided into three main sections: information input (dendrites), information processing (neuron nucleus) and information output (axon). The dendrites receive multiple inputs from a host of other neurons, some of which may be excitatory and some inhibitory. These inputs are summed, and then exhibit an ‘all-or-none’ response; if the amplitude reaches a sufficient threshold, depolarization will occur and the signal will continue to be passed to the following neuron, and if not it stops [93]. Paralleling this, an artificial neuron has multiple inputs (predictors) from other artificial ‘neurons’ or inputs that are summed together, passed through a threshold function (using either a tangential or sigmoid activation function), multiplied by a weight, and then passed/not passed to subsequent ‘neurons’ in the network. This ultimately leads to an outcome [90].

Machine learning has been used in concert with brain activity in several studies. Examples include its use in lie detection [94], emotional state classification [95], pattern recognition and line orientation classifications [96], and clinical psychological discriminations [97]. These have been focused on mental activity rather than physical action.

In the current research project, data from EEG and fMRI will be used to predict lower limb movement outcomes in a supervised fashion. That is, these data serve as predictors and the outcome is the correct classification of left versus right lower limb movement. Activity patterns associated with left and right lower limb movements during these tasks will contribute to future projects that develop BCIs to generate lower limb movements from imagined walking brain activity patterns. However, several cautions must be kept in mind with respect to the implementation of the proposed approach [98]: decoding the data is a difficult analytic process due to the unfavourable signal to noise ratio (SNR) in EEG, voluminous nature, and potential unreliability of the data. Inattention to these issues may result in spurious findings and nonsensical interpretation.

## **2.8 Hypotheses**

For the purposes of this research an indirect pathway (one that circumvents the spinal cord and the control of CPGs) will be used during conscious control of stepping. The reviewed literature and methodological considerations presented in this chapter give rise to the following hypotheses for the current research project:

*Hypothesis 1:* EEG data will demonstrate brain activity patterns that distinguish left from right leg movements for both imagined and executed conditions; this effect is expected to be particularly strong for the computer generated image based stimuli conditions.

*Hypothesis 2:* fMRI will identify areas of the brain that are differentially activated for lower limb movement across experimental conditions. Specifically, activation of the sensory motor areas is expected across all conditions. In the executed condition, areas of the cerebellum and basal ganglia will be activated. In the imagined condition, greater activation of the occipital, parietal and frontal lobes is expected. In addition, the CGI condition is expected to be a more robust

predictor and elicit a ventral visual pathway. Due to the sluggish response time of hemodynamic activity, differentiation between left and right knee extension is not anticipated.

*Hypothesis 3:* A computational approach exists that successfully allows accurate mapping of the spatial brain activity (fMRI) in relation to the temporal receptors (EEG electrodes) associated with lower limb movement.

*Hypothesis 4:* A pattern identification algorithm can be identified (using fMRI-informed EEG) that classifies left and right leg movement based on brain activity patterns from imagined lower limb movement significantly above chance classification.

Prior to conducting the study proper, two tasks needed to be accomplished. The first was a pilot study that illustrates a proof-of-concept to support the utilization of supine-generated data to test the hypotheses. This is presented in the next chapter. The second task was to design a device that would allow the data to be captured appropriately. This will be presented in Chapter 4.

## **CHAPTER 3: THE COMPARABILITY OF LEG MOVEMENT KINEMATICS DURING TYPICAL WALKING AND DURING SIMULATED WALKING IN A SUPINE POSITION**

### **3.1 Introduction**

Walking is fundamental to a healthy quality of life in humans, as it is both a means of exercise and a mode of transportation. The execution of normal walking is an intricate sensorimotor task involving the interactions of both dynamic and balancing neurological processes [6]. To study this interplay appropriately, concurrently gathered data from body movement and brain activity needs to occur. One way to do this is to utilize fMRI technology. However, current fMRI technology requires subjects to be in supine position within a spatially restrictive environment during data collection. Thus, a clear understanding of the comparability of supinely-generated walking movements and normal walking is required.

Little work has been done to investigate supine leg movement biomechanics and how these relate to those of upright walking. Studies that have been conducted to date use a variety of methodologies and show mixed results with most research on the biomechanics of supine movement has been as it pertains to applications involving weightless exercise (i.e., space travel/zero gravity) [99]. In another study the focus was on metabolic and kinetic features of supine walking in comparison to supine locomotion, not kinematic signatures, or the usefulness of supine locomotion in rehabilitation [100].

Thus, one purpose of this study was to compare supine knee flexion/extension with that during executed walking. The expectation was that supine leg movements would mimic a portion of an individual's natural gait cycle. The findings will help to determine the veracity of the assumption that neurological data collected in an fMRI scanner from supine leg movements will provide comparable neurological data to that of normal walking by mimicking stepping.

A second purpose was to assess the magnitude of head movement with respect to the trunk. Given the sensitivity of fMRI-gathered data to noise from head movements [101], the degree of head movement was quantified during the walking and supine motion tasks. No efforts were made to hold the head in a fixed position, as the purpose was to simply describe the extent to which this might be an issue.

### **3.2 Methods**

#### *3.2.1 Marker Setup*

Three healthy, male subjects (aged 19-24) took part in this pilot study. Thirty-five reflective markers constructed in the Clinical Movement Assessment Labortory (Foothills, HRIC3C48A) were used to define the lower body segments (i.e., left and right hip, knee and ankle joint centers and segments). Upper body markers were placed on each acromion, on the proximal and distal portions of the sternum, and on cervical vertebrae 7. The head was defined with four markers: on the right and left sides of the glabella, and on the left and right parietal bones. Figure 3.1 below displays the anatomical locations (left) and how these reflective markers appear in the software post-data collection (right).

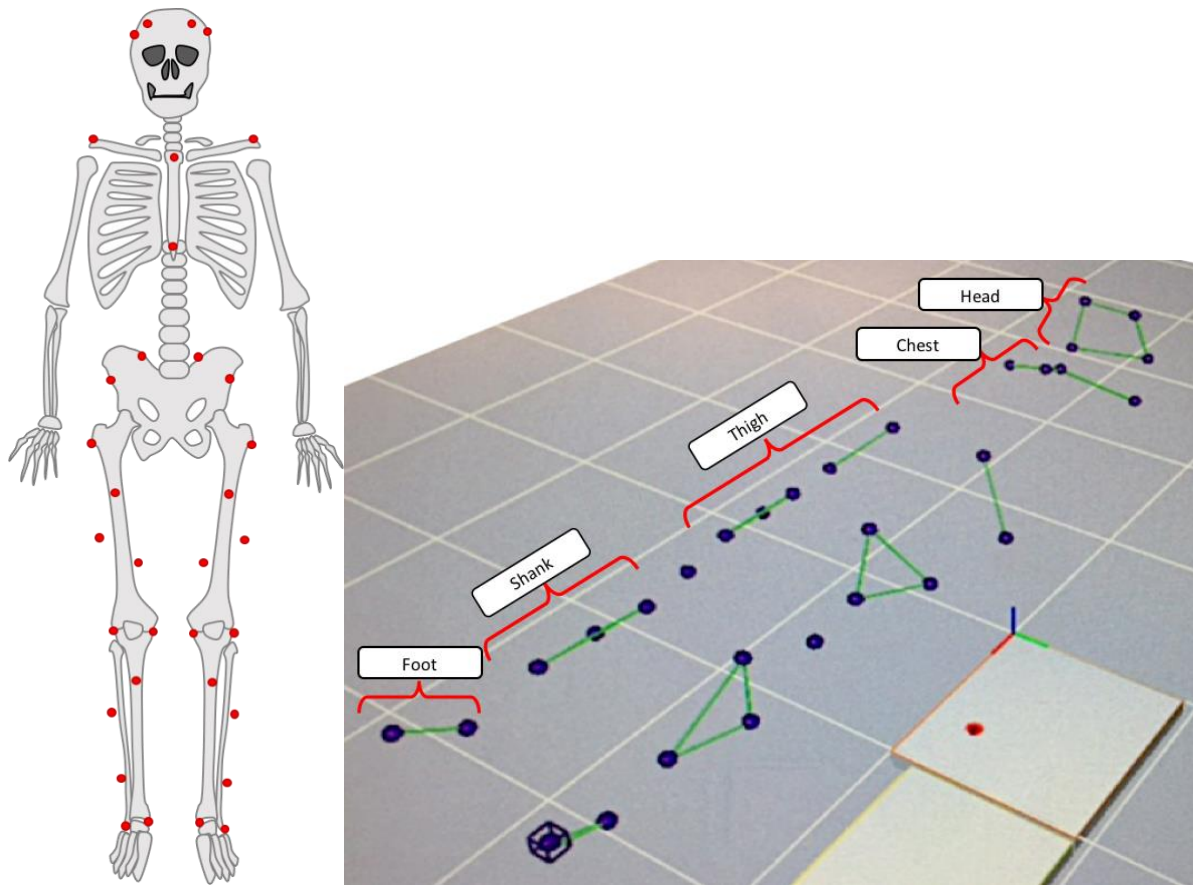


**Figure 3.1 Marker setup displaying the anatomical landmarks and the corresponding reflection seen by the motion analysis cameras when a participant is lying down, where A) notes the markers during a neutral trials and B) highlights the markers used during kinematic trials where the medial ankle and knee markers have been removed.**

### 3.2.2 Data Collection

Kinematic data pertaining to head motion and knee rotations in 3 planes were collected with eight *Kestrel Motion Analysis* (Motion Analysis Corporation™, Santa Rosa, CA) photogrammetric cameras at 120 Hz. Five trials for each of two conditions were performed and recorded, with rest breaks for the subject between trials. The two conditions were: normal walking gait (5 trials) and supine (on a physio training table) knee flexions/extensions, alternating between left and right knees for 5 flexions/extensions of each leg. In addition, 5 rates

of supine knee flexion/extension (40, 50, 60, 70, and 90/min) were tested with this paradigm. The head translation was recorded for each trial to ascertain the effect the rate of movement might have on controlling head motion. A towel and a foam cushion were used to support the head and neck during the supine condition.

Before kinematic trials, the joint and axis centers of the knee, ankle, hip, chest and head, were defined. For the knee, the joint center was taken as the midpoint between two reflective markers placed on either side of each knee in the joint space. The resulting center was located in the joint space between the distal end of the femoral epicondyles and the intercondylar eminences of the proximal tibia. The ankle joint center was taken as the midpoint between reflective markers on the left and right malleoli. Joint centers for each hip were calculated using Tylkowski's approach [102]: 11% of the inter-ASIS distance medially, 12% distally, and 21% posteriorly from each given anterior superior iliac spine (ASIS).

### *3.2.3 Data Processing and Analysis*

The software program *Cortex* (Motion Analysis™, Santa Rosa, CA) was used to track kinematic data, which entailed labelling markers in reference to their anatomical landmarks and interpolating for frames where markers were missing from view for the duration of the acquisition file. Files were saved in .trc file format and imported into *Matlab 2017b* (Mathworks®, Natick, MA), where data were low-passed filtered at 5 Hz to remove high-frequency noise, where the movement of interest occurred at 0.8-1.4 Hz.

Coordinate systems for the ankles, knees, hips, head and chest were defined using an Euler coordinate system. Figure 3.2 shows two coordinate systems: one before and one after a rotation about the point 'O'. An Euler coordinate system was selected as it made the

determination of the rotation matrix more streamlined. Euler coordinate systems are notable for the orthogonality of their axes (x,y,z). These coordinate systems were determined locally (on anatomical references) via determination of a mechanical axis. In the case of either thigh, the mechanical or ‘z’ axis was oriented vertically (superiorly) by using the vector from the hip joint center (femoral head) to the knee joint center, and in the shank from the ankle joint center to knee joint center. Ankle and knee axes were defined as the vector along the length of the medial and lateral markers on either side of the knee and ankle (oriented laterally for each joint). The cross product of the mechanical or ‘z’ axis with the joint axis resulted in an orthogonal ‘y’ axis, oriented laterally for each knee. Using cross products of the y-axis with the z-axis, the final orthogonal ‘x’ axis was determined and oriented anteriorly for the femoral and tibial reference vectors. Each axis (x,y,z) for each segment was then normalized with respect to itself.

To initiate the generation of the head and chest coordinate systems, the four markers placed on the head defined the joint center by taking an average of the four points locations. The joint center imbedded in the chest was defined by averaging the right and left acromion markers, and the proximal and distal sternum markers. Hip joint centers were used to determine a pelvis center (i.e., midway between the hip joint centers). This served as a reference point to define the z-axis of the chest (vector between chest center and pelvis center) and the distance between head joint center and chest joint center to define the z-axis of the head. The frontal axis of the head was defined using the two markers on the front (anterior) side of the head. The frontal axis of the chest was determined using the right and left acromion locations. Again, the cross products of each z-axis with their respective frontal axes were taken to define local y-axes and subsequently the cross products of the z-axes with the y-axes were calculated to determine x-axes. These operations led to the definition of the right and left femoral and tibial coordinate systems, and

head and chest Euler based coordinate systems. To highlight the orthogonality of an Euler system, Figure 3.2 below shows two coordinate systems, one rotated to indicated a change of reference frame.

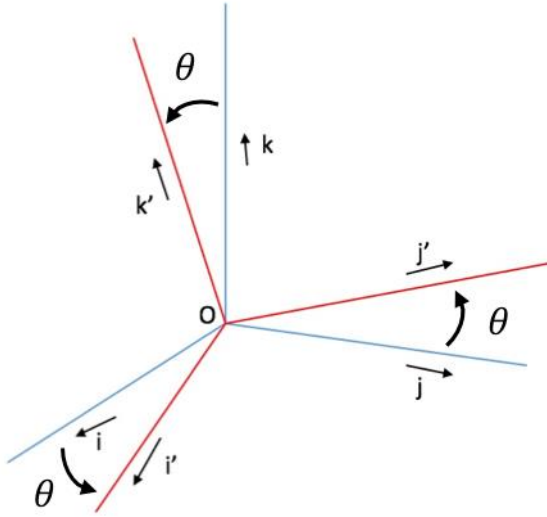


**Figure 3.2 Euler coordinate system, where the original axes are orthogonal to one another (i, j and k), and after undergoing a rotation, maintain their orthogonality and become the new axes i', j' and k'.**

The rotation matrix was computed using the Challis method, using equations 3.1-3.16 to compute the rotation, translation and scale factor [103].

$$\bar{x} = \frac{1}{n} \sum_{i=1}^n x_i \quad (3.1)$$

$$\bar{y} = \frac{1}{n} \sum_{i=1}^n y_i \quad (3.2)$$

Equation 3.1 above showcases the mean segment point in the static (neutral) condition (single frame) to obtain a 3-dimensional average point to defining the segment. Equation 3.2 utilizes the same approach except that the 'y' condition is captured during a dynamic trial, and so is associated with as many frames as are present in the tracked and filtered file.

$$\vec{x}_i = \vec{x}_i - \bar{\vec{x}} \quad (3.3)$$

$$\vec{y}_i = \vec{y}_i - \bar{\vec{y}} \quad (3.4)$$

By taking each marker ( $\vec{x}_i$ ) and subtracting from it the averaged ( $\vec{x}, \vec{y}$ , z) point, a vector is determined from the averaged point to the marker point (Eq., 3.3 and 3.4). The marker ‘n’ represents the number of markers used to define the segment.

$$[C] = \frac{1}{n} \sum_{i=1}^n (\vec{y}_i - \bar{\vec{y}})(\vec{x}_i - \bar{\vec{x}})^T \quad (3.5)$$

Variable [C] is a cross dispersion matrix (also known as the correlation matrix) [103]. The Single Value Decomposition of matrix [C] can be computed from Equation 3.5. The matrix [W] will contain the singular values of matrix [C], while the total number of singular values will indicate the rank of [C], [103]. Using the orthogonal matrices [U] and  $[V]^T$  the rotation matrix [R] can be calculated (Equation 3.7). However adding an additional component (identity matrix with derivative of  $[U][V]^T$ ) ensures that when describing rigid body rotation [R] its determinant doesn’t yield -1, but instead +1.

$$[C] = [U][W][V]^T \quad (3.6)$$

$$[R] = [U][V]^T \quad (3.7)$$

$$[R] = [U] \begin{bmatrix} 1 & 0 & 0 \\ 0 & 1 & 0 \\ 0 & 0 & \det([U] \cdot [V]^T) \end{bmatrix} \quad (3.8)$$

According to Challis [103], a scale factor ‘s’ can be computed that indicates the reliability of the assumption that the human body acts as rigid segments during motion. To do so the standard deviation associated with the initial condition (static/neutral trial) is calculated,

again accommodating for the number of markers present on the segment. This can be seen in Equation 3.9 while Equation 3.10 highlights the derivation of the scale factor. Using the trace function of the dot product of the transpose of the rotation matrix  $[R]^T$  the correlation matrix  $[C]$  can be computed.

$$\sigma_x^2 = \frac{1}{n} \sum_{i=1}^n (x_i - \bar{x})^2 \quad (3.9)$$

$$s = \frac{1}{\sigma_x^2} \text{tr}([R]^T \cdot [C]) \quad (3.10)$$

Bringing the variables ( $s$ ) and  $[R]$  together with the average of the segment markers from the neutral to the dynamic the variable ‘v’ is calculated (Equation 3.11). This represents the vector displacement or translation of the body in 3D space. The 3 variables;  $v$ ,  $s$  and  $[R]$  represent the displacement, accommodation for rigidity assumption and the rotation of a segment, allowing for definition of dynamic positions with accuracy.

$$v = \bar{y} - s \cdot [R] \cdot \bar{x} \quad (3.11)$$

Calculating knee angles was based on Ramakrishnan’s method [104]. Theta 1 ( $\theta_1$ ) represents flexion extension, with flexion being designated in the positive direction, theta 2 ( $\theta_2$ ) for adduction (+) and abduction (-) and theta 3 ( $\theta_3$ ) for internal (+) and external (-) rotation. The equations 3.12-3.15 are based on elements of the rotation matrix  $[R]$  (Equation. 3.12), as well as being dependent upon the calculation of  $\theta_2$ . When calculating Euler rotation angles ( $\theta_1, \theta_2, \theta_3$ ) it is critical to calculate the largest angle first (flexion) then adduction and internal/external rotation [104].

$$R = \begin{bmatrix} I' \cdot I & I' \cdot J & I' \cdot K \\ J' \cdot I & J' \cdot J & J' \cdot K \\ K' \cdot I & K' \cdot J & K' \cdot K \end{bmatrix} \quad (3.12)$$

$$\theta_1 = \arcsin(K' \cdot I / \cos(\theta_2)) \quad (3.13)$$

$$\theta_2 = \arcsin(-K' \cdot J) \quad (3.14)$$

$$\theta_3 = \arcsin(I' \cdot J / \cos(\theta_2)) \quad (3.15)$$

Also, this value must be rotated from the global coordinate system (0,0,0) in order to place these values in the local knee coordinate system. This can be done by calculating a rotation matrix of the global coordinate system (3x3) identity matrix to the vectors located on the shank. This rotation matrix is then multiplied with the angular velocity and acceleration. However, because this yields a value in radians, it was then converted to degrees by multiplying using  $180/\pi$ .

Pearson correlation coefficients were calculated to compare normal walking knee flexion with supine knee flexion over a normalized time period for a single stride. Head translation in 3D space was determined by performing a maximum value minus minimum value in the global coordinate system during supine movement. An ANOVA was used to test for differential effects of direction on head movement. Follow-up t-tests were used to specify the effects.

### 3.3 Results

To orient the reader, ‘normalized time’ describes a percentage of one cycle of gait (0-100), where ‘0’ denotes heel strike, followed by stance phase (10-40%) and finally swing phase from (40-100%), where the cycle would repeat again. Figure 3.3 showcases this for knee flexion during upright walking with a supplementary figure as to the rigid body mechanics behind it.

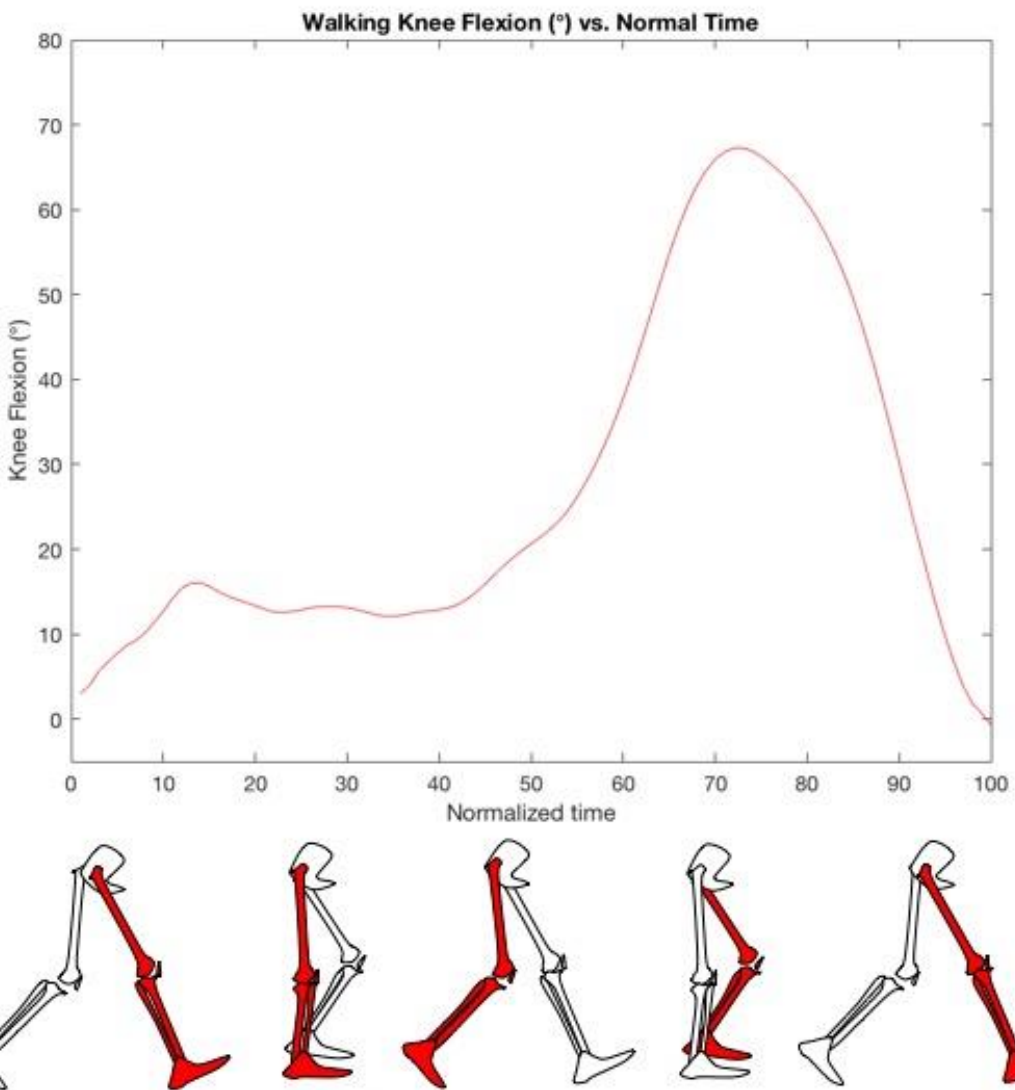


**Figure 3.3 Example of one cycle of knee flexion. The top portion of this figure alludes to the degree of knee flexion occurring in each point of the gait cycle from, heel strike, to stance phase, swing phase and heel strike again, with 0 knee flexion occurring at full knee extension.**

Results are separated into the following sections: Knee flexion for the walking and supine locomotion conditions; Head rotational motion associated with supine movement (as the experimental tasks used in this thesis requires head motion control); and Head movement globally and with respect to chest. Each graph displays one full cycle of knee movement

normalized from heel strike (or beginning of movement) ( $t=0$ ) through stance and swing phase to heel strike again (or end of movement) at ( $t=100$ ).

### *3.4.1 Knee Flexion During Walking and Supine Locomotion*

Results of right knee flexion for the 5 walking trials on a per subject basis. Maximum knee flexion was  $74^\circ$  during walking and occurred at approximately 75% (i.e.,  $t = 75$ ) of the stride, while maximum knee flexion in the supine condition was  $58^\circ$  and occurred at approximately 50% ( $t = 50$ ) of the stride. Upon further visual inspection it can be noted that walking has a small peak at  $t = 15$  (Figures 3.4-3.6).

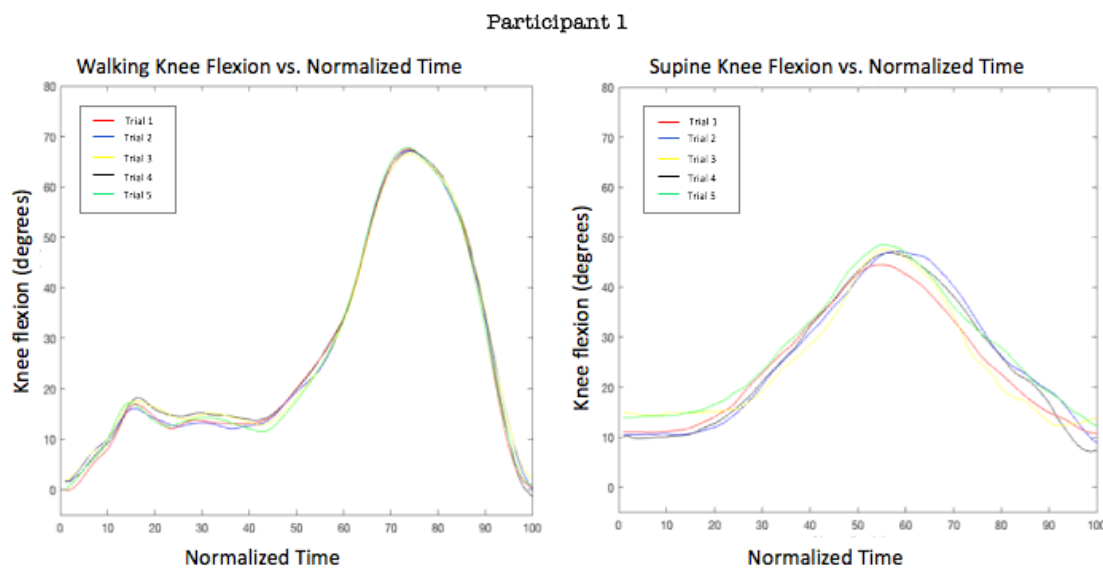


**Figure 3.4 Walking and supine knee flexion (measured in degrees) for participant 1, for 5 trials**

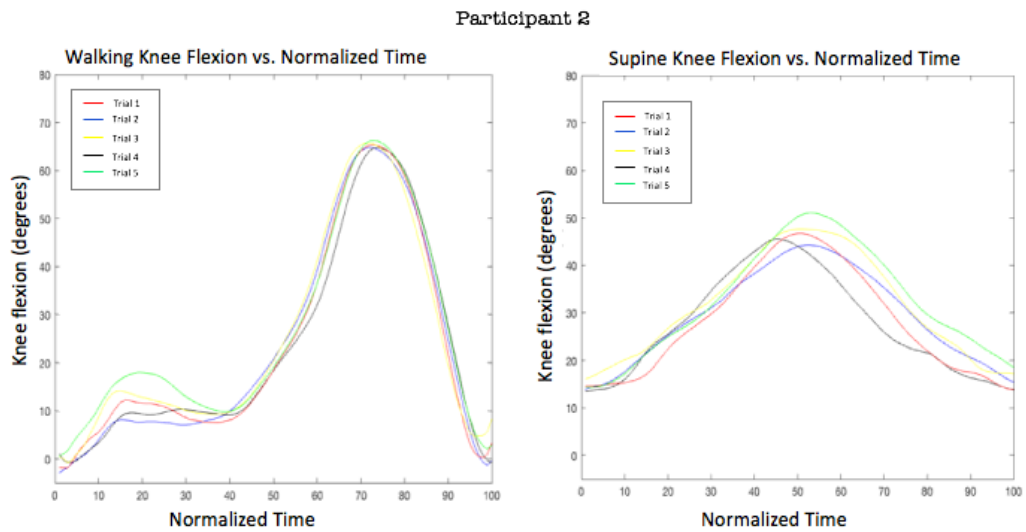


**Figure 3.5 Walking and supine knee flexion (measured in degrees) for participant 2, for 5 trials**

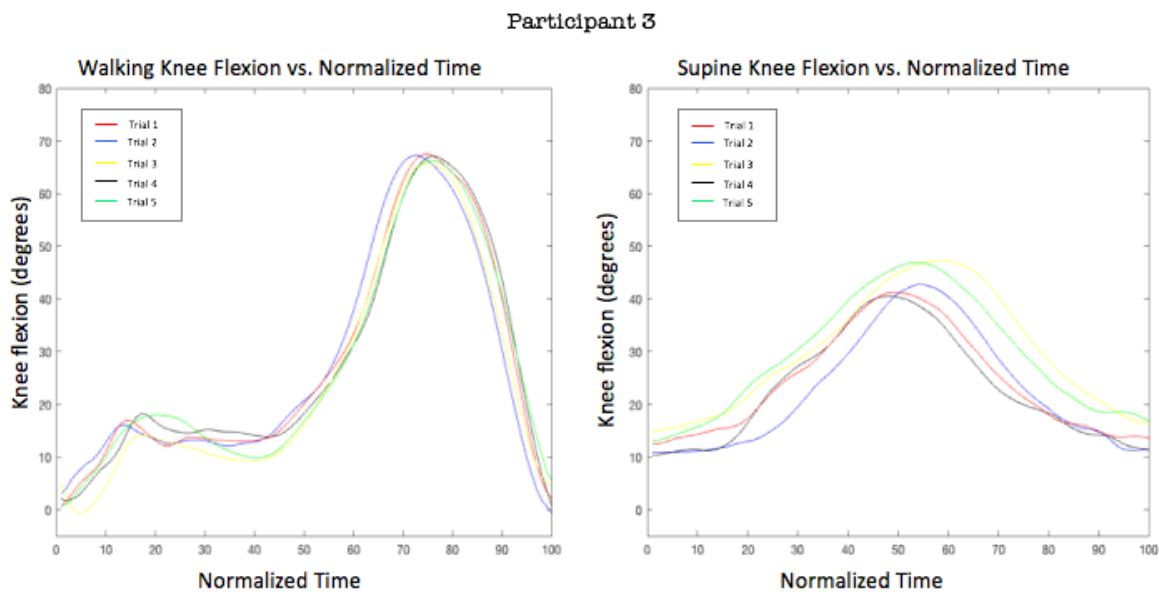


**Figure 3.6 Walking and supine knee flexion (measured in degrees) for participant 3, for 5 trials**

In order to accurately depict the correlation values, enough data had to be sampled from the supine condition in order for the swing and stances phases to line up during a normalized time plot, this entailed including more data points in the normalized time along the x axis at the beginning of each supine trial. Walking and supine knee flexion exhibited a strong association ( $r = 0.9152$ ) (Figure 3.7). As can be seen from this graph, the largest difference is the absence of stance phase (time 0-50) from a supine locomotion condition.

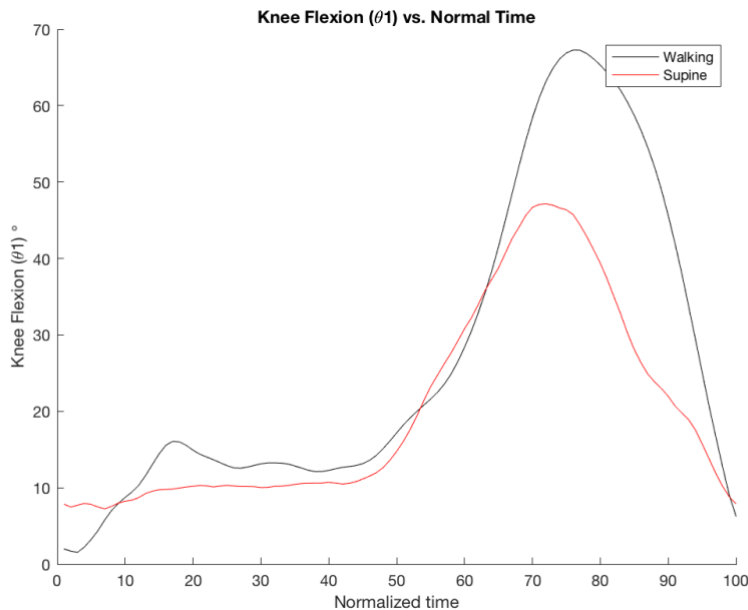


**Figure 3.7 An averaged knee flexion for upright walking and supine locomotion plotted together over normalized time.**

### 3.4.2 Head Motion During Supine Locomotion

Head flexion (pitch) during supine locomotion was calculated for 3 participants (Figure 3.8). The pitch of the head varied approximately  $3^\circ$  within a given trial with respect to the chest.

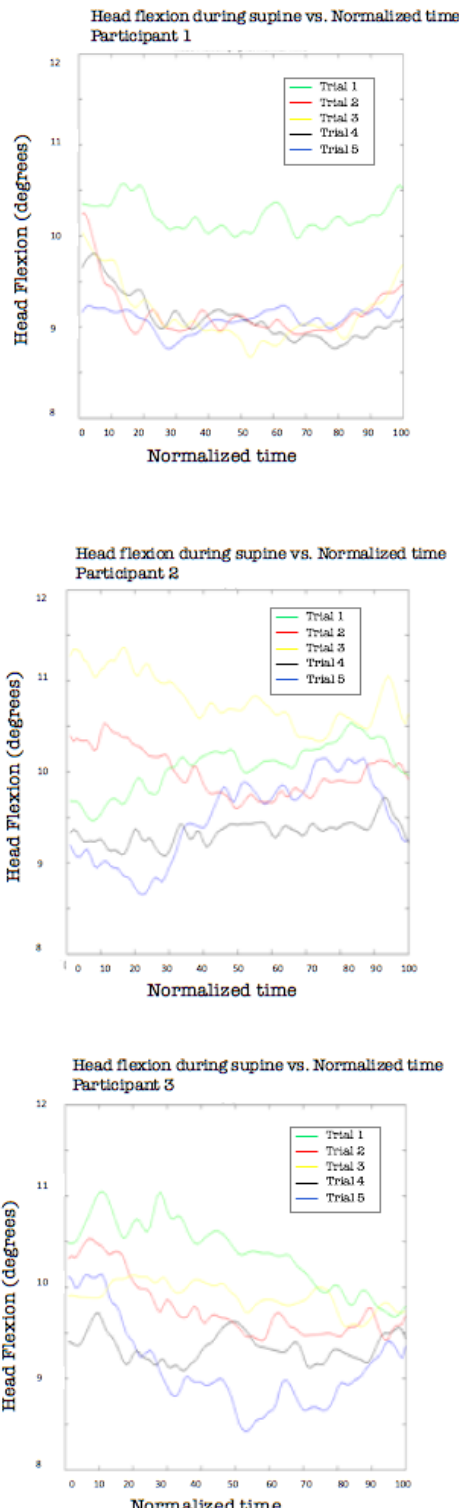


**Figure 3.8 Head flexion during supine locomotion over normalized time for 3 participants,  
A) participant 1 B) participant 2, C) participant 3 for 5 trials.**

To investigate how pitch in the head paired with flexion of the knee joint during supine phases the plot in Figure 3.9 was created. There was almost no rotation around the axis of rotation correlated with the single plane of movement (supine locomotion).

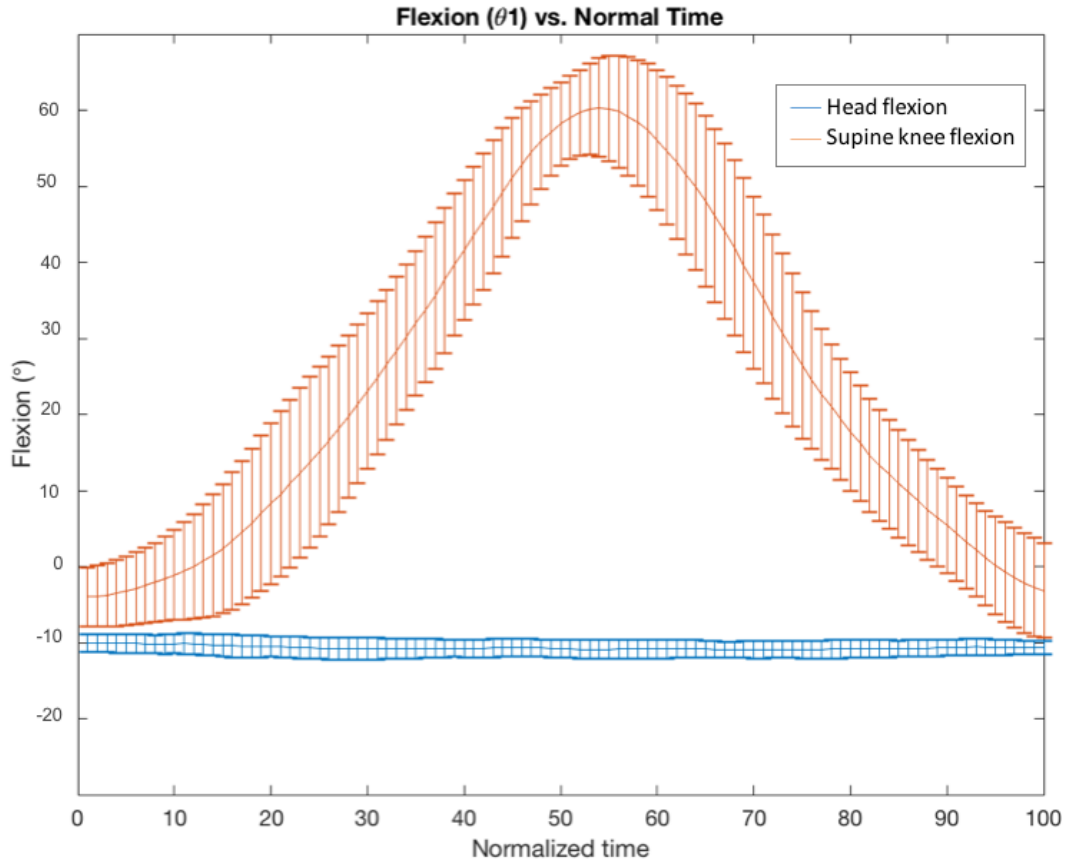


**Figure 3.9 Head flexion (blue) during normalized time of a supine knee flexion (orange). This plot is averaged over all 15 knee and head flexion trials across 3 participants (error bars indicate the standard deviation of the mean).**

Table 3.1 shows the average maximum head displacement in a global (lab) coordinate system over all trials of knee flexions in the supine position with standard error across trials represented by '+/−'. Maximum head displacement exceeded 2 mm in all directions and for all rates of movement (Table 3.1). These were averaged across the 5 supine trials and 3 participants.

The x-axis (oriented parallel to the length of the body) had the largest displacement (5.86 mm). The y-axis displacement was second largest (4.27 mm) and is associated with the movement of the head in left and right directions. The displacement along the global z-axis (pointed vertically up from ground) was 2.48 mm.

An ANOVA revealed a significant effect of direction on head displacement ( $F(2,4) = 27.0, p < 0.01$ ). Follow-up t-tests revealed that movement in the z direction (superior-inferior) was significantly greater than in the y direction ( $p < 0.05$ ) and the x direction ( $p < 0.05$ ), where the z axis is oriented parallel to the length of the body.

**Table 3.1 Average head displacement during supine knee flexion movements**

Flexion rate (steps per min)	Z (mm)	Y (mm)	X (mm)
40	7.2 +/- 0.4	3.0 +/- 1.0	2.1 +/- 0.6
50	4.0 +/- 0.6	2.9 +/- 0.1	2.2 +/- 0.2
60	5.6 +/- 0.8	4.4 +/- 0.8	2.9 +/- 0.6
70	8.0 +/- 1.2	3.9 +/- 0.4	3.6 +/- 0.2
90	7.0 +/- 1.3	6.4 +/- 4.2	4.6 +/- 2.3

Head movement with respect to chest displacement was investigated to determine displacement between the two body segments over time. The graph shown in Figure 3.10 is plotted across the 15 trials (across 3 participants) during supine locomotion at 50 steps per minute. All values overlap one another at a value of 0, and are of the magnitude ( $\pm 1 \times 10^{-5}$  mm). This value is negligible as photogrammetry errors are associated with approximately 1 millimeter of error when determining marker locations.

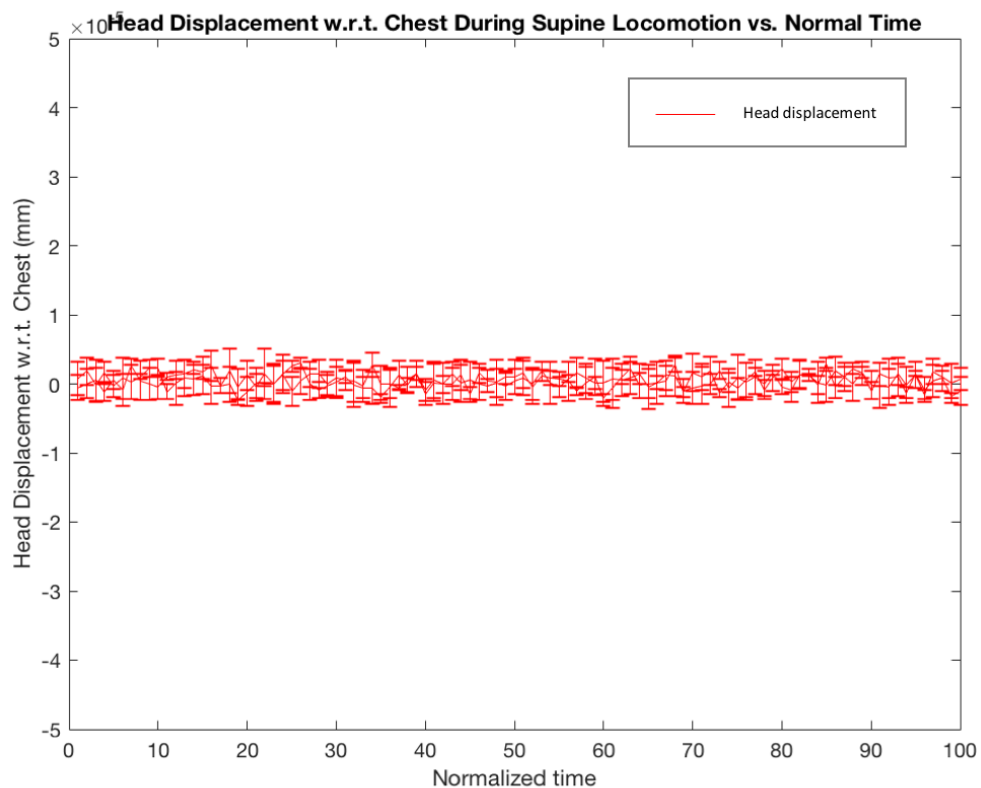


**Figure 3.10 Head translation with respect to chest.**

### 3.4 Discussion

This study demonstrated there is similarity between knee flexions occurring during upright walking and supine stepping but that measures are needed to align the knee flexion kinematics over time. The need to address head movement was also highlighted. Minimizing such movement to under 2 mm is essential to reduce the ‘noise’ in fMRI data, and left unchecked is more likely to be up to 5-6 mm. In addition, despite the lack of stance phase during a supine stepping task, the correlation between knee flexion during supine and walking locomotion remains high during swing phase.

### **3.5 Limitations**

This study had several limitations. The calculation of the knee and hip joint centers were somewhat subjective. Tylkowski's method is cited as being more accurate than Andriacchi's; however, it is still associated with approximately 1.90 cm of discrepancy from true radiographic hip joint center [102]. A combination of Tylkowski's and Andriacchi's method is superior than either one alone. This combined approach uses Tylkowski's frontal plane proportions and Andriacchi's sagittal plane ones, generating hip center results within 1.07 cm of the true radiographic hip joint center [102].

### **3.6 Conclusion**

The findings support the contention that the head and torso act as a rigid unit during supine knee flexion. Thus, constraining the torso will most likely limit head motion as both move as a single unit (Figure 3.10). The biokinematics of supine knee flexion strongly mimics walking knee flexion, supporting the rationale of using fMRI neurological data that are based on supine knee flexion. Results also demonstrated the need for head restraint via restraining the torso to enable to collection of locomotion data in the MR scanner.

To keep the coordinate definition consistent across tasks, the marker on cervical vertebrae 7 was excluded in the determination of the chest coordinate system for all movement conditions. This is because it was hidden from the cameras during the supine condition. Normalizing the data during walking, standing and supine movements allowed for direct comparisons between conditions. It is critical to select a full cycle of movement from the middle of each trial, as aliasing of the filter can cause distortions of the data at the beginning and at the end of any given set of data and the eight Kestrel Motionanalysis™ cameras produced the most

accurate marker location data in the middle of the capture volume. This is because each marker was located to maximize its ability to be seen by as many cameras as possible. This ensured reliable data were collected.

Lastly, these data were collected on a small ( $N=3$ ) sample of young, healthy male subjects and limits the generalizability of the findings to older or female populations.

Based on the results, and in light of the constraints of the MR scanner, a specially-designed MR-compatible rig was built to facilitate supine knee flexion. This process is described in the next chapter.

## CHAPTER 4: AN MR-COMPATIBLE APPARATUS FOR SIMULATED STEPPING

### 4.1 Introduction

Human locomotion (walking) has long been studied kinematically by biomechanists typically using electroencephalography (EEG) and neurologically by neuroscientists typically using functional magnetic resonance imaging (fMRI). Locomotion research using fMRI frequently is limited to ankle dorsiflexion data gathered while subjects are in the MRI scanner [105]. This limitation is due to study participants being required to lie in a supine position in the MR scanner. Another problem with fMRI methodology is that most MR scanners have a 3D voxel size of approximately 27mm<sup>3</sup>. Consequently, the MRI is very sensitive to movement artifacts resulting from human participant body motion [101], [106]. Head movement in any direction exceeding the size of a voxel (~1-3mm) is enough to introduce sufficient error artifacts rendering the MR data unusable. Despite these drawbacks, researchers are drawn to fMRI as a methodological technique, given that it results in high spatial resolution of deep and superficial brain activity data.

Some early research designs were created to allow for lower limb movement inside the MR scanner. However, walking incorporates movement in the lower body at the hip, knee and ankle, and these extant designs only allowed for knee motion. Therefore, extrapolation of the kinematic similarity to walking was less than ideal.

Raymer, *et al.* in 2006 developed an ankle exercise device that was MR compatible [107]. However, this design fell quite short, as it was only designed for ankle flexion and dorsiflexion. In addition, it was only designed for use with a single leg. Several years later in 2011, Ghomi, *et al.* [108] designed a lower body locomotion device. It, too, was only useful for a

single leg; however, this time a pulley weight was included to simulate gravity. More recently, Hollnagel, *et al.* in 2011 [109] created a bipedal device that allowed for hip, knee and ankle movement (as occurs during normal walking); however, their design incorporated several pneumatic pressurized cylinders to offer resistance, which is costly, and no quantification of how well it simulates upright walking was provided.

To address these issues a new device was created to allow controlled lower leg flexion/extension movement (hip, knee and ankle) that mimics stepping while the participant is in the MR scanner that keeps head motion to a minimum. This device is henceforth referred to as Locomotion Acquisition for Magnetic Resonance Imaging (LAMRI).

## 4.2 Methods

In designing an MR-compatible stepping simulator to study the brain's involvement in locomotion, several design criteria and constraints were established. These included physical dimension, materials, how well it simulates walking and how head motion is controlled.

### 4.2.1 Physical dimensions

The physical dimensions of the MR scanner can be seen in Figure 4.1. The two most relevant dimensions are the width of the scanner bed (without bumpers) and the length of the table. In addition, although not depicted here, the MR scanner bed is concave with a radius of 1.5 m.

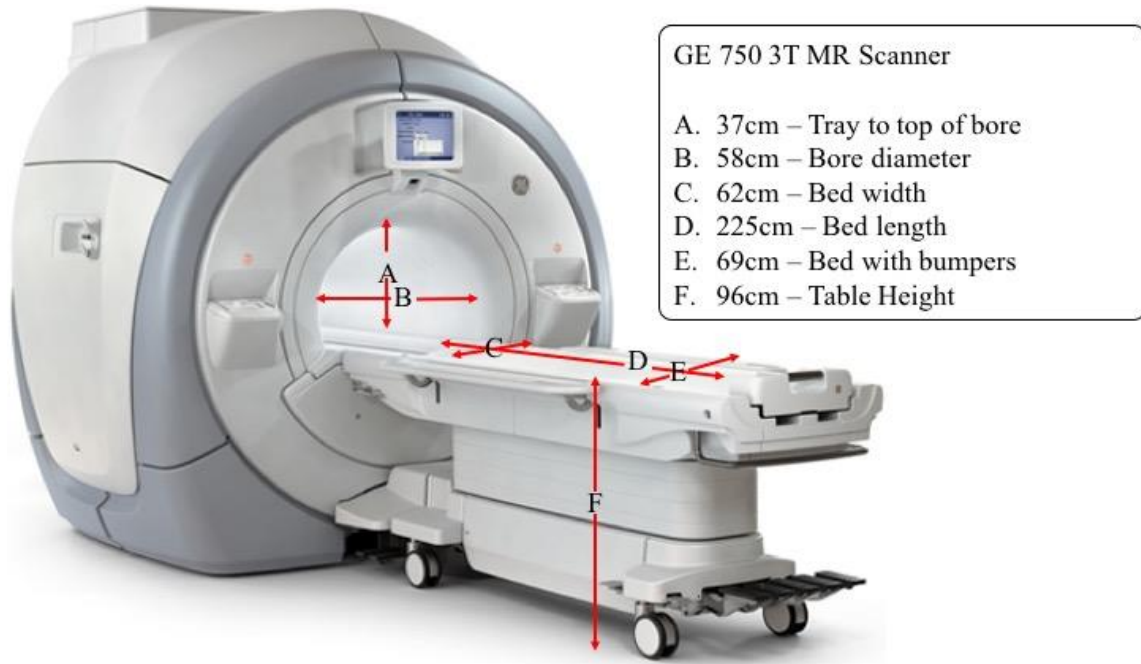


**Figure 4.1** MR scanner bed dimensions

#### 4.2.2 Materials

Construction is limited to non-ferromagnetic components and the overall design should be lightweight for ease of transport on and off the MR scanner bed. To address these parameters, it was decided to use aluminum, wood, polyurethane and brass. Pine was used for the backboard as it is light, durable and strong. The pedals and pulleys were made of Lexan, due to its very low coefficient of friction for both the pulley–rope and pedal-board interfaces, with brass rod and nylon bolts. Aluminum was used for the pulley mounts, with brass counter-sunk screws. Ribs were incorporated on the backside of the wooden board to provide a stable base and to distribute participants' weight across the entire board due to the concavity of the MR bed.

#### 4.2.3 Limiting Head Motion and Simulating Walking

To limit head motion, it was decided to include torso restraints to limit the movement of the chest that would, in turn, minimize the movement of the head translating in the direction of the

motion. Also, so that participants could ‘brace’ themselves against the movement of their torso, the design incorporated modular handholds (to accommodate various arm lengths). Several slits at the top half of the board allowed straps to be fed through to restrain movement of the upper body and head. Such straps criss-cross the body and go around the abdomen. To simulate the force of gravity experienced when walking, the pedals that slide within a near frictionless track were connected to pulleys with weights attached. Because the force of gravity for each participant would be specific to their own unique mass, a weighting system based on the participant’s anthropometric data was needed.

Based on these specifications, a computer-aided design (CAD) of the MR rig including the board, pedals, and pulley system was created (Figure 4.2). The constructed rig is shown in Figure 4.3. A rope was fastened to the end of the base plate and the groove of the pulley placed at 90-degree angles. This was done so that the weight tied to the end of the rope would be equal to that of gravity as experienced by the participant. Modular weights were applied, based on the anthropomorphic characteristics of the participant, using weights made of salt (contained within a fabric bag), incremented in 1kg units, and attached to the pulley system. Specifically, leg segment mass (thigh and shank) was calculated as a percentage of total mass based on anthropometric data for ‘normal’ individuals, equating to 17 % body weight for each leg [110]. Figure 4.4 shows a close up of the CAD design (left) and the actual design (right) of the pulley system for applying tension to the participants’ legs via a simulated gravity weight.

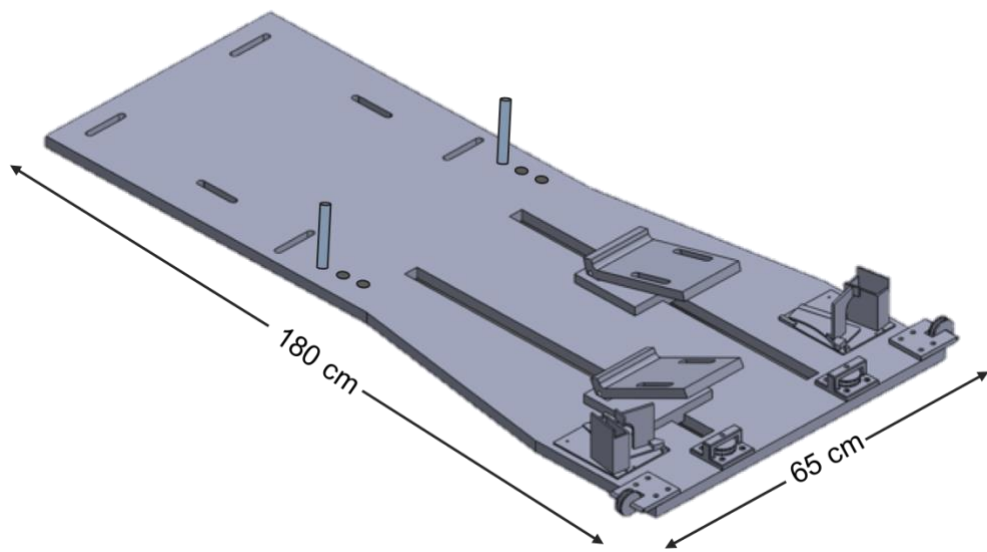


**Figure 4.2 CAD design of LAMRI including dimensions to assist with scale. This figure shows the pulley system, response button holders to time stamp stepping and hand holds for participants.**

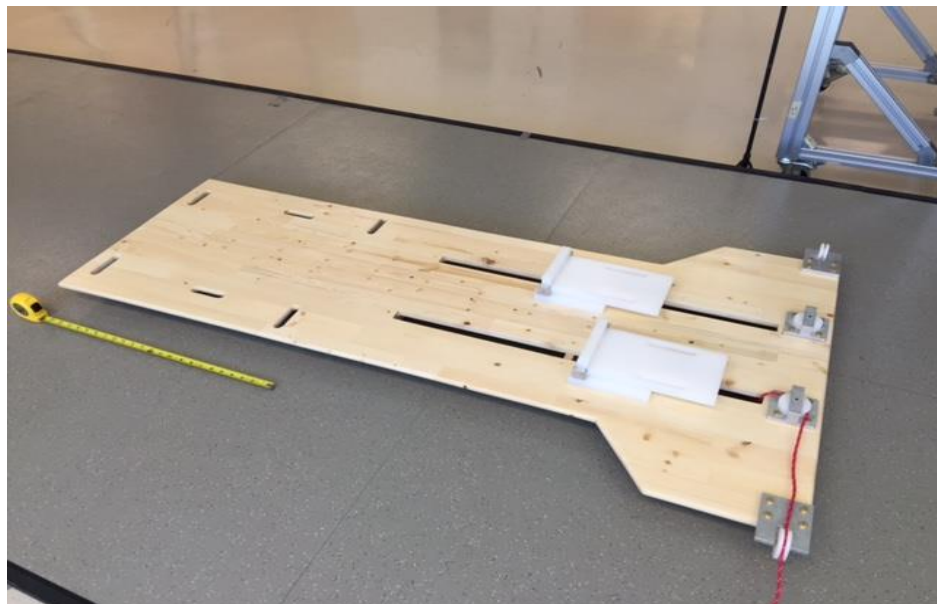


**Figure 4.3 MR compatible board. The tape measure in the picture denotes (2 ft) for scale.**

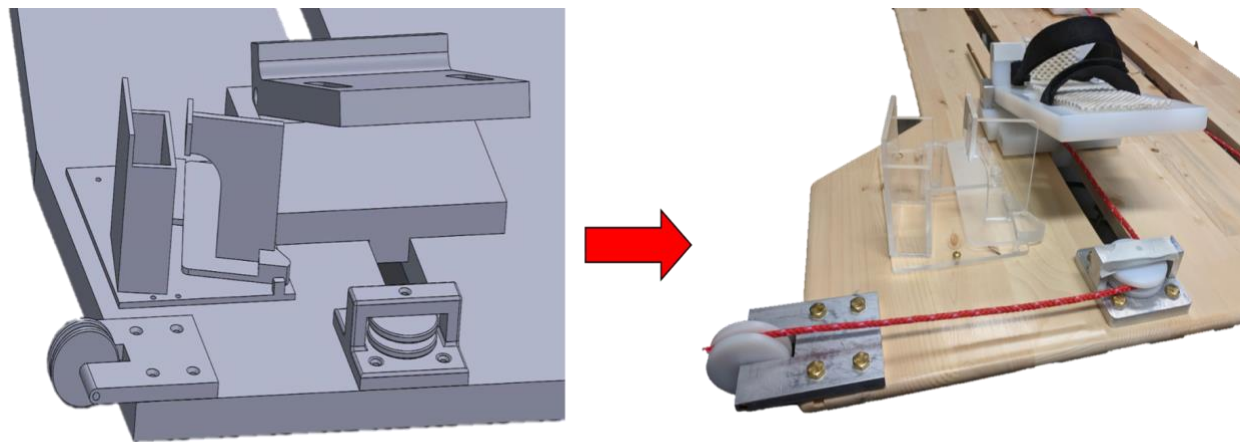


**Figure 4.4 Rig pedal from the end view. This highlights the pulley mechanisms and the foot pedal in conjunction with the response button holder.**

To record the timing of the participant's stepping (frequency, time of stepping versus stimulus, etc.), response button pads were incorporated into the design. These are usually hand held non-magnetic, non-electric fiber optic response buttons. However, these needed to be adapted for use in this study so lower limb movement could be time stamped into the neurological data collection. Figure 4.5 shows a close-up of the button pad holder from the CAD diagram (left), and Figure 4.5 (right) shows the actual response button pads that were incorporated into the design.

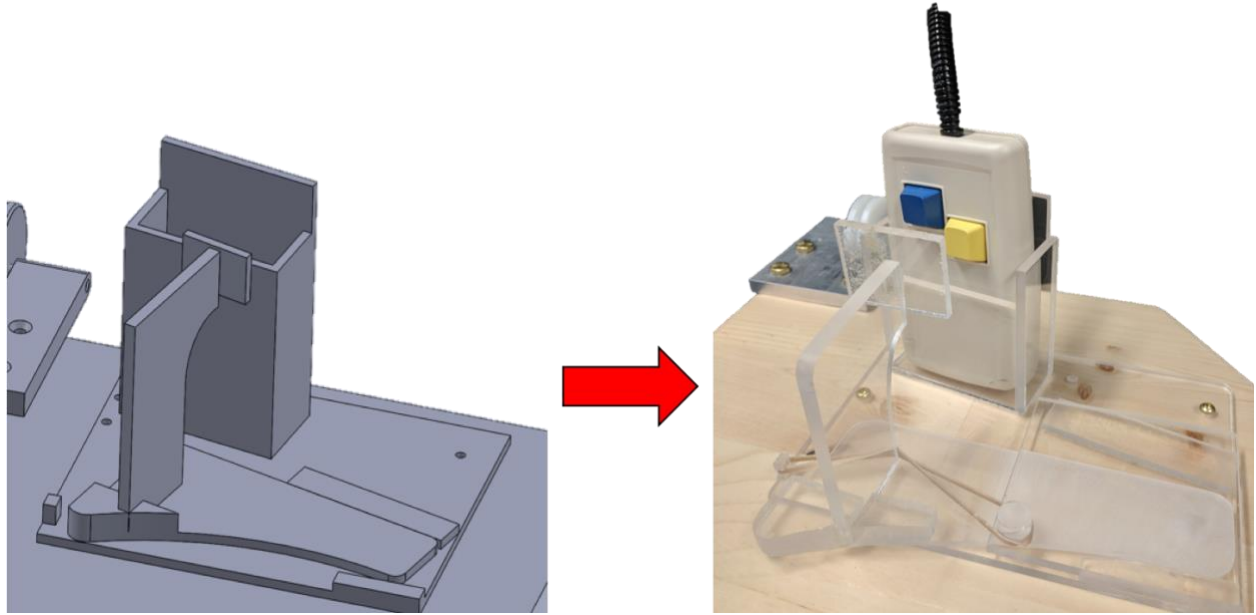


**Figure 4.5 Response button pad incorporated for time stamping data in EEGs**

Recall that participants alternate between flexion and extension of the knee joint. Upon flexion, the foot pedal slides past the spring-loaded depressor (towards the end of the board where the participants head is), releasing the response button. When the participant extends their leg back down and returns to a neutral position, it presses the spring loaded mechanism and depresses the response button. This design also provided individual left versus right time stamps so that differentiation during executed movement could be accurately identified for analysis. This is an important aspect of the design for stepping research, as it allows for the control and measurement of stepping speed. Figure 4.6 shows the MR compatible rig as it was used in the MR scanner.

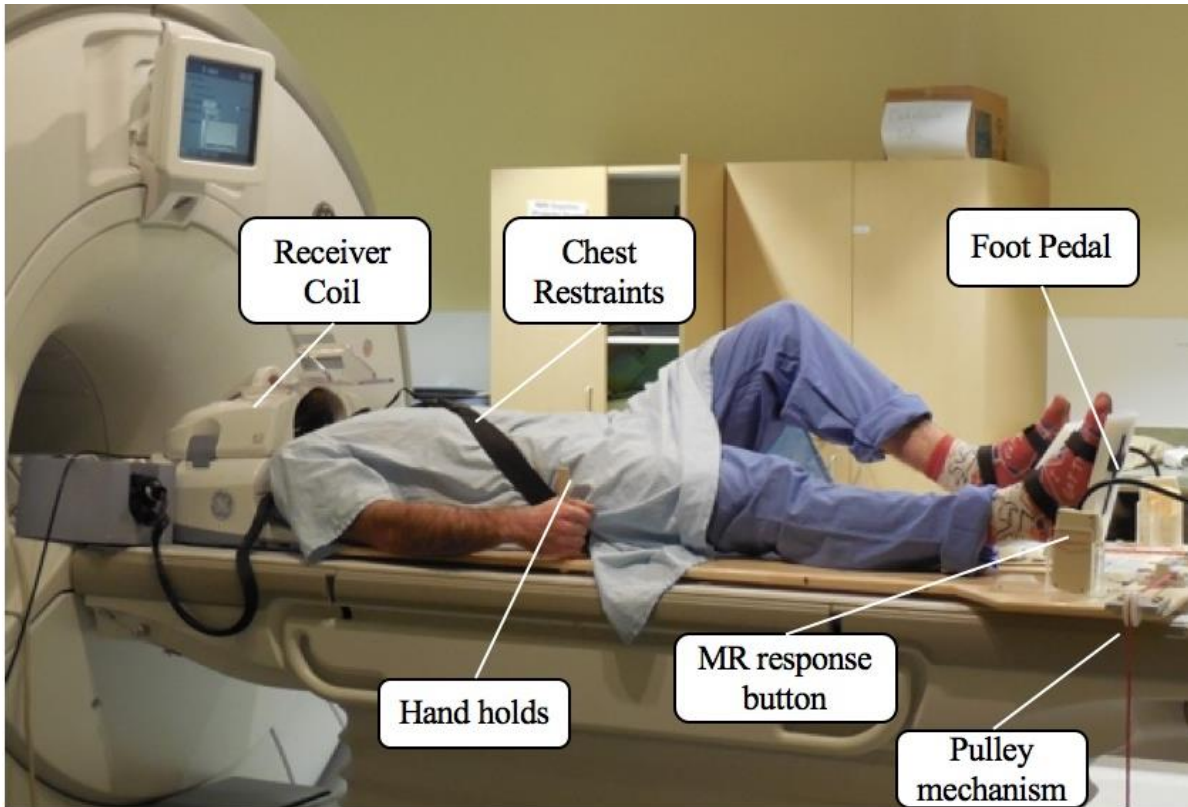


**Figure 4.6 MR compatible rig in MR scanner with participant positioned in stepping movement**

Once the rig was completed, the final design was pilot-tested to measure head motion of the participants, quantifying translations along the x, y and z axes. It was also important to establish the degree of similarity between the knee kinematics of supine stepping using LAMRI with upright walking in the Clinical Movement Assessment Laboratory (University of Calgary, HRIC3C48A), and follow up with testing head motion while participants were in the MR scanner.

Pilot testing of the LAMRI consisted of having three healthy participants perform supine stepping alternating right and left leg movement at a rate of 50 steps per minute (approximately half the speed of walking), where they followed along with a metronome, performing 5 trials of supine stepping, both with and without the rig. Head translation was recorded using 8 Kestrel

motion analysis cameras where movement was tracked using 4 reflective head markers (using the methodology explained in Chapter 3), where the 4 points on the head were averaged and head displacement was recorded relative to a global coordinate system (GCS). Absolute head movement was compared between the “without rig” and “with rig” conditions using paired sample t-tests.

Limiting head motion was then validated by implementing the LAMRI at the Seaman Family MR Center (Foothills Hospital) where head movement was estimated from FSL [111] translations. Any motion exceeding 3mm during a functional scan of 6 minutes where participants followed along with a stimulus alternating at 50 steps/minute would indicate the rig was not working.

### 4.3 Results

Head movement using the LAMRI was less than 3 mm in every direction (x,y,z) at a significance level of ( $p<0.05$ ), and was considered acceptable when the rig was implemented (Table 4.1). Paired sample t-tests revealed a significant reduction in head translation for all three axes when using the rig at the Clinical Movement Assessment Laboratory.

**Table 4.1 Head Translation During Supine Movement, (\*) denotes significantly different ( $p<0.05$ ) between conditions.**

Condition	Z (mm)	Y (mm)	X (mm)
Without Rig	$4.0 \pm 0.6$	$2.9 \pm 0.1$	$2.2 \pm 0.2$
With Rig	$1.3 \pm 0.4 *$	$0.7 \pm 0.5 *$	$0.3 \pm 0.2 *$

Head translations over the course of the fMRI portion of the experiment, in the x (anterior-posterior), y (left-right), and z (superior-inferior) directions, for the three participants performing the supine knee flexion movements using the MR-compatible rig are shown in Figure 4.7 and ranged from -1.5 to 2mm from the origin.

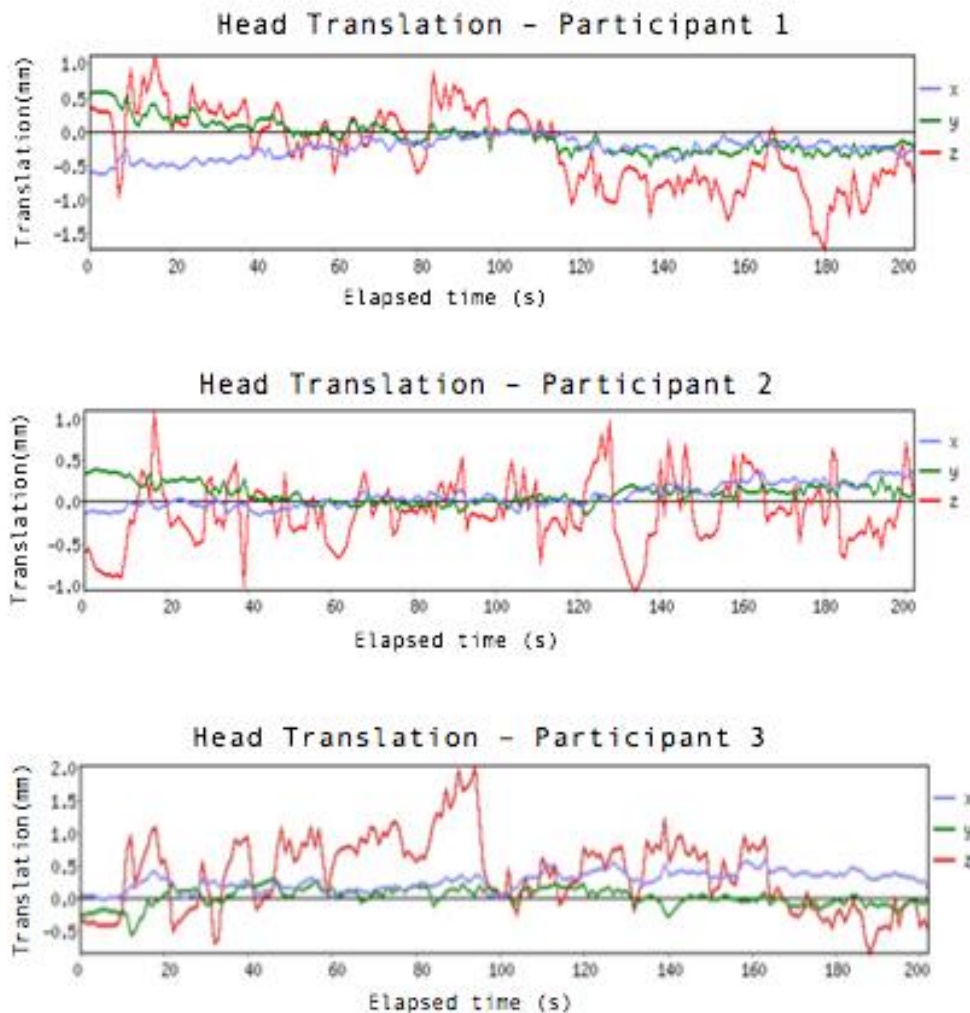


**Figure 4.7 Head translations of the 3 participants, A) Head translation of participant 1, B) Head translation of participant 2, C) Head translation of participant 3, while performing stepping movements in the supine position using the MR-compatible rig, estimated from FSL.**

Again, no head translation exceeding 3mm was present from the FSL estimated movements.

Supine knee flexion (where the participant used the LAMRI) is compared to upright walking in Figure 4.8. The maximum knee flexion angle and its location within the stride for supine leg movements with the rig more closely matched those for upright walking than for supine leg movement without the rig ( $t = \sim 60\text{-}70$ ).

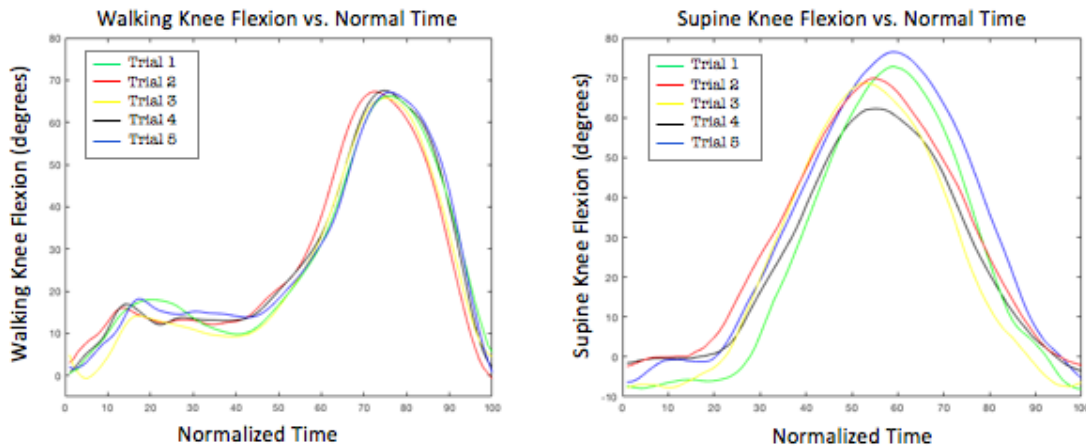


**Figure 4.8** Knee flexion angle over the course of a A) stride for upright walking and B) supine leg movements using the MR compatible device across 5 trials.

#### 4.4 Discussion

A MR-compatible rig was constructed to permit simulated walking while lying inside an MR scanner. The design significantly reduced head movement during stepping tasks, and the stride closely resembled that of natural upright walking.

The MR rig was intentionally designed to be modular so it could be adjusted for people of different heights and weights. The rig allows for hip, knee and ankle flexion/extension; thus, it can be used to assess all three actions associated with stepping. This design offers a relatively

inexpensive means to study lower body flexion/extension mimicking stepping and a component of locomotion using fMRI.

The next chapter describes the overall methods used to collect EEG and fMRI data during stepping tasks performed using the MR-compatible rig.

## **CHAPTER 5: MAIN STUDY METHODOLOGY**

### **5.1 Methods**

#### *5.1.1 Participants*

Sixteen healthy, right-handed males between the ages of 19 and 31 years (mean = 24.7, SD = 3.31), with no history of knee or hip injury or neurological deficiency participated in the study, similar to that of most published EEG fMRI technologies to analyze motor movements [11],[13],[18],[20],[79],[83]. This was done for two reasons. One was to methodologically control for sources of variance (e.g., age, gender). Given the paucity of studies, and thus current understanding, of brain activity resulting from lower limb movement under varying conditions is not well-known this was deemed a prudent approach. Second, young males (in the 15-29 year old categories) are the demographic group most likely to suffer from traumatic spinal cord injury [112], and so most likely to benefit from findings of the current research.

The study was approved by the University of Calgary's Conjoint Health Research Ethics Board (Ethics ID: REB15-1473). All participants provided written informed consent and passed MR safety screening. Participants were asked to indicate their dominant leg (i.e., the leg they use to kick a soccer ball) and their body weight (in order to calculate the appropriate amount of weight to attach to the MR-compatible rig pulleys) (Appendix A).

#### *5.1.2 Sessions and Data Collection*

Participants took part in three sessions during which they performed walking movements using the MR-compatible rig: 1) Baseline EEG; 2) EEG at one week; and (3) simultaneous EEG/fMRI at two weeks.

Sessions 1 and 2 were conducted at the Clinical Movement Assessment Lab (Foothills, HRIC3C48A). Participants were fitted with a 64-electrode EEG headcap (Compumedics Neuroscan, Charlotte, SC). The location of electrodes followed the conventional 10-20 electrode international placement system. EEG data were collected continuously during the tasks (described below) at a rate of 1 kHz. The participant lay on the MR-compatible rig, their feet were strapped to the pedals, and the appropriate weights were attached to the pulleys. The participant was positioned so that a video display could be viewed (Figure 5.1). Video stimuli (described below) were projected onto the screen using a TV monitor during time points 1 and 2, and a projector during time point 3, where the participants used a mirror in order to see the visual stimulus. This was done in an attempt to keep the set up as consistent as possible across all 3 data collection time points.

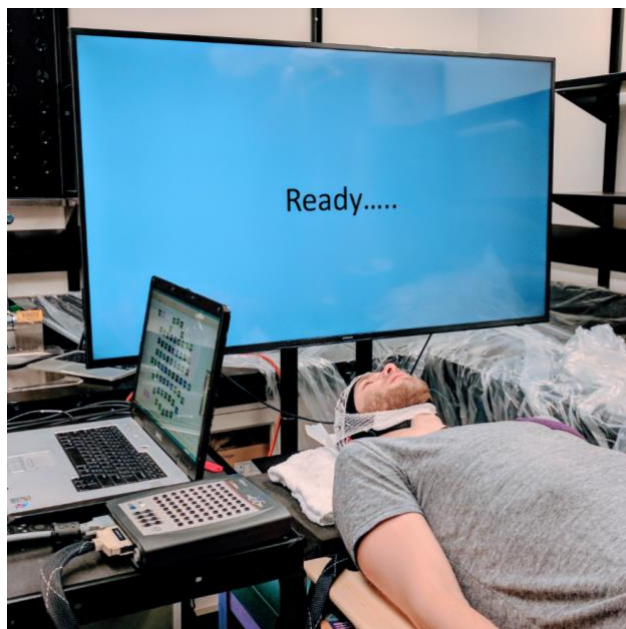


**Figure 5.1 Participant lying in a supine position on the MR- compatible rig while viewing a video display.**

Session 3 was conducted at the Seaman Family MR Research Centre. Participants were fitted with an MR-compatible 64-electrode EEG headcap with Ag-AgCl electrodes (Maglink RT; Compumedics NeuroScan). EEG was collected continuously at a rate of 10 kHz, to allow for removal of MR gradient-induced artifacts during simultaneous fMRI. MR data were collected using a 3 Tesla Discovery 750 MR scanner equipped with a 12-channel head array coil (GE Healthcare, Waukesha, WI). The MR-compatible rig was placed on the MR scanner bed, and participants lay on the rig in a supine position. The head coil for brain imaging was positioned over the participant's head and the EEG cables were led out the back opening of the coil, secured to the scanner bed, and attached to the EEG recording system. The participant's head was comfortably immobilized within the head coil using compressible foam cushions. An angled mirror secured to the head coil was positioned above the eyes to permit viewing of a video screen positioned at the back of the MR scanner. Video stimuli (described below) were projected onto the screen using a projector located at the back of the MR scanner (Silent Vision, Avotec Inc., Stuart, FL).

MR imaging first consisted of a localizer scan (0.5 min) to prescribe slice locations for all subsequent scans. A T1-weighted high-resolution structural brain scan (5 min) was then obtained for anatomical registration of the EEG and fMRI data. Next, fMRI data were collected using a T2\*-weighted echo planar imaging (EPI) sequence (matrix size = 64x64; field of view – 24x24 cm; 32 slices; 0.2-mm gap between slices; echo time = 30 ms; volume repetition time – 2000 ms; 189 total volumes) [113].

### 5.1.3 Visual Stimuli

Two different visual stimuli were presented to assess their possible differential effects on the ability to isolate the right versus left leg movements in both the executed and imagined walking conditions. One visual stimulus was of a custom computer-generated image (CGI) of a human walking generated in *Daz 3D* (Daz Productions Inc., Salt Lake City, Utah, U.S.) (Figure 5.2), and the other stimulus was a circle that switched colors between green and blue (Figure 5.3).

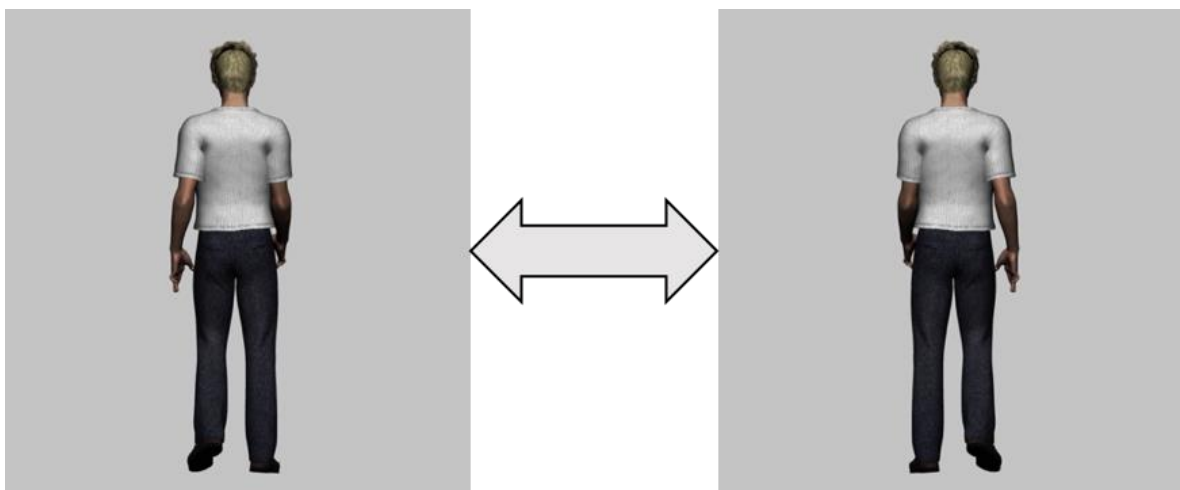


**Figure 5.2 CGI stimulus of a human. The stimulus was animated such that the legs moved in a walking fashion at the prescribed pace of 50 steps/min.**

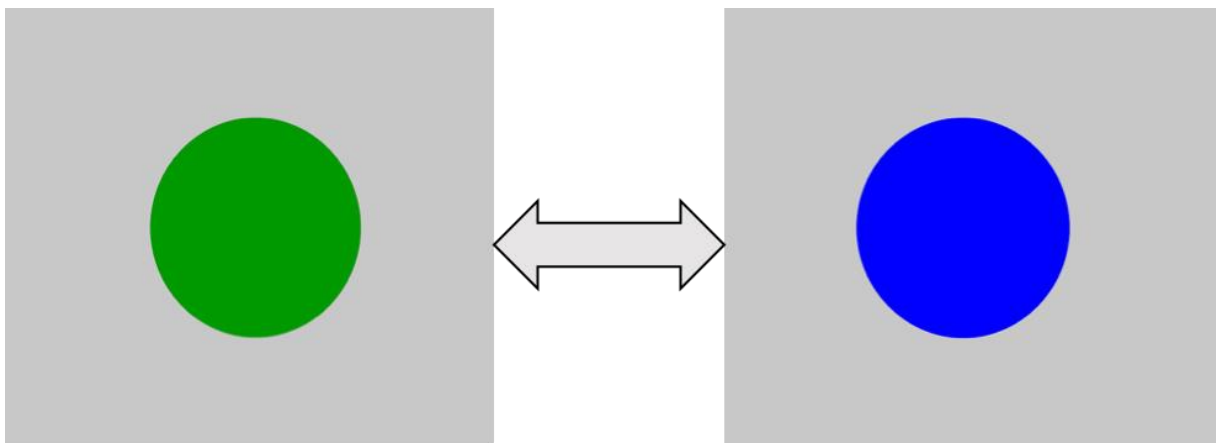


**Figure 5.3 Green (left) and blue (right) circle stimuli. Colors alternated at the prescribed rate of 50 steps/min.**

#### *5.1.4 Executed and Imagined Walking Tasks*

The video stimuli were presented in a ‘block’ format, alternating between rest and task blocks (Figure 5.4). A rest block lasted 18 seconds at which time participants were instructed to breathe and blink normally while maintaining visual focus on a fixation cross. A task block consisted of an 18-second display of the stepping task condition. In total there were 20 blocks each of rest and task. The length of visual stimulus presentation remained the same at all 3 time points.

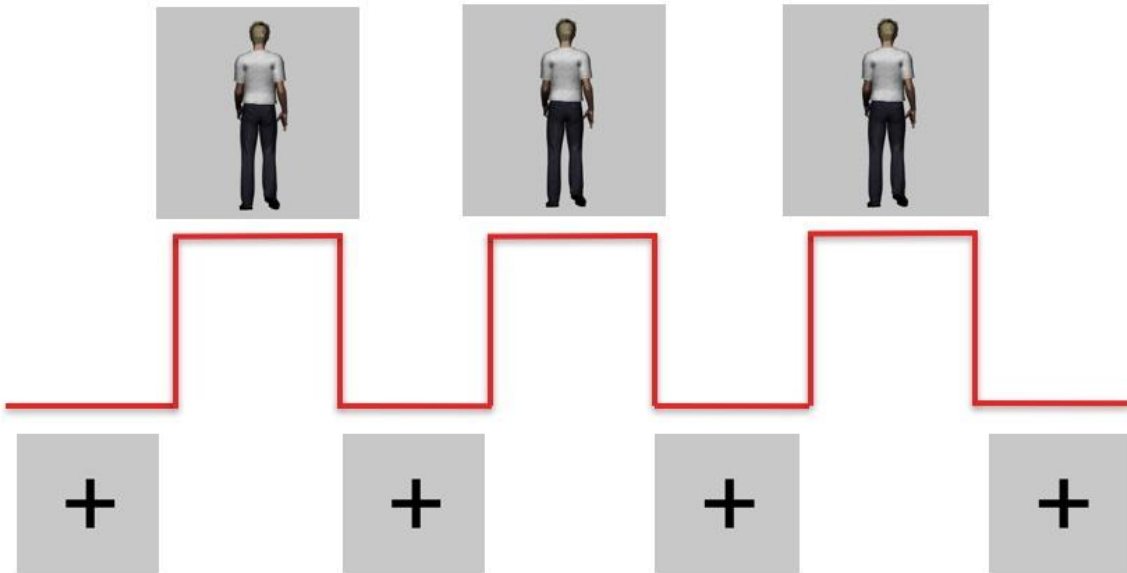


**Figure 5.4 Sample of block design of the stepping task, where each rest and active block lasted 18 seconds.**

In the executed stepping condition, participants were instructed to follow along and execute stepping in time with the visual stimulus, which was set to 50 steps per minute, which is approximately half of normal walking speed [114]. The slower rate helped to reduce head motion. As described in Chapter 4, the timing of stepping movements was recorded using the MR-rig response pads (Lumina LS-PAIR, Cedrus Corp., San Pedro, CA). In the imagined

stepping condition, the same visual stimuli were used. Participants were instructed to imagine the feeling of moving their legs (kinesthetic visualization) from a first-person perspective.

The tasks were performed in the following order for all participants: Blue-green Executed, Blue-green Imagined, CGI Executed and CGI Imagined. On average, total time for sessions 1 and 2 was 50 minutes, and 90 minutes for session 3. All data were collected between May and October 2017.

## **5.2 Next Steps**

The results of the studies, that combined make up this dissertation, are presented in the following four chapters. Each of the chapters is devoted to determining the viability of the four hypotheses that together move to realize the goal of this research project.

## **CHAPTER 6: DIFFERENTIATING THE CORTICAL CONTRIBUTIONS OF RIGHT AND LEFT STEPPING MOVEMENTS USING ELECTROENCEPHALOGRAPHY**

### **6.1 Introduction**

The purpose of this chapter is to assess hypothesis 1: EEG data will demonstrate brain activity patterns that distinguish left from right leg movements for both imagined and executed conditions; this effect is expected to be particularly strong for the computer generated image based stimuli conditions. Given the paucity of literature on lower limb movement, support for this hypothesis will help in achieving the goal of creating a BCI capable of assisting in lower limb locomotion.

Neuromotor control of walking has been studied using several methods, including decoding of intra-limb and inter-limb kinematics from EEG data [7], isolation of gait-related movement artifacts in EEG data [115], and distinguishing areas of activation in the brain between executed and imagined walking [116]. A study to distinguish between left and right steps for both executed and imagined walking has not yet been performed, which has important implications to enable BCIs to control individual limbs, and is the focus of this chapter.

Three EEG frequency bands have been found to be most commonly associated with lower limb locomotion: alpha (8 – 12 Hz), beta (12 – 30 Hz), and gamma (30-45 Hz) [52]. While EEG data are typically collected from 64 electrodes, the electrodes of focal interest for this study were the C1 and C2 electrodes. They are located on top of the head and in proximity to where the leg area of the primary motor cortex is located. The hypothesis of this study was that it would be possible to differentiate left and right steps using EEG frequency data, specifically collected

from the C1 and C2 electrodes, for both executed and imagined stepping. Furthermore, it was expected that the CGI stimulus would be more successful.

It was also important to determine the generalizability of the findings. The use of generalizability theory is becoming more prevalent in a number of research areas including center of pressure data collected with a force platform [117], ankle-complex laxity measures [118], electromyogram (EMG) power measures [119], and EEG interpretation [120]. This approach allows for a better understanding of the reliability of the data and sources of variance for generalizability purposes than does the simpler test-retest approach often used in EEG research [121], [122], [123], [124], [125].

## 6.2 Methods

The subjects, experimental setup and data collection were described in Chapter 5. The EEG data collected at time points 1 and 2 were used.

### 6.2.1 EEG Analysis

EEG data from the C1 and C2 electrodes were analyzed using customized software developed in *Matlab* (Mathworks, Natick, MA). Data were DC offset corrected, bandpass filtered between 5 and 55 Hz, and referenced to the global average of all 64 channels. Epochs of data were generated based on the timing of the visual stimuli onset/offset for each individual ‘step’ (200ms prior to stimulus and 823ms after stimulus). Because the visual stimulus altered every 1.5 seconds, it was important not to have overlap in the data from the ‘left’ and ‘right’ conditions. Therefore, a usable time frame of 1.024 seconds could be encapsulated within alternating 1.5 second durations. This time frame was also computationally efficient for performing a Fourier transform [126] (Figure 6.1).

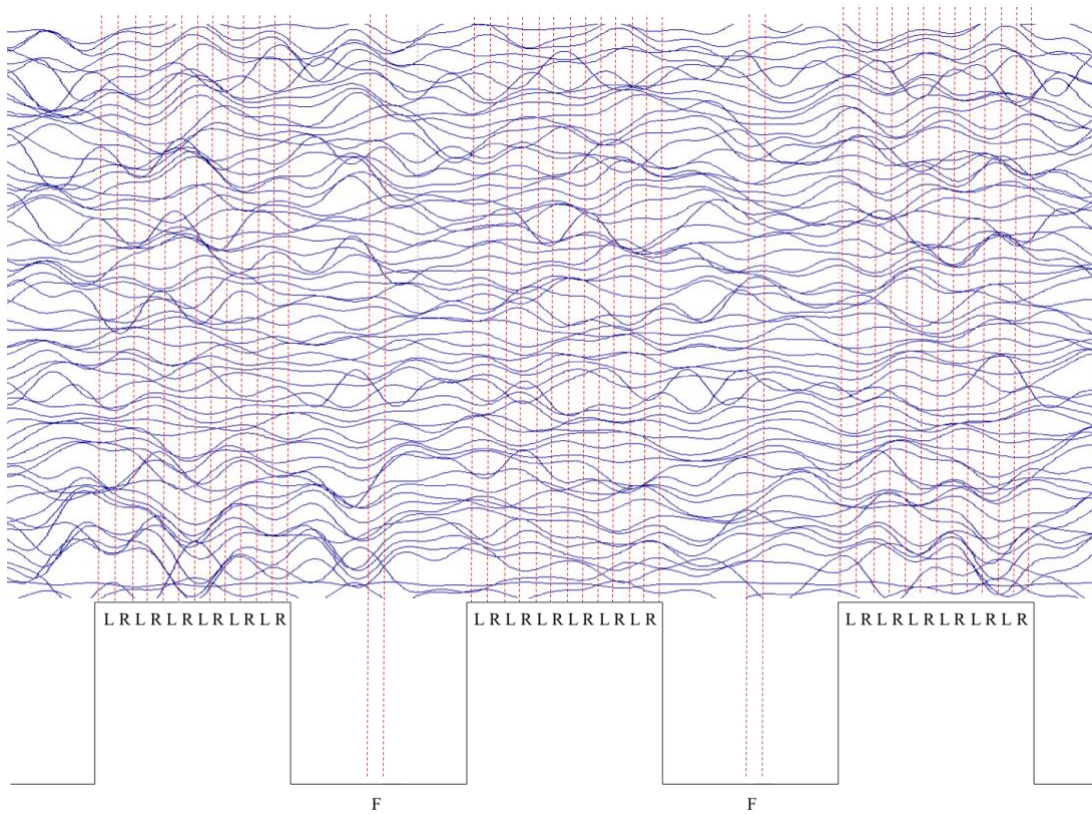


**Figure 6.1 Visual representation of epoching right (R) and left (L) stepping and the baseline fixation cross (F) condition that occurred within the software on a per channel basis.**

Once a discrete Fourier transform (DFT) was performed on these ‘left’, ‘right’ and ‘baseline – fixation cross’ epochs, summations of the spectral power over established EEG bands (alpha, beta and gamma) were performed. Left and right spectral data were normalized with respect to corresponding spectral data during the baseline fixation cross condition (keeping the epoch time constant) (Figure 6.2).

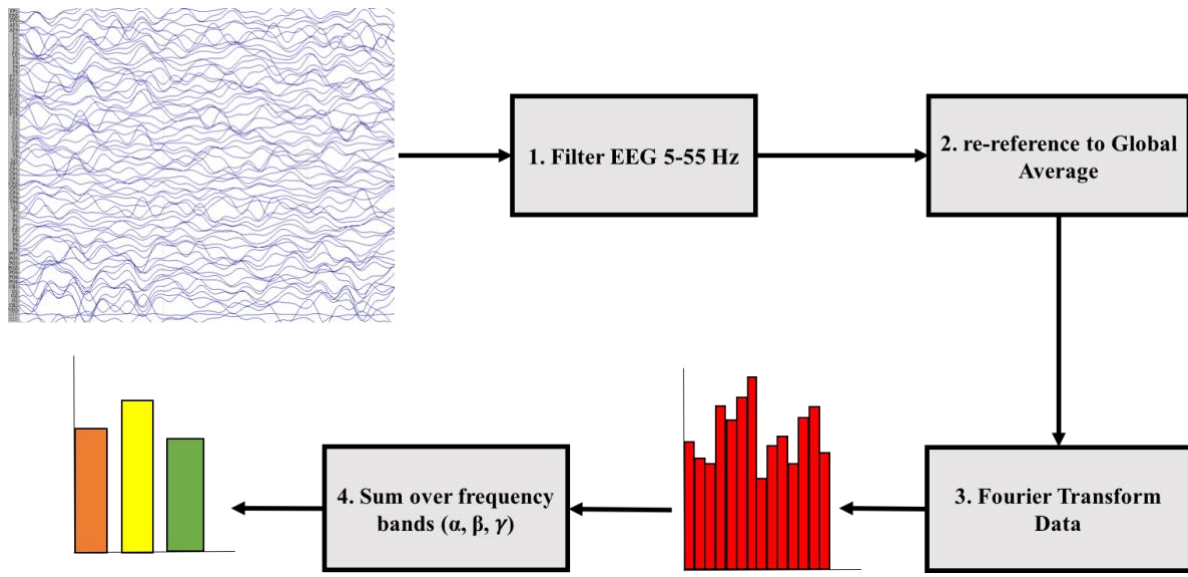


**Figure 6.2 EEG Processing Pipeline;** EEG data is imported, band pass filtered between 5 and 55 Hz, re-referenced to a global average of all 64 electrode channels, converted to spectral data via Fourier transform and summed over alpha, beta and gamma bands respectively.

The General Estimating Equations (GEE) routine in IBM® SPSS® (International Business Machines Corporation, Endicott, NY, U.S.) was used to assess the predictive utility of the C1 and C2 electrode data, using the alpha, beta and gamma frequency bands, in differentiating right from left stepping. Data for these bands were collapsed across time points. Each electrode and frequency band for each of the four conditions was run separately. GEE is an iterative approach that estimates the associations between predictors and criterion when the data represent repeated trials nested within individual participants. GEE was introduced as an extension of generalized linear models (GLM), that estimates the marginal expected outcome for binary outcomes while accounting for the correlation among repeated observations within participants [127].

GEE coefficients estimate population average models, also known as marginal models. These coefficients estimate the average response over the population. The coefficient estimates for binary outcomes in this study can be interpreted as the change in log odds ratios of the outcome for a unit change in the predictor across all of the participants. The estimates generated account for the non-independence of the observations when generating the variability estimates of the coefficients [128].

In this study, the working correlation matrix was specified as unstructured, as there is likely to be non-independence in the repeated measurements. An unstructured matrix is the most general and imposes no constraints on the matrix; each element is estimated uniquely. This results in the best possible model fit. In addition, robust estimation was specified as it provides consistent estimators of the covariance matrix of the predictor estimates, even if the working correlation matrix is unspecified [129].

Because GEE model parameters are estimated using quasi-likelihood procedures, there is no associated likelihood underlying the model. The Wald test, which is distributed as a chi-square, with the degrees of freedom equal to the difference in the number of predictors in the full (one predictor) and reduced (no predictors) models [129], is used to assess significance of the predictors.

### *6.2.2 Generalizability of the EEG Data*

The reliability of the EEG data was assessed using generalizability analyses across three facets: time points ( $N=2$ ), trials ( $N=60$ ), and subjects ( $N=16$ ). This was done for each of the left and right legs under each of the four experimental conditions. The generalizability coefficient is similar to the intra-class correlation coefficient (ICC). However, the ICC is subsumed under

generalizability theory; it is the case where there are only two facets: typically, participants and measurements [130].

There are two variations on the G-coefficient. The first is a *relative G-coefficient*, which reflects how well measures maintain their *relative* rank order. This is also sometimes referred to as the ‘consistency index’. The *absolute G-coefficient*, in addition to consistency in rank order, incorporates agreement on the elevation levels of the measures. This is sometimes referred to as the ‘agreement index’, ‘index of dependability’, or ‘phi coefficient’. It has been suggested that values less than 0.50 are poor, between 0.50 - 0.75 are acceptable, between 0.75 - 0.90 are moderate, and greater than 0.90 are excellent [131]. In addition to the generalizability coefficient generated, the analysis produces information on the variance components themselves. These are of interest because it highlights from which facet, or facets, the most variance in the data set arises.

IBM® SPSS® was also used to run the generalizability analyses. However, specialized syntax developed specifically to do so was employed [132]. To run the program, characteristics of the data were input (fully crossed and completely balanced), and all effects were set to be random.

### **6.3 Results**

Sample phase plots for right and left imagined stepping data for one participant in EEG electrodes are presented (Figure 6.3 and 6.4). These data were collected under the CGI imagined condition and represent the data collapsed across time points 1 and 2.

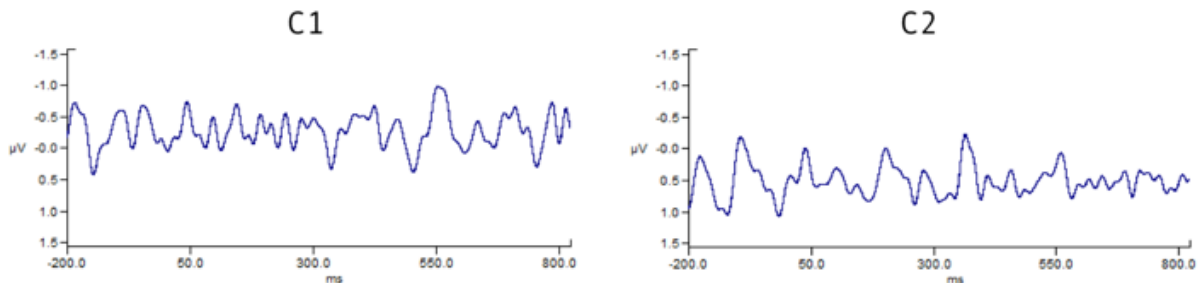


**Figure 6.3 Traces during a right step for electrodes C1 and C2, averaged over 120 epochs (across time points 1 and 2), over an interval of 200 ms before the stimulus and 823 ms after the stimulus during the CGI imagined stimulus for a single participant.**

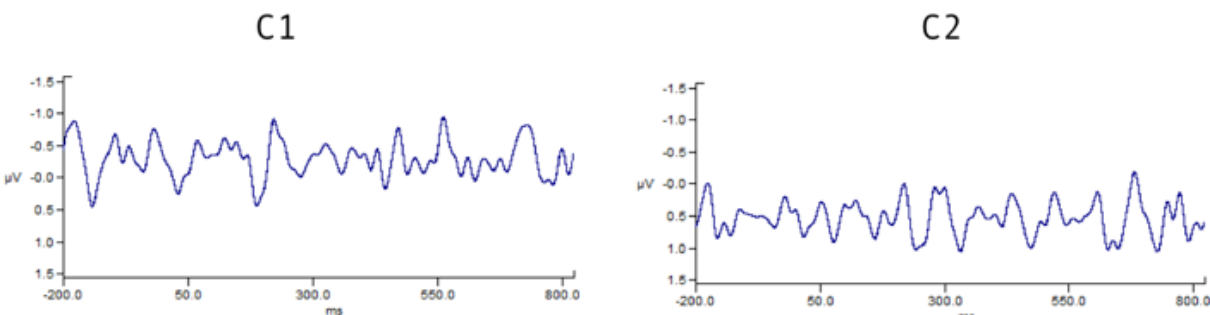


**Figure 6.4 Traces of during a left step for electrodes C1 and C2, averaged over 120 epochs (across time points 1 and 2), over an interval of 200 ms before the stimulus and 823 ms after the stimulus during the CGI imagined stimulus for a single participant.**

The results of the analysis to determine which electrodes/frequencies/conditions distinguished between left and right stepping movements are presented in Tables 6.1 and 6.2. The tables show: 1) the electrode and frequency band being assessed; 2) the B-value, or coefficient, associated with each analysis; 3) the Wald value of each coefficient; 4) the significance of each Wald value; and the average depolarization values across participants and trials for the left and right lower limb movements. For the CGI stimulus (Table 6.1), only the beta band of the C1 electrode and the alpha band of the C2 electrode successfully distinguished between executed left and right stepping movements. However, for imagined stepping movements, with the exception of the gamma band of the C2 electrode, all frequency bands for

each electrode successfully distinguished left and right stepping movements. For the alternating blue-green circle stimulus (Table 6.2), only the beta bands of the C1 and C2 electrodes successfully distinguished between executed left and right stepping movements for executed movements, while no electrodes/frequencies were successful for imagined movements.

**Table 6.1 EEG Differentiation of Right and Left Stepping Using the CGI Stimulus**

Electrode and Band	B-value	Wald	Significance ( $p < .05$ )*	Mean Frequency Left +/- (SE)	Mean Frequency Right +/- (SE)
<b>Executed</b>					
C1 Alpha	5.582E-12	.005	.943	239 +/- 16	241 +/- 16
C1 Beta	9.355E-11	3.825	.050*	852 +/- 23	797 +/- 22
C1 Gamma	3.413E-11	.173	.678	9 +/- 13	14 +/- 11
C2 Alpha	9.540E-11	4.026	.045*	311 +/- 19	273 +/- 18
C2 Beta	7.329E-11	1.625	.202	690 +/- 19	657 +/- 21
C2 Gamma	1.635E-11	.148	.700	-25 +/- 15	-30 +/- 17
<b>Imagined</b>					
C1 Alpha	1.908E-10	14.892	.000*	170 +/- 18	96 +/- 19
C1 Beta	1.007E-10	8.498	.004*	245 +/- 17	205 +/- 20
C1 Gamma	2.003E-10	7.108	.008*	72 +/- 8	57 +/- 9
C2 Alpha	1.772E-10	12.120	.000*	246 +/- 18	176 +/- 19
C2 Beta	8.694E-11	5.571	.018*	317 +/- 20	275 +/- 21
C2 Gamma	7.410E-11	1.503	.220	72 +/- 9	64 +/- 10

**Table 6.2 EEG Differentiation of Right and Left Stepping Using the Alternating Blue-green Stimulus**

Electrode and Band	B-value	Wald	Significance ( $p < .05$ )*	Mean Frequency Left +/- (SE)	Mean Frequency Right +/- (SE)
<b>Executed</b>					
C1 Alpha	6.873E-11	1.504	.220	65 +/- 17	89 +/- 18
C1 Beta	1.114E-10	4.783	.029*	629 +/- 22	690 +/- 22
C1 Gamma	2.205E-11	1.054	.305	224 +/- 20	234 +/- 20
C2 Alpha	6.685E-11	.676	.411	67 +/- 16	86 +/- 16
C2 Beta	1.393E-10	7.348	.007*	575 +/- 18	629 +/- 18
C2 Gamma	2.667E-13	.007	.934	414 +/- 39	415 +/- 39
<b>Imagined</b>					
C1 Alpha	2.318E-11	.140	.708	89 +/- 17	97 +/- 17
C1 Beta	7.794E-12	.027	.870	178 +/- 19	181 +/- 20
C1 Gamma	9.340E-11	.801	.371	36 +/- 8	30 +/- 7
C2 Alpha	2.338E-11	.330	.566	3 +/- 17	11 +/- 17
C2 Beta	6.301E-11	1.073	.300	168 +/- 19	143 +/- 19
C2 Gamma	2.649E-11	.120	.729	21 +/- 9	23 +/- 7

Figures 6.5 – 6.8 show the spectral plots for all 4 conditions at electrodes C1 and C2 for the 3 frequency bands of interest (alpha, beta, gamma), brought over from the results in Table 6.1 and 6.2.

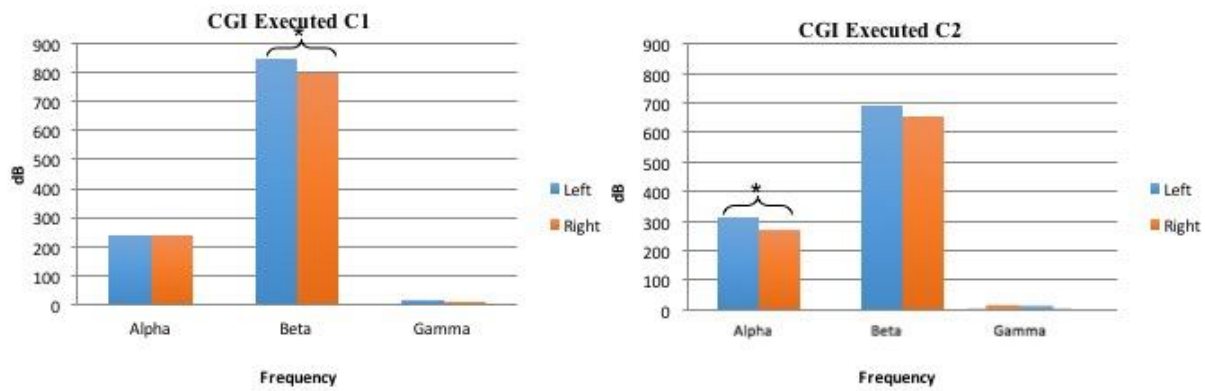


**Figure 6.5 Plots of EEG frequency band data for electrodes C1 and C2 for left and right executed stepping during the CGI stimulus, where significance is denoted (\*  $p<0.05$ ).**

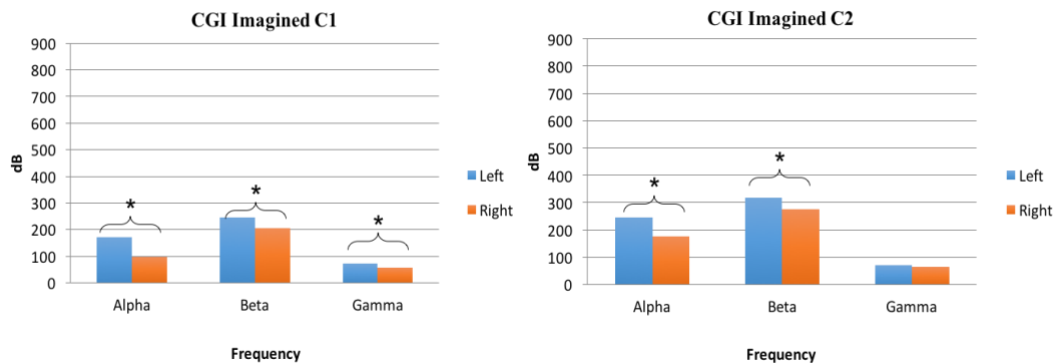


**Figure 6.6 Plots of EEG frequency band data for electrodes C1 and C2 for left and right imagined stepping during the CGI stimulus, where significance is denoted (\*  $p<0.05$ ).**

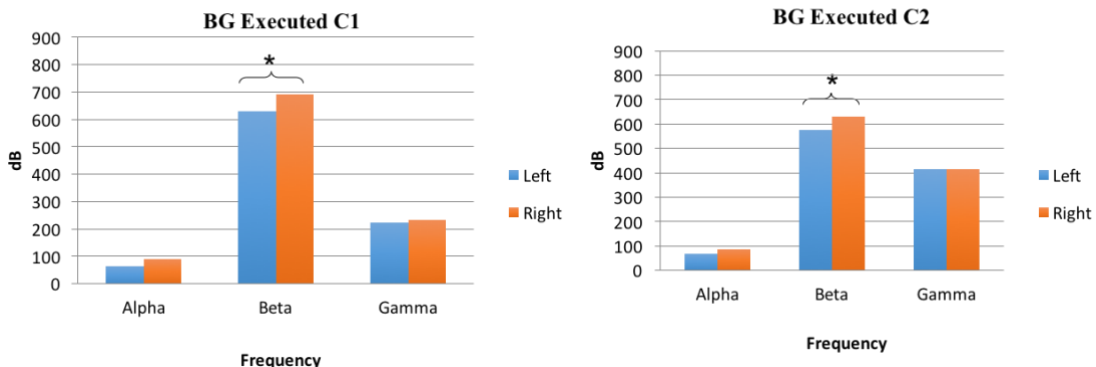


**Figure 6.7 Plots of EEG frequency band data for electrodes C1 and C2 for left and right executed stepping during the blue-green stimulus, where significance is denoted (\*  $p<0.05$ ).**

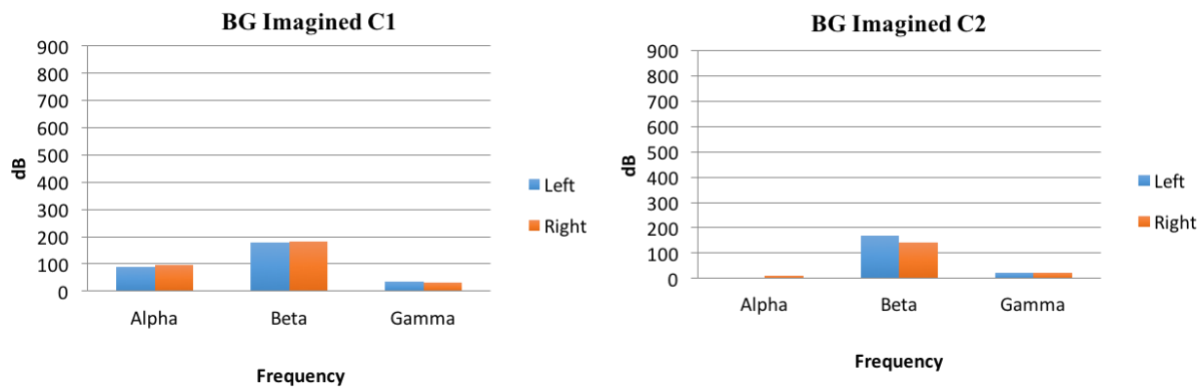


**Figure 6.8 Plots of EEG frequency band data for electrodes C1 and C2 for left and right imagined stepping during the blue-green stimulus, where significance is denoted (\* p<0.05).**

The generalizability results of the EEG data that were used to distinguish left from right stepping movements are shown in Tables 6.3-6.6. These values denote how reliable the data are specific to each facet (time, trial, participant). The tables are organized by stimulus condition (CGI and blue-green) and electrode (C1 and C2). Each table indicates the G-coefficient and the Phi-coefficient associated with the left and right limb movements for executed and imagined conditions. In addition, the variances associated with the three facets of the generalizability analyses are reported: for time point, for trials, and subjects. Results were reliable across time points and trials (within subjects) where the majority of the ascribed variance is due to between subject variance (0-90.4%).

**Table 6.3 Generalizability Findings for the CGI Executed and Imagined Conditions for Left and Right Leg at the C1 Electrode**

CGI Condition	G coeff.	Phi coeff.	Var. due to Time Point	Var. due to Trials	Var. due to Ss
Executed					
C1 Alpha Left CGI Executed	.473	.472	.000	.015	.125
C1 Alpha Right CGI Executed	.718	.712	.003	.045	.162
C1 Beta Left CGI Executed	.648	.647	.000	.014	.235
C1 Beta Right CGI Executed	.720	.718	.000	.065	.254
C1 Gamma Left CGI Executed	.000	.000	.000	.000	.000
C1 Gamma Right CGI Executed	.000	.000	.001	.004	.000
Imagined					
C1 Alpha Left CGI Imagined	.949	.934	.008	.000	.245
C1 Alpha Right CGI Imagined	.843	.800	.017	.016	.141
C1 Beta Left CGI Imagined	.559	.558	.000	.006	.086
C1 Beta Right CGI Imagined	.481	.480	.000	.016	.062
C1 Gamma Left CGI Imagined	.524	.524	.000	.003	.137
C1 Gamma Right CGI Imagined	.595	.593	.001	.010	.144

**Table 6.4 Generalizability Findings for the CGI Executed and Imagined Conditions for Left and Right Leg at the C2 Electrode**

CGI Condition	G coeff.	Phi coeff.	Var. due to Time Point	Var. due to Trials	Var. due to Ss
Executed					
C2 Alpha Left CGI Executed	.719	.719	.000	.010	.242
C2 Alpha Right CGI Executed	.732	.731	.000	.033	.201
C2 Beta Left CGI Executed	.525	.491	.036	.013	.139
C2 Beta Right CGI Executed	.712	.657	.040	.088	.185
C2 Gamma Left CGI Executed	.000	.000	.004	.000	.000
C2 Gamma Right CGI Executed	.033	.032	.005	.000	.002
Imagined					
C2 Alpha Left CGI Imagined	.793	.792	.000	.016	.198
C2 Alpha Right CGI Imagined	.763	.761	.000	.026	.146
C2 Beta Left CGI Imagined	.714	.713	.000	.023	.144
C2 Beta Right CGI Imagined	.731	.728	.000	.031	.131
C2 Gamma Left CGI Imagined	.000	.000	.000	.011	.000
C2 Gamma Right CGI Imagined	.000	.000	.000	.017	.000

**Table 6.5 Generalizability Findings for the Blue-green Executed and Imagined Conditions for Left and Right Leg at the C1 Electrode**

BG Condition	G coeff.	Phi coeff.	Var. due to Time Point	Var. due to Trials	Var. due to Ss
Executed					
C1 Alpha Left BG Executed	.689	.671	.013	.000	.174
C1 Alpha Right BG Executed	.685	.681	.004	.003	.189
C1 Beta Left BG Executed	.706	.688	.016	.003	.223
C1 Beta Right BG Executed	.673	.666	.007	.009	.248
C1 Gamma Left BG Executed	.000	.000	.000	.000	.000
C1 Gamma Right BG Executed	.000	.000	.000	.001	.000
Imagined					
C1 Alpha Left BG Imagined	.011	.011	.000	.000	.001
C1 Alpha Right BG Imagined	.000	.000	.000	.010	.000
C1 Beta Left BG Imagined	.637	.626	.003	.014	.072
C1 Beta Right BG Imagined	.562	.561	.000	.016	.061
C1 Gamma Left BG Imagined	.357	.342	.009	.013	.039
C1 Gamma Right BG Imagined	.298	.298	.000	.005	.041

**Table 6.6 Generalizability Findings for the Blue-green Executed and Imagined Conditions for Left and Right Leg at the C2 Electrode**

BG Condition	G coeff.	Phi coeff.	Var. due to Time Point	Var. due to Trials	Var. due to Ss
Executed					
C2 Alpha Left BG Executed	.714	.713	.000	.015	.158
C2 Alpha Right BG Executed	.599	.598	.000	.011	.138
C2 Beta Left BG Executed	.554	.548	.003	.050	.122
C2 Beta Right BG Executed	.493	.489	.003	.018	.138
C2 Gamma Left BG Executed	.000	.000	.000	.000	.000
C2 Gamma Right BG Executed	.000	.000	.000	.000	.000
Imagined					
C2 Alpha Left BG Imagined	.361	.358	.000	.013	.024
C2 Alpha Right BG Imagined	.000	.000	.000	.016	.000
C2 Beta Left BG Imagined	.768	.688	.026	.039	.089
C2 Beta Right BG Imagined	.716	.666	.020	.036	.099
C2 Gamma Left BG Imagined	.659	.572	.043	.018	.904
C2 Gamma Right BG Imagined	.695	.644	.031	.011	.141

#### 6.4 Discussion

The hypothesis of this study was that it would be possible to differentiate left and right steps using EEG frequency data, specifically collected from the C1 and C2 electrodes, for both executed and imagined stepping; it was expected that the CGI stimulus would be more successful. The hypothesis was partially supported. The significant results for isolating right from left stepping were found at both the C1 and C2 electrodes, suggesting both are important sources of information for isolating right from left stepping. Most of the significant results were

obtained at the alpha and beta frequencies. This is likely because these are the two EEG bands most closely linked to executed walking [133], [134]. However, there was one significant result at the gamma frequency. Many of the significant results occurred in the imagined condition. For those individuals with compromised mobility (i.e., unable to execute stepping movements), this finding is particularly exciting, as imagined data from such individuals would be all that is available for an individually-generated brain computer interface (BCI).

As expected, the CGI condition was more successful in distinguishing left and right stepping movements than the blue-green condition. One possible explanation for this finding is that the CGI character stimulus acts similarly to that of a mirror neuron where a person can ‘see’ the act of walking [44]. Although the blue-green visual stimulus cued for right-left leg change at the same rate as the CGI, it lacked any anthropomorphic quality. Given that the purpose of including these two quite different visual stimuli was to test the potential influence of mirror neurons associated with the stimulus, the results suggest that this is an important characteristic to induce significant differences in brain activation of lower limb locomotion.

Another CGI and blue-green difference was found in the depolarization levels (Table 6.1 and 6.2). Excitatory firing in EEG is marked by an increase in the depolarization of the signal coupled with desynchronization, and is indicative of strong activation in the brain. For the significant results in the CGI condition, there was more depolarization for the left leg than for the right leg. However, for the significant results in the blue-green condition, there was more depolarization for the right leg than for the left leg. This is a somewhat paradoxical finding and one that might be pursued in future research. This may be the result of the blue-green condition being a neutral one, so is manifested as more inhibitory or at the very least non-excitatory [135],

or perhaps this is result of the projection through the geniculostriate complex to the primary visual cortex [136].

Data that are not reliable are not able to predict other variables. Classical reliability theory assumes that the upper limit of validity - the relationship between a predictor and criterion - is the square root of the reliability of the variables involved [137]. The results of the current study showed that the generalizability coefficients were generally higher for the CGI conditions than for the blue-green conditions, suggesting that a simple stimulus, such as blue-green color alternation, does not generate data that is particularly reliable at differentiating left and right stepping movements. It is also notable that the coefficients for the CGI imagined condition were generally higher than for the CGI executed condition. There was very little variance due to the effects of time points (0% - 6.55%) or across trials (0% - 4.3%). Thus, collapsing across time points to assess the predictive utility of the data was justified.

## 6.5 Limitations

Limitations of this work include that the sample consisted of young, healthy, male subjects. However, this may be characteristic of the demographics for which lower limb BCI development might be of most use [138]. Only the C1 and C2 electrodes were investigated in this study. The assessment of additional electrodes in an attempt generate more features that are capable of distinguishing left and right leg lifts in both executed and imagined conditions is a possible avenue of future research. Finally, the frequency that the participants were presented with the stimulus (50 steps/min) is about half the frequency of normal walking. The ability to differentiate right from left stepping may decrease with an increased stepping pace if EEG sampling remains unchanged. This would need to be taken into consideration with future research.

## **6.6 Future Work**

To evaluate the generalizability of these results, further work will need to be done testing other demographic groups. Future work could also entail bringing the analysis to an online system for real-time classification of stepping movements. One aspect of participant differentiation is their leg dominance. A total of 13 participants in this study were right-foot and the other three identified themselves as left foot dominant. However, when this factor was included in the analyses it did not account for any of the differences observed. This may very well be due to the small sample of left-dominant individuals and may be of interest to pursue in future research.

## **6.7 Conclusion**

These results demonstrate that it is possible to differentiate left from right low limb movements using EEG data collected from the C1 and C2 electrodes. This was particularly true in the case in the imagined walking condition using the CGI stimulus, thus providing partial support for Hypothesis 1: EEG data will demonstrate brain activity patterns that distinguish left from right leg movements in both imagined and executed lower limb movement; this effect is expected to be particularly strong for the computer-generated image-based stimuli conditions.

The findings have important implications for studying lower limb movement with the end-goal of creating a BCI to assist those individuals with compromised mobility in that it demonstrates it is possible to isolate left from right lower limb movement solely with imagined EEG data. While this chapter focused on EEG data, which has excellent temporal resolution, to isolate left and right stepping, the next chapter takes up the challenge of identifying the locations in the brain that are activated when lower limb stepping occurs.

## **CHAPTER 7: DIFFERENTIATING THE BRAIN'S INVOLVEMENT IN EXECUTED AND IMAGING STEPPING USING FMRI**

### **7.1 Introduction**

The purpose of this chapter is to address hypothesis 2: fMRI will identify areas of the brain that are differentially activated for lower limb movement across experimental conditions. Specifically, activation of the sensory motor areas is expected across all conditions. In the executed condition, areas of the cerebellum and basal ganglia will be activated. In the imagined condition, greater activation of the occipital, parietal and frontal lobes is expected. Due to the sluggish response time of hemodynamic activity, differentiation between left and right knee extension is not anticipated. The degree to which this hypothesis is supported will determine how useful fMRI data may be in refining the input information that would go into lower limb BCI development.

Very few studies have used fMRI to investigate brain mechanisms governing executed lower limb movements; most have been limited to hand or arm movements or ankle flexion. This is due primarily to excessive head motion during task execution that leads to signal artifact. Some preliminary studies, however, have demonstrated limited success. One study using executed knee extensions observed activation of the primary and supplementary motor cortices, sensorimotor cortex, and the basal ganglia [71]. Newton, *et al.* 2008 found for multi-joint lower limb movements, there was activity in the primary sensorimotor cortex, paracentral lobule and secondary motor areas [16]. De Almeida, *et al.* 2015 reported activation for manually-facilitated multi-joint lower limb movements within the primary and secondary somatosensory areas as well as other motor areas [14]. Jaeger, *et al.* 2014 also reported activation of the sensorimotor areas,

cerebellar vermis, and putmen, for multi-joint lower limb movements [17]. In addition to motor regions, linguistic and auditory areas of the brain are activated even when carrying out such tasks [53].

The purpose of this study was to use fMRI to identify the areas in the brain activated during lower limb motion. The unique contribution of the current study to the extant literature is the inclusion of both executed and imagined task conditions for lower limb movements. It has been well-documented that imagined and executed actions share similar neural mechanisms [21], [24], [139], including several fMRI-based studies of finger movement [23], [25]. To date, there have been no studies that have utilized two different types of visual stimuli to cue lower limb movement, as a means to determine differential effects of cue.

Unlike EEG, fMRI does not possess the temporal resolution necessary to isolate right and left leg movements during natural stepping; fMRI sampling frequency is typically on the order of 2-3 seconds, and hemodynamic activity takes about six seconds to reach its maximum level. Despite these limitations, the excellent spatial resolution of fMRI (~5 mm) and its ability to measure brain activity throughout the entire brain, provide the opportunity to assist the interpretation of EEG findings as well as inform EEG on the observed differences between executed and imagined movements for both types of visual cues.

## 7.2 Methods

### 7.2.1 *Data Collection*

The subjects, experimental setup and data collection were described in Chapter 5. The data collected at time point 3 were used in this chapter's results.

### 7.2.2. Data Processing

fMRI data underwent standard pre-processing, including brain extraction, motion correction, intensity normalization, slice-timing correction, anatomical registration and 6-mm Gaussian kernel spatial smoothing using image analysis software (FSL; <http://www.fmrib.ox.ac.uk/fsl/>). To permit group comparisons, individuals' images were registered to anatomical images and subsequently to the Montreal Neurological Institute's (MNI) standard brain template using FSL's linear registration tool [111],[140] (Appendix B). Each participant's fMRI images then underwent temporal independent component analysis (ICA), as implemented in *MELODIC* (Multivariate Exploratory Linear Optimized Decomposition into Independent Components; part of *FSL*). Resulting temporal components were examined to identify those associated with movement artifacts (ring shaped artifacts), white matter artifacts, and cardiac artifacts, which were then regressed out of the fMRI data, using *regfilt* (part of *FSL*'s command line tools).

### 7.2.3 Functional Activation Modelling

A general linear model (GLM) was used to determine the voxels of the brain (~80,000) aligned with the model of activation and regions of the brain using FSL's FEAT program. First, a functional activation model that represented the task design was generated. Recall that this was a block design (square wave) based on the timing of the visual stimuli ('on' or 'off'). Because the shape of the BOLD hemodynamic response function (HRF) is known (as described in Chapter 2), and the on/off cycle of the experiment was also known, the model was generated by the HRF with the block sequence timing of the visual stimulus (Figure 7.1). Thus, a graphical representation of expected brain activation was modelled. The GLM can be represented as:

$$Y = X\beta + \epsilon \quad (7.1)$$

where ( $Y$ ) corresponds to a vector representing a voxel's time course, ( $X$ ) is a vector of the experimental ‘on/off’ predictor over that same time course, ( $\beta$ ) is the slope parameter or effect associated with the predictor, and epsilon ( $\varepsilon$ ) is a vector representing error in the data that cannot be accounted for in the model.

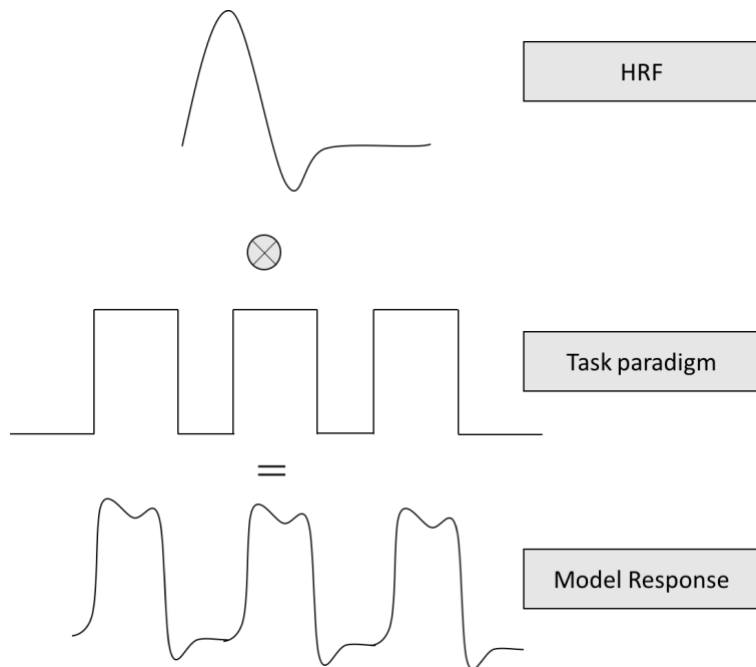


**Figure 7.1 A model for on/off voxel activation over time for a single voxel.**

For each voxel, the parameter in the model was estimated for each run of the tasks. Higher-level mixed-model analyses, as implemented in *FSL*, were then performed to obtain significant activity over the 16 participants for each task. Values for this group analysis were converted to Z-scores for ease of statistical interpretation. To control for Type-I error, given the large number of voxels subjected to the GLM, a cluster-wise approach was used as a multiple comparison correction. This is because brain activity tends to occur in clusters. Each map was thresholded at an individual voxel value of  $Z=2.3$ , and corrected for multiple comparisons using

a false discovery rate (FDR) threshold of 0.05, corresponding to a cluster volume of greater than 350 voxels, as determined by *AlphaSim* (part of the AFNI software package, <http://afni.nimh.nih.gov/afni>).

#### 7.2.4 *Atlas Overlay*

Areas of functional activity determined from the analyses were overlaid into the Harvard-Oxford cortical and subcortical structure atlas [68]. This atlas consists of labelled anatomical regions to permit identification of significantly activated clusters (Figure 7.2).

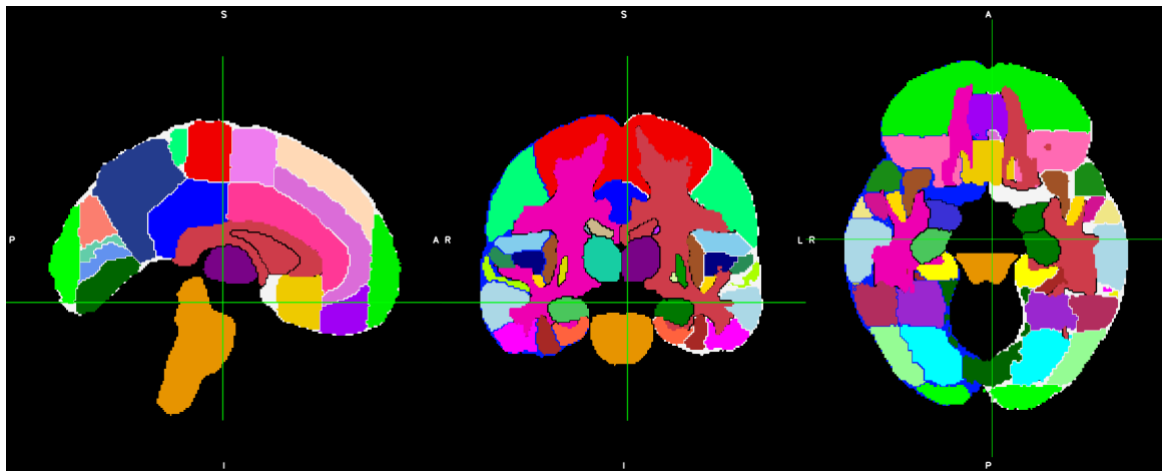


**Figure 7.2 Harvard-Oxford brain atlas used to ascribe functional clusters to particular structural areas of the brain.**

#### 7.2.5 *Between-Task Comparisons*

The final process was to determine if there were differences in voxel activation between the four different task conditions. FSL's higher level analysis tool was used to do this. Paired-sample t-tests were carried out to compare the voxel activations for the different conditions. Contrasts of interest were; 1) CGI imagined versus CGI executed, 2) CGI imagined versus blue-green

imagined, 3) CGI executed versus blue-green executed, and 4) blue-green imagined versus blue-green executed. The contrasting process essentially subtracts the activated voxels in one condition from that of the other condition, leaving only the activated voxels that are different between the conditions. Again, a cluster threshold of  $p < 0.05$  was applied to determine statistical significance. The model for contrasting conditions can be seen in Figure 7.3.

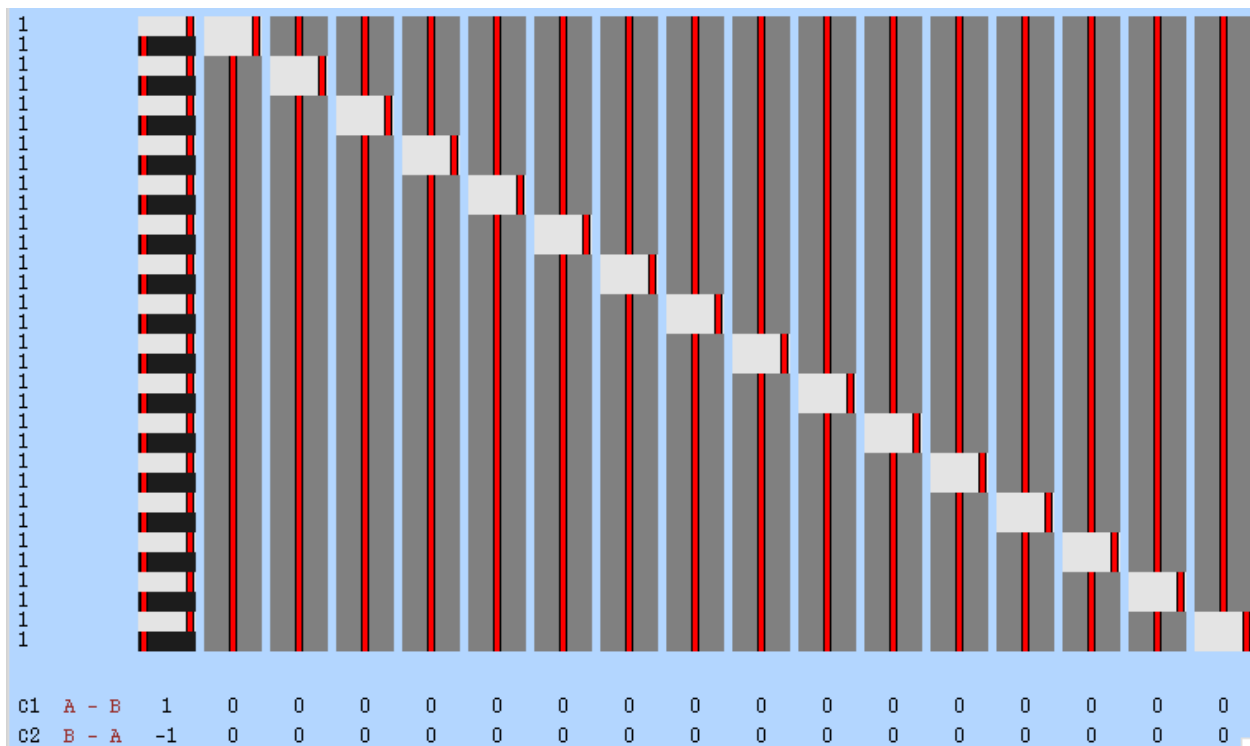


**Figure 7.3 Example of a paired-t test setup within FSL for between-task or between-stimuli conditions. Participants are represented in columns 2 to 16, while the contrast between conditions is encoded in black and white over all the participants in the first column.**

## 7.3 Results

### 7.3.1 Functional Activations for the Four Task Conditions

Brain regions significantly activated by each of the four task conditions are summarized in Tables 7.1 – 7.4. Brain maps of these regions are shown in Figures 7.4 – 7.7 as ‘heat maps’ of

the activated clusters corresponding to the individual voxel Z-scores within the clusters. These denote areas of the brain that are active during the activity relative to the baseline (fixation cross condition).

**Table 7.1 Brain regions significantly activated during ( $p < 0.05$ ) executed leg movements with the CGI stimulus, where the Z slice is in the upper left corner of Figure 7.4.**

Z (slices)	Harvard-Oxford Label
22-27	right planum temporale
10-18	bilateral medial cerebellum
28-39	bilateral primary motor (leg area) and supplementary motor cortex

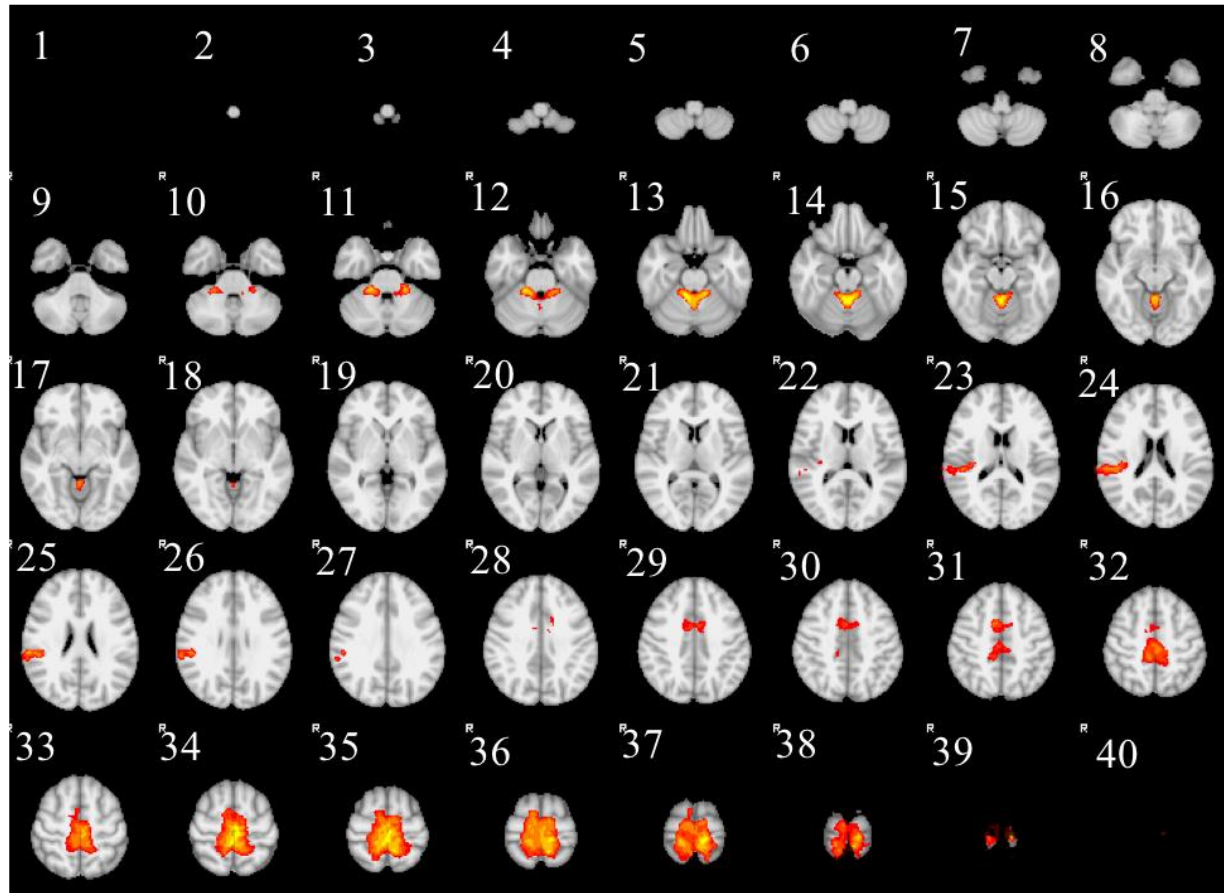


**Figure 7.4 Group maps of brain regions exhibiting significant activity during CGI-executed leg movements, color-coded in red-to-yellow heat maps where red = 2.3 and yellow > 4.7. Images are shown in radiological convention (i.e., right is on the left).**

**Table 7.2 Brain regions significantly activated during ( $p < 0.05$ ) imagined leg movements with the CGI stimulus, where the Z slice is in the upper left corner of Figure 7.5.**

Z (slices)	Harvard-Oxford Label
10-14	bilateral lateral cerebellum
17-24	bilateral pallidum and putamen
20-27	bilateral secondary motor area
28-35	left superior parietal lobule
15-22	bilateral lateral occipital cortex
24-39	bilateral supplementary motor and premotor cortices

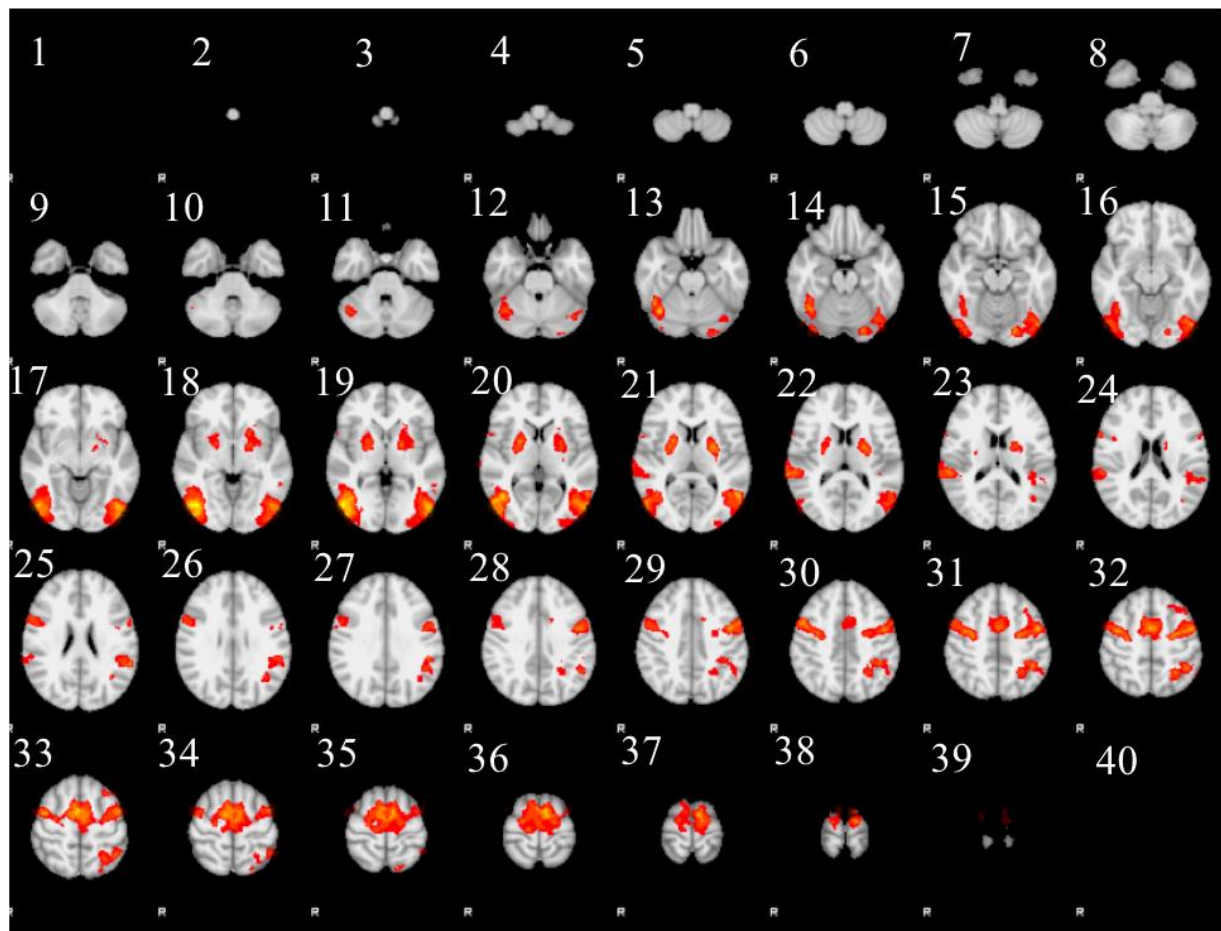


**Figure 7.5 Group maps of brain regions exhibiting significant activity during CGI-imagined leg movements, color-coded in red-to-yellow heat maps where red = 2.3 and yellow > 5.9. Images are shown in radiological convention (i.e., right is on the left).**

**Table 7.3 Brain regions significantly activated during ( $p < 0.05$ ) executed leg movements with the blue/green stimulus, where the Z slice is in the upper left corner of Figure 7.6.**

Z (slices)	Harvard-Oxford Label
18-25	bilateral insular cortex
22-26	bilateral secondary motor area
9-19	bilateral medial cerebellum
26-39	bilateral primary motor (leg area) and supplementary motor area

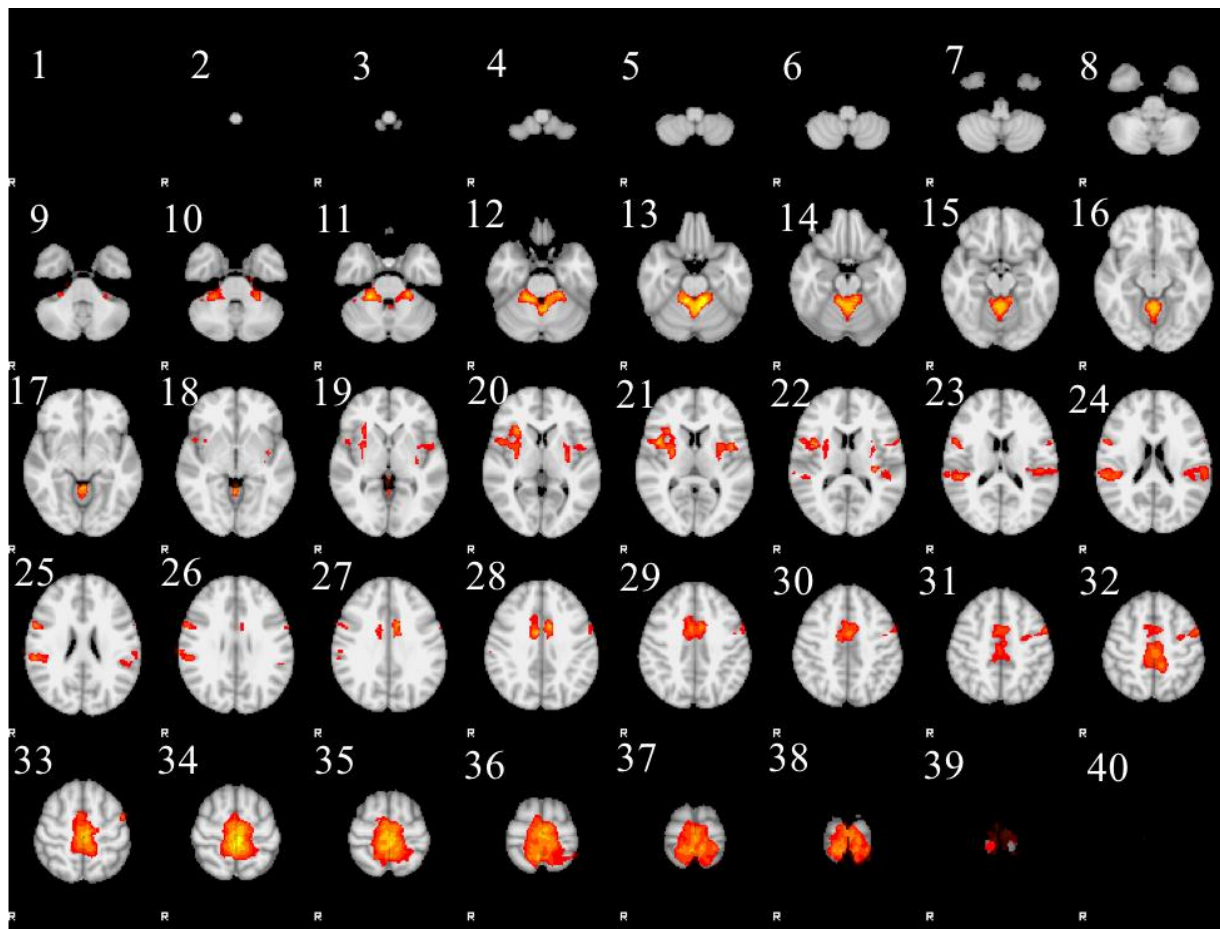


**Figure 7.6 Group maps of brain regions exhibiting significant activity during blue/green-executed leg movements, color-coded in red-to-yellow heat maps where red = 2.3 and yellow > 5.3. Images are shown in radiological convention (i.e., right is on the left).**

**Table 7.4 Brain regions significantly activated during ( $p < 0.05$ ) imagined leg movements with the blue/green stimulus, where the Z slice is in the upper left corner of Figure 7.7.**

Z (slices)	Harvard-Oxford Label
4-12	right lateral cerebellum
17-23	bilateral insular cortex
17-23	bilateral pallidum and putamen
25-33	bilateral secondary motor area
25-32	Bilateral superior parietal lobule
26-39	bilateral supplementary motor and premotor cortices

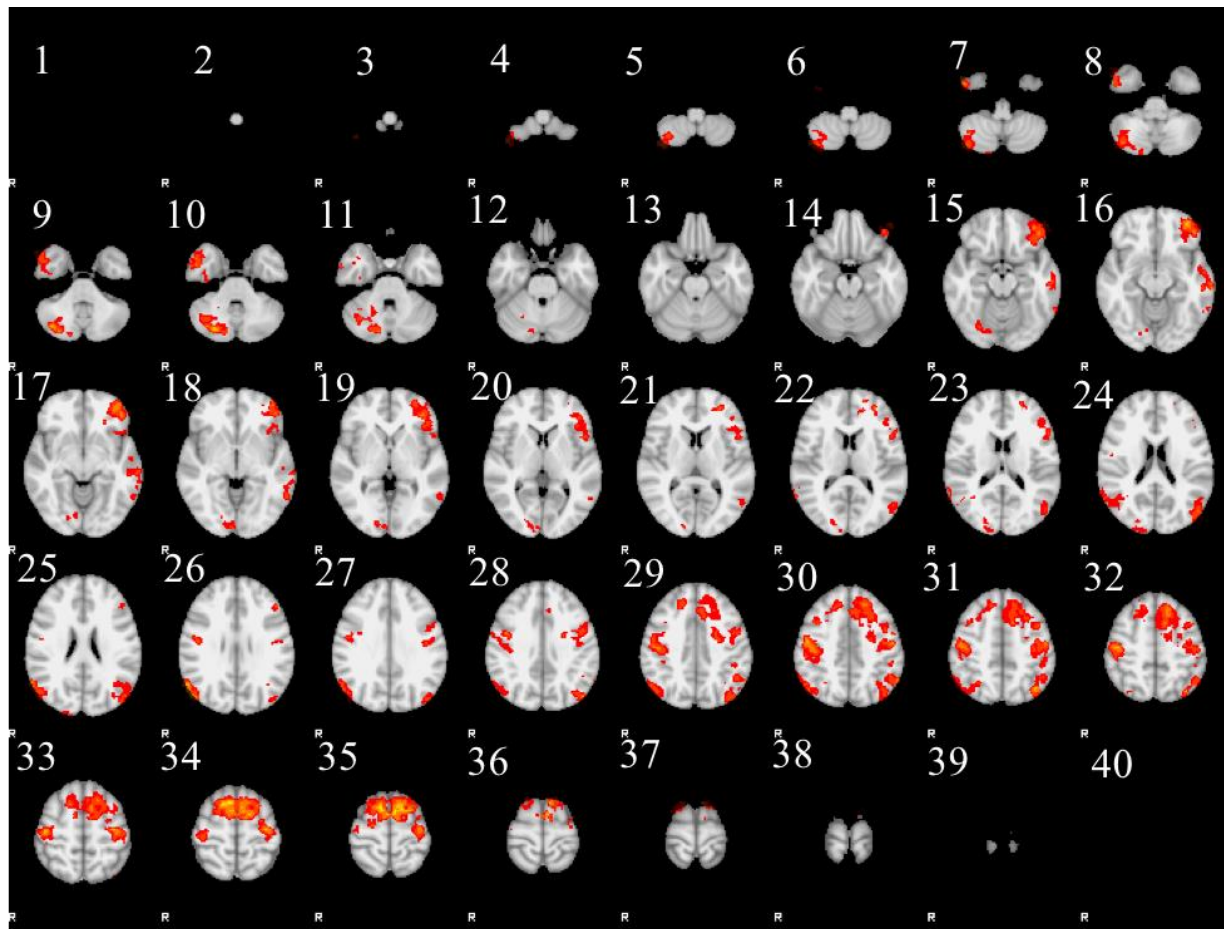


**Figure 7.7 Group maps of brain regions exhibiting significant activity during blue/green-imagined leg movements, color-coded in red-to-yellow heat maps where red = 2.3 and yellow > 4.7. Images are shown in radiological convention (i.e., right is on the left).**

### 7.3.2 Task Comparisons

Brain region activity levels that were significantly different between tasks are summarized in Tables 7.5 – 7.11. These regions denote areas of the brain being active that are unique to the task but different from its contrasted partner in an (A-B) and (B-A) fashion. Maps of these regions are shown in Figures 7.8 – 7.15.

**Table 7.5 Brain regions whose activity was significantly greater ( $p < 0.05$ ) during CGI-executed movements than during CGI-imagined movements, where the Z slice is in the upper left corner of Figure 7.8.**

Z (slices)	Harvard-Oxford Label
10-18	bilateral medial cerebellum
30-39	bilateral primary motor (leg area) cortex

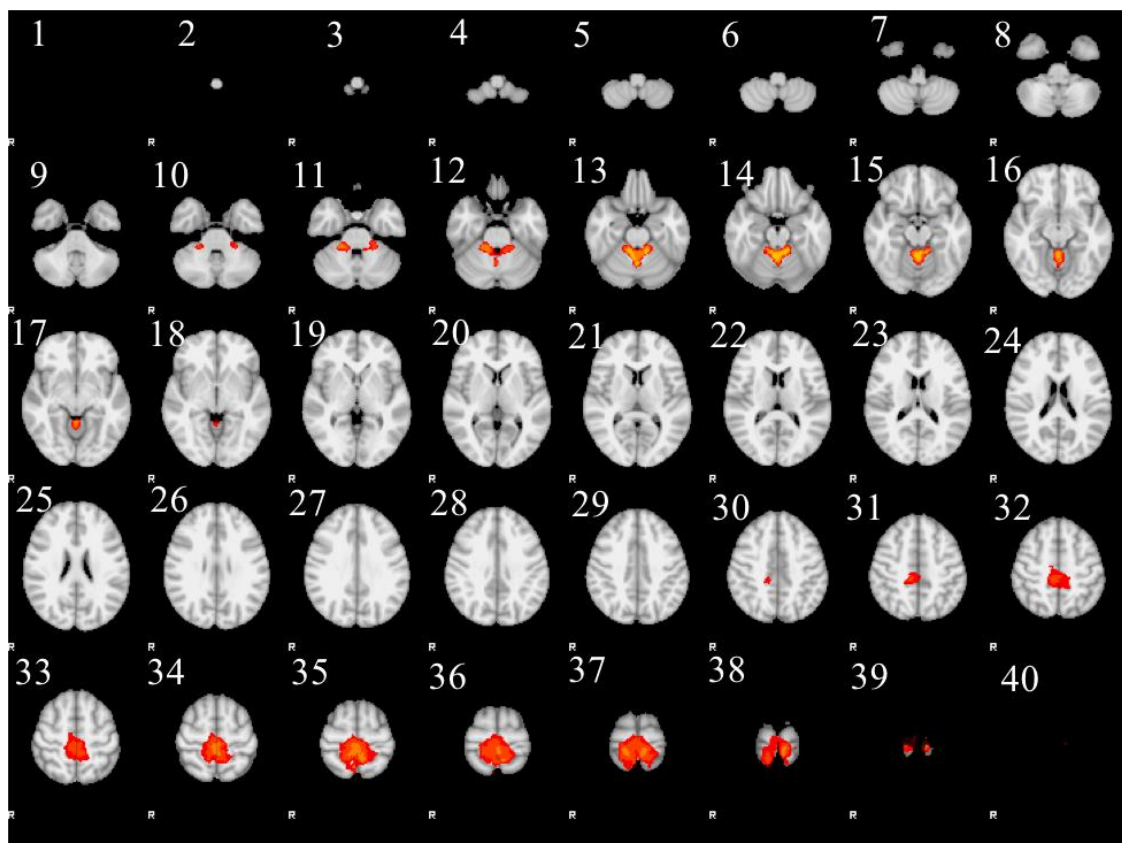


**Figure 7.8 Group maps of brain regions exhibiting significantly greater activity during CGI-executed leg movements than during CGI-imagined leg movements, color-coded in red-to-yellow heat maps where red = 2.3 and yellow > 4.7. Images are shown in radiological convention (i.e., right is on the left).**

**Table 7.6 Brain regions whose activity was significantly greater ( $p < 0.05$ ) during CGI-imagined movements than during CGI-executed movements, where the Z slice is in the upper left corner of Figure 7.9.**

Z (slices)	Harvard-Oxford Label
4-15	Right lateral cerebellum
16-20	Right temporal pole
16-23	Right lingual gyrus
14-20	Left inferior frontal gyrus
15-25	Bilateral lateral occipital cortex
23-30	Posterior cingulate cortex
29-37	Bilateral premotor cortex
29-34	Bilateral superior parietal lobule
20-23	Anterior cingulate cortex
31-36	Bilateral somatosensory cortex

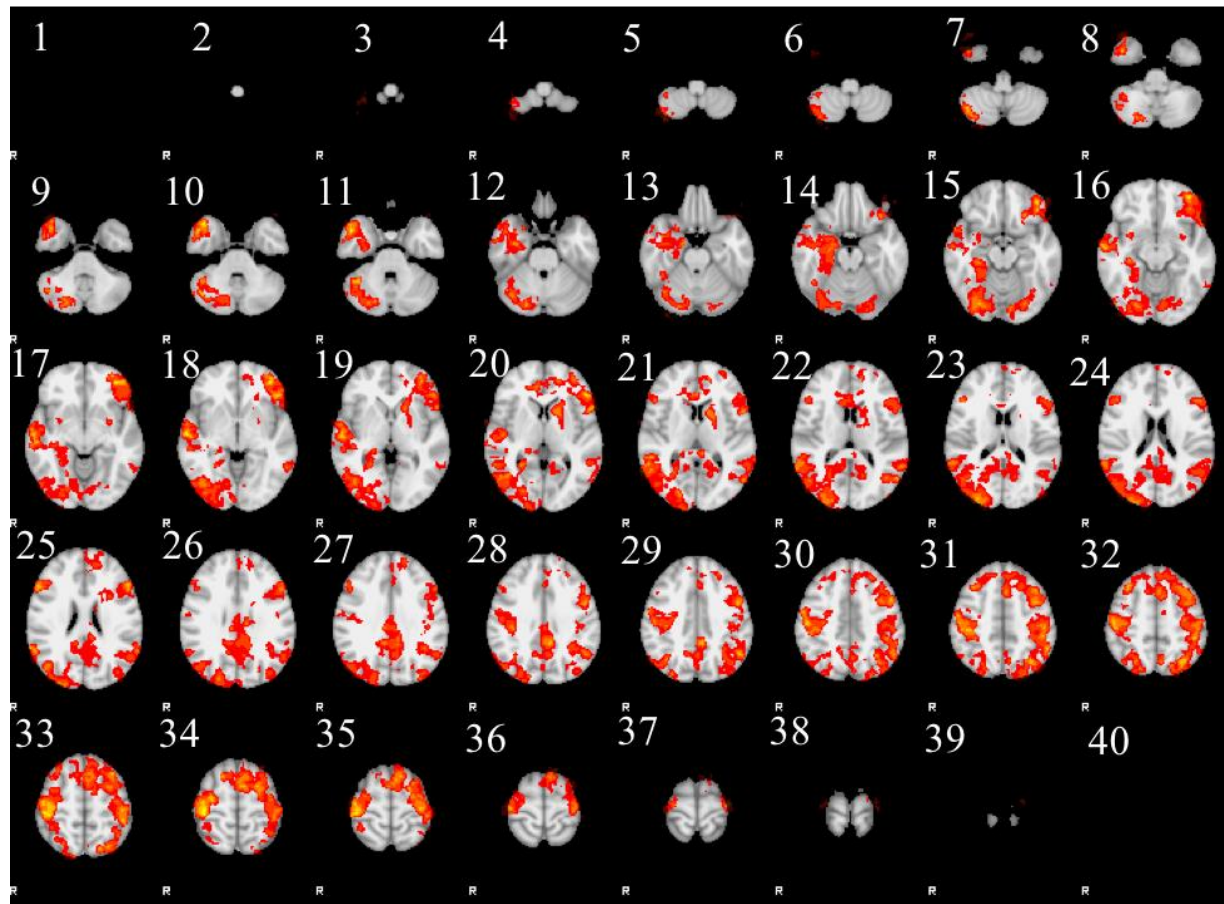


**Figure 7.9 Group maps of brain regions exhibiting significantly greater activity during CGI-imagined leg movements than during CGI-executed leg movements, color-coded in red-to-yellow heat maps where red = 2.3 and yellow > 4.7. Images are shown in radiological convention (i.e., right is on the left).**

**Table 7.7 Brain regions whose activity was significantly greater ( $p < 0.05$ ) during blue/green-executed movements than during blue/green-imagined movements, where the Z slice is in the upper left corner of Figure 7.10.**

Z (slices)	Harvard-Oxford Label
5-19	bilateral medial cerebellum
21-26	bilateral secondary motor area
27-40	bilateral primary motor (leg area) cortex

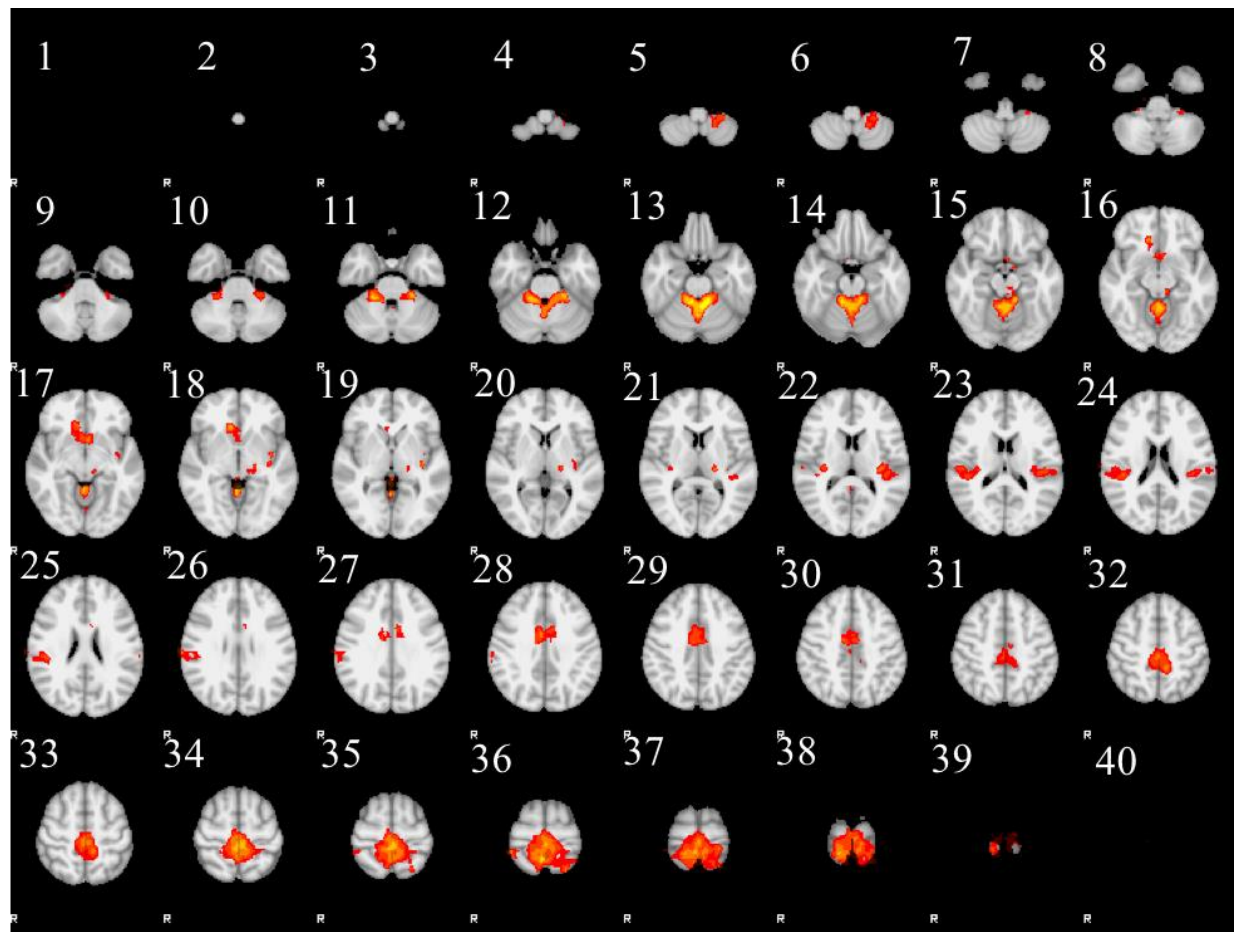


**Figure 7.10** Group maps of brain regions exhibiting significantly greater activity during blue/green-executed leg movements than during blue/green-imagined leg movements, color-coded in red-to-yellow heat maps where red = 2.3 and yellow > 4.7. Images are shown in radiological convention (i.e., right is on the left).

**Table 7.8 Brain regions whose activity was significantly greater ( $p < 0.05$ ) during blue/green-imagined movements than during blue/green-executed movements, where the Z slice is in the upper left corner of Figure 7.11.**

Z (slices)	Harvard-Oxford Label
4-12	Right lateral cerebellum
31-37	Bilateral supplementary motor area
29-31	Bilateral anterior cingulate cortex
29-32	Bilateral supramarginal gyrus
28-34	Bilateral precentral gyrus
15-20	Left frontal pole

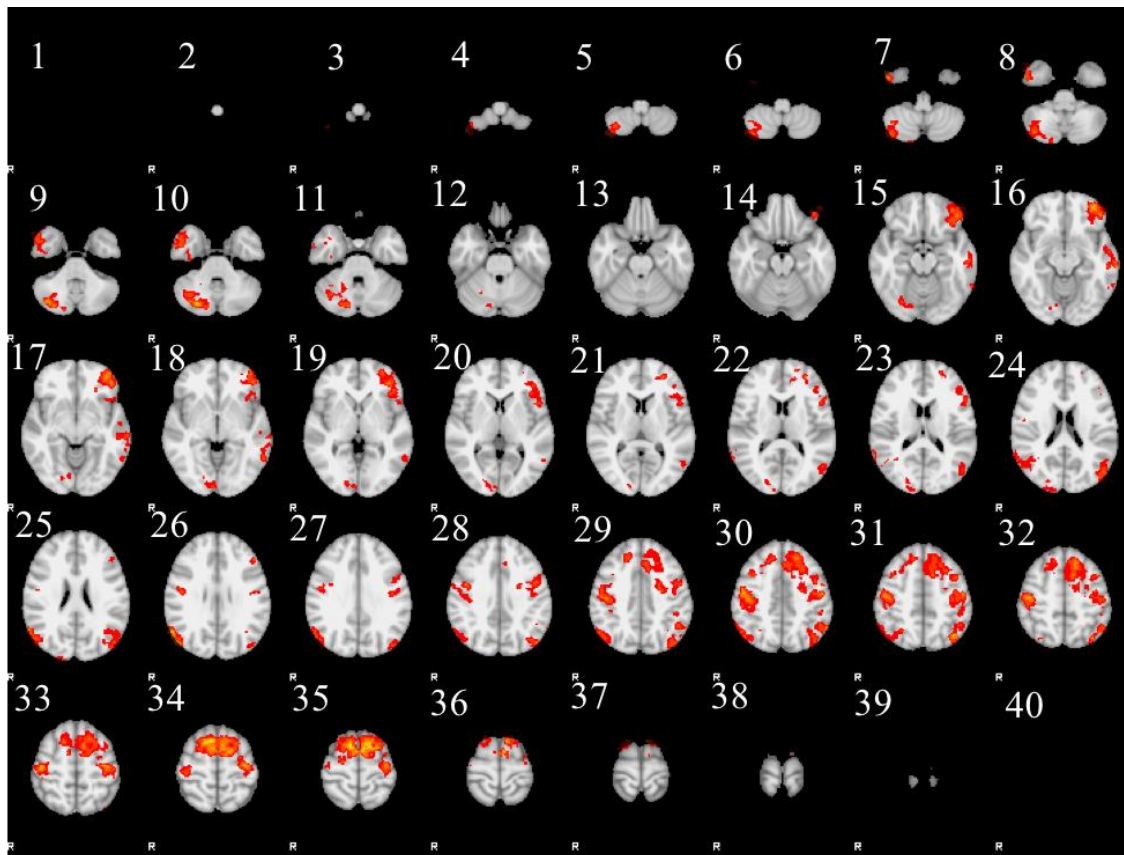


**Figure 7.11 Group maps of brain regions exhibiting significantly greater activity during blue/green-imagined leg movements than during blue/green executed leg movements, color-coded in red-to-yellow heat maps where red = 2.3 and yellow > 4.7. Images are shown in r radiological convention (i.e., right is on the left).**

**Table 7.9** Brain regions whose activity was significantly greater ( $p < 0.05$ ) during blue/green-executed movements than during CGI-executed movements, where the Z slice is in the upper left corner of Figure 7.12.

Z (slices)	Harvard-Oxford Label
16-21	Right temporal pole
15-33	Bilateral primary visual cortex

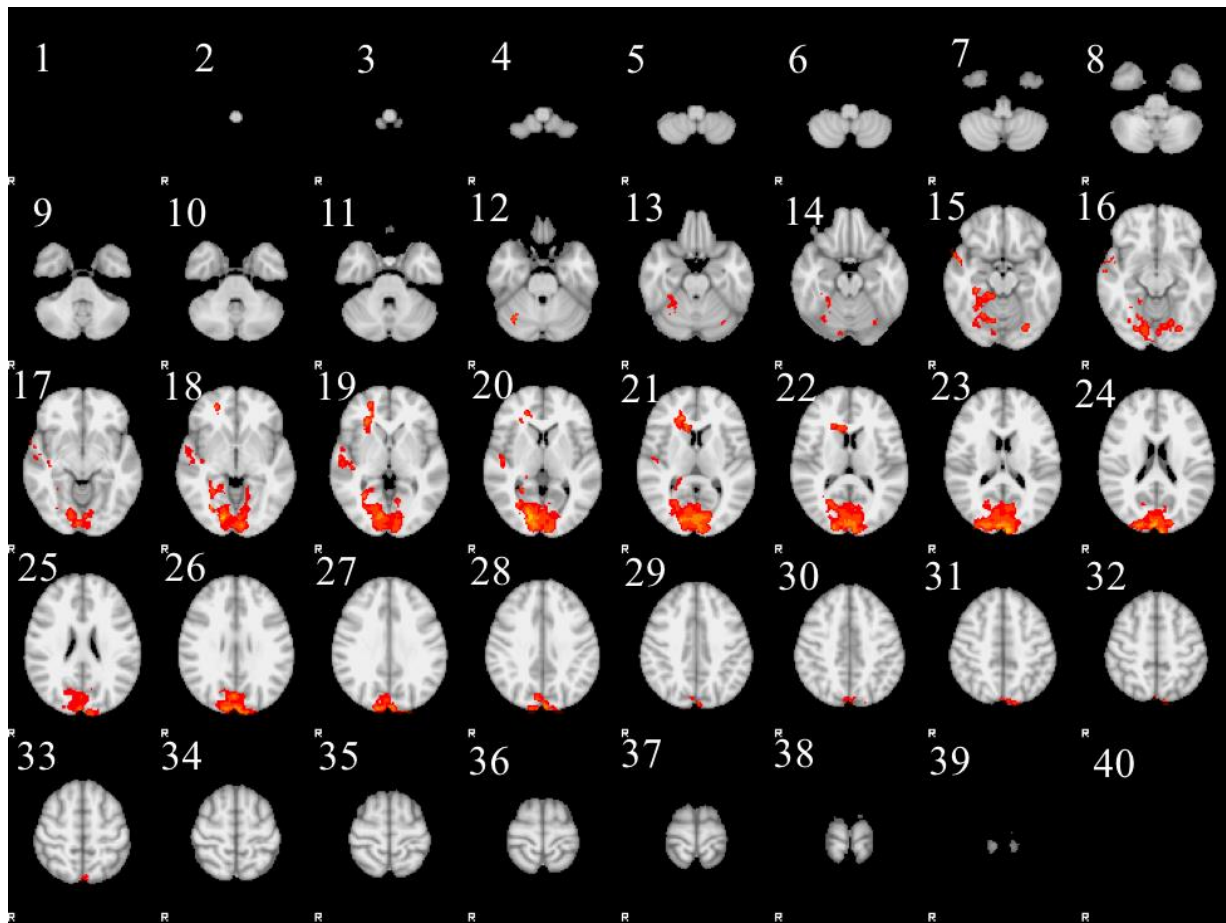


**Figure 7.12** Group maps of brain regions exhibiting significantly greater activity during blue/green-executed leg movements than during CGI-executed leg movements, color-coded in red-to-yellow heat maps where red = 2.3 and yellow > 4.7. Images are shown in radiological convention (i.e., right is on the left).

**Table 7.10 Brain regions whose activity was significantly greater ( $p < 0.05$ ) during CGI-executed movements than during blue/green-executed movements, where the Z slice is in the upper left corner of Figure 7.13.**

Z (slices)	Harvard-Oxford Label
14-22	Bilateral lateral occipital cortex

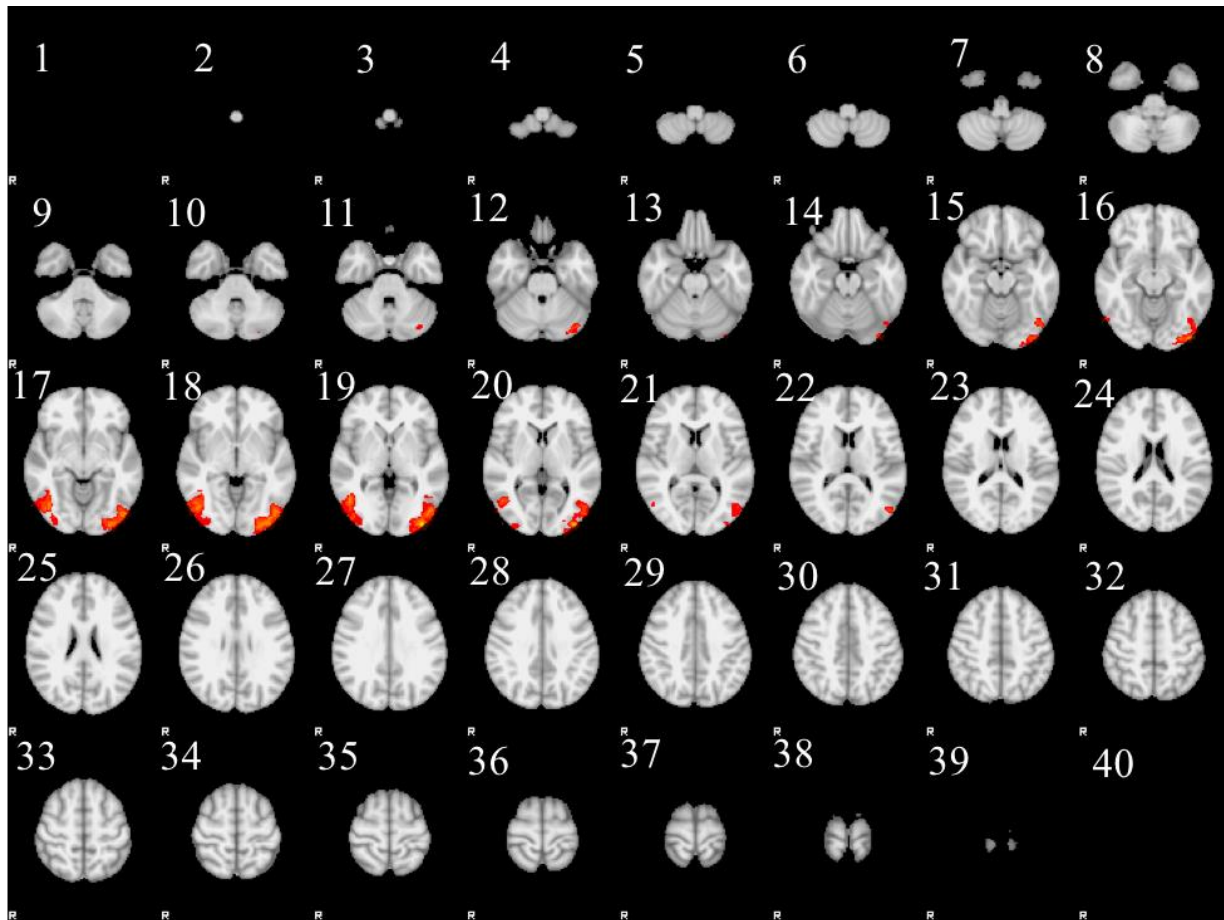


**Figure 7.13** Group maps of brain regions exhibiting significantly greater activity during CGI-executed leg movements than during blue/green-executed leg movements, color-coded in red-to-yellow heat maps where red = 2.3 and yellow > 4.7. Images are shown in radiological convention (i.e., right is on the left).

**Table 7.11 Brain regions whose activity was significantly greater ( $p < 0.05$ ) during blue/green-imagined movements than during CGI-imagined movements.**

Z (slices)	Harvard-Oxford Label
15-32	Bilateral primary visual cortex

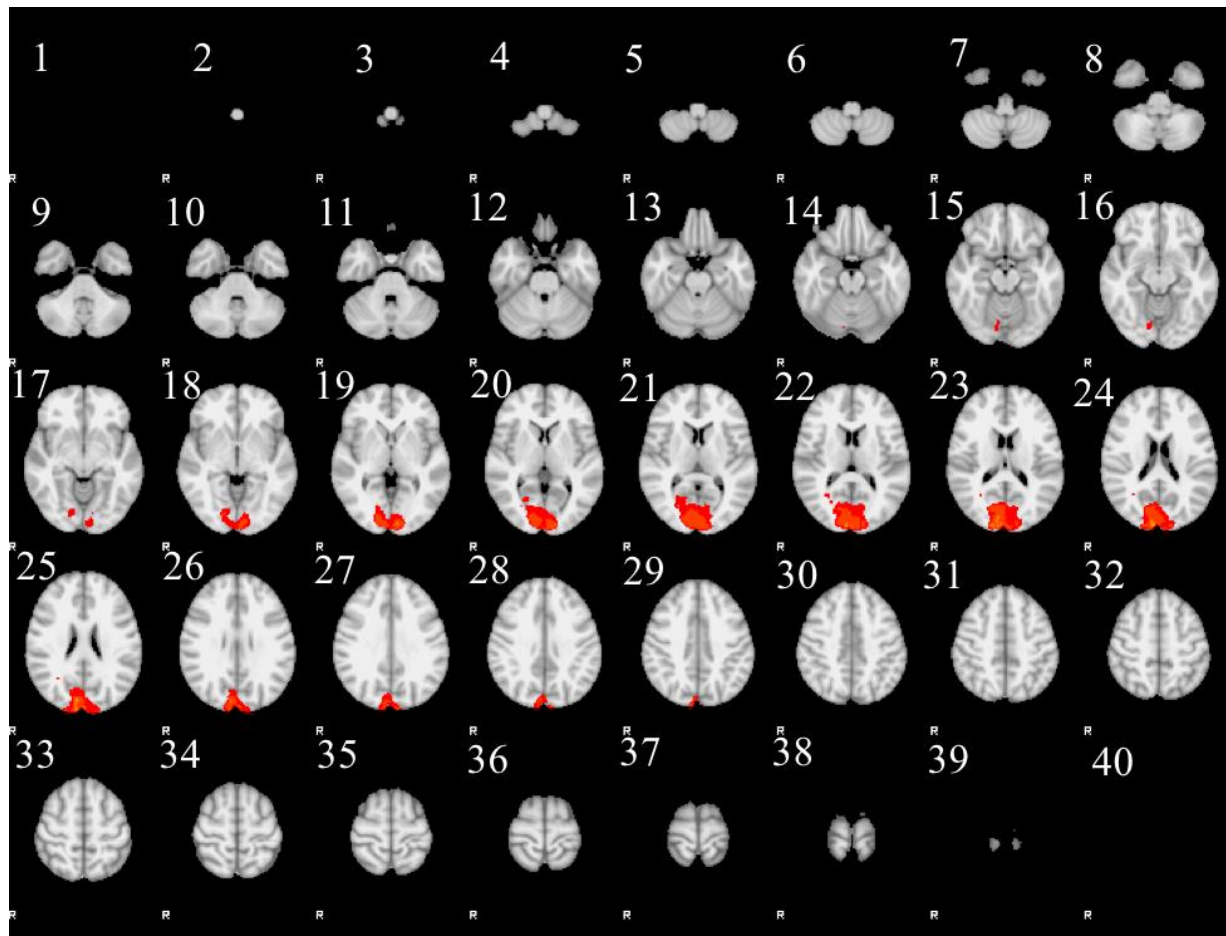


**Figure 7.14** Group maps of brain regions exhibiting significantly greater activity during blue/green imagined leg movements than during CGI imagined leg movements, color-coded in red-to-yellow heat maps where red = 2.3 and yellow > 4.7. Images are shown in radiological convention (i.e., right is on the left)

**Table 7.12 Brain regions whose activity was significantly greater ( $p < 0.05$ ) during CGI-imagined movements than during blue/green-imagined movements.**

Z (slices)	Harvard-Oxford Label
12-24	Bilateral lateral occipital cortex
31-37	Bilateral superior parietal lobule and postcentral gyrus

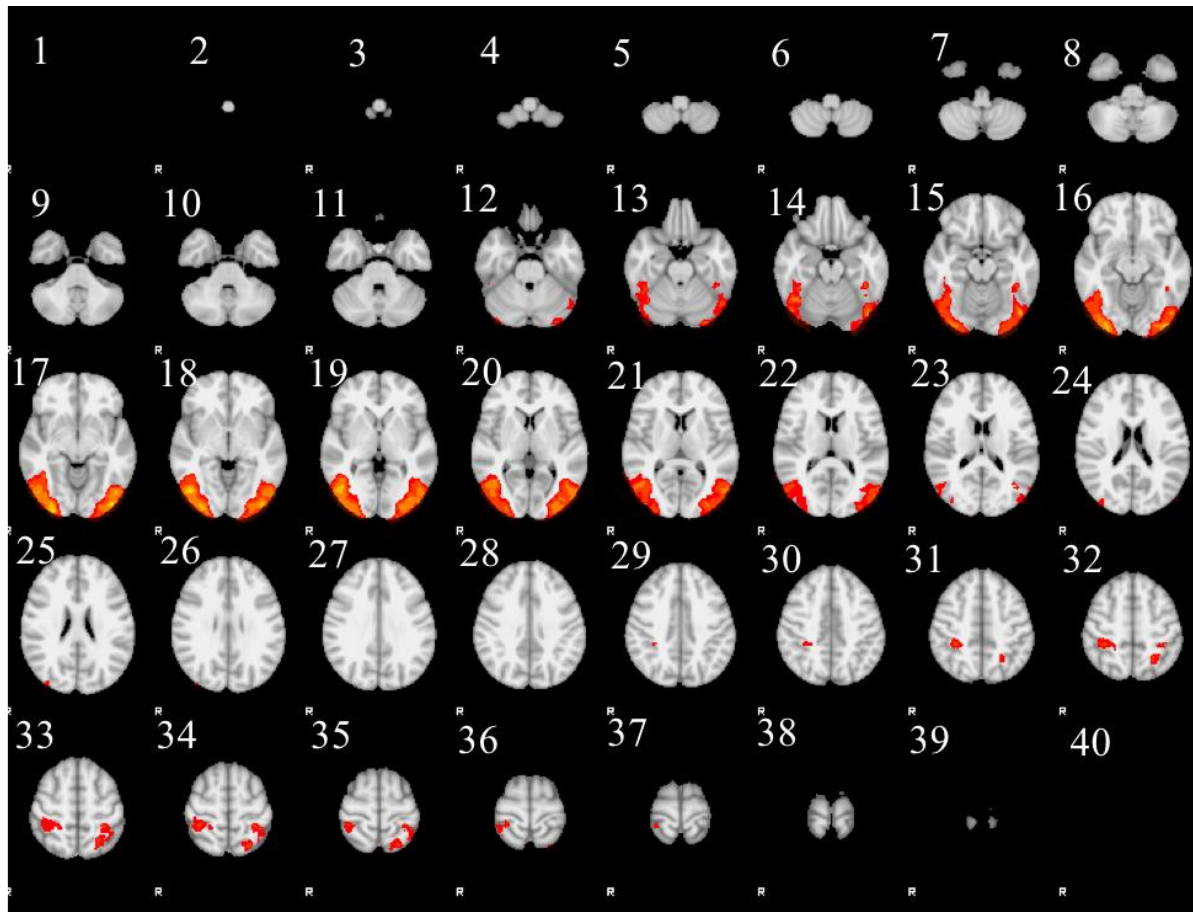


**Figure 7.15 Group maps of brain regions exhibiting significantly greater activity during CGI imagined leg movements than during blue/green imagined leg movements, color-coded in red-to-yellow heat maps where red = 2.3 and yellow > 4.7. Images are shown in radiological convention (i.e., right is on the left).**

## **7.4 Discussion**

The results of this study supported hypothesis 2 associated with the utility of fMRI to identify areas of the brain that would be differentially activated for lower limb movement across the four experimental conditions. This study was designed to accurately represent the activation patterns associated with lower limb movements across participants for the four experimental tasks. This task was accomplished using a carefully designed methodology and a multi-step analytical procedure. A second purpose was to determine if there were differences in the activation patterns between the four tasks. Again, the procedures used for assessing contrasts in the study allowed for these differences to be highlighted.

Consistent with the extant literature and methodological approach used, the current study showed that various sensory, motor and visual areas of the brain were activated. In addition, other temporal and parietal areas were also activated. Interpretation of these activations is a somewhat more speculative task due to the novelty of the study. However, with that caveat, discussion of these areas for each experimental condition is provided next.

### *7.4.1 CGI Executed*

During the executed CGI task most of the activation occurred in the primary and supplementary motor areas. This is a reasonable finding because motor execution and control would be needed for the task for which these areas are responsible. The additional activation at the medial cerebellum was also not unexpected, as the actual execution of the motor task occurred in this condition. Interestingly, there was activation in the right planum temporale area. This finding is consistent with reactions to coherent (repetitive) visual motion [141]. Given the type of visual stimulus, the current study supports these areas as being important in visual motion perception.

#### *7.4.2 CGI Imagined*

The highest activation in CGI imagined condition was in areas associated with movement control (premotor, motor and supplementary motor cortices and secondary motor area). Both the pallidum and putamen were activated bilaterally. They are located in the basal ganglia, are associated with regulation of movement [142], and have been established as important during the initiation of executed tasks in cats [143]. These areas would likely be activated in an imagined condition where the participant could be on the ‘verge’ of movement. The activation of the lateral cerebellum is consistent with findings on executed versus imagined hand movements as this area is thought to inhibit execution of movement [144].

Visual areas were also activated, specifically activation of the lateral occipital cortex in both left and right hemispheres indicates that shape/object recognition was being triggered [145]. This is likely due to the visual stimulus of the CGI with its unique shape and movement being important in carrying out this imagined task.

Finally, Wolpert, *et al.* 1998 [146] make a compelling case, using a single-subject study, that the superior parietal lobe is involved in the integration of sensory input and motor output, providing an internal representation of body state. The finding of activation in this area is consistent with the task presented to participants in the current study. He also argues [147] for this integration approach in building neural network and motor computational models.

#### *7.4.3 Blue-green Executed*

In the blue-green executed condition, as with the CGI executed condition, most of the activation occurred in the motor areas (primary motor leg area, supplementary and secondary motor areas).

Again, similar to the CGI condition, there was activation in the medial cerebellum due to the actual movement in this condition. Activation of the area that gives meaning to bodily states, including motor control (left and right insular cortex) [148] suggests the need for proprioceptive awareness for this task.

#### *7.4.4 Blue-green Imagined*

The blue-green imagined task was dominated by the activation of motor control areas (supplementary motor, premotor, and secondary motor cortices). It was also very similar to the CGI imagined task in terms of areas activated. There was activation of the right lateral cerebellum, as a possible inhibitor to the execution of movement [144], and bilaterally of the pallidum and putamen which also is associated with regulation of movement [142]. As in the CGI imagined task, there was also recruitment of the superior parietal areas to integrate sensory input and motor output [146]. Similar to the executed blue-green task, the bilateral activation of the insular cortex suggests the need for proprioceptive bodily meaning for this task [148].

#### *7.4.5 Executed and Imagined Task Contrasts*

Not surprisingly, the CGI executed task showed more activation in movement execution including the leg area of primary motor cortex and the medial cerebellum [72] relative to the CGI imagined task. The CGI imagined task relative to the CGI executed task showed many areas of differential activation. From a motor perspective, the somatosensory cortex and premotor cortex were activated relative to the executed condition rather than the actual motor output areas. The lateral cerebellum that is involved in inhibiting execution of movement was also activated in the imagined versus executed CGI condition [72].

In addition, several visual areas were activated including the: 1) right lingual gyrus that has been implicated in color vision perception [149] and face perception [150]; 2) left inferior frontal gyrus that plays a role in selective visual attention [151]; and 3) lateral occipital cortex associated with object recognition [145]. More cognitive functional areas were also activated. These included the posterior cingulate cortex that serves an evaluative function in monitoring sensory events [152] and the superior parietal areas that integrates sensory input and motor output [146]. Interestingly, two areas associated with emotions, the temporal pole (activated when processing social and emotional cues) [153] and the anterior cingulate cortex (related to emotional control of motor outputs) [152] were also activated.

For the blue-green tasks, the executed version relative to the imagined version showed more activation in motor areas (primary motor for the leg area, secondary motor area, and medial cerebellum). In contrast the blue-green imagined relative to the blue-green executed condition, showed right lateral cerebellum (that inhibits execution of movement [72], and bilateral supplementary motor area activity). There was also activation of the anterior cingulate cortex (related to emotional control of motor outputs) [152]. These findings are consistent with the CGI executed and imagined differences. There were some additional differences however, unique to this comparison. The left frontal pole that is linked to monitoring of task outcomes [154] was activated as was the precentral gyrus (motor control) and the supramarginal gyrus (proprioception [155]).

Overall, the executed tasks were notable by their additional activation of motor areas relative to the imagined tasks. The imagined tasks recruited several additional visual, proprioceptive, cognitive, and emotional areas relative to the executed tasks. This is not

surprising, as the task requires more effort to imagine oneself executing the task at a particular pace.

#### *7.4.6 CGI and Blue-green Task Contrasts*

The differences for the CGI and blue-green executed tasks were primarily in activations in different visual areas. The blue-green executed task showed higher activation than the CGI executed task in central vision (primary visual cortex). This contrast also showed activation of the cluster of the temporal pole (social and emotional cue processing) [153]. The CGI executed task showed higher levels of activation for object recognition (lateral occipital cortex) [145] relative to the Blue-green executed task.

The blue-green imagined task relative to the CGI imagined task showed more activation in primary visual cortex, while the CGI relative to the Blue-green imagined task showed more activation in the lateral occipital cortex (object recognition), a finding similar to that of the executed task comparison. There was also a cluster associated with sensory activation (postcentral gyrus) and integration of sensory input and motor output [146] in the CGI imagined relative to the blue-green imagined tasks. Given the complexity of the stimulus in the CGI executed condition relative to the blue-green condition, it was not surprising that there was more activation for recognition and less for basic visual processing.

Contrasts between the CGI condition and blue-green condition showed that blue-green activation was located predominantly in the primary visual cortex, while the information unique to the CGI condition was more temporal (ventral) in activation. This finding supports the two-stream model of visual processing, commonly referred to as the ‘what’ and ‘where’ pathways [156]. The dorsal pathway (parietal) is more responsible for where in space the object is, whereas

the ventral pathway is more responsible for object recognition. The more interesting and relatable CGI stimulus evoked a strong ventral pathway. This visually based finding was consistent across the contrasts performed between the two visual cues during executed and imagined tasks, providing support for this contention, given it occurs whether or not the participant is actually moving. The two pathways are presented in Figure 7.16.

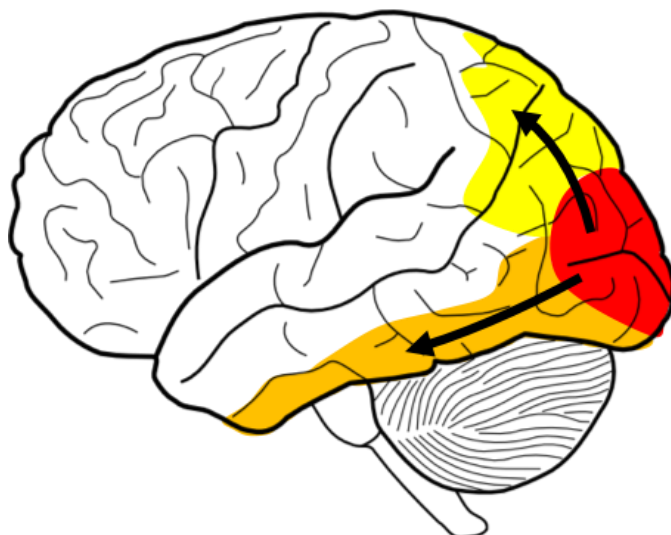


**Figure 7.16 Representation of dual-stream theory. Where visual activity moves from the primary visual cortex (red) to dorsal (yellow) and ventral (orange).**

## 7.5 Limitations

This portion of the study, while it provides fMRI-based insights into lower-limb stepping movement was conducted at a slow pace (~50 steps per minutes), which is about half the average speed of walking (~90-100 steps per minute). Therefore, these results may not generalize to the dispersion and amplitude of brain activation that would be observed with faster locomotion. A second limitation was that data associated with just the left or just the right movements were not separable. As was noted earlier, this is due to the fact that the metabolic response to the task was much slower than that of the task frequency. This issue is a methodological concern that would

need to be addressed using a much slower pace than actual walking. Third, two different visual stimuli were used to pace the participants, one a natural-looking figure of a person walking (CGI), and the other a more neutral stimuli (alternating blue-green circles). Several of the activated areas were likely due to these particular stimuli and thus would not be replicable under different conditions. It would be interesting to assess possible activation differences using visual, auditory, or no external stimuli.

Fourth, because there was not a second trial for the fMRI task at time 3, these data were not subjected to a reliability analysis. It has been shown that the overall reliability of fMRI data (cluster overlap) using the intraclass correlation (ICC) coefficient is roughly 0.50 [157], [158]. A study of the reliability of MRI functional connectivity using generalizability theory reports somewhat lower values (on the order of .30) [159]. Reliability of the data can be improved by increasing the length of the run, task training in advance of undergoing the MR scan, increasing the number of subjects and task trials to improve power, with most fMRI studies reviewed for reliability using fewer than 10 participants [158]. The current study employed several of the suggestions that should improve the assumed reliability of the data, including two training sessions, a large number of task repetitions ( $N = 60$ ) and collapsing the data across a relatively large number of participants ( $N = 16$ ).

Finally, the task was performed with the participants in a supine position. Thus, the activation of brain areas responsible for the maintenance of upright posture and balance were not captured in the data. However, to adequately address this issue, the MR scanner would need to be perpendicular to the ground such that participants are able to stand while they locomote.

## **7.6 Future Work**

Interesting results that warrant following up with subsequent studies include the results associated with the unilateral visual-temporal activation during fMRI on the left hemisphere of the brain, as well as the unilateral activation of the right rostral prefrontal cortex to ascertain the nature of these activations as either a product of visualization or cognitive processing. Using different stimuli modalities (e.g., visual, auditory, tactile) or even no stimuli at all to pace participants, answers to these questions might be uncovered.

## **7.7 Conclusion**

This work adds to the body of knowledge insofar as it isolates the differences and similarities between imagined and executed lower limb movements. In addition, this demonstrates the effects of using two quite different types of visual stimuli to complete the same task. These data can be used in the development of a brain-computer interface (BCI). More specifically, they can be used to inform where partial volume captures can be obtained that are highly correlated with brain activation, particularly during imagined locomotion. As such, the results presented in this chapter continue to push toward the overarching goal of the research project in facilitating the development of an efficient and effective lower limb BCI.

The findings from data collected separately using only EEG and then only fMRI on lower limb executed and imagined stepping were presented in the last two chapters. In order to capitalize on the strengths of each technological approach however, the information contained in each needs to be integrated. This integration is expected to assist in determining the most useful data for the input stage of BCI development. A process developed to do so is presented in the next chapter.

## **CHAPTER 8: FMRI INFORMED EEG FOR THE COMPUTER-GENERATED IMAGE TASKS**

### **8.1 Introduction**

The purpose of this chapter was to assess hypothesis 3: A computational approach exists that successfully allows accurate mapping of the spatial brain activity (fMRI) in relation to the temporal receptors (EEG electrodes) associated with lower limb movement. To do so, the use of an fMRI informed EEG procedure was implemented [77]. The goals of this chapter were to: 1) co-register the 64 EEG electrodes with respect to fMRI data and 2) determine the magnitude of an expected link between clusters of activated voxels and each electrode. This information was then used in a machine learning exercise that will help in the eventual creation of a brain computer interface (BCI) for lower limb movement (Chapter 9).

EEG and fMRI are two technologies that are capable of measuring brain activity. They are, however, measurements of two fundamentally different aspects of brain activity. fMRI is an indirect and metabolic measure of neuronal activity that can spatially be resolved to within millimeters [160] at all levels from deep brain to cortical structures. This makes it particularly effective at detecting where in the brain activity is taking place. EEG, on the other hand, is a direct measure of electrical activity that is captured at the scalp with spatial resolution in the cm<sup>3</sup> range [161]. It is precisely tied to the timing of neural activity. While deep brain activity adds to a summing of neurons as it radiates toward the cortical surface, it is cortical surface activation that dominates the detectable EEG signal. For this reason, fMRI and EEG are complementary technologies that can aid in creating a fulsome temporal and spatial model for understanding neural activity when carrying out tasks, including that of locomotion.

The data from the computer-generated image (CGI) conditions were selected to undertake this process. The CGI data performed much better in the predictive utility of left/right and showed higher generalizability relative to the blue-green condition (Chapter 6). In addition, the data from the imagined CGI condition would also be the most useful to translate for use to those with compromised lower limb mobility.

## 8.2 Methods

### 8.2.1 *Data Collection*

For a detailed explanation of how data were acquired please see Chapter 5. This chapter makes use of the concurrently-gathered fMRI and EEG data collected at time point 3 for the CGI executed and imagined conditions.

### 8.2.2 *Data Processing*

Recall that once the fMRI data were processed, significant clusters were established based on amplitude of activation and correlation with the GLM described in Chapter 7. The Harvard-Oxford Atlas locations of these significant clusters were also recorded. Because these clusters exist in 3D space within a standard MR image (MNI 2 mm), sets of (x, y, z) coordinates define each voxel in each cluster.

The EEG data, however, are captured in a different 3D space. Specifically, neural sources of the electrical signals are picked up by 64 different EEG electrodes that are wrapped around the participant's head in a cap. The unique EEG electrode locations, and their relationships to each other, are provided for each cap by the manufacturer.

### A. EEG Electrodes Mapped from Standard Brain Space to fMRI Space

As a result of these differences between the various 3D spaces, to tightly couple where the EEG electrodes sit in a 3D volume with respect to the hemodynamic activation observed in the fMRI data, several steps were undertaken. Figure 8.1 outlines these transformations and each one will be described in turn.

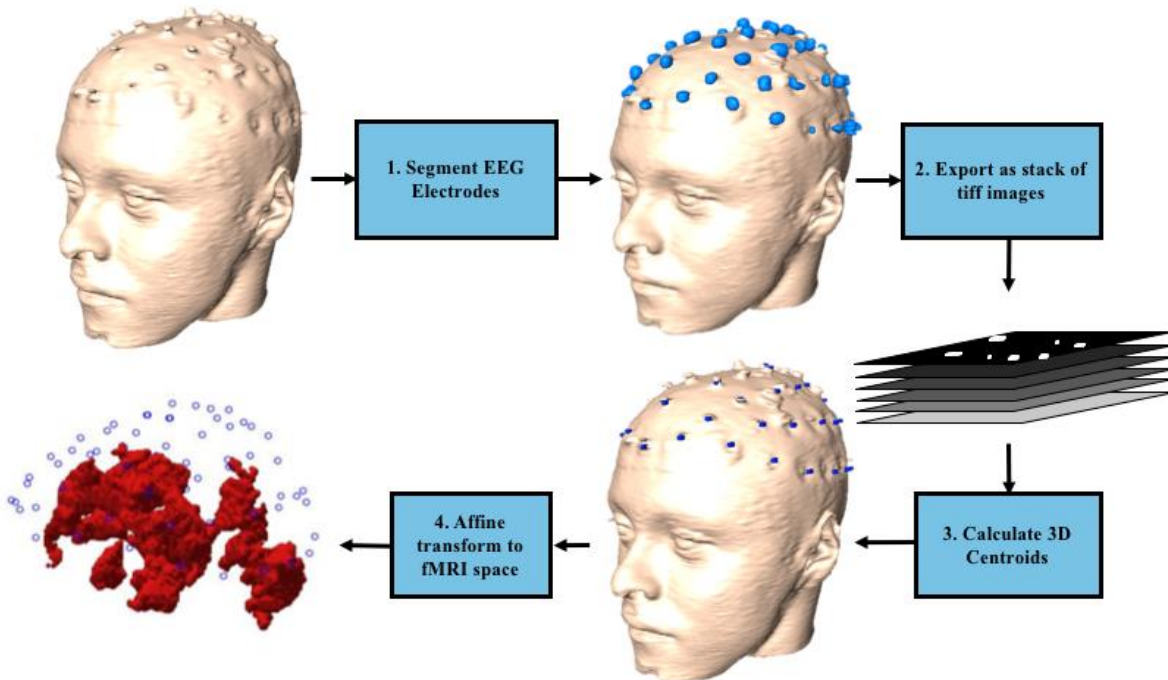


**Figure 8.1 Flowchart overview of the process used to co-register EEG electrodes in 3-dimensional fMRI space**

Step 1, as displayed in Figure 8.1, was to correctly identify and localize the EEG electrodes in the structural (no task) T1 weighted MRI scans. To do so the scans for each participant were loaded into *Amira* (Zuse Institute, Berlin) software and the EEG electrodes on these structural MRI scans showed up as artifacts ('bumps') on the surface of the skull. The user of the *Amira* software manually then 'draws' boundaries around the artifacts, a process called

segmentation. Segmentation of the EEG electrodes in multiple planes, for a single structural MR slice is shown in Figure 8.2.

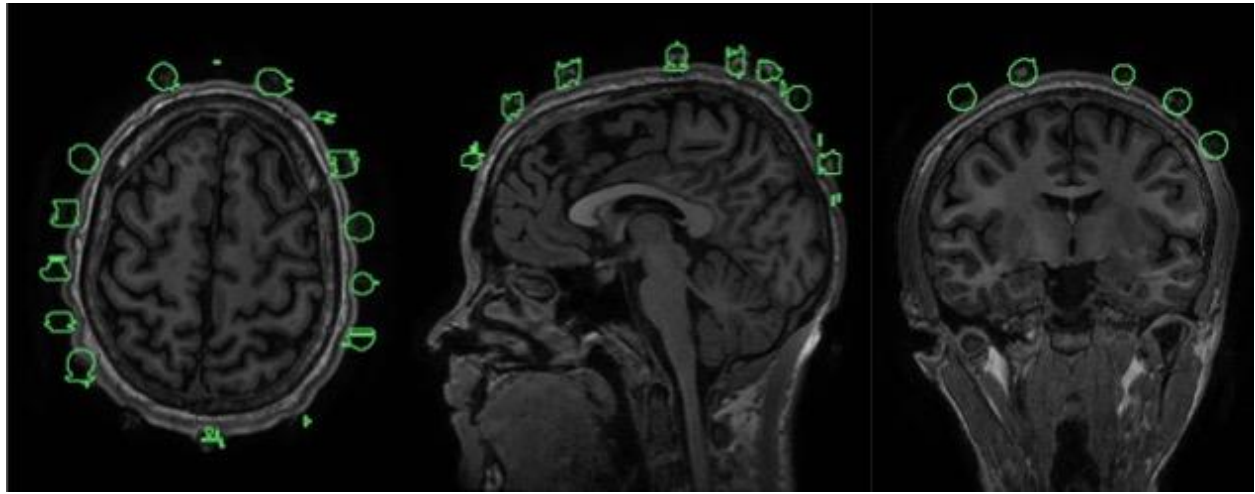


**Figure 8.2 Segmentation of the EEG electrodes in the transverse, sagittal and frontal planes of one slice of the structural MR in Amira software for one participant**

By iterating this process in multiple planes (frontal, sagittal and transverse) across all slices, a series of 2D image segments were generated. These data can only be exported as a stack of 2D binary, tagged image file format (tiff) images where the background is black (=0), and the electrodes are white (=1) (i.e., grey-scale). Step 2 in the process was the exportation of these segmented EEG electrode results.

Step 3 was to generate a 3D model of the EEG electrodes by interpolating across the multiple 2D images. To do so, the centroids for each of the EEG electrodes needed to be computed. Using the data across the 2D images the 3D centroid-based map required three separate equations, one for each of x, y, and z, for each EEG electrode using Equation 8.1:

$$C_x = \frac{\sum C_{ix} * A_i}{\sum A_i}, C_y = \frac{\sum C_{iy} * A_i}{\sum A_i}, C_z = \frac{\sum C_{iz} * A_i}{\sum A_i} \quad (8.1)$$

Using the equations, a 3D centroid representing the center of each EEG electrode was calculated.  $C_n$  are the centroids in a given plane, where the individual electrodes are broken into sets of smaller shapes ( $X_n$ ), and  $(A_i)$  is the area of the smaller shapes comprising the whole shape. This varies on an electrode basis, provided the segmentation varies.

By applying these equations to the stack of tiff files, the center of each EEG electrode was established in the same space in which the structural MRI was collected. This resulted in a 64-point ‘cloud’ representing the EEG electrodes using *Matlab 2017b* (Mathworks, MA, USA). This procedure was carried out for each subject separately, as each one was associated with the data from his unique structural MRI scan. The point cloud was fitted with a mesh to highlight the 3D nature of this space. Figure 8.3 shows an example of one participant’s 3D 64-point EEG-cap cloud.

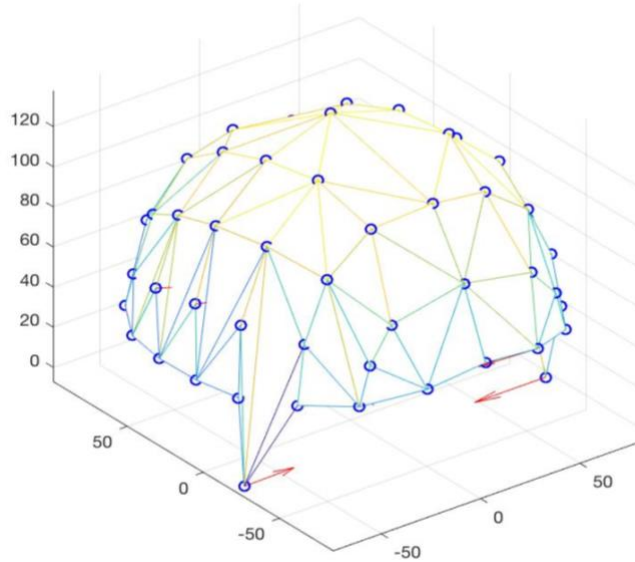


**Figure 8.3 Example of a Maglink 64 electrode EEG cap showing the locations of electrodes relative to one another in x, y, z space and fitted with a surface mesh**

Recall that the structural MRI space (no task), functional MRI data (task-based) space, and MNI 2 mm standard brain space all have unique frames of reference. Thus, Step 4 required a

co-registration process to align the structurally-mapped EEG electrodes to a standard fMRI space (MNI 2 mm). This meant that two more transformation matrices were required. This is similar to the step carried out in Chapter 7 to register the participant level functional scans into standard MNI 2 mm space using affine transformation. Specifically, the software program FSL [111] was used to calculate the 4x4 transformation matrices used and included parameters for the shear, scaling, rotation and translation necessary to register the data between the various spaces.

The affine transformation is shown in Equation 8.2, where  $t_x$ ,  $t_y$  and  $t_z$  represent translations in each of the three directions,  $b$  is a scale factor and the amalgamation of  $\sin(\theta)$  and  $\cos(\theta)$  are responsible for rotation in each of the three planes. This transforms the set of 3D coordinates  $(x, y, z)$  associated with the 64 EEG electrodes into new space  $(x', y', z')$ .

$$\begin{bmatrix} x' \\ y' \\ z' \\ 1 \end{bmatrix} = \begin{bmatrix} \cos(\theta) & b \cdot -\sin(\theta) & \sin(\theta) & t_x \\ \sin(\theta) & \cos(\theta) & -\sin(\theta) & t_y \\ -\sin(\theta) & \sin(\theta) & \cos(\theta) & t_z \\ 0 & 0 & 0 & 1 \end{bmatrix} * \begin{bmatrix} x \\ y \\ z \\ 1 \end{bmatrix} \quad (8.2)$$

After the EEG electrode coordinates were ascertained for each individual, they were averaged to generate a single EEG electrode coordinate system in which the fMRI group-level data could be imported.

#### *B. EEG and fMRI Data in a Single Standard Brain Space*

The stack of 2D fMRI data from the CGI conditions was then imported into this same 3D space. Once in the same space, participants' locations of metabolic activity were rendered using *Matlab 2017b* (Mathworks, MA, USA) as point clouds, keeping the z-stat (amplitude) of each voxel within each cluster intact. Figures 8.4 and 8.5 show these metabolic point clouds in 3D space for the clusters associated with brain activity for the imagined and executed CGI

conditions. Panel A in the figures show the clusters, their locations, and numbers while Panel B in the figures show overlay of the EEG electrode locations. A close-up view of a sample cluster and three EEG electrodes (C1, C4, and P4) are shown in Figure 8.6.

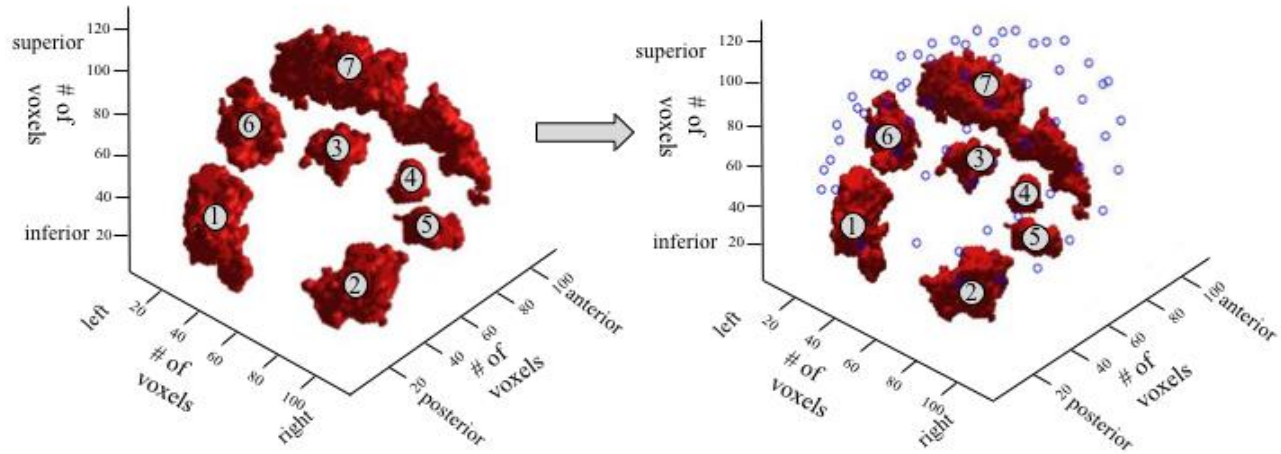


**Figure 8.4 A)** fMRI clusters from the CGI imagined condition, labelled 1 through 7; **B)** EEG locations overlaid on the fMRI clusters from the CGI imagined condition

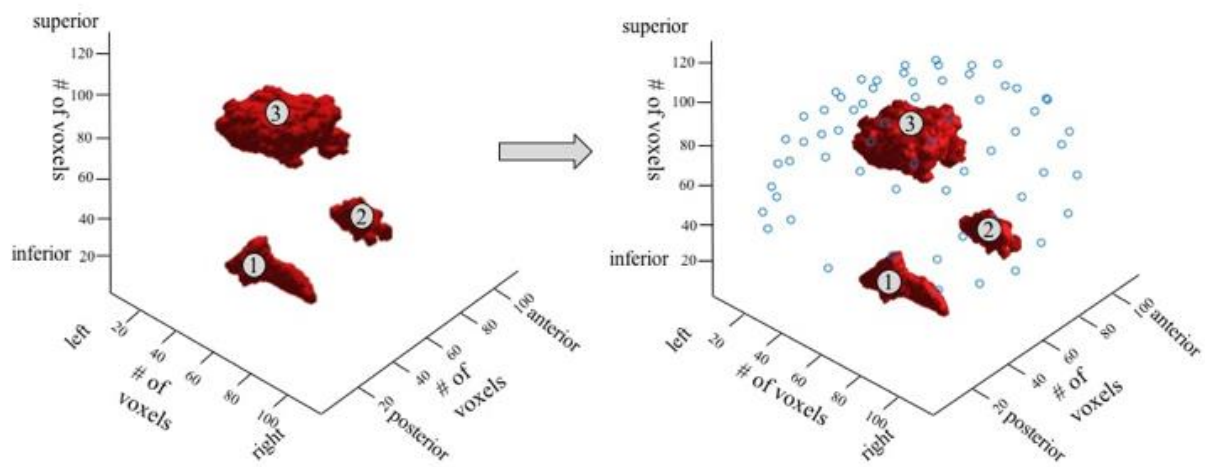


**Figure 8.5 A)** fMRI clusters from the CGI executed condition, labelled 1 through 3; **B)** EEG locations overlaid on the fMRI clusters from the CGI executed condition

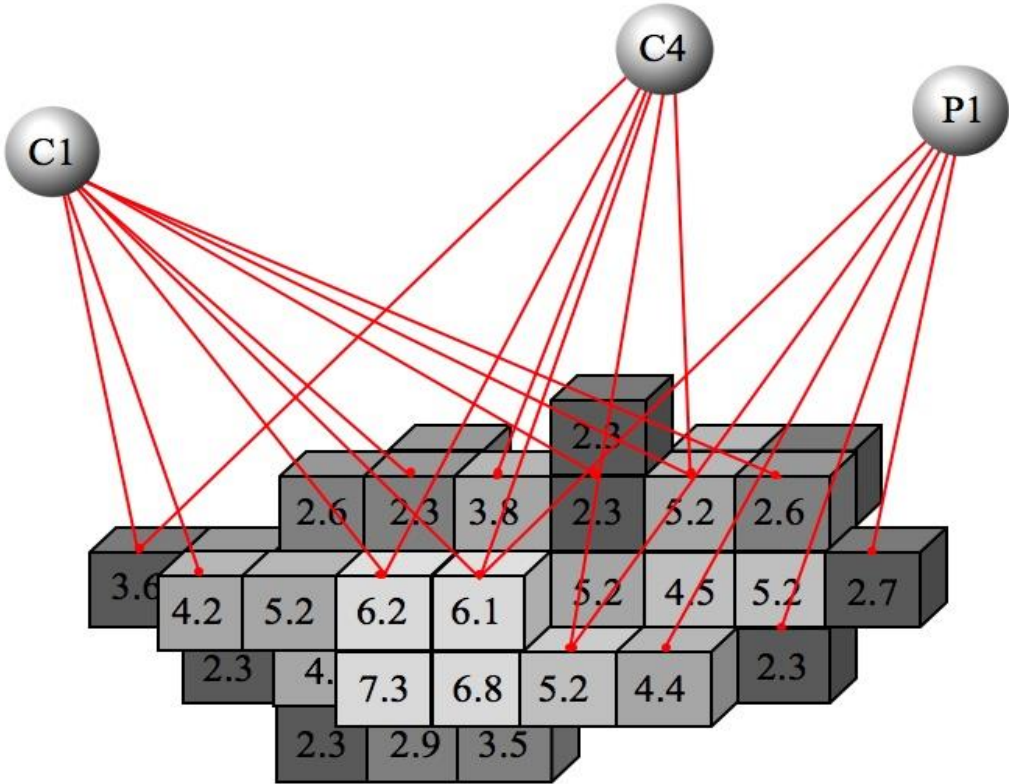


**Figure 8.6 Close-up of a mock up section of Figures 8.4 and 8.5 showing the distance vectors between electrodes C1, C4, and P1 and a cluster of voxels (with their z-stat scores – higher numbers indicating higher activation)**

#### *C. Strength of Relationship Between Clusters and EEG Electrodes*

At this point the group-level EEG electrode and fMRI data for the CGI imagined condition were in the same standard brain space with the correct distances of each electrode to the activated voxels in each cluster correctly determined. The next step in the fMRI informed EEG process was to model how effectively the neural activity in each cluster is likely to be ‘picked up’ by the 64 EEG electrodes. This information, then, can be used to determine the most appropriate weighting approach when creating a brain-computer interface (BCI) linking EEG activity to lower limb imagined or executed movement.

The expected activity level in the electrodes is based on both the distance from the voxel as well as the magnitude of its signal. Therefore, a customized equation that addressed both of these dimensions was developed that weighted the proximity of clusters to each electrode in 3D space. This was accomplished by first calculating the absolute distance between each voxel and each electrode for a given cluster ( $d_{ve}$ ). Equation 8.4 is the mathematical model used to generate the distances between the two sets of 3D points.

$$d_{ve} = \sqrt{(x_2 - x_1)^2 + (y_2 - y_1)^2 + (z_2 - z_1)^2} \quad (8.4)$$

Variable ( $d_{ve}$ ) denotes the Euclidean distance between each electrode and each voxel. Variables ( $x_2, y_2, z_2$ ) represent each electrode's location and ( $x_1, y_1, z_1$ ) represent each voxel's location. By using the inverse square of this distance, voxels that are closer to the electrode were more highly weighted.

An adjustment for voxel activation level was then incorporated. Voxel activation levels are reflected in their z-stat score. This information was also included in the equation such that if an electrode had a high activation but was further away, it was accounted for in the weight. Conversely, if an electrode had a small z-stat score but was closer this would also be accounted for in the equation. Equation 8.5 was used to generate these adjusted weights where ( $z_{stat}$ ) represents the z-stat score of the voxel, ( $d_{ve}$ ) is the distance between each voxel ( $v$ ) and electrode ( $e$ ) summed over the number of voxels in each cluster ( $n$ ) and finally ( $P_w$ ) is the proximity weighting.

$$P_w = \sum_{i=1}^n z_{stat} * \frac{1}{(d_{ve})^2} \quad (8.5)$$

These proximity weights were summed over the total number of voxels in the cluster. In order for this proximity score to be useful in the creation of the BCI, the  $P_w$  scores were normalized to range from ~0 to ~1. The reason for the ‘approximate 0’ and ‘approximate 1’ is that in a sigmoid weighting function (as is used in machine learning and described in the next chapter), weights range from ~0 to ~1 because the function asymptotes as it approaches 0 and 1.  $P_w$  scores were normalized by inserting them into Eq. 8.6, where  $P_N$  is the normalized weighting value of  $P_w$ .

$$P_N = \frac{(0.999-0.001)*(P_w - \min(P_w))}{\max(P_w) - \min(P_w)} + \min(P_w) \quad (8.6)$$

$P_N$  values take into account the  $P_w$  maxima and  $P_w$  minima in the entire data set (across electrodes). Therefore, they represent not only a simple rank-ordering magnitude system, but if a cluster is very close to the surface (close to several electrodes) this would represent a ‘global maximum’ and deeper brain activations a ‘global minimum’, and every weighting is based on the cohort of clusters, not simply within a cluster. These weights were calculated on a per cluster basis. Summing the activation levels over the total number of clusters on a per electrode basis should provide an overall likelihood of electrode activation associated with a given task.

### 8.3 Results

The resulting  $P_N$  values are recorded for use in an electrode selection tool (Tables 8.1 and 8.2). They show the weighting of each EEG electrode relative to each of the significant clusters in the CGI imagined and CGI executed conditions, as well as the sum across all clusters in the final column. Where the weighting would suggest an importance of each electrode relative to the hemodynamic response with a higher weighting denoting a higher likelihood of importance. For the imagined task FCZ, FC3, FC5, and FC1 all had summed values above 1.0.

**Table 8.1 Weighting of EEG electrodes on an fMRI cluster-wise basis for CGI Imagined condition**

EEG Electrode	Cluster 1	Cluster 2	Cluster 3	Cluster 4	Cluster 5	Cluster 6	Cluster 7	Summation
CZ	0.04	0.05	0.01	0.01	0.01	0.06	0.54	0.72
CPZ	0.05	0.05	0.01	0.00	0.01	0.07	0.26	0.45
C1	0.05	0.04	0.01	0.01	0.00	0.10	0.54	0.76
CP1	0.06	0.05	0.01	0.00	0.00	0.12	0.31	0.55
CP2	0.04	0.07	0.01	0.00	0.01	0.04	0.24	0.40
FC1	0.04	0.04	0.02	0.01	0.00	0.07	1.00	<b>1.17</b>
C2	0.04	0.06	0.01	0.01	0.01	0.04	0.44	0.61
PZ	0.05	0.06	0.01	0.00	0.01	0.06	0.19	0.38
FZ	0.03	0.03	0.01	0.01	0.01	0.03	0.65	0.76
FC2	0.03	0.05	0.01	0.01	0.01	0.03	0.71	0.86
P1	0.07	0.05	0.01	0.00	0.00	0.11	0.22	0.46
P2	0.04	0.08	0.01	0.00	0.01	0.04	0.18	0.35
F1	0.03	0.03	0.02	0.01	0.00	0.04	0.74	0.88
F2	0.02	0.04	0.01	0.01	0.01	0.02	0.58	0.70
CP3	0.08	0.04	0.01	0.00	0.00	0.22	0.32	0.69
C3	0.07	0.04	0.02	0.00	0.00	0.17	0.48	0.78
PO3	0.08	0.06	0.01	0.00	0.00	0.10	0.17	0.43
FC3	0.05	0.03	0.02	0.01	0.00	0.10	0.82	<b>1.03</b>
CP4	0.03	0.09	0.01	0.01	0.02	0.03	0.21	0.40
FC4	0.03	0.06	0.01	0.01	0.02	0.02	0.54	0.70
POZ	0.06	0.07	0.01	0.00	0.01	0.06	0.16	0.36
C4	0.03	0.08	0.01	0.01	0.03	0.03	0.34	0.52
PO4	0.05	0.09	0.01	0.00	0.01	0.04	0.14	0.34
P4	0.04	0.11	0.01	0.00	0.02	0.03	0.17	0.37
AFZ	0.02	0.03	0.02	0.01	0.00	0.02	0.36	0.45
F3	0.04	0.03	0.03	0.01	0.00	0.05	0.74	0.89
F4	0.02	0.04	0.01	0.01	0.01	0.02	0.51	0.64
AF4	0.02	0.03	0.01	0.01	0.01	0.01	0.32	0.42
AF3	0.03	0.02	0.02	0.01	0.00	0.03	0.40	0.51
F5	0.04	0.03	0.03	0.01	0.00	0.05	0.70	0.87
FC5	0.07	0.03	0.03	0.01	0.00	0.10	0.86	<b>1.10</b>
C5	0.10	0.03	0.02	0.00	0.00	0.21	0.38	0.75
F6	0.02	0.05	0.01	0.02	0.02	0.01	0.43	0.56
FP2	0.02	0.03	0.01	0.01	0.01	0.01	0.26	0.35

CP5	0.15	0.04	0.02	0.00	0.00	0.30	0.25	0.76
P5	0.18	0.04	0.01	0.00	0.00	0.22	0.18	0.64
C6	0.03	0.12	0.01	0.01	0.06	0.02	0.26	0.51
FP1	0.02	0.02	0.02	0.01	0.00	0.02	0.27	0.37
CP6	0.03	0.16	0.01	0.01	0.05	0.02	0.17	0.45
AF8	0.02	0.04	0.01	0.02	0.01	0.01	0.29	0.40
A7	0.03	0.02	0.03	0.01	0.00	0.03	0.36	0.49
FC7	0.02	0.08	0.01	0.02	0.04	0.02	0.42	0.61
FPZ	0.02	0.02	0.02	0.01	0.00	0.01	0.22	0.30
PO5	0.25	0.06	0.01	0.00	0.00	0.14	0.14	0.60
O1	0.19	0.07	0.01	0.00	0.00	0.09	0.12	0.48
O2	0.06	0.18	0.00	0.00	0.01	0.03	0.11	0.40
F8	0.02	0.06	0.01	0.02	0.03	0.01	0.33	0.47
F7	0.05	0.03	0.04	0.01	0.00	0.05	0.43	0.60
PO6	0.05	0.27	0.01	0.00	0.02	0.02	0.12	0.49
OZ	0.13	0.13	0.01	0.00	0.01	0.04	0.10	0.42
FT7	0.08	0.03	0.04	0.01	0.00	0.08	0.39	0.63
PO7	0.54	0.06	0.01	0.00	0.00	0.11	0.12	0.84
TP7	0.35	0.04	0.02	0.00	0.00	0.21	0.17	0.80
T7	0.16	0.03	0.03	0.00	0.00	0.17	0.25	0.65
PO8	0.05	0.44	0.01	0.00	0.02	0.02	0.10	0.64
TP8	0.03	0.28	0.01	0.01	0.11	0.02	0.14	0.59
P8	0.04	0.44	0.01	0.01	0.05	0.02	0.12	0.67
P7	0.63	0.05	0.02	0.00	0.00	0.14	0.13	0.97
FT8	0.02	0.09	0.01	0.02	0.06	0.01	0.28	0.50
T8	0.03	0.16	0.01	0.02	0.17	0.01	0.20	0.61
P6	0.04	0.23	0.01	0.01	0.04	0.02	0.15	0.49
P3	0.11	0.05	0.01	0.00	0.00	0.21	0.21	0.59
FCZ	0.03	0.04	0.01	0.01	0.01	0.04	0.90	<b>1.05</b>

**Table 8.2 Weighting of EEG electrodes on an fMRI cluster-wise basis for CGI Executed condition**

EEG Electrode	Cluster 1	Cluster 2	Cluster 3	Summation
CZ	0.01	0.01	1	<b>1.02</b>
CPZ	0.01	0.01	0.57	0.59
C1	0.01	0.01	0.88	<b>0.9</b>
CP1	0.01	0.01	0.67	0.68
CP2	0.01	0.01	0.42	0.45
FC1	0.01	0.01	0.81	<b>0.82</b>
C2	0.01	0.02	0.75	0.78
PZ	0.01	0.01	0.39	0.41
FZ	0.01	0.01	0.38	0.4
FC2	0.01	0.01	0.59	0.61
P1	0.01	0	0.43	0.45
P2	0.01	0.01	0.31	0.33
F1	0.01	0	0.4	0.41
F2	0.01	0.01	0.33	0.36
CP3	0.01	0	0.49	0.51
C3	0.01	0	0.49	0.5
PO3	0.02	0	0.31	0.33
FC3	0.01	0	0.45	0.47
CP4	0.01	0.02	0.29	0.33
FC4	0.01	0.03	0.33	0.37
POZ	0.01	0.01	0.29	0.31
C4	0.01	0.03	0.36	0.4
PO4	0.01	0.01	0.24	0.27
P4	0.01	0.02	0.24	0.28
AFZ	0.01	0	0.2	0.21
F3	0.01	0	0.31	0.33
F4	0.01	0.02	0.25	0.28
AF4	0.01	0.01	0.17	0.19
AF3	0.01	0	0.19	0.2
F5	0.01	0	0.22	0.24
FC5	0.02	0	0.25	0.27
C5	0.02	0	0.25	0.27
F6	0.01	0.02	0.17	0.21
FP2	0.01	0.01	0.14	0.15
CP5	0.02	0	0.24	0.26

P5	0.02	0	0.22	0.24
C6	0.02	0.07	0.2	0.29
FP1	0.01	0	0.14	0.15
CP6	0.02	0.05	0.18	0.25
AF8	0.01	0.01	0.14	0.16
A7	0.01	0	0.16	0.17
FC7	0.01	0.05	0.2	0.26
FPZ	0.01	0	0.12	0.13
PO5	0.02	0	0.18	0.21
O1	0.02	0	0.17	0.19
O2	0.02	0.01	0.14	0.18
F8	0.01	0.02	0.13	0.17
F7	0.01	0	0.15	0.17
PO6	0.02	0.02	0.15	0.19
OZ	0.03	0.01	0.13	0.16
FT7	0.02	0	0.15	0.17
PO7	0.03	0	0.14	0.17
TP7	0.03	0	0.14	0.17
T7	0.02	0	0.15	0.17
PO8	0.03	0.02	0.12	0.16
TP8	0.02	0.07	0.12	0.21
P8	0.03	0.04	0.12	0.18
P7	0.03	0	0.13	0.16
FT8	0.02	0.05	0.13	0.2
T8	0.02	0.12	0.13	0.27
P6	0.02	0.03	0.18	0.24
P3	0.02	0	0.33	0.35
FCZ	0.01	0.01	0.83	<b>0.85</b>

## 8.4 Discussion

Hypothesis 3 was supported in that a computational approach was designed that successfully allows accurate mapping of the spatial brain activity (fMRI) in relation to the temporal receptors (EEG electrodes) associated with lower limb movement. This approach was used for both the imagined and executed CGI condition data.

As can be seen in the second last column of Table 8.1 for the imagined condition, cluster 7 has many highly weighted electrodes, most of which correspond to the supplementary motor cortex and precentral gyrus.

The smaller number of clusters activated during the executed task (see Table 8.2) rendered a value of above 1.0 for only one electrode at CZ. For the executed task, electrodes CZ, C1, FC1, and FCZ ranked highest across electrodes. These would be the 4 EEG electrodes most likely to be associated with the BOLD response. Interestingly, C1 was one of the electrodes used in Chapter 6 (isolating left and right movements with a GEE), selected from the literature due to its expected association with lower limb movement based on the extant literature. Left hemisphere electrodes dominated the results of the EEG electrodes selected. This is a direct result of the brain activity in those areas as per the GLM via the fMRI results from Chapter 7, where left hemispheric activity was higher as it is associated with temporal pacing.

The purpose in identifying the 4 top ranking electrodes is that the subsequent chapter (Chapter 9) tests and compares the classification rates using a machine learning paradigm to isolate right and left imagined stepping. To avoid using too many predictors, and to keep the number of predictors constant when comparing literature-cited electrodes with those established from the proximity to BOLD responses, data from 4 electrodes was deemed a reasonable number.

Although the methodology outlined in the current chapter was developed and used for the data set for this thesis, it can easily be adjusted and used for other spatial-temporal tasks in which EEG and fMRI are data are collected simultaneously. An advantage of this method is that the outcomes can be generated on a per-subject basis or on a group (average) fMRI activation basis.

Performing this computation on an individual level may lead to unique electrodes selected for use that may or may not be different from the group results.

Often in the presence of epileptic events it is pertinent to find the origin of the seizures in the brain for pre-surgical planning [162]. However, this method is highly erroneous and subject to *a priori* parameters used and manually selected by the user. Therefore, this currently proposed method merges fMRI and EEG so that a weighting schematic for 3D source localization can potentially be improved (Appendix C). This could be followed up by future studies where EEG and fMRI data are collected simultaneously.

The development of the unique paradigm described in this chapter that generates a 3D map integrating EEG electrode and fMRI data of brain activity associated with imagined and executed lower limb movement is included as a novel contribution for co-registering EEG and fMRI in this thesis. It follows a reasoned logic and can be readily adopted by others.

## **8.5 Limitations**

An assumption of this work was that proximity can be calculated using simple Euclidean distance, but given the human brain is highly convoluted this may be an oversimplification.

## **8.6 Future Work**

Further work could be carried out to determine how this weighting approach based on proximity of electrodes to fMRI clusters explains the hemodynamic activity (fMRI) as it correlates with the electrical activity (EEG). A comparison could be made using 3D source localization from EEG, where the signal strength of the electrical activity is used to triangulate the current source via a dipole. Using this paradigm, this normally very ill-defined measure of source localization could

be represented by the number of dipoles as clusters, as well as the expected starting point in the 3D space as informed from the fMRI. The mathematical resolution and degree of overlap in the 3-dimensional areas of activation could be determined.

To address the convolutional nature of the human cortex, using Mahalanobis distances rather than Euclidean distances, may be attempted. To do so would require the extraction of the appropriate data from the structural MRIs. Finally, the normalized weights could be pre-allocated in a machine learning paradigm and thus perhaps work to resolve the initialization of the predictors neuronal weights.

## **8.7 Conclusion**

This is a novel method of co-registering EEG electrodes (electrical activity) with respect to fMRI data (hemodynamic activity). Although only performed for the CGI imagined and executed conditions, this technique could be applied to other EEG-fMRI data sets to determine the likelihood of electrodes picking up on the neural activation associated with hemodynamic activity.

Arriving at the point of being able to link fMRI activity to EEG electrodes for any task has important implications, as it drives the decisions regarding the EEG data that should be investigated for specific tasks in BCI development. In the context of the goals of the current research, using information garnered from lower limb fMRI to guide the most effective data as it is generated via EEG will ensure efficiency in BCI development and use.

The final results for this dissertation are presented in the next chapter. In it, a machine learning paradigm is used to determine how well EEG data can classify left and right stepping.

## CHAPTER 9: THE INTERPRETATION OF BRAIN ACTIVITY USING MACHINE LEARNING

### 9.1 Introduction

The purpose of this chapter is to address hypothesis 4: A pattern identification algorithm can be identified that classifies left and right leg movement based on brain activity patterns from imagined lower limb movement significantly better than chance; this algorithm will be optimized by using fMRI informed EEG. This portion of the study uses machine learning and ties directly into the development of a lower limb Brain-Computer Interface (BCI).

There are several phases associated with the development of a BCI (Figure 9.1). The first is to acquire and accurately interpret brain activity. To do so effectively is contingent on the modality for acquiring brain activity - EEG or fMRI, for example. Up to this point in the dissertation, the focus has been on these data acquisition techniques. The next phase includes the algorithms developed and used to classify subsets of that brain activity. The focus of the present chapter is associated with the development of such algorithms.

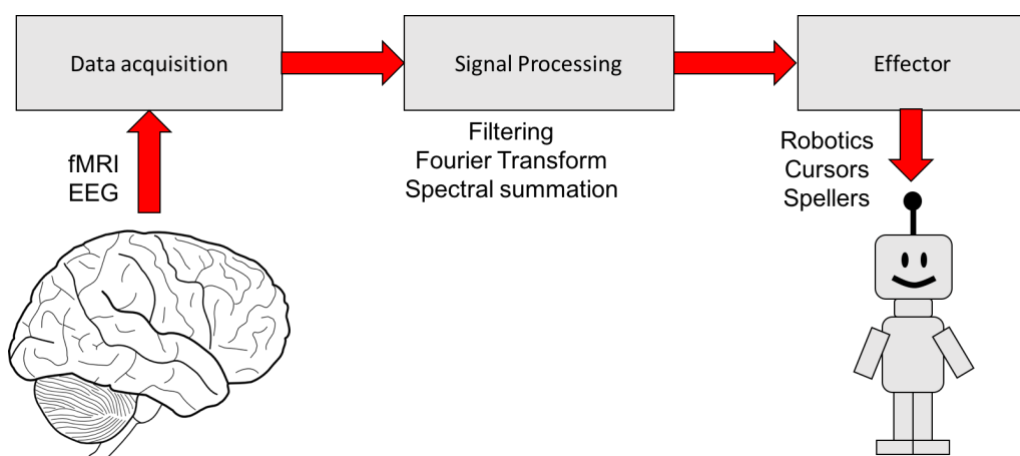


**Figure 9.1 Overview of a Brain-Computer Interface**

The final phase of BCI development is the control mechanism, which involves Boolean logic for controlling external devices such as actuators or cursors [163],[164]. While this last phase of BCI development will not be addressed in the current project, it is a natural extension and will be pursued in future research.

Non-invasive BCIs are used in multiple contexts including, but not limited to: helping individuals interact with social media, assisting individuals with mobility constraints with robotic devices, facilitating product design, and allowing performance of hands free gaming [165]. A recent study has shown it is possible to build a BCI that unlocks a prosthetic knee to allow for increased lower limb mobility [166]. BCIs that have been concerned with isolating imagined motor control (for those with paraplegia and quadriplegia) have centered on hand grasping tasks [167]. Some of these upper limb studies are able to differentiate between right and left hands [168].

This is no small feat, as there is a significant amount of cross talk in the EEG signals seen by electrodes covering the motor cortex. This issue becomes salient via a figure that diagrams a coronal slice of a cortical homunculus (Figure 9.2). It provides a map that shows which areas of sensorimotor cortex are responsible for which areas of the body. What is notable is that there is very little spatial difference between left and right lower limbs, and the lower limbs are more deeply located. Thus, while there is growing knowledge about upper limb left and right movements, BCIs focused on using EEG data for lower limb left and right classification face a unique and difficult challenge as signals arise from areas with very little spatial difference and the signal to noise ratio (SNR) is low. This study extends the extant literature regarding neural activity in the lower limb area by predicting left versus right leg movement from imagined data.

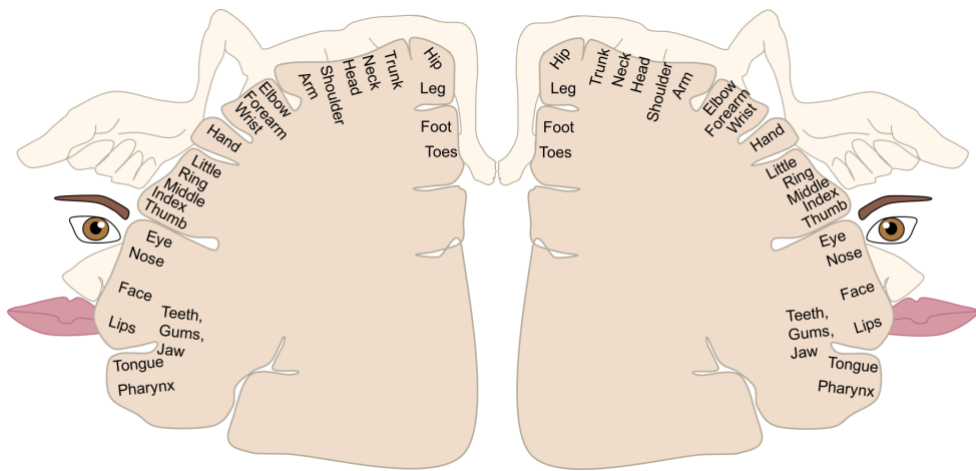


**Figure 9.2 Cortical homunculus (coronal slice), where leg areas occur within the longitudinal fissure of the brain**

The interface between the neurological input and the interpretation of that data for BCI development is the focus of this study and relies on the discipline of machine learning. One aspect of human learning has long been characterized as reinforcement-based, where the knowledge of results is fundamental [169]. That is, actions that are followed by positive outcomes are more likely to be repeated, whereas actions followed by negative outcomes are not [170]. Machine learning operates similarly to this characteristic in that reinforcement is used to train an autonomous system where the reinforcement is based on correct versus incorrect classification [171]. There have been recent machine learning studies that use EEG data for motor/imagery classification. For example, it has been used to: discriminate between rest, imaginary grasp movements, and imaginary elbow movements of the same limb [60]; classify imagined motor movements of the left hand, right hand, foot and tongue [56]; and classify left versus right hand movement [172]. The current study adds to this new and important area of research that can be used to create a lower limb BCI.

Machine Learning is an ever-growing field that encompasses many varied learning methods that were discussed in Chapter 2. Selecting the type of learning methodology to use is not a straightforward task, as it is outcome driven rather than theoretically driven. That is, depending on the idiosyncratic nature of the task and the particular interest of the user, quite different approaches might be taken. One needs to be clear as to what outcome, or outcomes, of the learning protocol is most relevant. Not surprisingly, then the evaluation of machine learning methods is multifaceted [173] and includes outcomes such as predictive accuracy, speed of training necessary, speed of classification, memory usage, and interpretability. For example, a support vector machine (SVM) for a simple binary classification will score well on memory usage, training speed and interpretability. However, if the classification becomes too multifaceted with many interacting variables, predictive accuracy may go down. Conversely, artificial neural networks (ANNs) tend to do well with variables in which interaction effects are present, but their interpretability may be quite low. For the purposes of this dissertation, due to the high number of predictors, the degree of correlation and complexity of the task being predicted, an ANN approach was selected, and classification accuracy was the relevant outcome. ANNs are comprised of an architecture of artificial neurons (ANs). Figure 9.3 shows the similarity between the manner in which biological neurons (BNs) intake, process, and output information and that used by ANs.

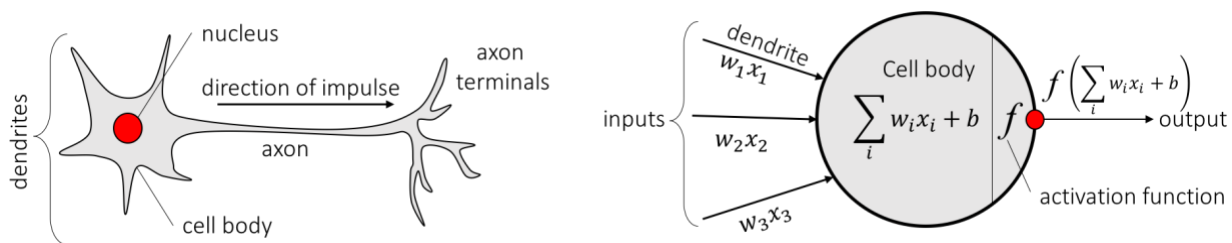


**Figure 9.3 A) Biological neuron (BN) and B) an artificial neuron (AN).**

Both ANs and BNs take input information, evaluate whether its level reaches a threshold, and based on the level reached, decides whether or not to move the information along. BNs exhibit an ‘all or none’ threshold based response for impulse propagation [49]. If the neuron has cumulatively received enough input from surrounding neurons, an action potential will take place and the signal will be passed through that neuron and onto its neighboring downstream neurons. A similar process occurs in ANs. Data provide inputs that are weighted and summed over the inputs, and then fed through an activation function (thresholding function) that determines how much and the character of the signal that is passed on to the next level AN. It is the culmination of the signals across multiple neurons that create both biological neural networks (BNNs) and artificial neural networks (ANNs). An example of an ANN with the data input, flowing through a hidden layer, and culminating in a classification into one of two outcomes is shown in Figure 9.4.

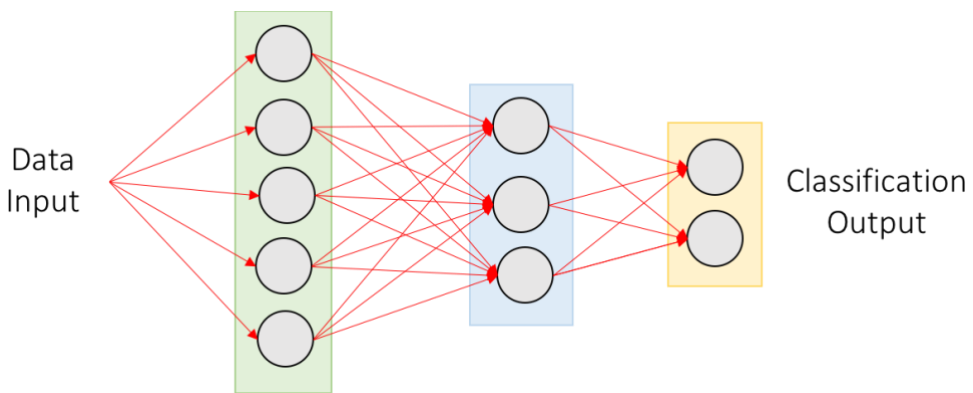


**Figure 9.4 Simple ANN, with 5 input neurons (green layer), 1 hidden layer (blue) and a binary output layer (yellow).**

In a supervised ANN methodology, the number of possible outputs is contingent on how many end-classifications exist. For binary outcomes, the number of classifications would be two. As with BNNs, ANNs are powerful because they are capable of learning. Supervised learning

occurs when the predicted output can be compared to a ground truth (expected output) and thus the degree of error can be determined (expected – predicted). The goal of the ANN is to minimize this error. A system such as this learns by using a weighting scheme adopted in the forward calculation of the output, obtaining the error, and then feeding the error back through the network. This is known as backpropagation (gradient descent optimization). The ANN will then update the weights. This iterative forward and backward calculation occurs over a selected number of training trials (epochs) with the goal of minimizing the error, or cost associated with a non-convex minimization. Thus, an ANN ‘learns’ by updating the weight (slopes) and bias (intercept) terms, which are determined by calculating the partial derivatives of the cost function selected.

This introduction has served as a brief overview of the machine learning process for an ANN. There were two ANNs tested in this study that correspond to the two decision levels of the flowchart presented in Figure 9.5. First was to determine how well the system separated out active or resting brain activity. Because the data were collected in a block design as described in Chapter 5, data for the ‘rest’ condition were acquired during the fixation cross. The data associated with each step (right and left) were grouped together into the ‘active’ brain activity. The second level decision point was the classification between left and right. The next section details the methodology used.

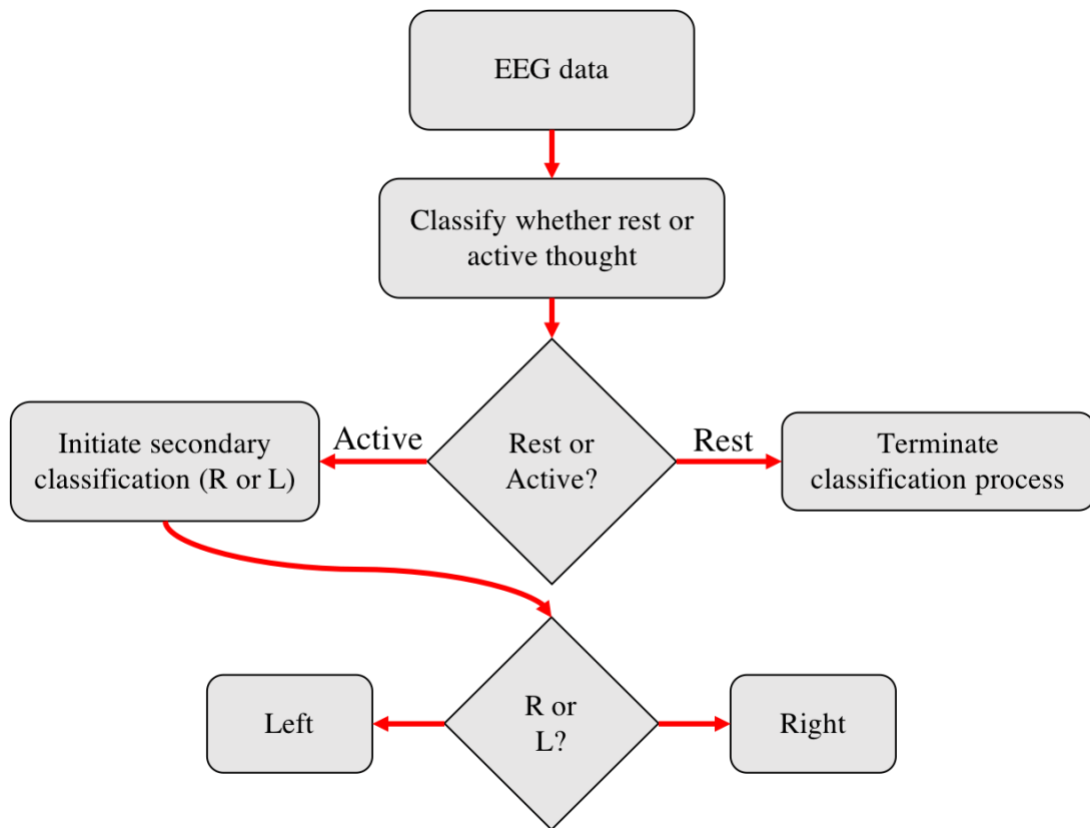


**Figure 9.5 Flow chart for determining right or left lower limb movement using the CGI imagined EEG data.**

## 9.2 Methods

### 9.2.1 Data Set Utilized

Please refer to Chapter 5 for a detailed explanation of data collection and experimental paradigm. Because there was extremely little variance due to trials (see Chapter 6) the data set for this study consisted of the time point 1 and time point 2 EEG data. The alpha, beta and gamma frequencies for each of four electrodes (C1, C2, PO3 and PO4) were selected to use in the machine learning paradigm. C1 and C2, above the sensorimotor cortex, have been shown to be important in lower limb movement [174],[175]. This research project also found significant left-right differentiation using the data from the C1 and C2 electrodes (Chapter 6). In addition to

the motor areas, the visual and parietal areas of the brain were expected to be important in left versus right classification. PO3 and PO4 are in the parietal/occipital areas of the brain and have been shown to be activated in visual tasks [176] and imagery tasks [177] particularly at the gamma frequency [178]. The fMRI data from this research project (Chapter 7) also suggested that these areas of the brain and their corresponding electrodes would be appropriate for use in the machine learning paradigm. It was determined that since each electrode has three frequency bands associated with it, limiting the number of electrodes to 4 for the machine learning process would be appropriate for this research project. This provides information based on 12 input features.

### *9.2.2 Software Program and Activation Function*

The software platform Python was used to generate the ANN, implementing both the Tensorflow (Google Brain Team) and NumPy toolboxes (Community Project). Data were imported into Python and shuffled, where left and right stepping data points were randomized so there were no effects of training order. This was particularly important as the right and left stepping alternated systematically across the time series of data. Thus, the ANN was forced to create a classification that was not contingent on knowing the previous data point, retaining predictor independence.

A sigmoid activation function was implemented for the input layer of the ANN, while the hidden layers used a rectified linear unit (ReLU) activation function, and finally a softmax function was used in the final output layer. This was done to mimic biological neural function more closely. Biological neuron activity is characterized by a leaky integrate and fire (LIF) model [179]. Cortical neurons are rarely at their full saturation, so only as many neurons fire as are needed to carry out a specific task. This means that many of their activations levels remain close to 0 [180],[181]. Thus, biological neurons encode information in a sparse and distributed

way [182]. Following this logic, using a sigmoid function the AN will fire when the function reaches 0.5. This is implausible from a biological standpoint (as this would correspond to half saturation). In addition, this has a negative effect on gradient based optimization [183], [184]. Instead of the more traditional sigmoid activation function, a ReLU function was used for the hidden layer ANs, keeping more of the weights towards 0, unless they were highly excitatory (see Figure 9.6). This models the BN more closely, and this sparse firing leads to mathematical advantages [185]. When information is presented in a sparse format, differentiation becomes easier.

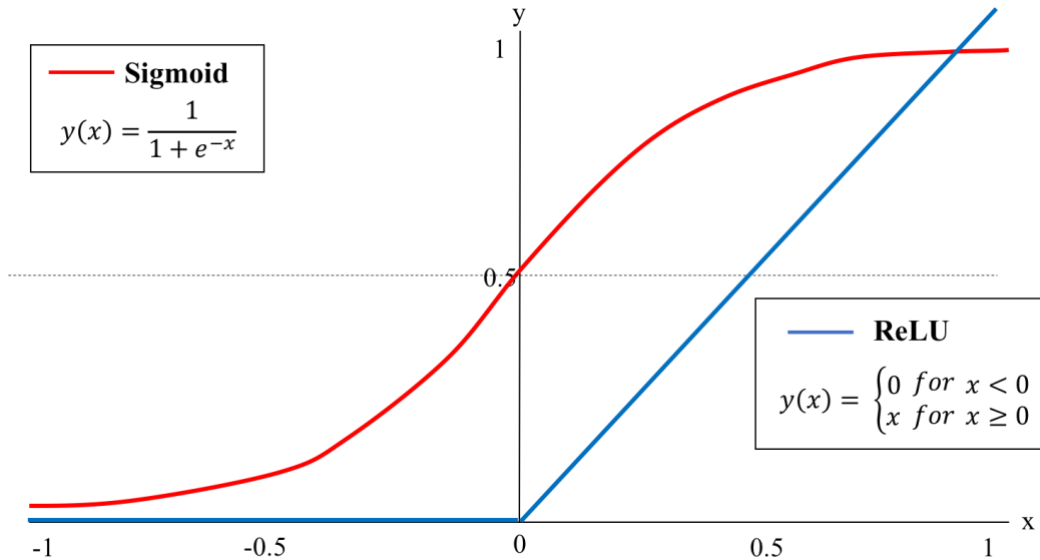


**Figure 9.6 Graphical representation of the sigmoid activation function (red) and ReLU activation function (blue).**

The softmax function is a generalization of the sigmoid function, and can be implemented for a binary classification (or a multiclass classification) at the output layer to bring the output values to be between 0 and 1. In this study it is a probability distribution, with values above 0.5 being more likely to belong to one class and those below 0.5 being more likely to belong to the other class. Error was calculated using the mean square error (MSE) between

predicted and expected values (Eq. 9.1), where  $\hat{y}_i$  is the predicted value and  $y_i$  is the observed value, where  $(i)$  denoted each observed value, and  $(n)$  the number of training epochs used.

$$MSE = \frac{1}{n} \sum_{i=1}^n (y_i - \hat{y}_i)^2 \quad (9.1)$$

Through the backpropagation process, weights and combinatorial rules (e.g., interactions) associated with the ANs change, calculated via partial derivatives of the cost function, to minimize the MSE, and through this process the ANN ‘learns’. If learning is slow, it simply means the derivatives are small. To avoid learning slow down, a cross-entropy function was implemented (Eq. 9.2) where  $C$  is the cost function,  $n$  is the number of training examples (batch size),  $y$  is the desired output, and  $a$  is the output from the neuron.

$$C = -\frac{1}{n} \sum [y \ln a + (1 - y) \ln(1 - a)] \quad (9.2)$$

A cross-entropy function is suitable for this task because it is non-negative and tends toward zero as the neuron gets better at computing the desired output during training. However, unlike the traditional sigmoid (quadratic function) cost function, it avoids learning slow down [186]. Biases (intercepts) are used to shift the activation function in phase.

### 9.2.3 Setting the Architecture and Hyperparameters

Several parameters must be specified prior to analysis for ANN training architectures and the learning algorithms associated with them. For example, neural network machine learning requires the specification of the number of hidden layers, the number of nodes (neurons) on each hidden layer, the number of epochs to train to train through, and the learning rate [187]. These parameters are termed ‘hyperparameters’ and the values they take on have not been formally evaluated [188]. In fact, this issue makes the data analysis procedure for machine learning somewhat arbitrary in that selecting an effective combination of hyperparameter values is

challenging [187]. The main concern with the parameters is to avoid having values that may under fit the data, lowering the classification accuracy, while also avoiding values that over fit the model. While various efforts have been made to automate the selection process (e.g., landmarking, use of values based on prior literature, random search), manual search is still very common and it is suggested that hyperparameters values be selected tried on a small sample data set to eliminate unpromising combinations early on and instead fine-tune more promising ones [187]. This was the approach taken in the current study given the paucity of extant literature in this area to provide more obvious guidance.

The data from one subject, who was randomly selected, was used to determine the most appropriate hyperparameter values. A 3-fold cross-validation was performed, where the participant's left versus right imagined EEG data was run through the network, changing one hyperparameter at a time, to generate the finalized network. Data for all analyses were split into a training set and a holdout (test) set to validate the classification rates. While it was also possible to use the 'leave one out cross-validation' approach (LOOCV), the training/holdout technique was adopted because the LOOCV tends to overfit the data, particularly when the model is complex and the sample size is relatively small [189]. The percent of data used for training varies widely across studies, from 50% [190] to 80% [168], [191] to 90% [177]. There were 120 trials for each right and left leg imagined movement per participant. The data were split into an 80% training set comprised of 96 training examples, and the 20% test set comprised of 24 examples for each leg, for each participant. Since the data were randomized when they were imported into the machine learning program, the 80%/20% split was always random.

The number of neurons for the input, output, and hidden layers as well as the number of hidden layers form the architecture of the ANN. Given that there were 12 input features, the

number of neurons at the input layer is set at 13 (number of input features plus one for the constant). The output layer was set to the number of classes (in this case 2). Simple machine learning examples are common in the literature, but classification systems for motor imagery tasks using EEG are not. However, one that used extreme machine learning utilized four hidden layers [192]. Multiple hidden layers allows for non-linear combinations of the data [193]. It was anticipated that the machine learning model for this research would be somewhat complex, and thus required more than a single hidden layer.

The number of neurons (sometimes called nodes) within the hidden layers were selected based on some rules of thumb [194]: 1) 2/3 the size of the input layer, plus the size of the output layer ( $2/3$  of 13 + 2 = 10.7); 2) less than twice of the number of neurons in input layer (less than 26); 3) between the input layer size and the output layer size. Since it is appropriate to have the same number of neurons in each hidden layer [195], each of them had 10 neurons in the initial architecture. Thus, the initial network consisted of 13 input neurons, 3 hidden layers (with 10 neurons in each), and 1 output layer with 2 neurons, using a learning rate of 0.03 [188], with 1000 epochs.

The learning rate in machine learning controls the magnitude of the adjustments of the weights as the iterations occur. Large learning rates are on the order of 0.1, while others can be extremely small (e.g., .0001). The larger the learning rate, the faster the learning, (i.e., the slopes change faster), but the most optimal weighting might be missed. The smaller the learning rate, the slower the learning, which can be time consuming. Keeping the network the same, the learning rate was altered beginning at 0.03, and reducing it by 0.01 at a time. In this study an optimal learning rate was identified as being .03. Smaller values (.02 and .01) provided a poorer and poorer fit (Table 9.1).

**Table 9.1 Effect of learning rate on training accuracy**

Learning rate ( $\eta$ )	Training set accuracy (%)
<b>0.03</b>	<b><math>86.5 \pm 5.1</math></b>
0.02	$78.8 \pm 1.4$
0.01	$71.6 \pm 4.6$

Therefore, the learning rate was kept at 0.03, while the other hyperparameters were adjusted. As mentioned, 3 hidden layers were initially utilized. Stepping down to 2 hidden layers provided a better fit but only 1 hidden layer provided a poorer fit (see Table 9.2). Therefore, the network was adjusted to have 2 hidden layers instead of the initial 3.

**Table 9.2 Effect of number of hidden layers on training accuracy**

Number of hidden layers	Training set accuracy (%)
1	$84.6 \pm 7.8$
<b>2</b>	<b><math>89.4 \pm 1.2</math></b>
3	$86.5 \pm 5.1$

To simplify the model for computation efficiency, the use of 10 neurons per hidden layer was driven down to 8 hidden neurons. This provided a marked improvement so it was simplified again to 6 hidden neurons, but this provided a poorer fit. Therefore, it was determined that eight neurons, gave the best accuracy (Table 9.3).

**Table 9.3 Effect of number of neurons in each hidden layer on training accuracy**

Number of hidden neurons	Training set accuracy
10	$89.4 \pm 1.2$
<b>8</b>	<b><math>93.4 \pm 2.6</math></b>
6	$88.2 \pm 3.4$

Lastly, the number of epochs also was set. One epoch indicates the number of full training cycles (one forward and one backward pass) on the training set. Given the large model,

1000 epochs were used initially and provided a good fit. Decreasing the epochs to 750 and 500 showed a decrease in fit. At about ~950 there was a plateau in the fit. Thus, 1000 epochs was settled on as the most useful hyperparameter for this study (Table 9.4). The final ANN architecture that was used in the analyses is shown in Figure 9.7.

**Table 9.4 Effect of number of training epochs on training accuracy**

Number of training epochs	Training set accuracy
<b>1000</b>	<b><math>93.4 \pm 2.6</math></b>
750	$93.3 \pm 2.4$
500	$83.3 \pm 4.2$

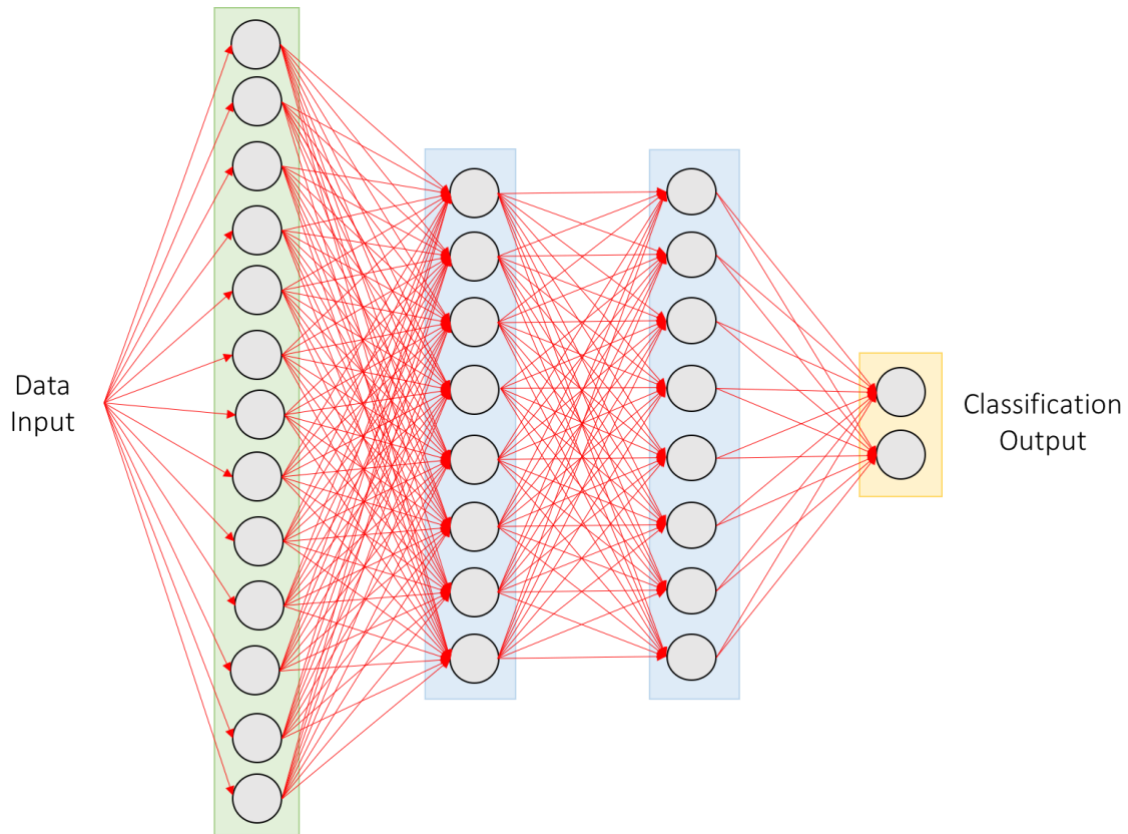


**Figure 9.7 Final network architecture, with input neurons in green, hidden layers in blue, and output layer in yellow.**

#### 9.2.4 Analysis Process

First the analyses were conducted for the active versus rest decision point in the flowchart. The data from the entire group of 16 individuals were analyzed together using the EEG predictors with the outcome of “rest” (baseline, at the fixation cross) versus “activation” (both left and right EEG data). As was determined in the repeatability study (Chapter 6), the largest source of main effect variance was due to the variation between participants (~15-25%). Therefore, it was decided to test the viability of the ANN using individually-trained data and compare the results to the grouped data. A similar approach was used to assess the left versus right classification. The analysis was conducted first at the group level, and then at the individual level. Figure 9.8 shows an example of training graphs for the group and for an individual, where hyperparameters were kept constant.

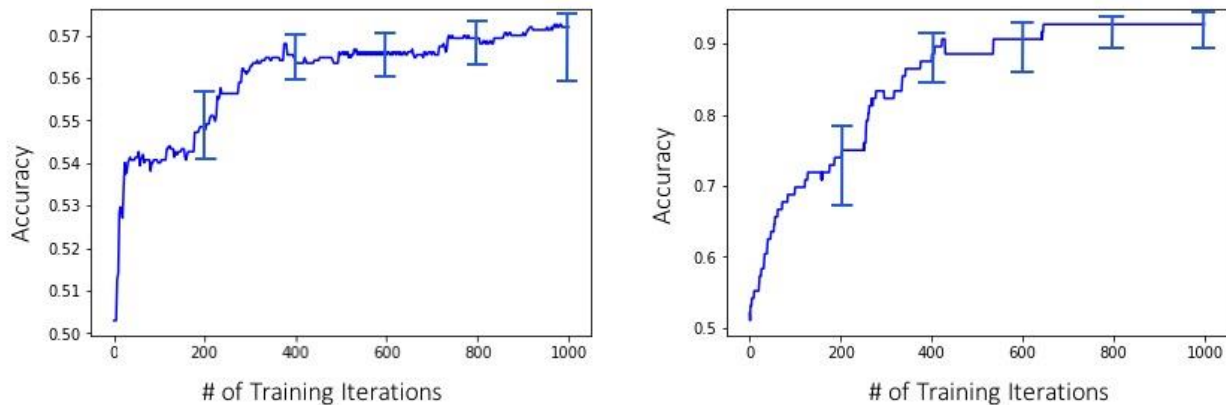


**Figure 9.8 An example of group training (left) and individual training (right) where accuracy is plotted against the number of training iterations for differentiating right and left imagined stepping from electrodes C1, C2, PO3, PO4.**

To assess if the classification accuracies for right versus left imagined stepping data from the electrodes that were selected based on prior EEG research (C1, C2, PO3, PO4) were different than those using an fMRI informed selection of alternative electrodes, both sets of data were

tested on the same network. Four electrodes were selected to maintain the same number of electrodes and architecture. Several options existed as to which four electrodes to select, based on various ways to conceptualize what might be most relevant. For the purposes of this thesis, the ones with the highest calculated proximity values summed across all clusters using the process outlined in Chapter 8 was used. This approach was taken as a reasonable first step, as it was assumed that these electrodes would be likely to carry the most information. It resulted in electrodes FC1, FCZ, FC3, FC5 being selected. Other options for selection of input features do exist and will be discussed later in this document.

Chi-square ( $\chi^2$ ) tests were used to assess classification accuracy significance and are based on the number of classification trials in the testing runs. For the active/passive test runs there were 1536 testing classification trials (48 active and 48 rest for each of 16 participants) and for the left/right test runs there were 768 testing classification trials (24 left and 24 right for each of 16 participants). Chi-square ( $\chi^2$ ) tests were also used to assess classification accuracy differences.

### **9.3 Results**

#### *9.3.1 Classification Accuracy of Test Trials*

The first set of analyses use the data from electrodes C1, C2, PO3, and PO4. The classification results of the group-level analysis for the ‘rest’ versus ‘active’ are presented in Table 9.5. The overall weighted correct classification average for this analysis was 71.35% (average of binary classifications) and is significantly better than chance ( $\chi^2=280$ ,  $p<.0001$ ), where the range of values is listed next to the classification rates.

**Table 9.5 Confusion matrix for group classification of active thought versus rest thought using electrodes C1, C2, PO3, and PO4.**

Confusion Matrix	True Rest (%)	True Active (%)
Predicted Rest (%)	<b>70.4 ± 8.2 (n=541)</b>	27.7 ± 7.6 (n=213)
Predicted Active (%)	29.6 ± 8.2 (n=227)	<b>72.3 ± 7.6 (n=555)</b>

The classification results of the aggregated individual-level analyses for the ‘rest’ versus ‘active’ are presented in Table 9.6. The overall weighted correct classification average for this analysis was 97.65% and is significantly better than chance ( $\chi^2=1396, p<.0001$ ). The individually-trained overall average correct classification was significantly better than that of the group-trained by 26.29% ( $\chi^2=376, p<0001$ ).

**Table 9.6 Confusion matrix for active thought versus rest thought using electrodes C1, C2, PO3, and PO4 performed within participants, and averaged across all 16 participants where each person’s data was trained individually.**

Confusion Matrix	True Rest (%)	True Active (%)
Predicted Rest (%)	<b>97.1 ± 1.3 (n=746)</b>	1.8 ± 0.5 (n=14)
Predicted Active (%)	2.9 ± 1.3 (n=22)	<b>98.2 ± 0.5 (n=754)</b>

The classification results of the group-level analysis for the ‘left’ versus ‘right’ are presented in Table 9.7. The overall weighted correct classification average for this analysis was 49.32% and is no different from chance ( $\chi^2=.13, p=.72$ ).

**Table 9.7 Confusion matrix for group classification for imagined left and imagined right stepping using electrodes C1, C2, PO3, and PO4.**

Confusion Matrix	True Left (%)	True Right (%)
Predicted Left (%)	<b>50.4 ± 2.1 (n=194)</b>	51.8 ± 1.8 (n=199)
Predicted Right (%)	49.6 ± 2.1 (n=190)	<b>48.2 ± 1.8 (n=185)</b>

The classification results of the aggregated individual-level analyses for the ‘left’ versus ‘right’ are presented in Table 9.8. The overall weighted correct classification average for this analysis

was 88.16%, is significantly better than chance ( $\chi^2=444$ ,  $p<.0001$ ), and is about 39% better than that using the group trained data.

**Table 9.8 Confusion matrix for individual classification for imagined left and imagined right stepping using electrodes C1, C2, PO3, and PO4 performed within participants, and averaged across all 16 participants where each person's data was trained individually**

Confusion Matrix	True Left (%)	True Right (%)
Predicted Left (%)	<b>87.1 ± 5.6 (n=334)</b>	16.9 ± 4.7 (n=42)
Predicted Right (%)	12.9 ± 5.6 (n=50)	<b>89.2 ± 4.7 (n=342)</b>

Given the low level of classification at the group level, the analyses from the electrodes using the fMRI informed EEG were only conducted at the individual-level. Tables 9.9 and 9.10 show the classification results using data from the FC1, FCZ, FC3, and F5 electrodes for the active/rest and left/right, respectively. The overall weighted correct classification average for the active/rest runs was 96.75% and is significantly better than chance ( $\chi^2=1343$ ,  $p<.0001$ ). In comparison to the active/rest overall classification accuracy using the information from the C1, C2, PO3 and PO4 electrodes (97.65%), there was no difference ( $\chi^2=2.22$ ,  $p=.14$ ).

**Table 9.9 Confusion matrix for fMRI informed EEG selected electrodes (FC1, FCZ, FC3, F5) for active thought versus rest thought performed within participants, and averaged across all 16 participants where each person's data was trained individually.**

Confusion Matrix	True Active (%)	True Rest (%)
Predicted Active (%)	<b>96.4 ± 3.6 (n=740)</b>	2.9 ± 2.5 (n=22)
Predicted Rest (%)	3.4 ± 3.6 (n=28)	<b>97.1 ± 2.5 (n=746)</b>

The overall weighted correct classification average for the left/right analysis was 79.79% and is significantly better than chance ( $\chi^2=276$ ,  $p<.0001$ ). However, contrary to expectations, it was significantly lower in comparison to the left/right overall classification accuracy using the information from the C1, C2, PO3 and PO4 electrodes, which was 88.16% ( $\chi^2=16.9$ ,  $p<.0001$ ).

**Table 9.10 Confusion matrix for fMRI informed EEG selected electrodes (FC1, FCZ, FC3, FC5) for imagined left and imagined right stepping performed within participants, and averaged across all 16 participants where each person's data was trained individually.**

Confusion Matrix	Predicted Left (%)	Predicted Right (%)
True Left (%)	<b>78.7 ± 7.1 (n=302)</b>	18.8 ± 3.6 (n=72)
True Right (%)	21.3 ± 7.1 (n=82)	<b>81.2 ± 3.6 (n=312)</b>

### 9.3.2 Classification Accuracy of Training Trials

The highest accuracy for any individual was 95.8% during the training trials for differentiating ‘right’ compared to ‘left’ using data from C1, C2, PO3, and PO4 electrodes. Given that this is a binary classifier for imagined left versus right lower limb movement, this is an excellent level of classification. For the same number of predictors, the group level analysis was a much poorer predictor a classification accuracy of 57.4% during the training to differentiate ‘right’ from ‘left’ using the data from the C1, C2, PO3, and PO4 electrodes. The holdout classification values (testing classifications) were somewhat lower, which was expected, given that the training trial values capitalize on the error variance of the data.

### 9.3.3 Additional Analyses

Given that the fMRI selected electrodes did not outperform those selected by the literature, *post-hoc* analyses were performed to ascertain the most effective electrodes in classifying left versus right movement. This was done in the Python environment using Tensorflow and the ReliefF toolboxes. Implementing a relief algorithm capable of identifying feature importance in a set of training data was conducted using a set of 192 predictors (64 electrodes, each with alpha, beta and gamma as separate predictors). The data were first split to create a randomized test set (80%) of the total number of trials across participants. Next, a feature importance scoring system was

calculated based on the test data set and the labels (right and left) associated with these trials. This algorithm was run three separate times to generate a mean and standard deviation within the tests and to keep analyses consistent, the top four predictors were identified. They are presented in Table 9.11 in descending order of importance (left to right) with the electrode and the associated frequency band. Most predictors selected were a combination of EEG literature selected electrodes and fMRI informed EEG selected electrodes (PO3, PO4, FC5, FCZ, FC1).

**Table 9.11 Top Four Predictors selected for BCI use by ReliefF algorithm from 192 predictors**

Trial Number	Predictor 1 Selected	Predictor 2 Selected	Predictor 3 Selected	Predictor 4 Selected
1	FCZ gamma	FC5 beta	PO3 beta	P7 beta
2	FCZ gamma	FC1 gamma	FC5 beta	C1 alpha
3	PO4 beta	FC5 beta	PO3 beta	FC1 gamma

#### 9.4 Discussion

The findings of the machine learning studies partially supported Hypothesis 4: A pattern identification algorithm can be identified that classifies left and right leg movement based on brain activity patterns from imagined lower limb movement significantly better than chance; this algorithm will be optimized by using fMRI informed EEG. The EEG alpha, beta and gamma frequency data from the C1, C2, PO3 and PO4 electrodes were able to effectively classify active versus rest (98%) activation of the lower limb as well as well as left versus right (88%) imagined movement. This classification accuracy compares favorably with other attempts to use EEG for BCI development that differentiates left/right imagined hand movements 70% [172], 86% [56]. Given that these rates are for upper limb movements, the 88% correct classification for lower limb obtained here rates as quite good.

Interestingly, while this high classification accuracy was observed for the individually-trained data, it was not similar for the group-level trained data analysis. At the group level these classifications were reduced to 71% for active/rest and 49% for left/right. These results suggest that while a network may be trained on group level data and refined for an individual user, it may be more effective to simply train the network on a per-subject basis to start with. This conclusion would be consistent with the findings from Chapter 6 that indicated 20-25% of the variance of the EEG data at the C1 and C2 electrodes was ascribed to participants, while it remained relatively consistent across time points and trials. This finding of individual variability is consistent with that of a study of three individuals classifying different types of imagined motor activity [56]. The researchers found that overall classification accuracy of the grouped data was much lower (71%) than the individually-trained accuracy rates (88%).

There was no significant difference in the classification accuracy using electrodes suggested by the fMRI informed EEG process conducted at the individual level for active versus rest (97%). However, while the overall classification accuracy using electrodes suggested by the fMRI informed EEG process for left/right was significantly different from chance and quite high (80%), this value represents a significant decrease in comparison to the left/right classification accuracy using the data from the C1, C2, PO3 and PO4 electrodes. While a variety of predictors could have been tested, those suggested by the highest average proximity weights across clusters from Chapter 8 (FC1, FCZ, FC3, FC5) were selected. These provided a similarly accurate classification for the active/rest categories, but a less accurate prediction of right versus left imagined stepping for the same number of predictors, when compared to electrodes that had been suggested by the extant literature, including findings from the present research project, used when studying imagined locomotion with EEG (C1, C2). Given that the electrodes suggested

with the fMRI informed EEG were all in the frontal cortex, these results are not surprising. The large number of voxels associated with cluster 7 (Chapter 7) as well as the short distance between those voxels and the scalp, would render them most likely to be activated during this task. However, as has been suggested in a review of BCI development research, many cortical areas participate in motor imagery control along with subcortical, brainstem and spinal cord circuits [196]. It is argued that BCI effectiveness can be improved by recording signals from multiple cortical areas and using the most appropriate algorithms to combine them for movement control. The current research substantiates these claims.

From the *post-hoc* analyses performed, it can be seen that the most important features as selected by the ReliefF algorithm were actually a combination of fMRI-based and literature-selected electrodes. This suggests that not all the predictors (i.e., all frequency bands) used in the fMRI-based and literature-selected analyses were necessarily important in the prediction of right and left stepping. These additional nuisance predictors could have been driving the predictive accuracy down. It also argues for adopting an approach that capitalizes on the interplay between theory and empirical data analyses in BCI development where fMRI informed EEG and literature information are taken in conjunction with new machine learning tools such as the ReliefF algorithm are used.

## 9.5 Limitations

While neural networks offer a robust and integrative method of interpreting predictors for the purposes of classification, they are costly both from a computational memory usage standpoint as well as a temporal one. Neural networks are also inherently ‘black—box’ in their reproducibility and transparency to both users and those who implement them.

The lack of support for improvement in classification using the 4 fMRI informed EEG electrodes does not lead to the conclusion that the fMRI-EEG co-registration procedure did not yield any advantages. The possible combinations and number of input features was extremely large, and the selection of different electrodes might very well have lead to different outcomes. This will be discussed further in future research.

## 9.6 Future Work

Continuing this BCI work would mean moving this network to a real-time situation. This is a reason to keep the number of predictors to a low enough level to classify appropriately without introducing unnecessary computational complexity. This would be done to allow the processing lag from data acquisition, to data processing, to control mechanism to be as short as possible. To be useful BCIs need to make few errors and provide commands quickly. BCIs using steady-state visually evoked potentials operate at an acceptable performance level with an 80% classification rate (using 4 classes) and can provide a new command every 200 ms [197]. However, the paucity of current research does not allow for such a level of responsiveness for lower limb robotic systems, with a recent review [198] reporting several-second delays, that they term a challenge that “*...should not be neglected*”. An acceptable level of performance for stepping would allow for normal walking to occur (100 steps/min).

An alternative way to approach the selection of input features would be to select the frequency data from a single electrode (and perhaps only at one frequency), then add features one at a time, modifying the ANN architecture as needed. The FFT process would be extremely time-consuming, and should use as small a window as possible to extract reliable feature data.

Data were randomized in their order of right and left to try to isolate for independence of order effects, however, as walking occurs in an alternation of right and left, a feedback system could be incorporated to aid in the classification of the next step. This may increase the accuracy of the overall network.

In addition, hyperparameters were adjusted one at a time, however a more fulsome approach may have been to use a genetic algorithm in order to account for how changing one hyperparameter affects others. This could be followed up on to see how it compares to the finalized network presented here.

Another area of future research would be to utilize the fMRI information to assist in electrode selection differently than was used in the current study. Part of the problem in selecting the electrodes arose due to the slow response time for the BOLD activity. It was not possible with the methodological paradigm used, to separate left from right movement with the fMRI outcomes. This was evident in the high classification accuracy at the rest/active decision point while there was a substantial decrease in classification accuracy at the left/right decision point using the electrodes suggested by the overall proximity data. A more in-depth analysis of the fMRI data that would allow for the left/right separation might shed some light on this issue and provide guidance for future work.

Another approach would be to use electrodes close to the clusters that were associated most highly with the differences between executed and imagined brain activity. It is also possible to differentially weight the various input features, which also might have an effect on the outcome. These are just a few of the possible ways to explore this rich data set in such ways that would contribute to determining the most effective and efficient input parameters for machine learning.

At a broader machine-learning level, the field is relatively new and its followers come from many different disciplines to utilize its functions. This has posed some research issues for the machine learning developers. As was noted earlier, hyperparameter specifications must be carried out in advance of the analysis. It is an area of current research [188], [199], [200], but needs refinement for the process to become more streamlined and clarified. In addition, as researchers publish in their area of expertise, indicating their hyperparameter values will help others to utilize that extant literature in the future.

Another issue in need of more research is that of interpretation. For example, the machine learning architecture specified in the machine learning model had two hidden layers. Most quantitative data classification problems can be solved with one or two hidden layers [195]. Deep learning typically uses more than two hidden layers and is more useful with data sets with multiple dimensions such as speech recognition [201] or image analysis [186]. As the data analysis moves forward through the hierarchy of hidden layers, it becomes more complex with non-linear transformations of the data [193]. Once the classification problem is solved, there is no standard method to visualize the weights to enhance the interpretability of the findings [193] – thus what occurs within the analysis remains largely a ‘black-box’. There are efforts underway to improve on this [193],[202], but it remains an area in need of research.

This leads to the final research issue and that is the importance of theory. Machine learning is excellent at mining large sets of data, handling numerous predictors, and combining them in ways that enhance decision-making. As such, it has tremendous potential to assist in health-related activities including prognosis estimation, image interpretation, and diagnostic accuracy [203]. However, it does not deal with issues of causality and understanding. It takes years before replicable findings using similar sets of data are published to fully understand an

area of research interest. In its usual plodding fashion, study by study, science will be able to not only predict, but to understand phenomena. It is in this manner that BCI development for lower limbs will most effectively move forward.

## **9.7 Conclusions**

Despite the inherent difficulties in building a BCI for isolating right versus left imagined locomotion tasks due to the location of motor cortex dedicated to lower limb movement, and thus the lack of spatial separation of signals within the EEG, the current study showed excellent left versus right classification using an ANN machine learning model. This study contributes to this extant literature, because much of work in this area has used SVM [172],[56],[60] rather than an NN approach. The present study showed that reliable, selected EEG imagined data applied to a network can be trained effectively to classify left and right lower limb movement using individual-level data. As this is the starting point for BCI development, these findings are both interesting and important for future research.

# **CHAPTER 10: REVIEW OF FINDINGS, SIGNIFICANCE, LIMITATIONS, FUTURE WORK, AND CONCLUSION**

## **10.1. Introduction**

This chapter summarizes the research associated with this project. It includes a reiteration of the pilot work involved in setting up the formal study, a review of the hypotheses and the level of support found for them, limitations of the research, significance of the findings, finally future research directions, and concluding statements.

There were two primary goals of this research program. One was to determine the similarities and differences between cortical activity associated with executed and imagined left and right lower limb movement, while observing two different visual stimuli, using the two technologies of EEG and fMRI. Achieving this goal has contributed to a better understanding of the spatial and temporal neural activity involved in imagined and executed stepping movements. The second goal was to use these data to predict left versus right lower limb movement in a machine learning context. Meeting this goal provides useful information that will assist in the development of a BCI that controls lower limb movement.

## **10.2 Pilot Work**

Studying lower limb movement using EEG and fMRI posed some unique and immediate methodological challenges that were handled in the pilot work of this study. Specifically, two issues were addressed. The first was to determine whether or not supine-generated lower limb movement was an appropriate methodology to utilize when studying this phenomenon. The results demonstrated that the kinematics of supine-generated knee flexion/extension mimic those of normal stepping, and thus gathering such data in a MR scanner would provide useful

information regarding lower limb movement. It was also revealed that head movement with respect to the trunk is potentially a large source of error. This finding indicated a need for an intervention that would control this movement when gathering fMRI data. Thus, a second task of the pilot work was to design a device that would allow the data to be captured appropriately within the confines and unique environment of the MR scanner. The Locomotion Apparatus for Magnetic Resonance Imaging (LAMRI) was created that allowed for controlled lower leg movement at the hip, knee and ankle while the participant was in the MR scanner. The LAMRI design also simulates gravity, provides a time-stamp for the left and right leg movements, keeps head motion to a minimum, is lightweight, and relatively inexpensive.

### **10.3 Support for Hypotheses**

Following the pilot work, the study proper was conducted. It entailed collecting data at three time points for 16 participants. EEG data were collected at time points 1 and 2, and EEG and fMRI data were collected at time point 3. Each time point was separated by about two weeks.

Hypothesis 1, that EEG data is able to distinguish left from right leg movements in both imagined and executed conditions, and that the effect was expected to be particularly strong in the CGI conditions was supported, as it was less neutral than the blue-green condition, meaning the CGI stimulus should be used for training over the blue-green one as it is a more robust predictor. The C1 and C2 electrodes were selected due to their representation of the leg areas of sensorimotor cortex, and their utility in being able to separate left from right movement is consistent with findings that these electrodes have been linked to the lower limb motion of pedaling [174]. In the imagined CGI condition, significantly higher levels of depolarization for the left lower limb relative to the right, were observed for the alpha, beta and gamma frequencies at the C1 electrode, and at the alpha and beta frequencies at the C2 electrode.

It was also found that the reliability coefficients of the CGI data were higher than in the BG conditions; particularly for the imagined CGI condition. These findings contributed to the decision to use the EEG data from the CGI imagined condition for use in machine learning, where in a supposed BCI, a person could interface with something like *Google Glass* (Google Inc., MountainView, California, U.S.).

Hypothesis 2 that fMRI data will allow for the identification of areas of the brain that are activated during lower limb movement was supported. The executed task findings from the current study are consistent with those that have used fMRI to examine lower limb motion [14]; [17], which found that many areas of the brain, most prominently those associated with sensorimotor activity, were activated. Like other imagined motor activity studies, the findings from this study showed that the occipital and parietal areas of the brain are also activated [25],[73]. This study found that while there were similarities across the experimental conditions in that the sensorimotor areas were always activated, differences between the conditions were also observed. These are briefly described next.

During the CGI and blue-green executed movement conditions, activation occurred primarily in the motor execution and control areas. Activation was highest in the CGI and blue-green imagined conditions in areas associated with movement control, inhibition of movement, integration of sensory input and motor output.

The CGI executed task showed more activation in movement execution relative to the CGI imagined task, as did the blue-green executed task relative to the blue-green imagined task. The CGI and blue-green imagined tasks relative to the CGI and blue-green executed tasks showed more activation in movement control and integration, visual areas, and emotional control of movement.

The differences for the CGI and blue-green executed and imagined tasks were primarily in the activation of different visual areas. The CGI relative to the blue-green activated areas were associated with object recognition while the blue-green showed basic visual processing activation.

Hypothesis 3 stated that it would be possible to develop a computational approach to accurately map spatial brain activity (fMRI) in relation to temporal receptors (EEG electrodes) associated with lower limb movement. This hypothesis was supported. A novel approach was used to co-register the 64 EEG electrodes with respect to the fMRI data and then determine the magnitude of the linkages between clusters of activated voxels and each electrode. While some attempts to link EEG to fMRI data have been successful, these have been focused on identifying both the spatial and temporal location of neural activity for auditory tasks [84], visual tasks [78],[89], cognitive tasks [83],[87],[204],[205], epileptic events [82], and hand motions [13],[206],[207], rather than utilizing the information gained to develop more efficient inputs to BCI development.

Data from the CGI imagined and executed conditions were used to demonstrate the process. Results tabulated the linkages (ranging from 0 – 1, with 1 being the highest) between voxel clusters and electrodes. It was anticipated that using this electrode linkage information would improve the effectiveness of a machine learning algorithm to isolate right and left stepping.

Hypothesis 4, that a pattern identification algorithm can be identified (using fMRI informed EEG) that classifies left versus right lower limb movement significantly above chance based on neural activity patterns from imagined lower limb movement, was supported. Training predictions between right and left stepping were >90% and the validation testing of this was

>85%. However, the information from the electrode linkage provided by the fMRI informed EEG process did not improve accuracy.

#### **10.4 Limitations**

Several limitations of this research were noted throughout the document. This section reiterates the most salient of them. First, data for the pilot work as well as the study proper were based on participants who were male, young, and healthy. The reason for doing so was that only a relatively small sample was possible, given the resource intensity of the project. By methodologically controlling some of the possible data variation due to demographic differences, the internal validity of the data was ensured. This, of course, comes at the expense of generalizing the findings; however, as has been noted, the demographic group for which lower limb BCI development might be of most use is that of young males [112], [138].

Second, all data were collected while participants were in a supine position. Upright walking does include tasks other than joint motion and flexing/extending of the lower limbs. However, due to the constraints of the MR scanner, participants were required to be in a supine position. To ensure comparability between the EEG and fMRI data, as well as providing training for the fMRI data collection point, participants engaged in the EEG-only data collection points also in supine position.

Third, the frequency that the participants were presented with the stimulus (50 steps/min) was about half the frequency of normal walking. This was done to allow for differentiation of right versus left stepping, and decrease movement in the MR scanner.

Not all available features from EEG were tested for the machine learning classifier. There exist electrodes with their associated frequency bands that went unanalyzed and untried in the development of this classifier. As well as the generation of new measurements from a cohort of

signal processing tools could have been used, but for computation simplicity it was decided to stick with spectral information, as this is how EEG is most often reported with regards to its power within particular frequency bands associated with particular tasks (sleeping, active thought, eyes closed etc.). Alternative ways to utilize the fMRI informed EEG linkage process were not explored in this particular study and will provide ample opportunity for future research.

All of the limitations that have been cited provide opportunities for future research directions that will be taken up shortly.

## **10.5 Significance**

Despite the limitations noted, this research has provided a number of significant findings for research in the area of lower limb movement. First, it was demonstrated that it is a reasonable approach to study lower limb movement while subjects are in a supine position because the kinematic signatures of supine versus upright lower limb motion are similar. Because it is not possible to study lower limb movement using fMRI technology unless participants are in a supine position or the scanner is oriented vertically, this assumption needed to be verified. Second, a lightweight, low-cost device, the LAMRI, was developed for use in the MR scanner. The design allows for the simulation of gravity for lower limb multi-joint motion, provides a time-stamp for the movement, and ensures minimal head movement. All of these characteristics enhance the possibility of collecting lower limb movement data using fMRI in the future using the LAMRI, which has been a barrier up to this point.

The findings that left versus right lower limb movement can be isolated utilizing the alpha, beta, and gamma frequencies at electrodes C1 and C2 are of particular import in that while EEG had been used to study lower limb movements, the detection of left versus right differences had not to this point been achieved. The fact that the effects were most robust for the imagined

condition is important insofar as the detection of left versus right movement is needed to build a BCI that will hold promise in assisting those with lower limb mobility issues.

It was demonstrated that using the LAMRI, lower limb movement that simulates executed walking as well as imagined walking can effectively be collected using fMRI technology. Areas of the brain that were anticipated to be activated across conditions (i.e., sensorimotor), were, indeed activated. Executed conditions activated areas of motor movement, while more of the visual and cognitive areas were activated during the imagined conditions.

The unique paradigm developed to generate a spatial map of brain activity associated with imagined walking and its weighted linkages to EEG electrodes can be used in BCI development. The process outlined can be easily followed and used in a variety of contexts other than that in the current study.

While some brain-computer interfaces utilize fMRI as a data acquisition tool may not be optimal from both logistic and financial points of view as MRI is expensive to acquire and the hardware is not portable. In addition the temporal resolution is so poor from an HRF, that lag time for a control mechanism would be on the order of (>10 seconds). However this is beneficial for the future of BCI development as they can be developed and implemented more cheaply using an fMRI informed EEG data to supplement information acquired with EEG.

This thesis also highlights the importance of training a BCI on an individual basis. Accuracy rates were nearly 40% different between group and individual level training for isolating right and left imagined brain activity.

## **10.6 Future Work – Based on Collected Data**

Several research projects present themselves that extend the findings of the current study. More EEG features that might distinguish these activations, such as wavelet spectrums, and

topographical activation intensity maps could be used to differential left/right stepping. These new features may or may not be beneficial to the assessed classification process.

Second would be to extend the BCI development process to include the use of an end device. That is, to extend the BCI model in creating a feed forward algorithm that would be able to mobilize a robotic device that uses left and right stepping to engage in forward motion. This process has actually started. A proof of concept bipedal robot (ROBBi) has been designed and testing has begun on completing this algorithm as an off-line brain-computer interface.

Another is to possibly analyze the EEG data collected simultaneously with the fMRI data at time 3. Doing so might allow for the differentiation of left and right stepping. This would require a multi-modal data fusion methodology. The various methodologies that have been proposed strongly differ on the basis of their physiological assumptions, the type of prior information required, and exactly how to treat various ICAs [77]. The complexity and newness of the analytic protocols suggest that to actually conduct this research would be a lengthy process.

The integration of the fMRI and EEG electrodes data into a 3D image, and the assessment of their linkages was carried out for only the CGI data. This was done as it is the most relevant for BCI development. However, it would be interesting to subject the data from the other conditions from this study to a similar process, examining similarities and differences regarding the linkage patterns.

Finally, another study could use an EEG informed fMRI approach to integrate the data (i.e, predicting fMRI activation after training based on solely EEG information). The weighting approach described in the current research relates the expected hemodynamic activity (fMRI) associated with electrical activity (EEG). The signal strength of the electrical activity can currently be used to triangulate the current source via a dipole using 3D source localization from

the EEG. Using this paradigm, this normally very ill-defined measure of source localization could be represented by the number of dipoles as clusters, as well as the expected starting point in the 3D space as informed from the fMRI. The mathematical resolution and degree of overlap in the 3-D areas of activation could then be determined. A proof-of-concept for this process can be made from the current data set. However, the data set from this study is a relatively small one, and this paradigm might prove more effective if trained on a larger data set and one in which it would have more impact (e.g., epilepsy). For those who suffer from epilepsy and in which medication is not working, surgical removal of the brain location becomes an advisable option. However, in surgical planning, locating the source of epileptic peaks is difficult to define in 3D space using only EEG. Using EEG informed fMRI would address this important issue.

## **10.7 Future Work – New Directions**

After each individual study presented in this thesis, possible future research areas were described and will not be reviewed in this section. Instead, broader implications for future studies based on the methodology adopted are described.

Extending the research by using participants from different demographic groups would increase the external validity of the findings. The degree to which the findings can be replicated with females and those of varying ages would increase the confidence of understanding the neural activations observed in the current study for lower limb executed and imagined movement. Another important group on which to collect similar data are those with compromised lower limb mobility. A review of animal and human cerebral plasticity, the potential of the brain to re-organize after damage (such as that from a spinal cord injury), shows promise primarily in animal models, and to some degree for upper limb function in humans [208],

particularly those with incomplete spinal cord injury [209]. This reorganization is likely due to synaptic plasticity in pre-existing circuits and the formation of new cirucuits. Such a re-organization of the sensory-motor cortex has implications for the findings of the current study insofar as EEG signals may differ in both strength and location from individuals with spinal cord injury. Obviously only the imagined condition would be relevant for such individuals, but this seems like a logical next step in ensuring that any BCI development process is built on the proper foundational information.

The CGI created for this study seemed to work well as a visual stimulus that allowed participants to keep pace when executing the task and to visualize oneself doing the task in the imagined conditions. No control (i.e., non-stimulus) condition was used in this study. It would be interesting to determine any differences between a CGI and no-stimulus condition. There would likely be less visual areas stimulated in the no-stimulus condition, and thus provide a “less noisy” set of data. However, the task might be more difficult to carry out by simply asking participants to ‘think about’ themselves walking with no visual cues to assist. Similarly, other types of cues (auditory or tactile) could be assessed as to their utility. In a similar vein, creating a heads-up display – perhaps in a set of glasses - that would carry the CGI stimulus would be an interesting avenue of future research.

The finalized network from Chapter 9 works to find a global minimum. Establishing a global minimum is preceded by the weighting or lack thereof in each neuron for each predictor. While it is customary to initialize these weights randomly, pertaining to the activation function selected (tangent function range -1 to 1 or the sigmoid function range 0 to 1), there exist alternative methods for pre-allocation of weights. An alternative presented here is to use the weighting scheme developed in the previous chapter (Chapter 8) in which weights for EEG

predictors were correlated with how well they represent the underlying hemodynamic activity. The purpose of testing these various schematics is to investigate whether or not using fMRI information provide a difference in how quickly the algorithm employed by the network converges.

The effect of pace variation was not studied. The pace of the task used was about half that of normal walking. Speeding up the task to that of normal walking might actually decrease the cognitive load, given that it would mimic a more natural gait. However, this would likely decrease the capability of differentiating right from left leg movement in the EEG data. The pace might also be slowed even further, thus allowing for even more differentiation. The effect of pace on the findings remains an empirical question yet to be answered.

This study used the neuroimaging techniques of EEG and fMRI to study lower limb movements. Other techniques such as: 1) diffuse optical imaging (DOI); event related optical signal (EROS); near infrared spectroscopy (NIRS); magnetoencephalography (MEG); Positron emission tomography (PET); and single-photon emission computed tomography (SPECT) offer other possible data acquisition options. Some require the use of radioactive material (PET and SPECT) while others are very costly (MEG), so would not likely be useful. However, it may be possible that one or more of these techniques might be useful in future research on lower limb movement, depending on the research question.

## **10.8 Conclusion**

The research conducted for this thesis adds to the existing body of knowledge in understanding psychomotor brain activity; specifically, that associated with thought coordination processes involved in the task of walking in normal persons represented by algorithmic patterns. Given how few studies there are of lower limb movement in fMRI this study is groundbreaking. The

degree of complementary and supplementary information derived the non-invasive techniques of EEG and fMRI during such a complex task will also help guide future research. The two most salient features of this research that are unique and novel are: left versus right differentiation using an indirect pathway approach and the merging of temporal and spatial resolution of brain activity (where and when).

Anticipated benefits to those affected by neurological disease or injury are tremendous in scope, including prosthetic devices that can ‘act’ by using solely neural input (i.e., thoughts). However, in order to accurately build models that compensate for deviations from a ‘normal brain’ we must first fully comprehend the cognitive processes that occur when carrying out tasks in a normal brain. The expectation is that the findings will add to the extant literature and eventually be used to assist those with compromised motor systems. For example, patients after anterior cruciate ligament (ACL) reconstruction compared with healthy normal individuals exhibited different EEG patterns while carrying out a knee angle reproduction task. Specifically, brain activity demonstrated significantly higher frontal theta-power in both limbs of the ACL group relative to the control group [210].

Knowing EEG and fMRI results based on normal subject brain patterns will help to assess deviations from them, including the extent to which it is neurologically or musculoskeletally controlled. The arithmetic relationships between executed and imagined brain activation can be used to develop more effective deep brain stimulators. Developing a real time fMRI and EEG pattern recognition algorithm for imagined limb movement will aid in the creation of real time devices that will assist motor movements for those with compromised mobility.

## REFERENCES

- [1] V. Dietz, “Degradation of neuronal function following a spinal cord injury: mechanisms and countermeasures,” *Brain*, vol. 127, no. 10, pp. 2221–2231, 2004.
- [2] T.D. Lalitharatne, K. Teramoto, Y. Hayashi, and K. Kiguchi, “Evaluation of perception-assist with an upper-limb power-assist exoskeleton using EMG and EEG signals,” In Proc. 11th IEEE Int. Conf. Networking Sensing Control, 2014, pp. 524-529.
- [3] R. Looned, J. Webb, Z. G. Xiao, and C. Menon, “Assisting drinking with an affordable BCI-controlled wearable robot and electrical stimulation: A preliminary investigation,” *J. Neuroeng. Rehabil.*, vol. 11, no. 1, pp. 1–13, 2014.
- [4] G. Leisman, A. A. Moustafa, and T. Shafir, “Thinking, walking, talking: integratory motor and cognitive brain function.,” *Front. Public Heal.*, vol. 4, p. 94, May 2016.
- [5] C. Wang, Y. Wai, B. Kuo, Y. Y. Yeh, and J. Wang, “Cortical control of gait in healthy humans: An fMRI study,” *J. Neural Transm.*, vol. 115, no. 8, pp. 1149–1158, 2008.
- [6] D. Hamacher, F. Herold, P. Wiegel, D. Hamacher, and L. Schega, “Neuroscience and biobehavioral reviews brain activity during walking: a systematic review,” *Neurosci. Biobehav. Rev.*, vol. 57, pp. 310–327, Oct 2015.
- [7] A. Presacco, L. W. Forrester, and J. L. Contreras-Vidal, “Decoding intra-limb and inter-limb kinematics during treadmill walking from scalp electroencephalographic (EEG) signals,” *IEEE Trans. Neural Syst. Rehabil. Eng.*, vol. 20, no. 2, pp. 212–219, 2012.
- [8] M. Wieser, J. Haefeli, L. Bütler, L. Jäncke, R. Riener, and S. Koeneke, “Temporal and spatial patterns of cortical activation during assisted lower limb movement,” *Exp. Brain Res.*, vol. 203, no. 1, pp. 181–191, 2010.
- [9] A. Kline and J. Desai, “Noninvasive Brain-Machine Interface to Control Both Mecha TE Robotic Hands Using Emotiv EEG Neuroheadset,” *Int. J. Med. Health Biomed. Bioeng. Pharm. Eng.*, vol. 9, no. 4, pp. 323–327, 2015.
- [10] F. Lotte, M. Congedo, A. Lecuyer, F. Lamarche, and B. Arnaldi, “A review of

classification algorithms for EEG-based brain – computer interfaces,” *J. Neural Eng.*, vol. 4, no. 2, pp. R1-R13, 2007.

- [11] M. Bönstrup, R. Schulz, J. Feldheim, F. C. Hummel, and C. Gerloff, “NeuroImage dynamic causal modelling of EEG and fMRI to characterize network architectures in a simple motor task,” *Neuroimage*, vol. 124 (Pt. A), pp. 498–508, 2016.
- [12] S. Fazli, J. Mehnert, J. Steinbrink, G. Curio, A. Villringer, K-R. Muller, et al., “Enhanced performance by a hybrid NIRS-EEG brain computer interface,” *Neuroimage*, vol. 59, no. 1, pp. 519–529, 2012.
- [13] R. Sclocco, M. G. Tana, E. Visani, I. Gilioli, F. Panzica, S. Franceschetti, et al., “EEG-informed fMRI analysis during a hand grip task: estimating the relationship between EEG rhythms and the BOLD signal,” *Front. Hum. Neurosci.*, vol. 8, pp. 1–13, April 2014.
- [14] P. de Almeida, A. Vieira, N. Canario, M Castelo-Branco and A. Caldas, “Brain activity during lower limb movement with manual facilitation – an fMRI study,” *Neurol. Res. Int.*, vol. 2015, pp. 1-14, 2015.
- [15] L. Marchal-Crespo, C. Hollnagel, M. Brügger, S. Kollias, and R. Riener, “An fMRI pilot study to evaluate brain activation associated with locomotion adaptation,” In Proc. IEEE Int. Conf. Rehabil. Robot., 2011, pp. 327–333.
- [16] J. M. Newton, Y. Dong, J. Hidler, P. Plummer-D-Amato, J. Marehbian, R. M. Albistegui-DuBois, et al., “Reliable assessment of lower limb motor representations with fMRI: Use of a novel MR compatible device for real-time monitoring of ankle, knee and hip torques,” *Neuroimage*, vol. 43, no. 1, pp. 136–146, 2008.
- [17] L. Jaeger, L. Marchal-Crespo, P. Wolf, R. Riener, L. Michels, and S. Kollias, “Brain activation associated with active and passive lower limb stepping,” *Front. Hum. Neurosci.*, vol. 8, pp. 1–14, Oct 2014.
- [18] R. D. Volta, F. Fasano, A. Cerasa, G. Mangone, A. Quattrone, and G. Buccino, “Walking indoors, walking outdoors: An fMRI study,” *Front. Psychol.*, vol. 6, pp. 1–10, Oct 2015.
- [19] H. M. Blumen, R. Holtzer, L. L. Brown, Y. Gazes, and J. Verghese, “Behavioral and

neural correlates of imagined walking and walking-while-talking in the elderly," *Hum. Brain Mapp.*, vol. 35, no. 8, pp. 4090–4104, 2014..

- [20] C. la Fougere, A. Zwergal, A. Rominger, S. Forster, G. Fesl, M. Dieterich, et al., "Real versus imagined locomotion: a [18F]-FDG PET-fMRI comparison," *Neuroimage*, vol. 50, no. 4, pp. 1589–1598, 2010.
- [21] J. Decety, "Do imagined and executed actions share the same neural substrate?," *Cogn. Brain Res.*, vol. 3, no. 2, pp. 87–93, 1996.
- [22] H. Sugata, M. Hirata, T. Yanagisawa, K. Matsushita, S. Yorifji, and T. Yoshimine, "Common neural correlates of real and imagined movements contributing to the performance of brain – machine interfaces," *Scientific Rep.*, vol. 6, pp. 1–11, April 2016.
- [23] M. Roth, J. Decety, M. Raybaudi, R. Massarelli, C. Delon-Martin, C. Segebarth, et al., "Possible involvement of primary motor cortex in mentally simulated movement: A functional magnetic resonance imaging study," *Cogn. Neurosci.*, vol. 7, no. 17, pp. 1280–1284, 1996.
- [24] G. Pfurtscheller and C. Neuper, "Motor imagery activates primary sensorimotor area in humans," *Neurosci. Lett.*, vol. 239, no. 2–3, pp. 65–68, 1997.
- [25] A. Guillot, C. Collet, V. A. Nguyen, F. Malouin, C. Richards, and J. Doyon, "Brain activity during visual versus kinesthetic imagery: an fMRI study," *Hum. Brain Mapp.*, vol. 30, no. 7, pp. 2157–2172, 2009.
- [26] F. Malouin, C. L. Richards, P. L. Jackson, F. Dumas, and J. Doyon, "Brain activations during motor imagery of locomotor-related tasks : a PET study," *Hum. Brain Mapp.*, vol. 19, no. 1, pp. 47–62, 2003.
- [27] C. E. King, P. T. Wang, L. A. Chui, A. H. Do, and Z. Nenadic, "Operation of a brain-computer interface walking simulator for individuals with spinal cord injury.," *J. Neuroeng. Rehabil.*, vol. 10, no. 1, pp. 1-14, 2013.
- [28] T. P. Luu, S. Nakagome, Y. He, and J. L. Contreras-Vidal, "Real-time EEG-based brain-computer interface to a virtual avatar enhances cortical involvement in human treadmill

walking,” *Sci. Rep.*, vol. 7, no. 1, pp. 1–12, 2017.

- [29] E. García-Cossio, M. Severens, B. Nienhuis, J. Duysens, P. Desain, N. Keijsers, et al., “Decoding sensorimotor rhythms during robotic-assisted treadmill walking for brain computer interface (BCI) applications,” *PLoS One*, vol. 10, no. 12, pp. 1–21, 2015.
- [30] C. E. King, P. T. Wang, C. M. McCrimmon, C. C. Y. Chou, A. H. Do, and Z. Nenadic, “The feasibility of a brain-computer interface functional electrical stimulation system for the restoration of overground walking after paraplegia,” *J. Neuroeng. Rehabil.*, vol. 12, no. 1, pp. 1–11, 2015.
- [31] D. G. Stuart and H. Hultborn, “Thomas Graham Brown ( 1882–1965 ), Anders Lundberg (1920 –), and the neural control of stepping,” *Brain Res. Rev.*, vol. 59, no. 1, pp. 74–95, 2008.
- [32] G. Brown, “The intrinsic factors in the act of progression in the mammal,” *Proc. R. Soc. London B*, vol. 84, no. 572, pp. 308–319, 1911.
- [33] W. O. Friesen, “Reciprocal inhibition : a mechanism underlying oscillatory animal movements,” *Neurosci. Biobeh. Rev.*, vol. 18, no. 4, pp. 547–553, 1994.
- [34] D. A. McCrea, “Spinal circuitry of sensorimotor control of locomotion,” *J. Physiol.*, vol. 533(Pt.1), pp. 41–50, 2001.
- [35] G. Cheron, M. Duvinage, C. De Saedeleer, T. Castermans, A. Bengoetxea, M. Petieau, et al., “From spinal central pattern generators to cortical network : integrated BCI for walking rehabilitation,” *Neural Plasticity*, vol. 2012, pp. 1 -13, 2012.
- [36] J. Haefeli, S. Vogeli, J. Michel, and V. Dietz, “Preparation and performance of obstacle steps: interaction between brain and spinal neuronal activity,” *Europ. J. Neurosci.*, vol. 33, no. 2, pp. 338–348, 2011.
- [37] M. Bakker, F. P. De Lange, R. C. Helmich, R. Scheeringa, B. R. Bloem, and I. Toni, “Cerebral correlates of motor imagery of normal and precision gait,” *Neuroimage*, vol. 41, no. 3, pp. 998–1010, 2008.

- [38] K. Jahn, A. Deutschlander, T. Stephan, R. Kalla, M. Wiesmann, M. Strupp, et al., “Imaging human supraspinal locomotor centers in brainstem and cerebellum,” *Neuroimage*, vol. 39, no. 2, pp. 786–792, 2008.
- [39] A. Zwergal, J. Linn, G. Xiong, T. Brandt, M. Strupp, and K. Jahn, “Aging of human supraspinal locomotor and postural control in fMRI,” *Neurobiol. Aging*, vol. 33, no. 6, pp. 1073–1084, 2012.
- [40] J. B. Nielsen, “How we walk: central control of muscle activity during human walking,” *Neuroscientist*, vol. 9, no. 3, pp. 195–204, 2003.
- [41] M. Lebedev, A. J. Tate, T. L. Hanson, Z. Li, J. E. O'Doherty, J. A. Winas, et. al, “Future developments in brain-machine interface research,” *Clinics*, vol. 66(Suppl. 1), pp. 25–32, June 2011.
- [42] A. I. Shapovalov, “Monosynaptic control over spinal motoneurons at different levels,” *Neurosci. Behv. Physiol.*, vol. 4, no. 4, pp. 123–134, 1970.
- [43] M. Lotze and U. Halsband, “Motor imagery,” *J. Physiol. Paris*, vol. 99, no. 4-6, pp. 386–395, 2006.
- [44] G. Rizzolatti and L. Craighero, “The mirror-neuron system,” *Annu. Rev. Neurosci.*, vol. 27, no. 1, pp. 169–192, 2004.
- [45] J. Decety and J. Grèzes, “The power of simulation: imagining one's own and other's behavior,” *Brain Res.*, vol. 1079, no. 1, pp. 4–14, 2006.
- [46] J. B. Nielsen, A. Butorina, A. Prokofyev, M. Nazarova, V. Litvak, and T. Stroganova, “The mirror illusion induces high gamma oscillations in the absence of movement,” *Neuroimage*, vol. 103, pp. 181–191, 2014.
- [47] M. Teplan, “Fundamentals of EEG measurement,” *Meas. Sci. Rev.*, vol. 2, pp. 1–11, 2002.
- [48] L. J. Colwell and M. P. Brenner, “Action potential initiation in the Hodgkin-Huxley model,” *PLoS Comput. Biol.*, vol. 5, no. 1, pp. 1–7, 2009.
- [49] J. Platkiewicz and R. Brette, “A threshold equation for action potential initiation,” *PLoS*

*Comput. Biol.*, vol. 6, no. 7, pp. 1-25, 2010.

- [50] I. Constant and N. Sabourdin, “The EEG signal: a window on the cortical brain activity,” *Paediatr. Anaesth.*, vol. 22, no. 6, pp. 539–552, 2012.
- [51] J. J. Carr, *Introduction to Biomedical Equipment Technology*, 4th ed. Upper Saddle River, NJ, 2001
- [52] J. T. Gwin, K. Gramann, S. Makeig, and D. P. Ferris, “Electrocortical activity is coupled to gait cycle phase during treadmill walking,” *Neuroimage*, vol. 54, no. 2, pp. 1289–1296, 2011.
- [53] V. Boulenger, B. Y. Silber, A. C. Roy, Y. Paulignan, M. Jeannerod, and T. A. Nazir, “Subliminal display of action words interferes with motor planning: a combined EEG and kinematic study,” *J. Physiol. Paris*, vol. 102, no. 1–3, pp. 130–136, 2008.
- [54] J. Wagner, T. Solis-Escalante, P. Grieshofer, C. Neuper, G. Müller-Putz, and R. Scherer, “Level of participation in robotic-assisted treadmill walking modulates midline sensorimotor EEG rhythms in able-bodied subjects,” *Neuroimage*, vol. 63, no. 3, pp. 1203–1211, 2012.
- [55] M. Seeber, R. Scherer, J. Wagner, T. Solis-Escalante, and G. R. Muller-Putz, “High and low gamma EEG oscillations in central sensorimotor areas are conversely modulated during the human gait cycle,” *Neuroimage*, vol. 112, pp. 318–326, May 2015.
- [56] S. S. Gupta and S. Agarwal, “Classification and analysis of EEG signals for imagined motor movements,” In Proc. 2015 IEEE Workshop Comput. Intell. Theor. Appl. Futur. Dir. (WCI), 2015, pp. 1-7.
- [57] G. Pfurtscheller, C. Brunner, A. Schlögl, and F. H. Lopes da Silva, “Mu rhythm (de)synchronization and EEG single-trial classification of different motor imagery tasks,” *Neuroimage*, vol. 31, no. 1, pp. 153–159, 2006.
- [58] B. Blankertz, G. Dornhege, S. Lemm, M. Krauledat, G. Curio, and K.-R. Müller, “The Berlin Brain-Computer Interface: machine learning based detection of user specific brain states,” *J. Univers. Comput. Sci.*, vol. 12, no. 6, pp. 581–607, 2006.

- [59] L. Qin, L. Ding, and B. He, "Motor imagery classification by means of source analysis for brain-computer interface applications," *J. Neural Eng.*, vol. 1, no. 3, pp. 135–141, 2004.
- [60] X. Yong and C. Menon, "EEG classification of different imaginary movements within the same limb," *PLoS One*, vol. 10, no. 4, pp. 1–24, 2015.
- [61] K. R. Müller, M. Tangermann, G. Dornhege, M. Krauledat, G. Curio, and B. Blankertz, "Machine learning for real-time single-trial EEG-analysis: from brain-computer interfacing to mental state monitoring," *J. Neurosci. Methods*, vol. 167, no. 1, pp. 82–90, 2008.
- [62] M. Severens, M. Perusquia-Hernandez, B. Nienhuis, J. Farquhar, and J. Duysens, "Using actual and imagined walking related desynchronization features in a BCI," *IEEE Trans. Neural Syst. Rehabil. Eng.*, vol. 23, no. 5, pp. 887–886, 2015.
- [63] Z. Matja, M. Zadravec, and A. Olen, "Feasibility of robot-based perturbed-balance training during treadmill walking in a high-functioning chronic stroke subject: a case-control study," *J. Neuroeng. Rehabil.*, vol. 32, no. 1, pp. 1–15, 2018.
- [64] D. T. Jeffery, J. A. Norton, F. D. Roy, and M. A. Gorassini, "Effects of transcranial direct current stimulation on the excitability of the leg motor cortex," *Exp. Brain Res.*, vol. 182, no. 2, pp. 281–287, 2007.
- [65] D. B. Plewes and W. Kucharczyk, "Physics of MRI: a primer," *J. Magn. Reson. Imaging*, vol. 35, no. 5, pp. 1038–1054, 2012.
- [66] K. Uludağ, K. Uğurbil, and L. Berliner, *fMRI: From Nuclear Spins to Brain Functions*. New York: Springer, 2015.
- [67] K. Smith, "fMRI 2.0," *Nature*, vol. 484, pp. 24–26, April 2012.
- [68] R. S. Desikan, F. Segonne, B. Fischl, B. T. Quinn, B. C. Dickerson, R. L. Buckner, et al., "An automated labeling system for subdividing the human cerebral cortex on MRI scans into gyral based regions of interest," *Neuroimage*, vol. 31, no. 3, pp. 968–980, 2006.
- [69] C. Cooreman, R. Sclocco, M. G. Tana, K. Vanderperren, E. Visani, F. Panzica, et al.,

“BOLD correlates of Alpha and Beta EEG-rhythm during a motor task,” In Proc. 2011 5th Int. IEEE/EMBS Conf. Neural Eng., 2011, pp. 25–28.

- [70] K. Isobe, T. Kusaka, K. Nagano, K. Okubo, S. Yasuda, M. Kondo, et al., “Functional imaging of the brain in sedated newborn infants using near infrared topography during passive knee movement,” *Neurosci. Lett.*, vol. 299, no. 3, pp. 221–224, 2001.
- [71] M. J. Callaghan, S. McKie, P. Richardson, and J. A. Oldham, "Effects of patellar taping on brain activity during knee joint proprioception tests using fuctional magnetic resonance imaging," *Phys. Therapy*, vol 92, no. 6, pp. 821-830, 2012.
- [72] M. Lotze, P. Montoya, M. Erb, E. Hulsmann, H. Flor, U. Klose, et al., “Activation of cortical and cerebellar motor areas during executed and imagined hand movements: an fMRI Study,” *J. Cogn. Neurosci.*, vol. 11, no. 5, pp. 491–501, 1999.
- [73] C.-J. Olsson, B. Jonsson, A. Larsson, and L. Nyberg, “Motor representations and practice affect brain systems underlying imagery: an fMRI study of internal imagery in novices and active high jumpers,” *Open Neuroimag. J.*, vol. 2, no. 1, pp. 5–13, 2008.
- [74] F. Fahoum, R. Lopes, F. Pittau, and J. Gotman, “Widespread epileptic networks in focal epilepsies: EEG-fMRI study,” *Epilepsia*, vol. 53, no. 9, pp. 1618–1627, 2012.
- [75] E. Formaggio, S. F. Storti, M. Avesani, R. Cerini, F. Milanese, A. Gasparini, et al., “EEG and fMRI coregistration to investigate the cortical oscillatory activities during finger movement,” *Brain Topogr.*, vol. 21, no. 2, pp. 100–111, 2008.
- [76] L. Yang, Z. Liu, and B. He, “EEG-fMRI reciprocal functional neuroimaging,” *Clin. Neurophysiol.*, vol. 121, no. 8, pp. 1240–1250, 2010.
- [77] R. J. Huster, S. Debener, T. Eichele, and C. S. Herrmann, “Methods for simultaneous EEG-fMRI: an introductory review,” *J. Neurosci.*, vol. 32, no. 18, pp. 6053–6060, 2012.
- [78] S. Vanni, J. Warnking, M. Dojat, C. Delon-Martin, J. Bullier, and C. Segebarth, “Sequence of pattern onset responses in the human visual areas: an fMRI constrained VEP source analysis,” *Neuroimage*, vol. 21, no. 3, pp. 801–817, 2004

- [79] J. Xu, J. Sheng, T. Qian, Y. J. Luo, and J. H. Gao, “EEG/MEG source imaging using fMRI informed time-variant constraints,” *Hum. Brain Mapp.*, vol. 39, no. 4, pp. 1700–1711, 2018.
- [80] W. Ou, A. Nummenmaa, J. Ahveninen, J. W. Belliveau, M. S. Hämäläinen, and P. Golland, “Multimodal functional imaging using fMRI-informed regional EEG/MEG source estimation,” *Neuroimage*, vol. 52, no. 1, pp. 97–108, 2010.
- [81] P. Ritter and A. Villringer, “Simultaneous EEG-fMRI,” *Neurosci. Biobehav. Rev.*, vol. 30, no. 6, pp. 823–838, 2006.
- [82] F. Moeller, H. R. Siebner, S. Wolff, H. Muhle, O. Granert, O. Jansen, et al., “Simultaneous EEG-fMRI in drug-naive children with newly diagnosed absence epilepsy,” *Epilepsia*, vol. 49, no. 9, pp. 1510–1519, 2008.
- [83] M. G. Philastides and P. Sajda, “EEG-Informed fMRI reveals spatiotemporal characteristics of perceptual decision making,” *J. Neurosci.*, vol. 27, no. 48, pp. 13082–13091, 2007.
- [84] C. G. Bénar, D. Schon, S. Grimault, B. Nazarian, B. Burle, M. Roth, et al., “Single-trial analysis of oddball event-related potentials in simultaneous EEG-fMRI,” *Hum. Brain Mapp.*, vol. 28, no. 7, pp. 602–613, 2007.
- [85] B. Horowitz and D. Poeppel, “How can EEG/MEG and fMRI/PET data be combined?,” *Hum. Brain Mapp.*, vol. 17, no. 1, pp. 1–3, 2002.
- [86] F. Miwakeichi, P. A. Valde, R. I. Goldman, and M. S. Cohen, “Concurrent EEG/fMRI analysis by multiway partial least squares,” *Neuroimage*, vol. 22, no. 3, pp. 1023–1034, 2004.
- [87] C. Bledowski, K. C., Kadosh, M. Wibral, B. Rahm, R. A. Bittner, K. Hoechstetter, et al., “Mental chronometry of working memory retrieval: a combined functional magnetic resonance imaging and event-related potentials approach,” *J. Neurosci.*, vol. 26, no. 3, pp. 821–829, 2006.
- [88] A. M. Dale, A. K. Liu, B. R. Fischl, R. L. Buckner, J. W. Belliveau, J. D. Lewine, et al.,

“Dynamic statistical parametric mapping: combining fMRI and MEG for high-resolution imaging of cortical activity,” *Neuron*, vol. 26, pp. 55–67, April 2000.

- [89] K. Mullinger, S. Debener, R. Coxon, and R. Bowtell, “Effects of simultaneous EEG recording on MRI data quality at 1.5, 3 and 7 tesla,” *Int. J. Psychophysiol.*, vol. 67, no. 3, pp. 159–60, 2008.
- [90] T. J. Cleophas and A. H. Zwinderman, *Machine Learning in Medicine - a Complete Overview*. New York: Springer, 2015.
- [91] Q. V. Le, “Building high-level features using large scale unsupervised learning,” In Proc. 2013 IEEE Int. Conf. Acoust. Speech Signal Process., 2013, pp. 8595–8598.
- [92] B. P. Battula and R. S. Prasad, “An overview of recent machine learning strategies in data mining,” *Int. J. Adv. Comput. Sci. Appl.*, vol. 4, no. 3, pp. 50–54, 2013
- [93] M. Tsang, D. Cheng, and Y. Liu, “Detecting statistical interactions from neural network weights,” In Proc. Sixth Int. Conf. Learning Representations, 2018, pp. 1–21.
- [94] C. Davatzikos, K. Ruparel, Y. Fan, D. Shen, and M. Acharyya, “Classifying spatial patterns of brain activity with machine learning methods : application to lie detection,” *Neuroimage*, vol. 28, no. 3, pp. 663–668, 2005
- [95] X. W. Wang, D. Nie, and B. L. Lu, “Emotional state classification from EEG data using machine learning approach,” *Neurocomputing*, vol. 129, pp. 94–106, April 2014.
- [96] K. A. Norman, S. M. Polyn, G. J. Detre, and J. V. Haxby, “Beyond mind-reading: multi-voxel pattern analysis of fMRI data,” *Trends Cogn. Sci.*, vol. 10, no. 9, pp. 424–430, 2006..
- [97] J. Richiardi, S. Achard, H. Bunke, and D. Van De Ville, “Machine learning with brain graphs: predictive modeling approaches for functional imaging in systems neuroscience,” *IEEE Signal Process. Mag.*, vol. 30, no. 3, pp. 58–70, 2013.
- [98] S. Lemm, B. Blankertz, T. Dickhaus, and K. R. Müller, “Introduction to machine learning for brain imaging,” *Neuroimage*, vol. 56, no. 2, pp. 387–399, 2011.

- [99] W. L. Boda, D. E. Watenpaugh, R. E. Ballard, and A.R. Hargens, “Supine lower body negative pressure exercise simulates metabolic and kinetic features of upright exercise,” *J. Appl. Physiol.*, vol 89, no. 2, pp. 649–654, 2015.
- [100] J. Fang, S. Galen, A. Vuckovic, B. A. Conway, and K. J. Hunt, “Kinetic analysis of supine stepping for early rehabilitation of walking,” *Proc. Inst. Mech. Eng. Part H J. Eng. Med.*, vol. 228, no. 5, pp. 456–464, 2014.
- [101] K. R. A. van Dijk, M. R. Sabuncu, and R. L. Buckner, “The influence of head motion on intrinsic functional connectivity MRI,” *Neuroimage*, vol. 59, no. 1, pp. 431–438, 2012.
- [102] A. Bell, D. Pedersen, and R. Brand, “A comparison of the accuracy of several hip center location prediction methods,” *J. Biomech.*, vol. 23, no. 6, pp. 617-621, 1990.
- [103] J. Challis, “A procedure for determining rigid body transformation parameters,” *J. Biomech.*, vol. 28, no. 6, pp. 733–737, 1995.
- [104] H. K. Ramakrishnan and M. P. Kadaba, “On the estimation of joint kinematics during gait,” *J. Biomech.*, vol. 24, no. 10, pp. 969–977, 1991.
- [105] B. H. Dobkin, A. Firestone, M. West, K. Saremi, and R. Woods, “Ankle dorsiflexion as an fMRI paradigm to assay motor control for walking during rehabilitation,” *Neuroimage*, vol. 23, no. 1, pp. 370–381, 2004.
- [106] M. Reuter, M. D. Tisdall, A. Qureshi, R. L. Buckner, A. J. W. van der Kouwe, and B. Fischl, “Head motion during MRI acquisition reduces gray matter volume and thickness estimates,” *Neuroimage*, vol. 107, pp. 107–115, Feb 2015.
- [107] G. H. Raymer, B. L. Allman, C. L. Rice, G. D. Marsh, and R. T. Thompson, “Characteristics of a MR-compatible ankle exercise ergometer for a 3.0 T head-only MR scanner,” *Med. Eng. Phys.*, vol. 28, no. 5, pp. 489–494, 2006.
- [108] R. H. Ghomi, M. A. Bredella, B. J. Thomas, K. K. Miller, and M. Torriani, “Modular MR-compatible lower leg exercise device for whole-body scanners,” *Skeletal Radiol.*, vol. 40, no. 10, pp. 1349–1354, 2011.

- [109] C. Hollnagel, M. Brugger, H. Vallery, P. Wolf, V. Dietz, S. Kollias, et al., "Brain activity during stepping: a novel MRI-compatible device," *J. Neurosci. Methods*, vol. 201, no. 1, pp. 124–130, 2011.
- [110] M. Damavandi, N. Farahpour, and P. Allard, "Determination of body segment masses and centers of mass using a force plate method in individuals of different morphology," *Med. Eng. Phys.*, vol. 31, no. 9, pp. 1187–1194, 2009.
- [111] M. W. Woolrich, S. Jbabdi, B. Patenaude, M. Chappell, S. Makni, T. Behrens, et al., "Bayesian analysis of neuroimaging data in FSL," *Neuroimage*, vol. 45, no. 1 Suppl, pp. S173–S186, 2009.
- [112] V. K. Noonan, M. Fingas, A. Farry, D. Baxter, A. Singh, M. G. Fehlings, et al., "Incidence and prevalence of spinal cord injury in Canada: a national perspective," *Neuroepidemiology*, vol. 38, no. 4, pp. 219-226, 2012.
- [113] M. Martinez, F. Villagra, F. Loayza, M. Vidorreta, G. Arrondo, E. Luis, et al., "MRI-compatible device for examining brain activation related to stepping," *IEEE Trans. Med. Imaging*, vol. 33, no. 5, pp. 1044–1053, 2014.
- [114] M. C. Chiu, H. C. Wu, and L. Y. Chang, "Gait speed and gender effects on center of pressure progression during normal walking," *Gait Posture*, vol. 37, no. 1, pp. 43–48, 2013.
- [115] J. E. Kline, H. J. Huang, K. L. Snyder, and D. P. Ferris, "Isolating gait-related movement artifacts in electroencephalography during human walking," *J. Neural Eng.*, vol. 12, no. 4, pp. 1-16, 2015..
- [116] J. Yinlai, S. Wang, R. Tan, K. Ishida, T. Ando, & M. G. Fujie, "Comparison of cortical activation during real walking and mental imagery of walking – the possibility of quickening walking rehabilitation by mental imaginary of walking," in *Infrared Spectroscopy - Life and Biomedical Sciences*, T. Theophandies, Ed., intechopen.com 2012, pp. 189-194.
- [117] R. J. Doyle, E. T. Hsiao-Wecksler, B. G. Ragan, and K. S. Rosengren, "Generalizability of

center of pressure measures of quiet standing," *Gait Posture*, vol. 25, no. 2, pp. 166–171, 2007.

- [118] R. J. Heitman, J. E. Kovaleski, and S. F. Pugh, "Application of generalizability theory in estimating the reliability of ankle-complex laxity measurement," *J. Athl. Train.*, vol. 44, no. 1, pp. 48–52, 2009
- [119] D. G. Wastell and G. R. Barker, "Intraclass correlations: a two-facet case study and some comments on the concept of reliability," *Bull. Psychonomic Soc.*, vol. 26, no. 6, pp. 583–586, 1988.
- [120] A. C. Grant, S. G. Abdel-Baki, J. Weedon, V. Arnedo, G. Chari, E. Koziorynska, et al., "EEG interpretation reliability and interpreter confidence: A large single-center study," *Epilepsy Behav.*, vol. 32, pp. 102–107, 2014.
- [121] L. Maes, B. M. Vinck, E. De Vel, W. D'haenens, A. Bockstael, H. Keppler, et al., "The vestibular evoked myogenic potential: A test-retest reliability study," *Clin. Neurophysiol.*, vol. 120, no. 3, pp. 594–600, 2009.
- [122] T. Harmony, T. Fernández, M. Rodríguez, A. Reyes, E. Marosi, and J. Bernal, "Test-retest reliability of EEG spectral parameters during cognitive tasks: II coherence," *Int. J. Neurosci.*, vol. 68, no. 3–4, pp. 263–271, 1993.
- [123] M. C. Salinsky, D. C. Spencer, B. S. Oken, and D. Storzbach, "Effects of oxcarbazepine and phenytoin on the EEG and cognition in healthy volunteers," *Epilepsy Behav.*, vol. 5, no. 6, pp. 894–902, 2004.
- [124] R. W. Thatcher, "Validity and reliability of quantitative electroencephalography," *J. Neurother.*, vol. 14, no. 2, pp. 122–152, 2010.
- [125] L. M. Williams, E. Simms, C. R. Clark, R. H. Paul, D. Rowe, and E. Gordon, "The test-retest reliability of a standardized neurocognitive and neurophysiological test battery: 'Neuromarker,'" *Int. J. Neurosci.*, vol. 115, no. 12, pp. 1605–1630, 2005.
- [126] J. W. Cooley and J. W. Tukey, "An algorithm for the machine calculation of complex

fourier series,” *Math. Comput.*, vol. 19, no. 90, p. 297-301, 1965.

- [127] Y. Kwon, Y. G. Choi, T. Park, A. Ziegler, and M. C. Paik, “Generalized estimating equations with stabilized working correlation structure,” *Comput. Stat. Data Anal.*, vol. 106, pp. 1–11, 2017.
- [128] A. E. Hubbard, J. Ahern, N. L., Fleischer, M. Van der Laan, S. A. Lippman, N. Jewell, et al., “To GEE or not to GEE: comparing population average and mixed models for estimating the associations between neighborhood risk factors and health,” *Epidemiology*, vol. 21, no. 4, pp. 467–474, 2010.
- [129] I. Owusu-Darko, I. K. Adu, and N. K. Frempong, “Application of generalized estimating equation (GEE) model on students’ academic performance,” *Appl. Math. Sci.*, vol. 8, no. 68, pp. 3359–3374, 2014.
- [130] L. J. Cronbach, R. Nageswari, and G. C. Cleser, “Theory of generalizability: a liberalization of reliability theory,” *Br. J. Stat. Psychol.*, vol. 16, no. 2, pp. 138–163, 1963.
- [131] T. K. Koo and M. Y. Li, “A guideline of selecting and reporting intraclass correlation coefficients for reliability research,” *J. Chiropr. Med.*, vol. 15, no. 2, pp. 155–163, 2016.
- [132] C. Mushquash and B. P. O’Connor, “SPSS and SAS programs for generalizability theory analyses,” *Behav. Res. Methods*, vol. 38, no. 3, pp. 542–547, 2006.
- [133] R. Salazer-Varas, Á. Costa, E. Iáñez, A. Úbeda, E. Hortal, and J. M. Azorín, “Analyzing EEG signals to detect unexpected obstacles during walking,” *J. Neuroeng. Rehabil.*, vol. 12, pp. 1–15, Nov 2015.
- [134] C. Cevallos, D. Zarka, T. Hoellinger, A. Leroy, B. Dan, and G. Cheron, “Oscillations in the human brain during walking execution, imagination and observation,” *Neuropsychologia*, vol. 79, pp. 223–232, 2015.
- [135] S. Ocklenburg, J. Peterburs, J. Mertzen, J. Schmitz, O. Güntürkün, and M. Grimshaw, “Effects of emotional valence on hemispheric asymmetries in response inhibition,” *Symmetry*, vol. 9, no. 8, pp. 1–13, 2017.

- [136] M. Koivisto, L. Henriksson, A. Revonsuo, and H. Railo, “Unconscious response priming by shape depends on geniculostriate visual projection,” *Eur. J. Neurosci.*, vol. 35, no. 3–4, pp. 623–633, 2012.
- [137] N. Schmitt, “Uses and abuses of coefficient alpha,” *Psychol. Assess.*, vol. 8, no. 4, pp. 350–353, 1996.
- [138] M. Wyndaele and J. J. Wyndaele, “Incidence, prevalence and epidemiology of spinal cord injury: what learns a worldwide literature survey?,” *Spinal Cord*, vol. 44, no. 9, pp. 523–529, 2006.
- [139] F. Tremblay, L. E. Tremblay, and D. E. Colcer, “Modulation of corticospinal excitability during imagined knee movements,” *J. Rehabil. Med.*, vol. 33, no. 5, pp. 230–234, 2001.
- [140] S. M. Smith, M. Jenkinson, M. W. Woolrich, et. al, “Advances in functional and structural MR image analysis and implementation as FSL,” *Neuroimage*, vol. 23, no. 1, pp. 208–219, 2004.
- [141] A. Antal, J. Baudewig, W. Paulus, and P. Dechent, “The posterior cingulate cortex and planum temporale/parietal operculum are activated by coherent visual motion,” *Vis. Neurosci.*, vol. 25, no. 1, pp. 17–26, 2008.
- [142] J. Park, “Movement disorders following cerebrovascular lesion in the basal ganglia circuit.,” *J. Mov. Disord.*, vol. 9, no. 2, pp. 71–9, 2016.
- [143] F. Cheruel, J. F. Dormont, M. Amalric, A. Schmied, and D. Farin, “The role of putamen and pallidum in motor initiation in the cat - I. Timing of movement-related single-unit activity,” *Exp. Brain Res.*, vol. 100, no. 2, pp. 250–266, 1994.
- [144] M. Lotze, G. Scheler, B. Godde, M. Erbt, W. Groddi, and N. Birbaumer, “Comparison of fMRI-activation maps during music execution and imagination in professional and non-professional string players,” *Neuroimage*, vol. 11, no. 5 Suppl., p. S67, 2000.
- [145] K. Grill-Spector, Z. Kourtzi, and N. Kanwisher, “The lateral occipital complex and its role in object recognition,” *Vision Res.*, vol. 41, no. 10–11, pp. 1409–1422, 2001.

- [146] D. M. Wolpert, S. J. Goodbody, and M. Husain, “Maintaining internal representations: the role of the human superior parietal lobe,” *Nat. Neurosci.*, vol. 1, no. 6, pp. 529–533, 1998.
- [147] D. M. Wolpert, “Computational approaches to motor control,” *Trends Cogn. Sci.*, vol. 1, no. 6, pp. 209–216, 1997.
- [148] H.-O. Karnath, B. Baier, and T. Nagele, “Awareness of the functioning of one’s own limbs mediated by the insular cortex?,” *J. Neurosci.*, vol. 25, no. 31, pp. 7134–7138, 2005.
- [149] S. Zeki, J. D. Watson, C. J. Lueck, K. J. Friston, C. Kennard, and R. S. Frackowiak, “A direct demonstration of functional specialization in human visual cortex,” *J. Neurosci.*, vol. 11, no. 3, pp. 641-649, 1991.
- [150] A. Puce, T. Allison, J. C. Gore, and G. McCarthy, “Face-sensitive regions in human extrastriate cortex studied by functional MRI,” *J. Neurophysiol.*, vol. 74, no. 3, pp. 1192–9, 1995.
- [151] T. Higo, R. B. Mars, E. D. Boorman, E. R. Buch, and M. F. S. Rushworth, “Distributed and causal influence of frontal operculum in task control,” *Proc. Natl. Acad. Sci.*, vol. 108, no. 10, pp. 4230–4235, 2011.
- [152] B. A. Vogt, D. M. Finch, and C. R. Olson, “Functional heterogeneity in cingulate cortex: The anterior executive and posterior evaluative regions,” *Cereb. Cortex*, vol. 2, no. 6, pp. 435–443, 1992.
- [153] I. R. Olson, A. Plotzker, and Y. Ezzyat, “The enigmatic temporal pole: a review of findings on social and emotional processing,” *Brain*, vol. 130, no. 7, pp. 1718–1731, 2007.
- [154] E. Koechlin, “Frontal pole function: what is specifically human?,” *Trends Cogn. Sci.*, vol. 15, no. 6, p. 241, 2011.
- [155] E. Ben-Shabat, T. A. Matyas, G. S. Pell, A. Brodtmann, and L. M. Carey, “The right supramarginal gyrus is important for proprioception in healthy and stroke-affected participants: a functional MRI study,” *Front. Neurol.*, vol. 6, pp. 1–14, Dec 2015.
- [156] R. Farivar, “Dorsal-ventral integration in object recognition,” *Brain Res. Rev.*, vol. 61, no.

2, pp. 144–153, 2009.

- [157] L. Jaeger, L. Marchal-Crespo, P. Wolf, R. Riener, S. Kollias, and L. Michels, “Test-retest reliability of fMRI experiments during robot-assisted active and passive stepping.,” *J. Neuroeng. Rehabil.*, vol. 12, no. 1, p. 102, 2015.
- [158] C. M. Bennett and M. B. Miller, “How reliable are the results from functional magnetic resonance imaging?,” *Ann. N. Y. Acad. Sci.*, vol. 1191, pp. 133–155, Mar 2010.
- [159] S. Noble, D. Scheinost, E. S. Finn, X. Shen, X. Papademetris, S. C. McEwen, et al., “Multisite reliability of MR-based functional connectivity,” *Neuroimage*, vol. 146, pp. 959–970, Feb 2017.
- [160] A. T Vu, K. Jamison, M. F. Glasser, S. M. Smith, T. Coalson, S. Moeller, et al., “Tradeoffs in pushing the spatial resolution of fMRI for the 7T Human Connectome Project,” *Neuroimage*, vol. 154, pp. 23–32, Nov 2017.
- [161] C. H. Im, A. Gururajan, N. Zhang, W. Chen, and B. He, “Spatial resolution of EEG cortical source imaging revealed by localization of retinotopic organization in human primary visual cortex,” *J. Neurosci. Methods*, vol. 161, no. 1, pp. 142–154, 2007.
- [162] G. Strobbe, S. Santens, P. Van Mierlo, H. Hallez, F. Van Opstal, Y. Rosseel, et al., “Comparison of fMRI activation and EEG source localization using beamformers during motor response in the Stroop task : preliminary results,” In Proc. 2011 8<sup>th</sup> Int. Symp. on Noninvasive Func. Source Imaging of the Brain and Heart and the 8<sup>th</sup> Int. Conf. on Bioelectromagnetism, 2011, pp. 98–102.
- [163] T. Stieglitz, B. Rubehn, C. Henle, S. Kisban, S. Herwik, P. Ruther, et al., "Brain-computer interfaces: an overview of the hardware to record neural signals from the cortex," in *Progress in Brain Research*, vol. 175, Neurotherapy: Progress in Restorative Neuroscience and Neurology, J. Herhaagen et al. (Eds), Amsterdam :Elsevier, 2009, pp. 297-215
- [164] T. O. Zander and C. Kothe, “Towards passive brain-computer interfaces: applying brain-computer interface technology to human-machine systems in general,” *J. Neural Eng.*,

vol. 8, no. 2, 2011.

- [165] B. Blankertz, M. Tangermann, C. Vidaurre, S. Fazli, C. Sannelli, S. Haufe, et al., “The Berlin brain-computer interface: non-medical uses of BCI technology,” *Front. Neurosci.*, vol. 4, pp. 1–17, Dec 2010.
- [166] D. P. Murphy, O. Bai, A. S. Gorgey, J. Fox, W. T. Lovegreen, B. W. Burkhardt, et al., “Electroencephalogram-based brain-computer interface and lower-limb prosthesis control: a case study,” *Front. Neurol.*, vol. 8, pp. 1–8, Dec 2017.
- [167] G. Pfurtscheller, C. Guger, G. Müller, G. Krausz, and C. Neuper, “Brain oscillations control hand orthosis in a tetraplegic,” *Neurosci. Lett.*, vol. 292, no. 3, pp. 211–214, 2000.
- [168] E. S. Nurse, P. J. Karoly, D. B. Grayden, and D. R. Freestone, “A generalizable brain-computer interface (BCI) using machine learning for feature discovery,” *PLoS One*, vol. 10, no. 6, pp. 1–22, 2015..
- [169] A. W. Salmon, R. A Schmidt, and C. B. Walter, “Knowledge of results and motor learning : a review and critical reappraisal,” *Psychol. Bull.*, vol. 95, no. 3, pp. 355–386, 1984
- [170] C. B. Holroyd and M. G. H. Coles, “The neural basis of human error processing: reinforcement learning, dopamine, and the error-related negativity,” *Psychol. Rev.*, vol. 109, no. 4, pp. 679–709, 2002.
- [171] V. Mnih, Y. Zhan, H. B. Ammar, and M. E. Taylor, “Theoretically-grounded policy advice from multiple teachers in reinforcement learning settings with applications to negative transfer,” In Proc. Twenty-fifth Int. Jt. Conf. Artif. Intell., 2016, pp. 2315–2321.
- [172] I. Dokare and N. Kant, “Classification of EEG signal for imagined left and right hand movement for brain computer interface applications,” presented at International Technological Conference-2014, Mumbai, India, 2014, pp. 1-8.
- [173] S. B. Kotsiantis, “Supervised machine learning : a review of classification techniques,” *Informatica*, vol. 31, no. 3, pp. 249–268

- [174] S. Jain, K. Gourab, S. Schindler-Ivens, and B. D. Schmit, "EEG during pedaling: evidence for cortical control of locomotor tasks," *Clin. Neurophysiol.*, vol. 124, no. 2, pp. 379-390, 2013.
- [175] Y. Hashimoto and J. Ushiba, "EEG-based classification of imaginary left and right foot movements using beta rebound," *Clin. Neurophysiol.*, vol. 124, no. 11, pp. 2153–2160, 2013.
- [176] M. S. Treder, A. Bahramisharif, N. M. Schmidt, M. A. Van Gerven, and B. Blankertz, "Brain-computer interfacing using modulations of alpha activity induced by covert shifts of attention," *J. Neuroeng. Rehabil.*, vol. 8, no. 1, 2011.
- [177] P. Bobrov, A. Frolov, C. Cantor, I. Fedulova, M. Bakhnyan, and A. Zhavoronkov, "Brain-computer interface based on generation of visual images," *PLoS One*, vol. 6, no. 6, 2011.
- [178] T. Gruber, M. M. Muller and A. Keil, "Modulation of induced gamma band response in a perceptual learning task in the human EEG," *J. Cogn. Neurosci.*, vol. 14, no. 5, 732-744, 2002.
- [179] P. Dayan and L. F. Abbott, "Theoretical neuroscience: computational and mathematical modeling of neural systems," *J. Cogn. Neurosci.*, vol. 15, no. 1, pp. 154-155, 2003.
- [180] P. Bush and T. Sejnowski, "Inhibition synchronizes sparsely connected cortical neurons within and between columns in realistic network models," *J. Comput. Neurosci.*, vol. 3, no. 2, pp. 91–110, 1996.
- [181] R. J. Douglas, K. A. C. Martin, and D. Whitteridge, "A canonical microcircuit for neocortex," *Neur. Comp.*, vol. 1, no. 4, pp. 480-488, 1989.
- [182] D. Attwell and S. B. Laughlin, "An energy budget for signaling in the grey matter of the brain," *J. Cereb. Blood Flow Metab.*, vol. 21, no. 10, pp. 1133–1145, 2001.
- [183] Y. Lecun, L. Bottou, Y. Bengio, and P. Haffner, "Gradient-based learning applied to document recognition," *Proc. IEEE*, vol. 86, no. 11, pp. 2278-2324, 1998.
- [184] X. Glorot, A. Bordes, and Y. Bengio, "Deep sparse rectifier neural networks," In Proc.

14th Int. Conf. Artif. Intell. Stat., 2011, pp. 315–323.

- [185] E. Candes, J. Romberg, and T. Tao, "Stable Signal Recovery from Incomplete and Inaccurate Measurements" *Comm. Pure Appl. Math.*, vol. 59, no. 8, pp. 1207–1223, 2005.
- [186] G. Luo, "A review of automatic selection methods for machine learning algorithms and hyper-parameter values," *Netw. Model. Anal. Heal. Informatics Bioinforma.*, vol. 5, no. 1, p. 1-18, 2016.
- [187] Y. Bengio, "Practical recommendations for gradient-based training of deep architectures," in *Neural Networks: Tricks of the Trade*, G. Montavon, G. Orr, and K-R. Muller (Eds). New York: Springer, 2012, pp. 437–478.
- [188] H. J. Hwang, K. Kwon, and C. H. Im, "Neurofeedback-based motor imagery training for brain-computer interface (BCI)," *J. Neurosci. Methods*, vol. 179, no. 1, pp. 150–156, 2009.
- [189] R. B. Rao, G. Fung, and R. Rosales, "On the dangers of cross-validation. an experimental evaluaion," In Proc. 2008 SIAM International Conference on Data Mining, 2008, pp. 1-9..
- [190] V. Morash, O. Bai, S. Furlani, P. Lin, and M. Hallett, "Classifying EEG signals preceding right hand, left hand, tongue, and right foot movements and motor imageries" *Clin. Neurophysiol.*, vol. 119, no. 11, pp. 2570–2578, 2008.
- [191] L. Duan, M. Bao, J. Miao, Y. Xu, and J. Chen, "Classification based on multilayer extreme learning machine for motor imagery task from EEG signals," *Procedia Comput. Sci.*, vol. 88, pp. 176–184, 2016.
- [192] S. Vieira, W. H. L. Pinaya, and A. Mechelli, "Using deep learning to investigate the neuroimaging correlates of psychiatric and neurological disorders: methods and applications," *Neurosci. Biobehav. Rev.*, vol. 74, pp. 58–75, 2017.
- [193] F. S. Panchal and M. Panchal, "Review on methods of selecting number of hidden nodes in artificial neural network," vol. 3, no. 11, pp. 455–464, 2014.
- [194] S. Karsoliya, "Approximating number of hidden layer neurons in multiple hidden layer

BPNN architecture," *Int. J. Eng. Trends Technol.*, vol. 3, no. 6, pp. 714–717, 2012.

- [195] J. R. Wolpaw, "Brain-computer interface research comes of age: traditional assumptions meet emerging realities," *J. Mot. Behav.*, vol. 42, no. 6, pp. 351–353, 2010.
- [196] J. Bergstra, D. L. K. Yamins, and D. D. Cox, "Making a Science of Model Search: Hyperparameter Optimization in Hundreds of Dimensions for Vision Architectures," *Icml*, pp. 115–123, 2013.
- [197] P. Gergondet, A. Kheddar, C. Hintermüller, C. Guger, and M. Slater, "Multitask humanoid control with a brain-computer interface: user experiment with HRP-2," In Proc. ISER'12 13th International Symposium on Experimental Robotics, 2012, pp 1-15.
- [198] Y. He, D. Eguren, J. M. Azorin, R. G. Grossman, T .P. Luu, and J. L. Contreras-Vidal, "Brain-machine interfaces for controlling lower-limb powered robotic systems," *J. Neural Eng.*, vol. 15, no. 2, pp. 1-15, 2018.
- [199] D. Stathakis, "How many hidden layers and nodes?," *Int. J. Remote Sens.*, vol. 30, no. 8, pp. 2133–2147, 2009.
- [200] G. Hinton, L. Deng, D. Yu, G. E. Dahl, A. Mohamed, N. Jaitly, et al., "Deep neural networks for acoustic modeling in modern speech recognition," *IEEE Signal Process. Mag.*, vol. 29, no. 6, pp. 82–97, 2012.
- [201] D. Shen, G. Wu, and H. Suk, "Deep learning in medical image analysis," *Annu. Rev. Biomed. Eng.*, vol. 19, no. 1, pp. 221–248, 2017.
- [202] W. Samek, A. Binder, G. Montavon, S. Lapuschkin, and K. R. Müller, "Evaluating the visualization of what a deep neural network has learned," *IEEE Trans. Neural Networks Learn. Syst.*, vol. 28, no. 11, pp. 2660–2673, 2017.
- [203] Z. Obermeyer and E. J. Emanuel, "Predicting the future-big data, machine learning, and clinical medicine," *N Engl J Med*, vol. 375, no. 13, pp. 1216–1219, 2016.
- [204] S. Debener, M. Ullsperger, M. Siegel, and A. K. Engel, "Single-trial EEG-fMRI reveals the dynamics of cognitive function," *Trends Cogn. Sci.*, vol. 10, no. 12, pp. 558–563,

2006.

- [205] S. Debener, M. Ullsperger, M. Siegel, K. Fiehler, D. Y. von Cramon, and A. K. Engel, “Trial-by-trial coupling of concurrent electroencephalogram and functional magnetic resonance imaging identifies the dynamics of performance monitoring,” *J. Neurosci.*, vol. 25, no. 50, pp. 11730–11737, 2005.
- [206] P. Ritter and A. Villringer, “Simultaneous EEG-fMRI,” *Neurosci. Biobehav. Rev.*, vol. 30, no. 6, pp. 823–838, 2006.
- [207] M. Uji, R. Wilson, S. T. Francis, K. J. Mullinger, and S. D. Mayhew, “Exploring the advantages of multiband fMRI with simultaneous EEG to investigate coupling between gamma frequency neural activity and the BOLD response in humans,” *Hum. Brain Mapp.*, vol. 39, no. 4, pp. 1673–1687, 2018..
- [208] R. Nardone Y. Holler, F. Brigo, M. Seidl, M. Christova, J. Bergmann, et al., "Functional brain reorganization after spinal cord injury: systematic review of animal and human studies," *Brain Res.*, vol. 1504, pp. 58-73, April 2013.
- [209] O. Rainteau and M. E. Schwab, "Plasticity of motor systems after incomplete spinal cord injury," *Nat. Rev. Neurosci.*, Vol. 4, no. 4, pp. 263-273, 2001.
- [210] J. Baumeister, K. Reinecke, and M. Weiss, “Changed cortical activity after anterior cruciate ligament reconstruction in a joint position paradigm: an EEG study,” *Scand. J. Med. Sci. Sport.*, vol. 18, no. 4, pp. 473–484, 2008.

## APPENDIX A: SAMPLE MRI SCREENING FORM



### Functional Connectivity in Lower Limb Movement Using EEG and fMRI: Understanding Locomotion to Design a BCI Questionnaire

First Name: \_\_\_\_\_ Last Name: \_\_\_\_\_

Age: \_\_\_\_\_

Weight (lbs): \_\_\_\_\_

Email: \_\_\_\_\_

Telephone Number: \_\_\_\_\_

Do you suffer from any previous or existing neurological conditions: (E.g. Epilepsy, brain lesions, strokes etc.)?

Do you have any existing knee ailments: (E.g. surgery, ligament strains/ruptures, meniscus tears etc.)?

Do you have any of the following (please mark)? If you do you will not be permitted to participate in the study.

Item	Yes	No
------	-----	----

Bone pins/screws/plates

Joint replacements

Pacemaker

Recent tattoos

-----  
For researcher use:

Subject ID #: \_\_\_\_\_

Principal Investigator: Dr. Janet Ronsky

Student Investigator: Adrienne Kline

## **APPENDIX B: REGISTRATION OF MRI DATA**

Functional scans underwent slice timing correction. Because slices were collected in an interleaved fashion, it was necessary to perform a linear sinc interpolation between every other slice. These scans were then registered to structural scans on a per participant basis. Specifically, each of the four functional runs unerwent a boundry based registration (BBR) process where the individual voxel values served to isolate changes in boundaries (white and grey matter, brain and skull, skull and air) to register to each person's T1 MRI. This was accomplished with the FLIRT graphic user interface (GUI) in FSL. This information was then, in turn, registered to standard image space (i.e., atlas space). Registration to non-linear group average (MNI152 2mm brain) used an affine transformation with 12 degrees of freedom (3 translations, 3 rotations, 3 shear, 3 scales). Cost functions for both of these registrations were done using ordinary least squares.

## APPENDIX C: PREDICTING fMRI FROM EEG

This thesis has demonstrated the strength in merging EEG and fMRI to understand brain function and the current capabilities of machine learning to explore the complex connections between electrical activity and hemodynamic activity. As such, something I wish to follow up on is implementing machine learning on a simultaneous fMRI and EEG data set, and determine using a Generative Adversarial Network (GAN) the accuracy of this model in predicting fMRI based solely on EEG data. The data from the current study is a relatively small set, but this paradigm could be more effective if trained on a larger data set and one in which it would have more impact (i.e., the field of epilepsy). For those who suffer from epilepsy and for whom medication is not working, surgical removal of the brain location becomes an advisable option. However, in surgical planning, locating the source of epileptic peaks is hard to define in 3D space using only EEG, due to the ill-defined nature of EEG-3D source localization.

A more useful approach in localizing the source of epileptic peaks would combine fMRI and EEG data. Using a cascade of convolutional networks, implementation of a Laplacian pyramid architecture to generate fMRI data in a coarse to fine fashion would simplify the fMRI data into a single 2D image (comprised of all available slices). A variety of network architectures would need to be tested for this, where the final model would be decided on based on both manual inspection (image output) and heuristics (minimization of the  $\ell_2$  error in pixel space).

Given the number of predictors present in fMRI, a large training set would be required in order to pursue this approach (i.e., on the order of hundreds). Given the current study is comprised of only 16 data sets, and generating fMRI for a healthy population is low yielding, the plan would be to make this a future area of research for a project that focuses on epilepsy.